Self adaptive turbulence models for unsteady compressible flows Modèles de turbulence auto-adaptatifs pour la simulation des écoulements compressibles instationnaires

Grégoire Pont

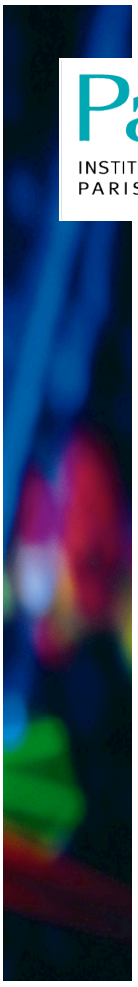

ParisTech
INSTITUT DES SCIENCES ET TECHNOLOGIES
PARIS INSTITUTE OF TECHNOLOGY

ARTS ET MÉTIERS ParisTech

2015-ENAM-0008

École doctorale n° 432 : science des métiers de l'ingénieur

Doctorat ParisTech
T H È S E

pour obtenir le grade de docteur délivré par

l'École Nationale Supérieure d'Arts et Métiers

Spécialité " Mécanique "

présentée et soutenue publiquement par

Grégoire Pont

le 8 avril 2015

Self adaptive turbulence models for unsteady compressible flows

Modèles de turbulence auto-adaptatifs pour la simulation des écoulements compressibles instationnaires

Directeurs de thèse : **Paola Cinnella, Jean-Christophe Robinet**
Co-encadrement de la thèse : **Pierre Brenner**

Jury

M. Jean-Pierre CROISILLE,	**Professeur, Université de Lorraine et CNRS**	**Président**
Mme. Maria-Vittoria SALVETTI,	Professeur, Unité de recherche, Université de Pise	Rapporteur
M. Philippe SPALART,	Senior Technical Fellow, Boeing	Rapporteur
M. Ivan MARY,	Ingénieur de recherche, DSNA, ONERA	Examinateur
Mme. Paola CINNELLA,	Professeur, Université de Salento	Examinateur
M. Jean-Christophe ROBINET	Professeur, Arts et Mériers ParisTech	Examinateur
M. Pierre BRENNER,	Expert CFD, Airbus Defence & Space	Examinateur

T H È S E

Arts et Métiers ParisTech - Centre de Paris
Nom de l'Unité de recherche

Remerciements

Ma thèse s'est déroulée conjointement à Dynfluid (laboratoire des Arts et Métiers Paristech) et dans le service Fluid Mechanics d'Airbus Defence & Space (Les Mureaux). Réaliser l'interface entre un laboratoire de recherche et un industriel fut une expérience des plus enrichissantes qui m'a permis de participer directement à l'évolution du code FLUSEPA® en étant totalement en prise avec ses utilisateurs industriels. Ce fut aussi l'opportunité de consolider le Pont entre industrie et recherche scientifique :-)

Je remercie Monsieur Jean-Pierre Croisille qui m'a fait l'honneur de présider mon jury de thèse.

Je remercie tout particulièrement Maria-Vittoria Salvetti, Philippe Spalart et Ivan Mary pour leurs rôles d'examinateurs et de rapporteurs, pour l'intérêt qu'ils ont porté à mes travaux et pour m'avoir fait part de remarques constructives. Ce jury a pu me faire profiter d'un point de vue tant industriel qu'académique en adéquation avec le contexte de ma thèse.

Je remercie Jean-François Pallegoix sans qui cette thèse n'aurait pas vu le jour. Je le remercie de m'avoir donné la chance d'intégrer son équipe au sein d'Airbus Defense & Space.

Je remercie Pierre Brenner, encadrant industriel de cette thèse et expert CFD chez Airbus Defence & Space. Tout au long de sa carrière, Pierre a su à la fois inventer des méthodes très innovantes mais aussi, et c'est une étape cruciale, les implémenter de façon efficace dans un code industriel. Il en résulte que FLUSEPA est devenu l'un des codes de calcul les plus innovants et des plus compétitifs dans le monde de la CFD. Il est utilisé quotidiennement par Airbus Defense & Space (et MBDA) pour modéliser des configurations complexes (tant géométriquement que phénoménologiquement) de lanceurs spatiaux. Pierre m'a montré l'existence de différents chemins de pensée grâce auxquels, certains problèmes jugés insolubles ont pu être surmontés. L'innovation ne peut naître que dans une constante remise en question des pensées conventionnelles : ne jamais s'arrêter aux idées reçues. J'ai appris, tous les jours pendant ma thèse, et je continue, aujourd'hui, car j'ai la chance de travailler avec cet Ayatollah des volumes finis quotidiennement.

Je remercie Paola Cinnella, ma directrice de thèse, pour les échanges particulièrement constructifs que nous avons eus tant sur l'analyse des méthodes numériques que sur les modèles de turbulences. Je la remercie surtout de m'avoir encouragé et aidé à participer à des conférences scientifiques qui figureront parmi mes meilleurs souvenirs de thèse. En effet, présenter ses travaux mais surtout échanger ses points de vue avec les concepteurs ou utilisateurs des différentes méthodes (que cela concerne les modèles de turbulence ou les schémas numériques), est une étape indispensable à la recherche scientifique : ces échanges permettent de conforter ou de remettre en cause les choix et directions empruntés.

Un grand merci aussi à Jean-Christophe Robinet, mon second directeur de thèse, pour tous les échanges que nous avons eus et pour son implication dans mon travail. C'est vraiment un grand plaisir et une importante source d'inspiration que de discuter avec Jean-Christophe. En effet, je suis toujours reparti avec une idée nouvelle ou un nouvel axe de recherche en ressortant de ces échanges : partager sa vision phénoménologique de la physique a participé d'une façon très importante à mes travaux.

Merci beaucoup à Bruno pour cette collaboration fructueuse. J'espère que nous pourrons encore travailler ensemble à l'avenir.

Merci à toute l'équipe du laboratoire Dynfluid. Ça a été un vrai plaisir de côtoyer chaque jour cette équipe de chercheurs dynamiques. Merci à Cédricou, Xavier G et Simon pour leur disponibilité, pour avoir répondu à chacune de mes interrogations dans leur domaine de prédilection. Merci à tous les thésards qui ont contribué à l'excellente ambiance de ces trois années : Elie, Florian, Mathieu, Jean-Christophe, Miloud, Karim, Wouter, Ronan et Corentin.

Merci aussi à toute l'équipe d'Airbus Defence & Space : TomTom, le corse, Juan Marco de la vega, Fabichou, Lorris, Bob, Max d'avoir contribué à l'excellente ambiance de travail. Merci à David Deprés de m'avoir partagé son expérience des écoulements massivement décollés. Merci à Davidou et au Basque pour

toute l'aide qu'ils m'ont apportée lors de la préparation des calculs sur lanceurs dans un laps de temps très court. Merci beaucoup à Jean-Marie qui, par son travail dans le domaine du HPC, a considérablement accéléré le code de calcul et m'a aidé à me familiariser avec le nouvel environnement de programmation.

Je remercie infiniment mes parents qui m'ont permis de faire mes études sans lesquelles je ne serai pas là aujourd'hui. Et pour finir un immense merci à ma petite Hélène qui m'a supporté pendant ces trois années et m'a redonné du courage dans les moments difficiles.

"S'il n'y pas de solution, c'est qu'il n'y a pas de problème."

(Les Shadocks)

Contents

Chapter 1

Context of the study

Contents

1.1 Context

The domain of aerospace is an interesting and vast playing field for aerodynamics engineers. The physics of flows encountered in the aerospace domain is mostly composed of a series of more or less unsteady and violent transient phase which brings out, at the same time, compressible effects, highly turbulent flow separations, aerothermals phenomena, multi-species chemistry loaded by particles... For industries, it is essential to reproduce these phenomena using numerical simulation on realistic geometries, in order to design vehicles and wind tunnel tests or to understand and try to control this phenomena. Aerodynamics plays a very important role in the design chain of space vehicles. Unsteady transient phases like blast waves or stage separation for example are simulated using unsteady averaged Navier-Stokes equations for many years in Airbus Defence & Space [1] (see section 3.1 page 37 for more details).
Many of these problems are actually related to the presence of massive separated flows with highly unsteady turbulence and nowadays, it becomes affordable for industrial to simulate them, thanks to increased computational resources. These simulations give access to unsteady loads caused by significant pressure fluctuations and their dominating frequencies. For example, payloads carried out in space launcher fairings are sensitive to aerodynamic and aeroacoustic perturbations which may come from the blast wave coming from the ducts on the launch pad during the take off, from the massive flow separation on the shrinkages during the atmospheric flight, from interactions between the propulsive jets and the external flow during the phases of stages separations or violent heat flux and aerodynamic stability at atmospheric reentry... These pressure fluctuations are due to, for example, highly turbulent flow separations which expose the mechanical parts (cylinders, nozzle...) of the launcher engine to unsteady and potentially intense loads (figure 1.1). Numerical simulations of these phenomena enable industrial users to achieve more accurate safety margins during the design process. It becomes also more and more important to understand the physics of these flows, in order to, in second hand, try to control and reduce their potentially harmful effects (thermal fluxes, fluid structure interaction, re-combustion phenomena ...). Space launchers are not

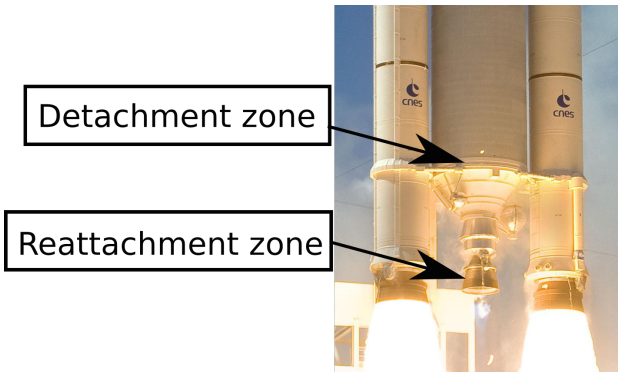

Figure 1.1: Location of the binding area on Ariane 5 space launcher

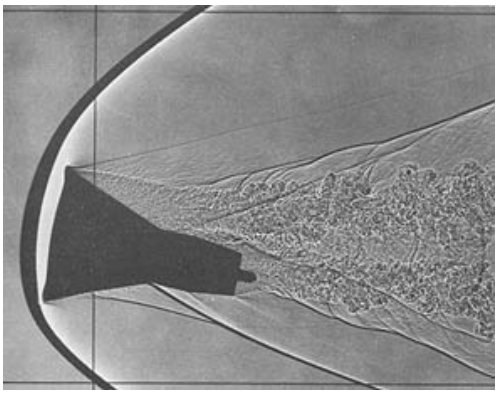

Figure 1.2: Shadowgraph of Gemini capsule model in flight-stability tests[2]

the only examples of vehicles where unsteady turbulence plays a significant role. Re-entry capsules are also a good illustration. The dynamic stability of re-entry capsules is largely influenced by laminar-turbulence transition, strong shock waves and wake unsteadiness. This family of flows is an exciting challenge for CFD [1] and require accurate and robust simulation tools.

The present study is a contribution to the development of a reliable simulation tool for aerospace launcher aerodynamics. The work is divided into four main parts which are the ingredients of such a CFD tool. First, we describe the aerodynamic phenomena encountered in space launcher aerodynamics, and we discuss of the validity of turbulence models to simulate this family of flow, with focus on self-adaptive, hybrid RANS[2]/LES[3] models. Then, we describe the simulation tool FLUSEPA [4], developed by Airbus Defense & Space. A high order numerical method for compressible turbulent flow calculations is described in detail, and some improvements are proposed to increase its resolvability and make it more suitable for scale-resolving computations. The following chapter deals with hybrid RANS/LES turbulence models, their improvement and their validation in conjunction with the present numerical strategy. Finally, we apply the resulting global strategy to real-world space launcher configurations.

[1] Computational Fluid Dynamics
[2] Reynolds Averaged Navier-Stokes
[3] Large Eddy Simulation
[4] http://www.bulletins-electroniques.com/actualites/36354.htm

1.1.1 Aerodynamic of space launchers and physical mechanisms

Boundary-layer separation

We can distinguish two major types of boundary-layer separations: the first one is separation induced by the geometry. In this case, the separation is clearly imposed by geometrical elements, e.g. sharp corners. The second one is separations induced by adverse pressure gradients. In this case, the separation is strongly influenced by the dynamics of the incoming boundary-layer and specifically by its turbulence rate. The more intense the turbulence is, the more the boundary-layer can resist to adverse pressure gradients. From a computational point of view, it is obviously easier to simulate the first type of separation than the second type. Aerodynamics of space launchers are dominated by massive separations which occur in the flow around the after-body. Flow separation is a highly three- dimensional process which can result in dynamic loads that disturb the launcher stability. In the separation bubble generated behind the after-body, a primary source of turbulent fluctuations is the free shear-layer generated downstream of the separation point. Kelvin-Helmholtz convective instabilities, develop in this shear-layer and are convected downstream, up to the reattachment point.

Separating/reattaching flows

The domain of space launcher aerodynamics is widely dominated by separating/reattaching flows. The objective of this paragraph is to provide an overview of this family of flows, to give an idea of the difficulties associated to such phenomena, and especially for their simulation. The simplest and most popular separating/reattaching flow is the backward facing step flow. This configuration is two-dimensional with regard to the geometry and the mean flow but fully three-dimensional concerning the unsteady flow motion. Several experiments have been conducted to investigate this flow, for instance : Hall *et al.* [3], Kostas *et al.* [4], Lee *et al.* [5], Spazzini *et al.* [6], Moreau *et al.* [7], as well as several: like the DES [5] of Sainte- Rose *et al.* [9] the ZDES of Deck [10], the DNS of Hung Le *et al.* [11], Driver *et al.* [12]. Backward facing step flows are a good prototype for after-body aerodynamics, and exhibit several unsteady phenomena. First, a Kelvin-Helmholtz vortex shedding appears at the separation point followed by a pairing process highlighted by the hot-wire techniques experiment of Troutt *et al.* [13] . Hairpin-like vortical structures have been observed in the recirculation bubble by Kiya and Sisaki [14]. On the other side, several researcher describe the presence of another unsteady phenomena, called flapping motion, which is a low frequency instability. The backward facing step flow is a very good test case for self-adaptive hybrid RANS/LES models because the Kelvin-Helmholtz instability is difficult to be captured without delay due to the convective character of this instability and of the turbulent viscosity coming from the boundary-layer (in the RANS mode) before the separation point. The mean flow is also interesting to be studied and changes according to the Reynolds number or the characteristics of the incoming boundary-layer. Figure 1.3 shows a sketch of a characteristic mean flow for a turbulent backward facing step. This mean flow is characterized by a separation point, located at the step corner point, a recirculation bubble, a reattachment point where the boundary-layer starts to recover, and a secondary corner vortex, whose the dimensions are larger or smaller depending on several flow parameters. The mean flow is interesting to be studied because it generates the main steady loads such as drag and lift . It is also a convergence indicator for unsteady calculations. Note that when the flow is confined by an upper wall as in figure 1.3, the increase in the channel section dowstream of the step section generates an adverse pressure gradient, which can lead to thickening or separation of the upper boundary-layer, as can be seen on figure 1.3. In this study, we use this flow to assess several turbulence models and numerical schemes in section 4.1, page 76.

A more complex separating/reattaching flow also considered in the present research, with features closer to those of an aerospace launcher, is represented by the axisymmetric backward facing step. This was investigated experimentally by Deprés *et al.* [15] and Meliga *et al.* [16]. The after-body retained for this numerical study was originally designed to be representative of a space launcher vehicle first stage. This case has been studied in details by Weiss [17] in his PhD through a zonal DES on a very fine grid. These results are taken as a reference hereafter. This test case is also used in this study to assess several turbulence models and numerical strategies in section 4.2 page 82.

[5] Detached Eddy Simulation [8]

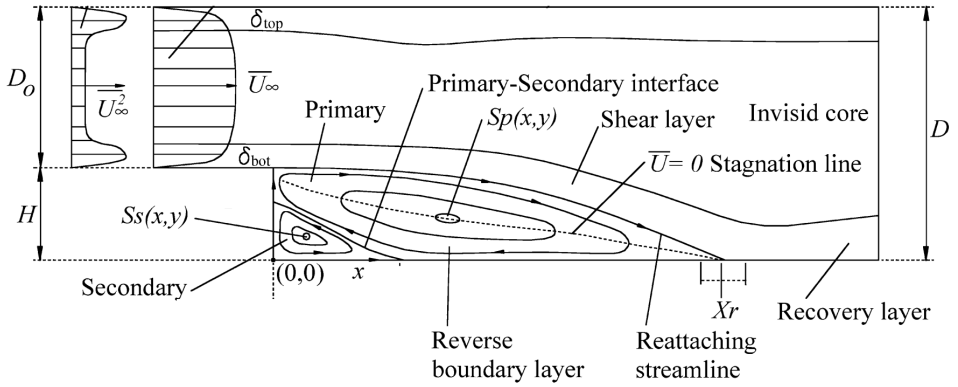

Figure 1.3: Mean flow regions of a turbulent backward facing step flow in the longitudinal plane [3]

Boundary-layer to shear-layer : the transition region

Especially to validate the hybrid RANS/LES approaches, it is essential to know if and how the incoming boundary-layer plays a role in separations induced by geometry. Attached boundary-layers are fully modeled (RANS mode) with RANS/LES methods. Since there is no spectral content in a RANS attached boundary-layer, only information about the integral quantities, such as the boundary-layer thickness and the velocity profile are available at the RANS/LES interface. However, turbulent structures in the incoming attached boundary-layer may influence formation of the separated region. The so-called transition region, where the incoming boundary-layer gives origin to the shear-layer at the boundary between the separated region and the main flow, has been studied by several authors, at least for low Reynolds number flows. Since the scope on this study is the flow past spatial launchers, we focus the bibliography study on high Reynolds number flows. Morris and Foss [18] studied the transition region between a boundary-layer and a single-stream shear-layer. Using a correlation technique on a backward facing step flow at high Reynolds number ($Re_\theta = 4650$ where θ is the momentum thickness of the boundary-layer) they found that there is no correlation between velocities measured in the boundary-layer and in the shear-layer. They conclude that only the integral properties of the boundary-layer are important in the separation process. Abbott and Kline [19] come to the same conclusion. They varied the turbulence intensity in the boundary-layer (1 to 18 %) for a double-step flow at high Reynolds number ($1 \times 10^{-4} < Re_\delta < 2 \times 10^{-4}$) where δ is the boundary-layer thickness) . They concluded that the upstream boundary layer characteristics (especially the spectral properties) do not affect the separation region for such a Reynolds number range. Based on such study, we conclude that it is possible to apply hybrid RANS/LES strategies to the numerical simulation of massively separated/reattached flows, and that the spectral content of the upstream boundary-layer has a negligible effect on the separation bubble: only the thickness of the incoming boundary-layer matters.

Low frequency aerodynamics loads on spatial launchers

Buffeting is a low-frequency unsteady phenomenon which occurs at the base of spatial launchers experiences large pressure fluctuations. It is important not to confuse with the buffeting which can occur on aircrafts wings : this is also a low frequencies but it results from a shock/boundary-layer interaction. Weiss, in his PhD [20], studies this phenomenon using multi-dimensional Fourier analysis and orthogonal decomposition on a simplified launcher after-body, namely, the axisymmetric backward facing step. He brings out the spatial organization of the fluctuating energy for several range of frequencies 1.4. He distinguishes three main frequency on the emergency along the wall. Figure 1.4 shows that the normalized dominating frequencies are $St_D = 0.08$, $St_D = 0.2$, $St_D = 0.6$ (where St_D is a Strouhal number based on the diameter of the bigger cylinder on figure 1.4). After integration of pressure fluctuations on the launcher wall, Marié *et al.* [21] bring out aerodynamic load on an axi-symmetric backward facing step. The resulting load

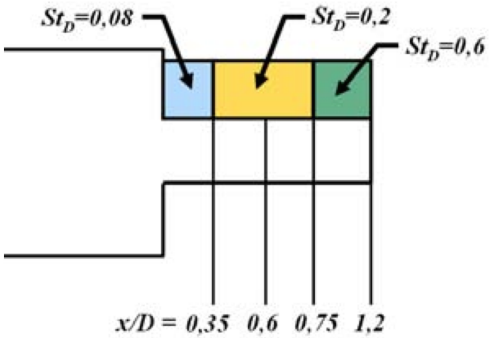

Figure 1.4: Spatial organization of the dominating frequencies on antisymmetric backward facing step [20]

recovered after the integration is the buffeting phenomenon ($St_D = 0.2$). The study of Marié *et al.* shows also the influence of the sensor distribution to calculate correctly the dynamic loads on the launchers.

For industry, it is very important to capture these phenomena: not only their dominating frequencies but also their levels. In this study, we develop numerical strategy, based on high-accurate approximation schemes and advanced turbulence models, to calculate correctly the pressure fluctuations in the recirculation area of spatial launchers.

On the importance of the grid resolution in the spanwise direction

Turbulence is a three-dimensional mechanism. This can be seen by taking into account the vorticity transport equation, for barotropic compressible flows:

$$\frac{\partial \boldsymbol{\omega}}{\partial t} + \mathbf{u}.\boldsymbol{\nabla}\boldsymbol{\omega} = \boldsymbol{\omega}.\boldsymbol{\nabla}\boldsymbol{u} + \nu\boldsymbol{\nabla}^{\mathbf{2}}\boldsymbol{\omega} \tag{1.1}$$

The left hand side of the previous equation represents the material derivative of the vorticity $\boldsymbol{\omega}$, $D\boldsymbol{\omega}/Dt$. The term $\nu\boldsymbol{\nabla}^{\mathbf{2}}\boldsymbol{\omega}$ on the right hand side is the viscous diffusion. The term $\boldsymbol{\omega}.\boldsymbol{\nabla}\boldsymbol{u}$, coming from the nonlinear term on the Navier-Stokes equations, is called the stretching-rotating term. It represents the effect of the gradients $\boldsymbol{\nabla}\boldsymbol{u}$ on the vorticity field $\boldsymbol{\omega}$. It can be seen as a production of vorticity $\boldsymbol{\omega}$ by the velocity gradient $\boldsymbol{\nabla}\boldsymbol{u}$. This this term is responsible for the inertial energetic cascade. In 2D, one can prove that $\boldsymbol{\omega}.\boldsymbol{\nabla}\boldsymbol{u}$ is equal to zero: the turbulence is necessarily a 3D mechanism. This 3D mechanism can be explained by the figure 1.5 . The vortical structures ω_1 are stretched in the shear direction, and generate shear in the perpendicular direction which interact with the ω_2 vortical structure .
Therefore, it is essential not to overlook the grid resolution in the spanwise direction, if this is not the case, the turbulence mechanism is blocked and the vortical structures remain too large compared to the physical ones. The effect of spanwise grid resolution is studied on a 2D backward facing step in section 4.1 page 76 and by Deck and Torigny [22] on a axisymmetric backward facing step. A low resolution in the spanwise direction has exactly the same effect than a too high numerical dissipation. To be more convinced, we can take a little ahead and see the figure 1.6 which is discussed more in detail in the chapter concerning the validation of turbulence models (chapter 4 page 76). This figure represents a backward facing step calculation where only the number of point in the spanwise direction is doubled, twice. It demonstrates the importance of grid refinement in the spanwise direction, which is a very crucial parameter in hybrid RANS/LES simulations.

1.2 Scale separation

Turbulence is due to the non-linearity of the convection term of the Navier-Stokes equations. For high Reynolds numbers, velocity fluctuations cover a large band of wave numbers and frequencies but the energy spectrum does not extend to infinity. Indeed, smaller turbulent structures are subject to the viscosity effects, which transform the kinetic energy into heat and which ensure the non-reversibility of

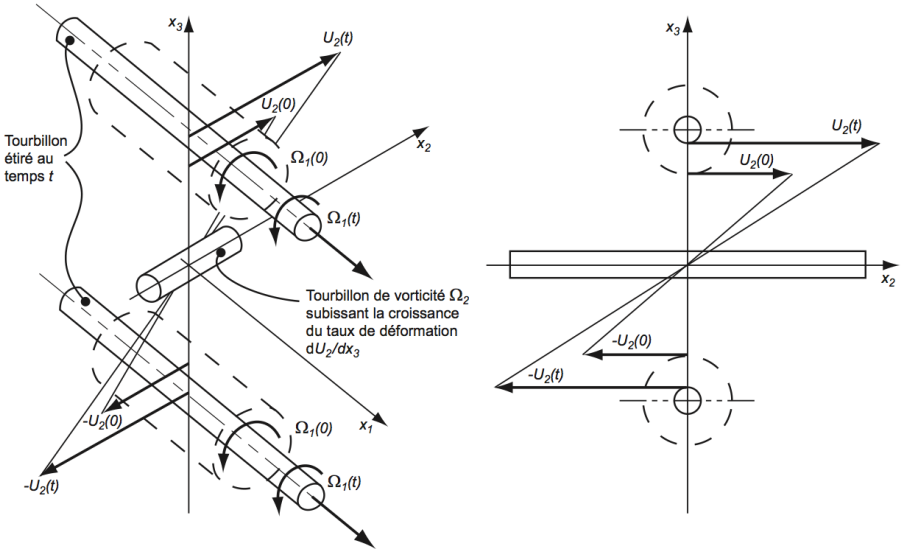

Figure 1.5: Sketch of the turbulence mechanism [23, 24]

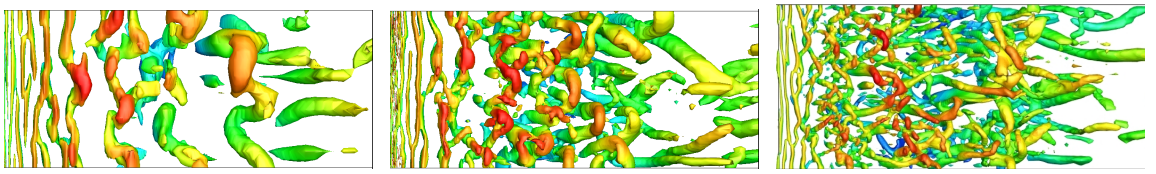

(a) Grid 1

(b) Grid 2: Grid 1 x 2 in the spanwise direction

(c) Grid 3: Grid 2 x 2 in the spanwise direction

Figure 1.6: Iso surface of $\lambda_2 = -7000$ colored by mean velocity.

the flow. This phenomenon play an essential role in the evolution of turbulent flows. Dissipative scales may be very small compared with the most energetic structures of the flow but stay large compared to the molecular scales. Thus, Navier-Stokes equations are theoretically suited to describe turbulent flows. However, current computing resources do not allow to industrially resolve directly Navier-Stokes equations. In many turbulent flows, for sufficiently high Reynolds numbers, the statistics in the scale range $l_0 \ll l \ll \eta$ define the inertial part of the energy spectrum (where l_0 represents the largest scale, l the integral scale and η the dissipative scale of turbulence) which have a universal behavior determined by l and the dissipation rate ϵ. This concept is called Kolmogorov's similarity hypothesis and the famous '$-5/3$' slope is directly related to it. Under this hypothesis, a scale separation can be set up in order to explicitly resolve large scales and model dissipative ones. In practice, this separation is made by filtering Navier-Stokes equations :

$$f(\mathbf{x},t) = \overline{f}(\mathbf{x},t) + f'(\mathbf{x},t), \tag{1.2}$$

where $\overline{f}(\mathbf{x},t)$ is the resolved part and $f'(\mathbf{x},t)$ the modeled part of a given aerodynamic filed. We write the compressible Navier Stokes equations using the Favre averaged variables:

$$\widetilde{f} = \frac{\overline{\rho f}}{\overline{\rho}} \tag{1.3}$$

Note that the operator $\overline{\bullet}$ is an arbitrary scale separation operator. Introduction of this decomposition in the Navier-Stokes equations gives for the conservation of mass :

$$\frac{\partial \overline{\rho}}{\partial t} + \frac{\partial}{\partial x_j}\left(\overline{\rho}\widetilde{u}_i\right) = \mathcal{A}, \tag{1.4}$$

and for the conservation of momentum :

$$\frac{\partial \overline{\rho}\widetilde{u}_i}{\partial t} + \frac{\partial}{\partial x_j}\left(\overline{\rho}\widetilde{u}_i\widetilde{u}_j\right) = -\frac{\partial \overline{p}}{\partial x_i} - \frac{\partial}{\partial x_i}\widetilde{\tau}_{ij} + \frac{\partial}{\partial x_j}\widetilde{\tau}_{sgs} + \mathcal{B}, \tag{1.5}$$

in which $\overline{p}$ is the filtered pressure and $\widetilde{\tau_{ij}}$ is the viscous stress tensor, defined as :

$$\widetilde{\tau_{ij}} = \overline{\mu}\left(\frac{\partial \widetilde{u}_i}{\partial x_j} + \frac{\partial \widetilde{u}_j}{\partial x_i} - \frac{2}{3}\delta_{ij}\frac{\partial \widetilde{u}_k}{\partial x_k}\right), \tag{1.6}$$

and $\widetilde{\tau_{sgs}}$ is the turbulent stress tensor, is given by :

$$\widetilde{\tau_{sgs}} = \overline{\rho}\left(\widetilde{u_i u_j} - \widetilde{u}_i\widetilde{u}_j\right) \tag{1.7}$$

where $\overline{\mu}$ denotes the mean dynamic viscosity, and δ_{ij} denotes the Kronecker delta function. It is important to note that, for the general case, the filtering operator and the spatial and temporal derivative operators are not commutative. The two quantities $\mathcal{A}$ and $\mathcal{B}$ are additional terms which come from this non-commutativity specified in the following.

1.2.1 Large Eddy Simulation (LES)

We consider the scale separation operator defined by:

$$\overline{f} = \int G(\mathbf{x}-\boldsymbol{\eta},\Delta) f(\boldsymbol{\eta}) d\boldsymbol{\eta}, \tag{1.8}$$

where G is a filter function and Δ is a filter width. In the following, we find the expression of the non-commutativity terms. We can differenciate the resolved field $\overline{f}$:

$$\frac{\partial \overline{f}}{\partial x_i} = \int \frac{\partial G(\mathbf{x}-\boldsymbol{\eta},\Delta)}{\partial x_i} f(\eta) d\eta + \int G(\mathbf{x}-\boldsymbol{\eta},\Delta)\frac{\partial f(\boldsymbol{\eta})}{\partial x_i} d\boldsymbol{\eta} \tag{1.9}$$

$$= \int \frac{\partial G(\mathbf{x}-\boldsymbol{\eta},\Delta)}{\partial x_i} f(\boldsymbol{\eta}) d\boldsymbol{\eta} + \overline{\frac{\partial f}{\partial x_i}}. \tag{1.10}$$

$$\tag{1.11}$$

The relationship between $\overline{\frac{\partial f}{\partial x_i}}$ and $\frac{\partial \overline{f}}{\partial x_i}$ finally reads:

$$\overline{\frac{\partial f}{\partial x_i}} = \frac{\partial \overline{f}}{\partial x_i} - \frac{\partial \Delta}{\partial x_i} \int \frac{\partial G(\mathbf{x}-\eta,\Delta)}{\partial \Delta} f(\eta) d\eta. \tag{1.12}$$

We can see, by looking the expression of the non-commutativity term in equation (1.12), that this extra term depends on the variation of the grid spacing. We can assume that, when the grid spacing changes smoothly, the terms $\mathcal{A}$ and $\mathcal{B}$ can be neglected. In section 1.2.3, we discuss about these terms and their influence on the simulation and especially when different filtering strategy are coupled.

For conventional LES, the grid spacing changes smoothly, thus, we can assume that $\mathcal{A} = \mathcal{B} = 0$ in the following. The conservation of mass equation becomes:

$$\frac{\partial \overline{\rho}}{\partial t} + \frac{\partial}{\partial x_j}\left(\overline{\rho}\widetilde{u}_i\right) = 0, \tag{1.13}$$

and for the conservation of momentum:

$$\frac{\partial \overline{\rho}\widetilde{u}_i}{\partial t} + \frac{\partial}{\partial x_j}\left(\overline{\rho}\widetilde{u}_i\widetilde{u}_j\right) = -\frac{\partial \overline{p}}{\partial x_i} - \frac{\partial}{\partial x_i}\widetilde{\tau}_{ij} + \frac{\partial}{\partial x_j}\widetilde{\tau}_{sgs} \tag{1.14}$$

$$\widetilde{\tau}_{ij} = \overline{\mu}\left(\frac{\partial \widetilde{u}_i}{\partial x_j} + \frac{\partial \widetilde{u}_j}{\partial x_i} - \frac{2}{3}\delta_{ij}\frac{\partial \widetilde{u}_k}{\partial x_k}\right) \tag{1.15}$$

$$\widetilde{\tau}_{sgs} = \overline{\rho}\left(\widetilde{u_i u_j} - \widetilde{u}_i\widetilde{u}_j\right) \tag{1.16}$$

$\widetilde{\tau}_{sgs}$ is called the subgrid stress tensor. It represents the impact of the modeled scale on the resolved ones. The LES closure consist in finding a model for $\widetilde{\tau}_{sgs}$. The most famous closure model for LES is the Smagorinsky one [25]:

$$(\widetilde{\tau}_{sgs})_{ij} - \frac{1}{3}(\widetilde{\tau}_{sgs})_{kk}\delta_{ij} = -2\mu_{sgs}S_{ij}, \tag{1.17}$$

where

$$\mu_{sgs} = \rho(C_s\Delta)^2 \mid \sqrt{2S_{ij}S_{ij}} \mid, \tag{1.18}$$

where Δ is a characteristic grid size ($\Delta = (\Delta_x\Delta_y\Delta_z)^{1/3}$)), and S_{ij} is the strain rate tensor

$$S_{ij} = \frac{1}{2}\left(\frac{\partial \widetilde{u}_i}{\partial x_j} + \frac{\partial \widetilde{u}_j}{\partial x_i}\right). \tag{1.19}$$

This subgrid scale model is simple but it allows to understand the philosophy of LES [6]. The idea is to model the Kolmogorov dissipation, in other words, to model the phenomenon responsible for the transformation of kinetic energy into heat at small scales of turbulence. In the Smagorinsky model, an artificial viscosity μ_{sgs} plays the role of dissipation. The Smagorinsky model is based on the characteristic grid size Δ. To be consistent, the computational grid has to be refined to reach the Kolmogorov length. In some alternative approaches called ILES [7] [26], the filter is not explicit. It is represented by the combination between the numerical dissipation and the computational grid. Such strategies need, to be consistent, a good knowledge about the numerical dissipation in use. More particularly, the user has to know exactly the transfer function of the numerical scheme in the spectral space. For example, Garnier [27] studied the properties of a large variety of highly dissipative shock capturing numerical schemes and suggests conditions to be consistent with LES approaches.

[6] There are several subgrid model in the literature more efficient that the Smagorinsky one, but it is not the purpose of this study

[7] Implicit Large Eddy Simulation

1.2.2 Reynolds Averaged Navier Stokes (RANS)

In most of engineering applications, averaged quantities (lift, drag, mean pressure repartition...) are sufficient in order to design a system. The most widely used method consists in using a scale separator based on average values. The ensemble average is the most general operator. It is based on the hypothesis of an infinite number of realizations of the same flow:

$$\overline{f}_o = \lim_{N\to\infty}\left[\frac{1}{N}\sum_{n=0}^{N} f(\mathbf{x},t)\right] \tag{1.20}$$

Obviously, having an infinite number of realizations of a same flow is impossible in practice. The arithmetic average is a good estimator of the ensemble average (1.20), if the number of realization is large enough. In the case of a steady flow, the ergodicity theorem [28] allows to transform the overall average into a time average:

$$\overline{f}_T = \lim_{T\to\infty}\left[\frac{1}{T}\int_t^{t+T} f(\mathbf{x},t)\right] \tag{1.21}$$

The ergodicity hypothesis is based on the steadiness of the mean aerodynamic field. If a unsteady mean flow is considered, using a time average instead of a ensemble average is not straightforward. For example, let us call T_2 the period of slow oscillation (mean value $\overline{f}(\mathbf{x},t)$) and T_1 the period of fluctuations. The ergodicity hypothesis can be applied if it exists an interval T such as $T_1 \ll T \ll T_2$. In other words, characteristic times T_1 and T_2 have to be separated by several order of magnitude (see figure1.7). However, in engineering applications, according to Wilcox [29], this hypothesis is almost never verified. For this reason, unsteady RANS simulations (URANS) have to be used very carefully. The scale separation

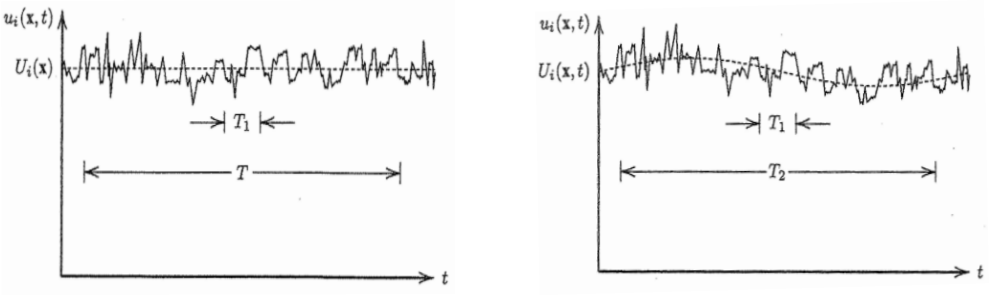

(a) Steady Turbulence (b) Unsteady Turbulence

Figure 1.7: Validation domain of ergodicity hypothesis [29].

of equation (1.2) is called the Reynolds decomposition if the scale separation operator is the time average (1.21). We can point out that the time averaged operator is directly commutative with derivatives. In this case, we have $\mathcal{A} = \mathcal{B} = 0$. In other words the URANS equations are, for the conservation of mass:

$$\frac{\partial\overline{\rho}}{\partial t} + \frac{\partial}{\partial x_j}\left(\overline{\rho}\widetilde{u}_i\right) = 0, \tag{1.22}$$

and for the conservation of momentum:

$$\frac{\partial\overline{\rho}\widetilde{u}_i}{\partial t} + \frac{\partial}{\partial x_j}\left(\overline{\rho}\widetilde{u}_i\widetilde{u}_j\right) = -\frac{\partial\overline{p}}{\partial x_i} - \frac{\partial}{\partial x_i}\widetilde{\tau}_{ij} + \frac{\partial}{\partial x_j}\widetilde{\tau}_{RANS} \tag{1.23}$$

$$\widetilde{\tau_{ij}} = \overline{\mu}\left(\frac{\partial\widetilde{u}_i}{\partial x_j} + \frac{\partial\widetilde{u}_j}{\partial x_i} - \frac{2}{3}\delta_{ij}\frac{\partial\widetilde{u}_k}{\partial x_k}\right) \tag{1.24}$$

$$\widetilde{\tau}_{RANS} = \overline{\rho}\left(\widetilde{u_i u_j}\right). \tag{1.25}$$

First, we can remark that the LES (equations (1.16)) and the URANS equations are formally equivalent, only the nature of scale separator changes. In the RANS formulation, $\widetilde{\tau}_{RANS}$ is called the Reynolds stress tensor. This tensor represents the interaction between the mean flow and the unresolved turbulent structures. Here again, a mathematical closure is necessary to complete RANS equations. The most famous closure is the Boussinesq hypothesis [30]:

$$(\widetilde{\tau}_{RANS})_{ij} - \frac{1}{3}(\widetilde{\tau}_{RANS})_{kk}\delta_{ij} = -2\mu_t S_{ij}, \tag{1.26}$$

where S_{ij} is the strain rate tensor and μ_t is called the turbulent viscosity. This coefficient is expressed as a function of turbulence scales, for example a characteristic length and velocity: $\mu_t = ul$. The scales u and l can be obtain by using transport equations. Finally, we can remark that the Boussinesq closure equation is similar to the Smagorinsky closure (see equation (1.17)).

1.2.3 Hybrid RANS/LES strategies

The philosophy of RANS/LES is to locally model attached boundary-layer or poorly resolved regions of the computational domain by using RANS, and switch to LES in order to resolve unsteady phenomena, such as boundary-layer separations or turbulent shear-layers, if the resolution is fine enough. This approach is based on the fact that the RANS and LES equations are formally the same, only the scale separator changes [31].

Limitations of RANS strategies

URANS approaches are limited in term of resolved frequencies and scales. For example, let us consider a transport equation for an arbitrary quantity Θ:

$$\frac{D\Theta}{Dt} = P^{\Theta} - D^{\Theta}_{\text{est}} + D^{\Theta}_{\text{iff}} \tag{1.27}$$

Where $\frac{D}{Dt}$ is the operator for total derivative. P^{Θ}, D^{Θ}_{est} and D^{Θ}_{iff} are respectively the production, dissipation and diffusion term of Θ. In most turbulence models, the production term is written as a function of the strain rate tensor S_{ij} or as a function of vorticity tensor ω_{ij}. Similarly, S_{ij} or ω_{ij} are written as a function of mean velocity gradients. Therefore we can write S_{ij} (or ω_{ij})$\sim 1/T$, where $1/T$ is the characteristic frequency of the mean flow. This means that, the only information that the turbulence model capture from the external flow is the characteristic frequency of the mean flow. On the other hand, the diffusion term can be written as follow:

$$D^{\Theta}_{\text{iff}} = \frac{\partial}{\partial y}\left(\frac{\mu_t}{\sigma}\frac{\partial \Theta}{\partial y}\right) \propto \mu_t \frac{\Theta}{\delta^2} \tag{1.28}$$

where σ is a diffusion coefficient and δ the thickness of mean shear-layer. This means that all of the scales that are lower than δ are dissipated by the turbulent viscosity μ_t. In other words, the only frequency which can be resolved by an URANS strategy is the characteristic frequency of the mean flow and scales of the order of magnitude of the mean shear-layer. For example, in the case of a turbulent flow past a cylinder, an URANS turbulence model resolves an unsteady flow composed of vortical structures of a diameter $D/2$ at the frequency of $Str_D = 0.2$ (Str_D is the Strouhal number based on the diameter of the cylinder), which is the classical von Kármán eddy street frequency.
The second limitation is due to the roughness of the Boussineq closure equation, according to which the Reynolds stress tensor and the strain rate tensor are linearly related. As a consequence, history effects, anisotropic and time relaxation of turbulence are not taken into account by this model. A good example of this is provided by the Tucker-Reynolds experiment (see figure 1.8 (a) and (b)): a constant strain is applied to a flow and then stops brutally. We see that, when the strain rate is stopped, the turbulent kinetic energy, represented by the symbols on figure 1.8 (b), decreases slowly, by effect of a kind of inertia, whereas, the turbulence modeled by the Boussinesq hypothesis vanishes brutally.

To overcome this limitation, one option is to add quadratic terms to the Boussinesq model, or to write a transport equation for each component of the Reynolds stress tensor as in the so called Reynolds Stress, or RSM models. Some authors propose to add another transport equation to take into account the history of turbulence. Olsen et Coackey [32], for example, introduce a transport equation for eddy viscosity in order to model the non-equilibrium effect on the Reynolds stress tensor.

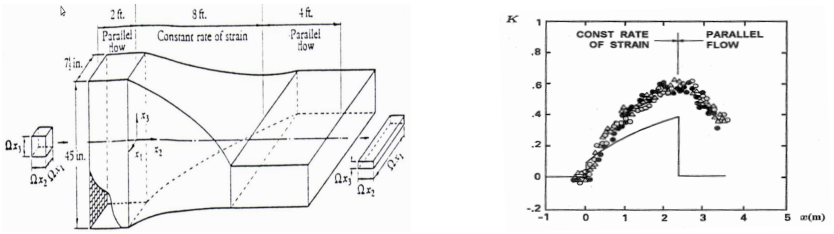

(a) Experimental set up

(b) Results

Figure 1.8: Tucker-Reynolds experiment [29]

Limits of LES strategies

A well resolved LES means that the dissipation model, the numerical filter, or the explicit filter used only operates from the Kolmogorov scales of turbulence. Concerning industrial applications, for a well resolved LES, the grid has to be fine enough to resolve all the turbulence spectrum until the dissipative scales everywhere in the flow (even in attached boundary-layers). Actually, LES methods can lead to inaccurate results if the mesh size and/or the scheme accuracy are not good enough to resolve correctly most of the relevant flow scales. In complex industrial applications, the energy spectrum is often ill defined and changes from one point to another of the simulation, so that it is difficult to warrant a sufficient resolution everywhere, unless extremely fine meshes are used.

On the importance of the extra terms

We said previously that in the LES part of the flow, where the grid size and so the filter width varies very smoothly, and in the RANS part of the flow, we can consider that the extra terms due to the non-commutativity are equal to zero: $\mathcal{A} = \mathcal{B} = 0$. Nevertheless, in the interface between RANS and LES, where the filter width varies rapidly, this extra terms may not be negligible. Hamba [33] carried out a study to demonstrate the influence of the extra terms. Precisely, he considered a Germano's [34] hybrid RANS/LES filtering strategy through a blending parameter k such as:

$$\overline{f} = k\overline{f}^{LES} + (1-k)\overline{f}^{RANS}. \tag{1.29}$$

Hamba considers the extra terms appearing in the LES part of the flow and especially in the RANS/LES interface. It is particularly interesting to study the influence of the extra terms which appear in the resolved and modeled kinetic energy transport equation (which is derived from the Navier-Stokes equations). The extra terms in the modeled kinetic energy and resolved kinetic energy transport equation are similar and opposite. They represent the energy transfer between the modeled and the resolved part of the flow due to the change of filter width. Thanks to a turbulent channel flow simulation, the author shows that in this interface between RANS and LES, the rms of the extra terms exhibit non-zero values as large as the rms of resolved terms. These extra terms are responsible for resolved kinetic energy production in the LES part of the flow. Figure 1.9 shows the energy budget of the resolved and modeled kinetic energy. We can see that the diffusion generated by the extra terms in the modeled part of the flow is cannot be neglected and negative and there is the same diffusion in the resolved part but positive. This study demonstrates that there is an energy transfer from the modeled kinetic energy toward the resolved one and this transfer is due to the non-commutativity terms between the filter operation and the spatial derivative. This energetic balance between the resolved and modeled kinetic energy is necessary to ensure the conservation of energy through RANS/LES interfaces. Taking into account these extra terms seems to be very important to ensure energy conservation in regions characterized by a quick variation of filter width. Rocha [35] in his paper shows also this dependency of the extra terms in a boundary-layer simulation. Moreover, taking into account these extra terms, reduces the influence of blending function k choice. It is important to note that both studies are realized on boundary-layer and channel flow. Including the extra terms avoids log-layer mismatch. Additionally, these studies are realized with zonal Hybrid RANS/LES approach where the blending function is imposed locally in the grid and where RANS and LES filters are explicitly known.

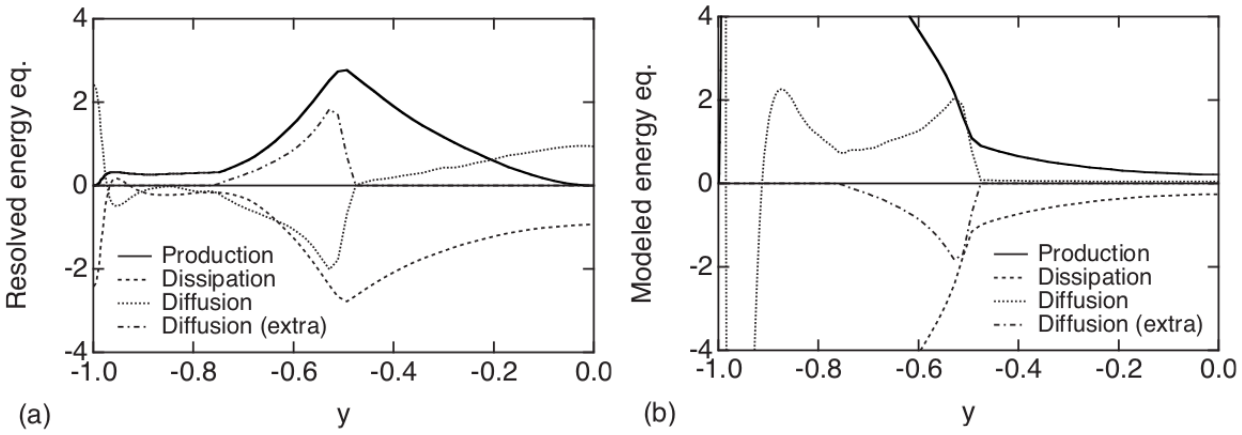

Figure 1.9: Kinetic energy budget in the turbulent channel flow .a) Resolved kinetic energy ; b) Modeled kinetic energy. [33].

Further studies are required to prove that the hybrid terms are also important in more complex flows, specially when massive flow separation controls the flow dynamics. In practice, for industrial applications it is difficult to consider these extra terms in the Navier-Stokes equations, especially for global (non-zonal) Hybrid RANS/LES approaches. In general, the filters are not explicitly known, and the extra terms cannot be calculated because they depend on the filter width. Another difficulty is that the nature of Navier-Stokes and transport equations could change with the addition of these terms, which may require significant modifications of the discretization scheme

Zonal RANS/LES strategies

The idea of the so-called zonal approach requires specifying beforehand regions of the computational domain where LES and RANS models are applied [10],[36],[37]. Indeed, there is not a better solution than a RANS solution for an attached boundary-layer with a RANS grid resolution [8]. With zonal RANS/LES, there is no log layer mismatch or grid induced separation as mentioned by Spalart [38]. For these reasons, zonal approaches seems to be powerful. The problem is that the user has to explicitly define different regions as RANS or as LES, which is very hard to do for complex geometries considered in an industrial context. Zonal approaches are very useful for research in fluid dynamics to understand in details complex physical mechanisms but cannot be easily transferred to industry due to their non-predictive nature. Note that zonal approach has proved its interest for investigating fine flow features for well-calibrated configurations (see for example [10, 39]).

Global RANS/LES strategies

Global RANS/LES strategies [38, 40, 41, 42, 43] are the opposite side of zonal strategies. The interface between RANS and LES parts of the flow is not defined by the user. In theory, the solution self adapts to the grid and corresponds automatically to the best solution, i.e, a RANS solution for attached boundary-layer for very low resolved part of the flow and a LES solution in the well resolved part of the flow. The common pathology for all global RANS/LES models is the well known grey zone (each model has its own). The grey zone is characterized by the difficulty for a model to switch automatically from RANS to LES mode or vice versa at the right place in the flow. This may lead to grid-induced separation or log-layer mismatch (see e.g. [38]). For massively separated flows, which are the object of this study, the most important issue is to preserve attached RANS boundary-layers. In other words, in an attached boundary-layers, the kinetic energy have to be 100 % modeled, because a grid suited for RANS is unable to support an LES resolution.
The other weakness of these strategies concerns a possible delay in the triggering of convective instabilities.

[8] RANS models are calibrated so as to modeled perfectly attached boundary-layer

This weakness is principally due to the amount of RANS eddy viscosity coming from upstream attached boundary-layers. This problem is even greater for space vehicles which measure tens of meters long. Nevertheless, we will see in section 4 that the thickness of incoming boundary is not the only element responsible for the delay of convective instabilities. Indeed, the numerical viscosity introduced by the discretization sensitivity plays also a very important role.
Global methods remain the most suitable ones from an engineering point of view, since they require less user-defined parameters than zonal approaches. Thus, even if they cannot be finely tuned to the same extent of the zonal approach for a given configuration, they have better potential for predictive flow simulations. A variety of automatic hybrid RANS/LES model has been proposed in the literature [38, 40, 41, 42, 43]. In this study, we investigate and assess the hybrid model by Perot & Gadebush [41], the DDES (Delayed Detached Eddy Simulation)approach of Spalart [38] and the scale adaptive simulation (SAS) of Menter [42] (see Section 2 page 22 for details).

1.3 Accurate and robust, finite-volume methods for industry

1.3.1 Finite volume method

Finite volume method is the name of a discretization technique by which the integral formulation of the conservation laws are discretized directly in the physical space. This method's strength lies in the fact that it is totally mesh independent, as long as the meshes are made of closed cells. The finite volume method is naturally conservative. We look for the numerical solutions of the compressible Navier-Stokes equations in Reynolds-Averaged form or in filtered form, and supplemented by a turbulence or subgrid model, respectively. Both of them can be formally written as a system of conservation laws of the form:

$$\frac{d}{\partial t}\iiint_{\Omega_{CV}} \mathbf{w} d\Omega = -\oiint_{A_{CV}} \mathbf{F}\mathbf{n} dS + \iiint_{\Omega_{CV}} \mathbf{S} d\Omega \tag{1.30}$$

where Ω_{CV} is a fixed control volume with boundary A_{CV}, $\mathbf{n}$ is the outer-oriented unit normal, $\mathbf{w}$ is the conservative variable vector, $\mathbf{F}$ is the flux density and $\mathbf{S}$ is the source terms vector. For a single species flow, these quantities are given by:

$$\mathbf{w} = (\rho, \rho\mathbf{u}, \rho E, W_{tm})^T \tag{1.31}$$

$$\mathbf{F} = \mathbf{F_E} + \mathbf{F_D} \tag{1.32}$$

where the inviscid flux $\mathbf{F_E}$ is given by:

$$\mathbf{F_E} = (\rho\mathbf{u}, \rho\mathbf{u}\otimes\mathbf{u} + p\mathbf{I}, \rho\mathbf{u}H, F_{tm})^T \tag{1.33}$$

and the viscous flux $\mathbf{F_D}$ is

$$\mathbf{F_D} = (0, \boldsymbol{\tau} + \boldsymbol{\tau_t}, (\boldsymbol{\tau} + \boldsymbol{\tau_t}).\mathbf{u} - \mathbf{q} - \mathbf{q_t})^T \tag{1.34}$$

In equation (3.10), W_{tm} is the variables comes from the turbulence model in use. For example, for a $k-\epsilon$ model, $W_{tm} = \rho k, \rho\epsilon$. In equation (1.33), F_{tm} represents the numerical fluxes due to the turbulent variables. In equations (3.10) and (1.34), ρ is the density, $\mathbf{u}$ the velocity vector, p the pressure, E the specific total energy, H the specific total enthalpy, $\boldsymbol{\tau}$ the viscous stress tensor and $\mathbf{q}$ the head flux vector. The preceding flow properties have to be integrated as averaged or filtered quantities, according to the equation in use (RANS or LES). More generally, $\mathbf{w}$ represents the resolved part of the flow, i.e, the average field or the large scale of the turbulence flow, for RANS ans LES, respectively. In addition, $\boldsymbol{\tau_t}$ is the Reynolds/subgrid stress tensor, and $\mathbf{q_t}$ the turbulent heat flux, which models the effect of the non-resolved part of the flow on the resolved one. In the following, $\boldsymbol{\tau_t}$ is described by using an eddy viscosity model (Boussinesq), and is supposed to be related to the average/filtered velocity gradient via an eddy viscosity coefficient ν_t. A simple turbulent Fourier law introducing a constant turbulent Prandl number is used to model $\mathbf{q_t}$.
The numerical resolution of the equation (3.10) is presented in the section 3.2 page 41. To compute ν_t, automatic hybrid RANS/LES models are considered in section 2 page 22.

1.3.2 Turbulence models and numerical schemes: a strong coupling

There are three kinds of viscosity in a numerical simulation of turbulent flow: the laminar viscosity ν, the eddy viscosity ν_t introduced by RANS (Boussinesq hypothesis) or SGS model in use, and numerical viscosity ν_n intrinsic to the numerical scheme [9]. The main idea of a hybrid turbulence model is to reduce the turbulent viscosity ν_t to locally capture unsteady turbulent structures. In the resolved part of the turbulent spectrum, the numerical viscosity must be negligible compared to eddy viscosity, otherwise, turbulent structures will be dissipated by the numerical scheme.
Keeping the formal order and accuracy of numerical schemes is also very important for industry. The geometries are often complex and Cartesian grids are not possible. The finite volume numerical strategy we describe in this study (3.2 page 41) is the foundation of the whole method. We perform numerical test, not only in Cartesian grids, to validate the numerical method: robustness, order and accuracy on general mesh.

1.4 Conclusions

Technically, RANS models can be suitably modified and used to model turbulence at any mesh resolution (which is the purpose of RANS/LES approaches). The fundamental reason that this is possible is that the governing equations are formally the same for RANS and LES. The use of hybrid RANS/LES approaches for our applications needs however to introduce reasonable hypotheses about the the extra terms coming from the non-commutativity between the spatial derivatives and the LES filter.
A bibliography study concerning highly separated flows justified the use of hybrid RANS/LES approaches since only the integral quantities about the incoming boundary-layers is important at high Reynolds numbers.
Turbulence models and numerical schemes cannot be studied without taking into account their interactions. The following study addresses this point as a first step we select suitable hybrid RANS/LES strategies, afterwards, we develop a numerical method, which is consistent with hybrid RANS/LES models.

[9] Note that the second kind of viscosity is equal to zero for the so called "implicit" modelling approaches (see e.g Ref[26])

Chapter 2

Hybrid RANS/LES models and improvements

Contents

In this section we present three hybrid RANS/LES models in their most promising formulation for our applications : the Detached Eddy Simulation (DES) of Spalart [8], the Scale Adaptive Simulation (SAS) of Menter [44] and the Perot & Gadebush [41] model. Each of these models has his own philosophy, they share several common features. The common points are shown up specially when the models are compared using the same discretization scheme since, as we will see later, the impact of the numerical filter introduced by the discretization method may be at least as large as, if not bigger, than the impact of the turbulence model. In this Section, each validation case is computed using the VC scheme presented in section 3.3 on page 54. A common weakness of SAS and DDES [45] models is their failure in predicting the departure of convective instabilities, which is unacceptable for our applications. Kelvin-Helmholtz convective instabilities play an indispensable role in the spectral content in a separating/reattaching flow. Deck [10] demonstrates the failure of the DDES in his classical formulation for a free shear layer (figure 2.1 (a)), a backward facing step (figure 2.1 (b)) and a multi-element airfoil (figure 2.1 (c)). Menter in several ANSYS communications [46] and in [47] illustrates the failure of SAS for backward facing step flow computations (figure 2.1 (c)) and advocates "zonal forcing" to triggering convective instabilities. This pathology cannot be resolved in the same way for all the hybrid RANS/LES models, and it will be discussed in the following. Zonal strategies proposed by Menter (ZFLES) or Deck (ZDES), where the user has to locally impose LES or RANS zones in the flow are not readily applicable for our applications that often involve very complex geometries and where RANS and LES regions cannot be specified by the user. Unlike zonal strategies, we look for a methodology that remains as predictive as possible and does not require too much prior knowledge of the flow field. These zonal methods may nevertheless be very useful to study flows for which it is possible to closely predict the main behaviour beforehand, especially for research aims and when the geometries are not too complex.

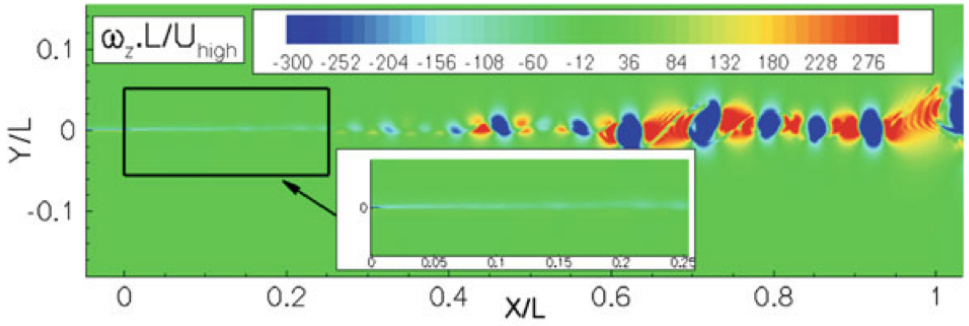

(a) DDES free shear flow [10]

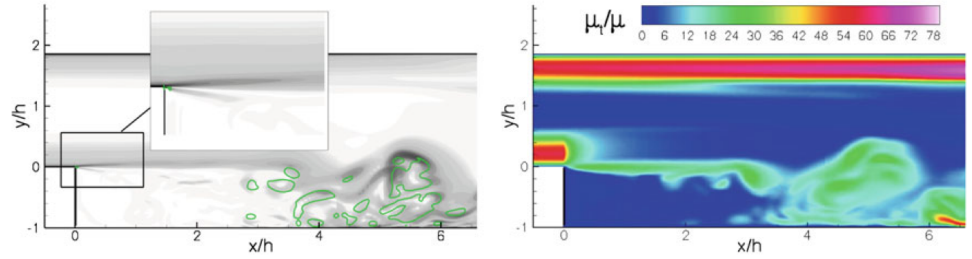

(b) DDES Backward facing step [10]

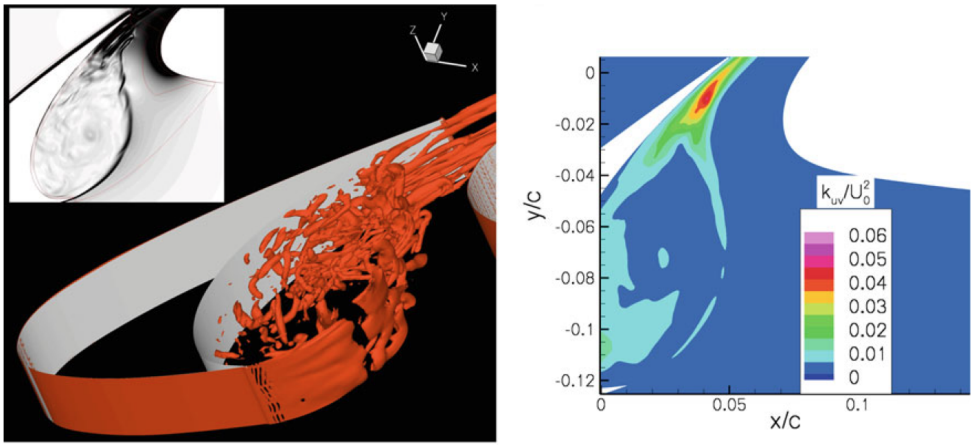

(c) DDES Multi elements airfoil [10]

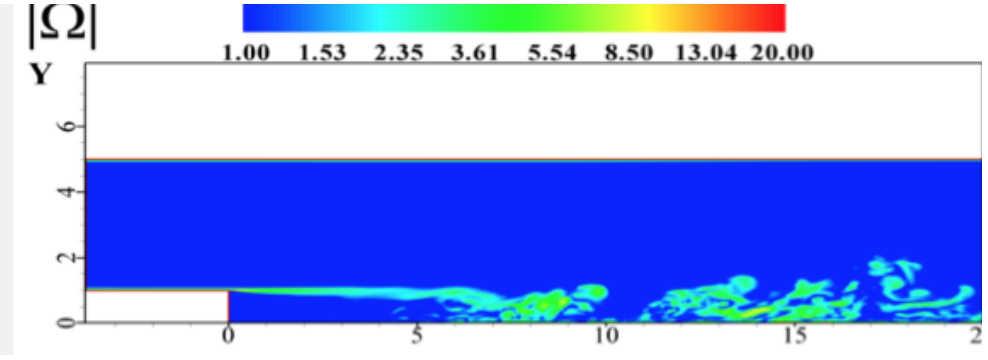

(d) SAS Backward facing step[46]

Figure 2.1: The common pathology of DDES and SAS models in their original formulation

2.1 Hybrid RANS/LES models

In this section, we present three hybrid RANS/LES turbulence models with improvements and recommendations necessary for accurate simulation of compressible flows around space launchers.

2.1.1 Scale Adaptive Simulation (SAS) strategy

Model formulation

The SAS approach introduced by Menter [44] is originally based on the $k-kL$ model of Rotta [48]. For a flow dominated by shear strain in y-direction, we can define an integral length scale L such that :

$$kL = \frac{3}{16}\int_{-\infty}^{\infty} R_{ii}dr_y \tag{2.1}$$

where,

$$R_{ij} = \overline{u_i(\mathbf{x})u_j(\mathbf{x}+r_y)}, \tag{2.2}$$

where the overline represents a time average (or an ensemble average). Quantities $\mathbf{x}$ and $\mathbf{x}+r_y$ are the location of two probes, separated in the y direction, by a distance r_y. Rotta builds an exact transport equation for the quantity kL from the Navier-Stokes equation for shear flows:

$$\underbrace{\frac{\partial(kL)}{\partial t} + \overline{u_j}\frac{(kL)}{\partial y} + \frac{3}{16}\int_{-\infty}^{\infty}\left[\frac{\partial\overline{u}(\mathbf{x}+r_y)}{\partial x} - \frac{\partial\overline{u}(\mathbf{x})}{\partial x}\right]R_{ii}dr_y =}_{\text{Convection}}$$

$$\underbrace{-\frac{3}{16}\frac{\partial\overline{u}(\mathbf{x})}{\partial x}\int_{-\infty}^{\infty}R_{21}dr_y - \frac{3}{16}\int_{-\infty}^{\infty}\frac{\partial\overline{u}(\mathbf{x}+r_y)}{\partial y}R_{12}dr_y}_{\text{Production}}$$

$$\underbrace{+\frac{3}{16}\int_{-\infty}^{\infty}\frac{\partial}{\partial r_k}(R_{(ik)i} - R_{i(ik)})dr_y + \nu\frac{3}{8}\int_{-\infty}^{\infty}\frac{\partial^2 R_{ii}}{\partial r_k r_k}dr_y}_{\text{Dissipation}}$$

$$\underbrace{-\frac{\partial}{\partial y}\left\{\frac{3}{16}\int_{-\infty}^{\infty}\left[R_{(i2)i} + \frac{1}{\rho}(\overline{p'v'} + \overline{v'p'})\right]dr_y - \nu\frac{\partial(kL)}{\partial y}\right\}}_{\text{Diffusion}}$$

where y denotes the coordinate across the shear layer. In the transport equation for kL the most interesting aspect is the production term, which contain the spatial derivative of the mean velocity at point $\mathbf{x}+r_y$:

$$\frac{3}{16}\int_{-\infty}^{\infty}\frac{\partial\overline{u}(\mathbf{x}+r_y)}{\partial x}R_{12}dr_y, \tag{2.3}$$

to model this term, Rotta suggest to use a Taylor expansion:

$$\frac{\partial\overline{u}(\mathbf{x}+r_y)}{\partial y} = \frac{\partial\overline{u}(\mathbf{x})}{\partial y} + r_y\frac{\partial^2\overline{u}(\mathbf{x})}{\partial y^2} + \frac{r_y^2}{2}\frac{\partial^3\overline{u}(\mathbf{x})}{\partial y^2} + \mathcal{O}(r_y^3) \tag{2.4}$$

$$\int_{-\infty}^{\infty}\frac{\partial\overline{u}(\mathbf{x}+r_y)}{\partial y}R_{12}dr_y = \frac{\partial\overline{u}(\mathbf{x})}{\partial y}\int_{-\infty}^{\infty}R_{12}dr_y + \frac{\partial^2\overline{u}(\mathbf{x})}{\partial y^2}\int_{-\infty}^{\infty}r_yR_{12}dr_y + \frac{1}{2}\frac{\partial^3\overline{u}(\mathbf{x})}{\partial y^2}\int_{-\infty}^{\infty}r_y^2R_{12}dr_y + \mathcal{O}(r_y^3)\int_{-\infty}^{\infty}R_{12}dr_y \tag{2.5}$$

At this point, Rotta decides to consider the third derivatives in the equation (2.5) as the leading term, assuming that the second derivative is equal to zero, based on the observation that, in homogeneous turbulence, the function R_{12} is symmetric with respect to r_y, and builds a two equation model for incompressible shear flow:

$$\frac{\partial k}{\partial t} + \overline{u}_j \frac{\partial k}{\partial x_j} = P_k - c_\mu^{3/4} \frac{k^{3/2}}{L} + \frac{\partial}{\partial y}\left(\frac{\nu_t}{\sigma_k}\frac{\partial k}{\partial y}\right) \tag{2.6}$$

$$\frac{\partial (kL)}{\partial t} + \overline{u}_j \frac{\partial (kL)}{\partial x_j} = -\overline{u'v'}\left(\xi_1 L \frac{\partial u}{\partial y} + \xi_2 L^3 \frac{\partial^3 u}{\partial y^3}\right) - \xi_3 k^{3/2} + \frac{\partial}{\partial y}\left(\frac{\mu_t}{\sigma_{kL}}\frac{\partial (kL)}{\partial y}\right) \tag{2.7}$$

$$P_k = -\overline{u_i' u_j'}\frac{\partial (kL)}{\partial x_j}; \qquad \nu_t = c_\mu^{3/4}\frac{kL}{\sqrt{k}}; \qquad P_k = \overline{u_i' v_j'}\frac{\partial \overline{u_i}}{\partial x_j} \tag{2.8}$$

All the constants of the model are listed in tab 2.1:

ξ_1	ξ_2	ξ_3	σ_k	σ_{kL}	c_μ
1.2	(-2.88)-(-3.24)	0.11 - 0.13	1.0	1.0	0.09

Table 2.1: Closure coefficients of the Rotta model

Menter and Egorov [42] give several reasons to explain why the third derivative is not desirable in a turbulent model. The first reason is that it is not intuitive. There is no physical reason why the third derivative should have a strong influence on the turbulent length scale. The second reason is that it produces an incorrect sign in the logarithmic layer. And the last reason is that it is difficult to compute a consistent third derivative in an industrial CFD code. Menter and Egorov[42] argue that the term in second derivative, in equation (2.5) should be kept as the leading term. This term is equal to zero only under homogeneous conditions or in a constant shear environment. Actually, the second derivative is an inhomogeneity detector: diffusion is a physical mechanism, mathematically represented by a second derivative, which tends to homogenize a given property, in this case the velocity. If the flow is already homogeneous, the diffusion mechanism vanishes and the second derivative is equal to zero.
Menter and Egorov built the von Kármán length scale thanks to the leading term in equation (2.5), based on the second derivative:

$$L_{\nu K} = \kappa \left| \frac{\partial \overline{u}/\partial y}{\partial^2 \overline{u}/\partial y^2} \right| \tag{2.9}$$

The absolute value is used to ensure the positivity of $L_{\nu K}$. The von Kármán length scale is used as a detector of strain rate variation since the second spatial derivative of the velocity can be seen as the first spatial derivative of the strain rate. The von Kármán length scale is a flow parameter which detects the smallest vortical structures which can be resolved in the flow. The model detects the spatial variation of the local strain rate and decreases the turbulent viscosity to avoid over-damping the turbulent structures. Menter and Egorov[42] propose a two equation model for the quantity $\sqrt{k}L$, which is directly proportional to the turbulent viscosity:

$$\frac{\partial \rho k}{\partial t} + \overline{u}_j \frac{\partial \rho k}{\partial x_j} = P_k - c_\mu^{3/4}\frac{k^{3/2}}{L} + \frac{\partial}{\partial y}\left(\frac{\mu_t}{\sigma_k}\frac{\partial k}{\partial y}\right) \tag{2.10}$$

$$\frac{\partial (\rho\sqrt{k}L)}{\partial t} + \overline{u}_j \frac{\partial (\rho\sqrt{k}L)}{\partial x_j} = \frac{\sqrt{k}L}{k} P_k \left(\xi_1 - \xi_2 \left(\frac{L}{L_{\nu K}}\right)^2\right) - \xi_3 \rho k + \frac{\partial}{\partial x_j}\left(\frac{\mu_t}{\sigma_{\sqrt{k}L}}\frac{\sqrt{k}L}{\partial x_j}\right) \tag{2.11}$$

$$L_{\nu K} = \kappa \left|\frac{u'}{u''}\right|; \quad u'' = \sqrt{\frac{\partial^2 u_i}{\partial x_k^2}\frac{\partial^2 u_i}{\partial x_j^2}}; \quad u' = S = \sqrt{2 S_{ij} S_{ij}}; \quad S_{ij} = \frac{1}{2}\left(\frac{\partial \overline{u}_i}{\partial x_j} + \frac{\partial \overline{u}_j}{\partial x_i}\right) \tag{2.12}$$

All the constants of the model are given in Tab. 2.2.

ξ_1	ξ_2	ξ_3	σ_k	$\sigma_{\sqrt{k}L}$	c_μ
0.8	1.47	0.0288	2/3	2/3	0.09

Table 2.2: Closure coefficients of the $k-\sqrt{k}L$ model of Menter and Egorov

The von Karman length $L_{\nu K}$ can be introduced in the second transport equation of other transport-equation models ($k-\epsilon$ or $k-\omega$ for example). For the widely used $k-\omega$ SST model, we can write the transport equation for ω:

$$\frac{\partial(\rho\omega)}{\partial t}+\overline{u}_j\frac{\partial(\rho\omega)}{\partial x_j}=\frac{\gamma}{\nu_t}P_k-\beta\rho\omega^2+Q_{SAS} \tag{2.13}$$

$$+\frac{\partial}{\partial x_j}\left[(\mu+\sigma_\omega\mu_t)\frac{\partial\omega}{\partial x_j}\right]+(1-F_1)\frac{2\rho}{\sigma_{\omega 2}}\frac{1}{\omega}\frac{\partial k}{\partial x_j}\frac{\partial\omega}{\partial x_j} \tag{2.14}$$

where,

$$Q_{SAS}=\rho\max\left[\xi_2 S^2\left(\frac{L}{L_{\nu K}}\right)^2-C\frac{2}{\sigma_\Phi}k\max\left(\frac{1}{\omega^2}\frac{\partial\omega}{\partial x_j}\frac{\partial\omega}{\partial x_j},\frac{1}{k^2}\frac{\partial k}{\partial x_j}\frac{\partial k}{\partial x_j}\right),0\right] \tag{2.15}$$

The standard $k-\omega$ SST turbulence model can be transformed into a SAS model in a straightforward manner: only by adding the Q_{SAS} source term to the transport equation for ω. In practice, for the $k-\omega$ SST, all the required quantities for the model are calculated as follows and the coefficients are listed in Tab. 2.3.

$$L_{\nu K}=\kappa\left|\frac{u'}{u''}\right|;\quad u''=\sqrt{\frac{\partial^2\overline{u}_i}{\partial x_j^2}\frac{\partial^2\overline{u}_j}{\partial x_i^2}};\ u'=S=\sqrt{2S_{ij}S_{ij}}\quad S_{ij}=\frac{1}{2}\left(\frac{\partial\overline{u}_i}{\partial x_j}+\frac{\partial\overline{u}_j}{\partial x_i}\right), \tag{2.16}$$

$$L=\frac{\sqrt{k}}{c_\mu^{1/4}\omega} \tag{2.17}$$

$$\mu_t=\frac{\rho a_1 k}{\max(a_1\omega,F_2\Omega)} \tag{2.18}$$

$$F_1=\tanh(arg_1^4) \tag{2.19}$$

$$arg_1=\min\left[\max\left(\frac{\sqrt{k}}{\beta^*\omega d},\frac{500\nu}{d^2\omega}\right);\frac{4\rho\sigma_{\omega_2}k}{CD_{k\omega}d^2}\right] \tag{2.20}$$

$$CD_{k\omega}=\max\left(2\rho\sigma_{omega2}\frac{1}{\omega^2}\frac{\partial\omega}{\partial x_j}\frac{\partial\omega}{\partial x_j}\right) \tag{2.21}$$

$$F_2=\tanh(arg_2^2) \tag{2.22}$$

$$arg_2=\max\left(\frac{2\sqrt{k}}{\beta^*\omega d},\frac{500\nu}{d^2\omega}\right) \tag{2.23}$$

$$\gamma=F_1\gamma_1+(1-F_1)\gamma_2 \tag{2.24}$$

$$\beta=F_1\beta_1+(1-F_1)\beta_2 \tag{2.25}$$

ξ_2	σ_Φ	C	$\sigma_{\omega 1}$	$\sigma_{\omega 2}$	β_1	β_2	a_1	γ_1	γ_2
3.51	2/3	2	0.5	0.856	0.075	0.0828	0.31	5/9	0.44

Table 2.3: Closure coefficients of the SAS model

Model limitations

This formulation has been investigated by Menter and Erogov for self decaying turbulence. They find that the length scale $L_{\nu K}$ has to be limited for the smallest scales of turbulence to avoid energy accumulation. Without introducing a limiter, the eddy viscosity of the SST-SAS can be lower than the lowest viscosity accepted by the grid. To obtain this lower bound, they find a lower bound for the von Kármán length (equation (2.26)) which leads to an equilibrium relationship for the turbulent viscosity.

$$L_{\nu K} = \max\left(L_{\nu K}, C_s\sqrt{\frac{\xi_2\kappa}{\beta/c_\mu - \gamma}}\Delta_{vol}\right), \tag{2.26}$$

see Tab. 2.3 for β and x_{i2}. The closure coefficient C_s may take different values according to the numerical scheme in use. In the following, we choose $C_s = 0.11$ as in [49]. In the lower limit of $L_{\nu K}$ (LES limit), the equivalent subgrid viscosity reached by the SAS model is:

$$\mu_t^{eq} = \left(\sqrt{\frac{1}{\xi_2\kappa}\left(\frac{\beta}{c_\mu} - \gamma\right)}L_{\nu K}\right)^2 S_{ij}, \tag{2.27}$$

this formulation is clearly similar to the Smagorinsky formulation:

$$\mu_{sgs} = \rho(C_s\Delta_{vol})^2 S_{ij}. \tag{2.28}$$

So, the lower limit of the SAS model is the Smagorinsky one. The choice of the characteristic length scale Delta is discussed in the following.

As anticipated at the beginning of this chapter, a pathology often observed with this kind of automatic HRL model is a delay in the triggering of convective instabilities. To circumvent this problem, Menter proposed several ways to trigger instabilities by introducing *ad hoc* local forcing. One such methodology is the HTG (Harmonic Turbulence Generator) of [47]. In order to keep the predictive capabilities of HRL strategy, in this work we avoid such *ad hoc* treatments. Recently, Benyoucef [49] analyzed the behaviour of the von Karman length scale $L_{\nu K}$ in a boundary-layer and in a shear layer and proposed a modification to the SAS model. He points out that Kelvin-Helmholtz instabilities are triggered at the inflexion point of a velocity profile. At this location, the second derivative of the velocity profile is equal to zero while the first derivative takes a finite value. As a consequence, $L_{\nu K}$ tends to infinity. In other terms, the scale $L_{\nu K}$ may increase in convective instabilities, which is contrary to what is expected. This may explain the delay observed for the triggering of convective instabilities. For this reason, Benyoucef [49] introduces a limiter for $L_{\nu K}$ to avoid the wrong behavior of $L_{\nu K}$ in free shear layers while enforcing the RANS mode in attached boundary-layers:

$$L_{\nu K} = \min(L_{\nu K}, F_1 L_{\nu K} + (1 - F_1)\alpha L), \tag{2.29}$$

where F_1 is the same function used in the RANS-SST model. F_1 is a shielding function which is equal to 1 in the greatest part of the boundary-layer ($y/\delta < 0.7$) and zero elsewhere. The original role of F_1 in the SST model is to switch from the $k-\omega$ near the wall to the $k-\epsilon$. Using this function for the von Kármán length scale allows to preserve RANS behaviour of the model within attached boundary-layers. Benyoucef calibrates α in Equation (2.29) and suggests a value of 2.5 [49]. The limiters applied to the von Kármán length scale $L_{\nu K}$ are:

$$C_s\sqrt{\frac{\xi_2\kappa}{\beta/c_\mu - \gamma}}\Delta_\omega \leqslant L_{\nu K} \leqslant F_1 L_{\nu K} + (1 - F_1)\alpha L. \tag{2.30}$$

The choice of Δ_ω instead of Δ_{vol} is discussed in more detail later in this chapter in Section 2.2 on page 33. These are used for all the calculations carried out with the SAS turbulence model in the following. In order to prove the effectiveness of the limitation of Benyoucef's limiter, we can take a little ahead on the validation section 4.2 page 82. Figures 2.2 (a) and (b) show the turbulent viscosity of two SAS calculations, one without the Benyoucef limiter (figure 2.2 (a)) and the second one using the limiter (figure 2.2 (b)). This comparison clearly shows that the limiter (2.29) is essential for the triggering of convective instabilities: without Benyoucef's limiter, there is no Kelvin-Helmholtz vortices.

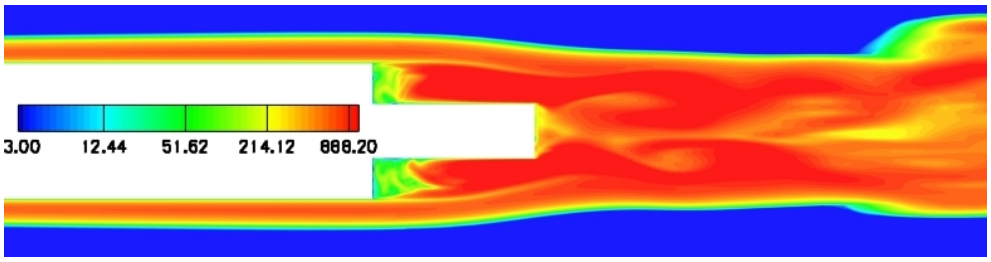

(a) Axisymmetric backward facing step, SAS calculation without the limitation (2.29) of Benyoucef

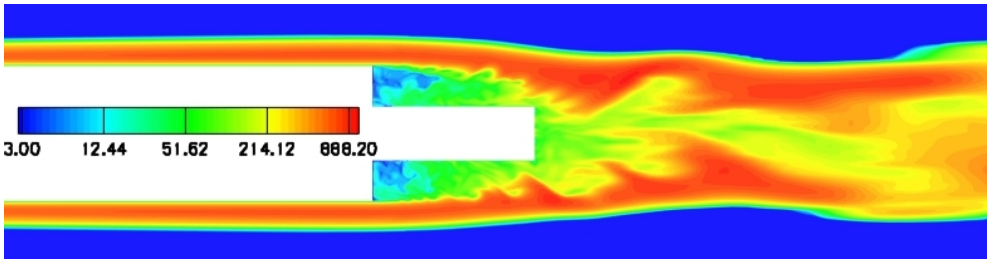

(b) Axisymmetric backward facing step, SAS calculation with the limitation (2.29) of Benyoucef

Figure 2.2: Axisymmetric backward facing step, SAS calculations, ν_t/ν ratio

2.1.2 Detached Eddy Simulation (DES)

Model formulation

The DES approach was initially proposed as a modification to the S-A [50] turbulence model. For our applications, which are highly compressible, we chose to implement the "density corrected" version of S-A model of Catris and Aupoix [51], written as:

$$\frac{\partial(\rho\widetilde{\nu})}{\partial t}+\overline{u}_j\frac{\partial(\rho\widetilde{\nu})}{\partial x_j}=c_{b1}\mid\omega\mid\rho\widetilde{\nu}+\frac{1}{\sigma}\frac{\partial}{\partial x_j}\left(\mu\frac{\partial\widetilde{\nu}}{\partial x_j}\right)+\frac{1}{\sigma}\frac{\partial}{\partial x_j}\left(\sqrt{\rho\widetilde{\nu}}\frac{\partial\sqrt{\rho\widetilde{\nu}}}{\partial x_j}\right)+\frac{c_{b2}}{\sigma}\frac{\partial\sqrt{\rho\widetilde{\nu}}}{\partial x_j}\frac{\partial\sqrt{\rho\widetilde{\nu}}}{\partial x_j}-c_{w1}f_w\rho\left[\frac{\widetilde{\nu}}{d_w}\right]^2, \tag{2.31}$$

where, $\mid\omega\mid$ is the magnitude of the vorticity, d_w is the distance from the nearest wall, and:

$$f_w=g\left(\frac{1+c_{w3}^6}{g^6+c_{w3}^6}\right)^{1/6},\quad g=r+c_{w2}(r^6+r),\quad r=\frac{\nu_t}{S\kappa^2d_w^2}, \tag{2.32}$$

The model closure coefficients are given in Tab.2.4.

c_{b1}	c_{b2}	σ	κ	c_{w1}	c_{w2}	c_{w3}
0.1355	0.622	2/3	0.41	$c_{b1}/\kappa^2+(1+c_{b2})/\sigma$	0.3	2

Table 2.4: Closure coefficients of the S-A model

The basic idea of the original DES approach is to modify the destruction term in the transport equation (2.31) by replacing the distance from the wall by:

$$\widetilde{d}=\min(d_w,C_{DES}\Delta)$$

where $\Delta=\Delta_{max}=\max(\Delta_x,\Delta_y,\Delta_z)$ is a characteristic mesh size and, $C_{DES}=0.65$. With this choice, the model works as a S-A RANS model when $\widetilde{d}=d_w$, and as a S-A subgrid model when $\Delta<<d_w$. However, its behaviour is ambiguous for $\Delta\sim d_w$. The region of the computational domain where $\Delta\sim d_w$ is called

the "grey zone". The model is expected to work in the RANS mode as long as the maximum grid size is greater than the wall distance. This is based on the hypothesis that in a RANS grid, the longitudinal or the spanwise grid size is greater than the wall distance.

Model Stress Depletion and remedy

As discussed in Section 1.1.1 on page 12, spanwise resolution is essential to capture correctly the three-dimensionalization of the Kelvin-Helmholtz instabilities. This avoids to stop the energy cascade and favors the three-dimensionalization of vortical structures. For a backward facing step flow, for example, the spanwise refinement controls the diffusion length $\widetilde{d}$ before the separation point. Regarding the figure 2.5, just before the separation flow, $\widetilde{d} = C_{DES}\Delta_z$ because the grid in all directions is much smaller than the boundary-layer thickness, and the RANS eddy viscosity starts to be affected by the DES limiter but the grid resolution is not fine enought to support a LES solution. A solution is to generate the grid in such a way as to switch instantaneously from a RANS to a LES refinement, but this solution is not a good option for numerical reasons and also for energy conservation, reasons as discussed in Section 1.2.3 on page 18. This issue is called the Model Stress Depletion by Spalart and can cause wrong boundary-layer separations since the RANS turbulent viscosity is impacted by DES limiter because of the grid, topology, leading to so-called "Grid Induced Separation". To overcome this difficulty, Spalart *at al* [45] introduces a shielding function f_d to "protect" the RANS boundary layer from switching to the LES mode. The modified modeling strategy is then called in the DDES (Delayed Detached Eddy Simulation). The shielding function writes:

$$f_d = 1 - \tanh((8r_d)^3), \tag{2.33}$$

with,

$$r_d = \frac{\nu + \nu_t}{\sqrt{\frac{\partial u_i}{\partial x_j}\frac{\partial u_i}{\partial x_j}}\kappa^2 d_w^2}. \tag{2.34}$$

The quantity f_d is equal to 0 in the boundary-layer and 1 elsewhere. Other solutions can be adopted to protect RANS boundary layers, which will be discussed in the following. We can visualize the f_d shielding function on the boundary-layer profile of figure 2.5.
It is vital that, regardless of the hybrid RANS/LES model in use, attached boundary-layers remains fully modeled. No resolved kinetic energy has to be allowed in attached boundary layers. For instance, this is why PANS [52] (Partially Averaged Navier Stokes) in its original version cannot lead to a correct solution: the modeled to total kinetic energy ratio is imposed by the user at the beginning of the simulation and in the whole computational domain, including boundary layers, instead of switching to zero near the walls. Several modifications have been proposed by Girimaji [40] to overcome this problem but we do not retain this approach for our applications.
Concerning SAS model, shielding function to protect the boundary-layers is already included in underlying $k-\omega$ SST RANS model and it will be illustrated in Section 2.1.1.

Convective instabilities departure: remedy

The DDES approach allows to protect RANS boundary-layers and avoid grid-induced separation, but the issue concerning the delayed triggering of convective instabilities is not resolved. In order to correct this flaw while taking into account the typical anisotropy of industrial grids, we introduce a flow dependent characteristic grid size based on vorticity, Δ_ω (see equation (2.45)) originally proposed by Chauvet [53], and discussed in more detail later in this chapter in Section 2.2 on page 33. Finally, the formulation of DDES used in this study is similar to the ZDES mode II proposed by Deck [10]:

$$\Delta = (0.5 - sign(0.5, f_d - f_{d0}))\Delta_{max} + (0.5 + sign(0.5, f_d - f_{d0}))\Delta_\omega, \tag{2.35}$$

the Δ is an hybrid characteristic length which involves the usual characteristic length Δ_{max} in boundary-layers and Δ_ω elsewhere; moreover, it is flow-dependent since Δ_ω depends on the local vorticity (see equation (2.45)). The limiting value of f_{d0} is taken equal to 0.8.
To be convinced of the usefulness of using Δ_ω instead of Δ_{max} in the DDES formulation, consider figures 2.3 (a) and (b). The figures show the turbulent viscosity for the calculation of the axisymmetric backward

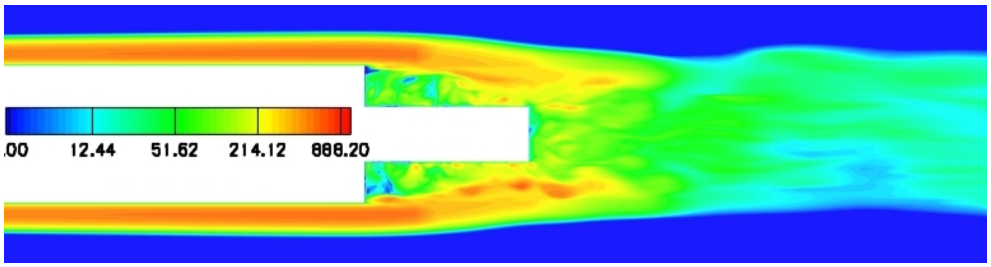

(a) Axisymmetric backward facing step, DDES calculation with Δ_{max}

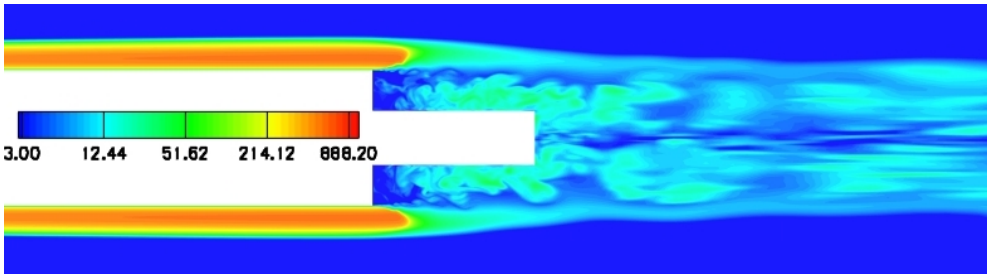

(b) Axisymmetric backward facing step, DDES calculation with Δ_{ω}

Figure 2.3: Axisymmetric backward facing step, DDES calculations,ν_t/ν ratio

facing step that we will study in section 4.2, figure 2.3 (a) was obtained by using the Δ_{max} length scale everywhere and figure 2.3 (b) by using the Δ_{ω} length scale. We can see that, the DDES in it is original formulation fails to predict the Kelvin-Helmholtz instability and exhibits a strong delay in their triggering, whereas the modified DDES does not introduce any delay.

2.1.3 Perot & Gadebush (PG) turbulence model

Model formulation and improvement

Perot and Gadebush [41] start again from the idea that a suitably modified RANS model can be used to model turbulence at any mesh resolution, because the governing equations are the same for RANS, URANS, LES and DNS (see Section 1.2 page 14). To sensitize a RANS model to the grid, they introduce a function based on the local grid size and on the local resolved kinetic energy. This function, which is independent of the specific form of the model in use, depends only on the amount of kinetic energy that is locally resolved compared to the local mesh size. This allows to locally adapt the level of subgrid viscosity to the grid. This approach is very promising: for instance, it allows to get rid of the delay of the triggering of the Kelvin-Helmholtz instabilities because of the locality of the adaptation function. Given this, Perot and Gadebusch [41] propose a new HRL model based on a modification to the standard $k-\epsilon$ model. For this purpose, they introduce an energy transfer parameter α:

$$\alpha = 1.5\left(1 - C^*\left(\frac{k}{k+k_r}\right)^2\left[\left(\frac{\Delta x_i}{\sqrt{k_r}}\frac{\partial\sqrt{k_r}}{\partial x_i}\right)^2 + 0.11\right]^{-1}\right) \tag{2.36}$$

where k_r is the resolved turbulent kinetic energy, k the modeled kinetic energy and $C^* = 0.28$. The α parameter, comprised between -1 and 1, detects well-resolved flow regions and turns the baseline two-equation model into a subgrid model, while keeping a classical $k-\epsilon$ model in under-resolved regions. This function is analog to functions used in automatic mesh adaptation. The model is calibrated on homogeneous turbulence: the length scale predicted by the model should be proportional to the grid size in the LES mode. Figure 2.4, taken from [41] shows that the modified two- equation $k-\epsilon$ model can be applied as a turbulence/subgrid model for LES ($L_m = k^{3/2}/\epsilon$ is proportional to the grid size), and recovers the RANS mode (L_m is independent to the grid size).

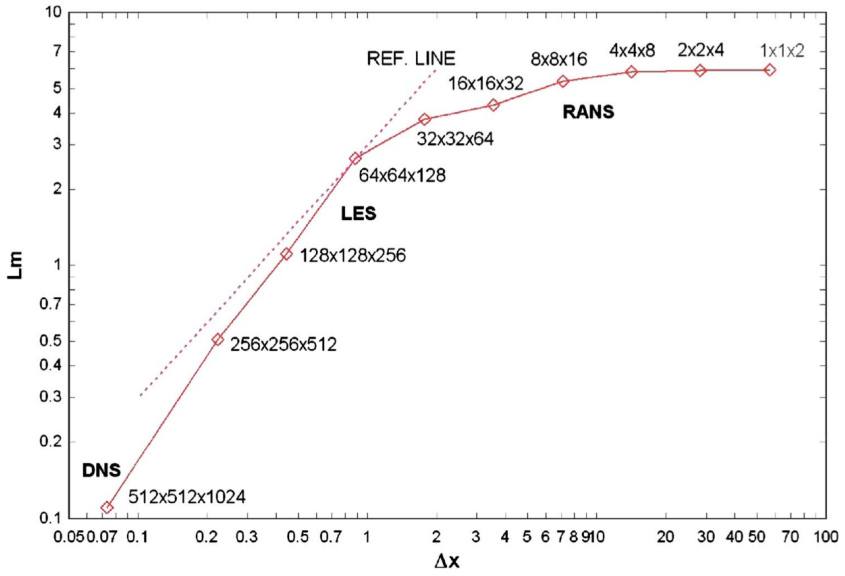

Figure 2.4: Model length scale vs grid size for homogeneous turbulence[41]

For the same physical reason that lead lead us to adopt Chauvet's length scale Δ_ω in DDES (see Section 2.2 on page 33 for a discussion), we reformulate the term $\frac{\Delta x_i}{\sqrt{k_r}}\frac{\partial\sqrt{k_r}}{\partial x_i}$ in order not to take into account the useless grid direction (Δ_z at the beginning of the detachment point of figure 2.5 for example):

$$\alpha = 1.5\left(1 - C^*\left(\frac{k}{k+k_r}\right)^2\left[\left(\boldsymbol{N_\omega}.\frac{\boldsymbol{\Delta_\eta}}{\sqrt{\boldsymbol{k_r}}}\frac{\boldsymbol{\partial\sqrt{k_r}}}{\boldsymbol{\partial\eta}}\right)^2 + 0.11\right]^{-1}\right) \tag{2.37}$$

with

$$\frac{\boldsymbol{\Delta_\eta}}{\sqrt{\boldsymbol{k_r}}}\frac{\boldsymbol{\partial\sqrt{k_r}}}{\boldsymbol{\partial\eta}} = \left(\frac{\Delta_x}{\sqrt{k_r}}\frac{\partial\sqrt{k_r}}{\partial x}, \frac{\Delta_y}{\sqrt{k_r}}\frac{\partial\sqrt{k_r}}{\partial y}, \frac{\Delta_z}{\sqrt{k_r}}\frac{\partial\sqrt{k_r}}{\partial z}\right)^T \tag{2.38}$$

and with

$$\boldsymbol{N_\omega} = \begin{pmatrix}1\\1\\1\end{pmatrix} - \frac{1}{\|\boldsymbol{\omega}\|}\begin{pmatrix}\omega_x\\\omega_y\\\omega_z\end{pmatrix} \tag{2.39}$$

The vector $\boldsymbol{N_\omega}$ allows to take into account only the characteristic grid sizes which are perpendicular to the vorticity vector $\boldsymbol{\omega}$. The Expression (2.39) is inspired by the idea of Chauvet [53] and it is particularly well suited for shear layers. The additional turbulent transport equations introduced by the PG turbulence model are then:

$C_{\epsilon 1}$	$C_{\epsilon 2}$	C_μ	σ_k	σ_ϵ
1.44	1.92	0.09	1.0	1.3

Table 2.5: Closure coefficients of the PG model

$$
\begin{aligned}
\frac{\partial(\rho k)}{\partial t} + \frac{\partial(\rho u_j k)}{\partial x_j} &= \alpha P_k - \rho\epsilon + \frac{\partial}{\partial x_j}\left[(\mu + \frac{\mu_t}{\sigma_k})\frac{\partial k}{\partial x_j}\right], \\
\frac{\partial(\rho \epsilon)}{\partial t} + \frac{\partial(\rho u_j \epsilon)}{\partial x_j} &= \frac{\epsilon}{k}(C_{\epsilon 1} P_k - C_{\epsilon 2}\rho\epsilon) - \frac{\partial}{\partial x_j}\left[(\mu + \frac{\mu_t}{\sigma_\epsilon})\frac{\partial \epsilon}{\partial x_j}\right], \\
P_k &= \rho \tau_{ij}\frac{\partial u_i}{\partial x_j}. \\
\nu_t &= c_\mu \frac{k^2}{\epsilon}\left(\frac{k}{k + k_r}\right) \\
\rho \bar{t}_{ij} &= 2\mu \overline{S}_{ij} \\
\overline{S}_{ij} &= \frac{1}{2}\left(\frac{\partial u_i}{\partial x_j} + \frac{\partial u_j}{\partial x_i}\right) - \frac{1}{3}\frac{\partial u_k}{\partial x_k}\delta_{ij},
\end{aligned}
$$

where ϵ is the dissipation rate and u_i, $(i = 1, 2, 3)$ the component of $\mathbf{u}$. Note that the preceding equations correspond to a modification of the high-Reynolds version of the $k-\epsilon$ model [54], since we make use of wall functions [55] to avoid resolving the viscous sublayer and increase the maximum allowable y^+ of the computational grid. However, this is small enough to avoid direct overlapping of the region modeled through wall functions with LES regions. The closure coefficients for the model are listed in Tab. 2.5. The resolved kinetic energy k_r has to be computed during the calculation. Equation (2.40) shows how k_r is computed in practice:

$$
k_r = \frac{1}{2}(\overline{u_i^2} - \overline{u_i}^2) \quad \text{where } \overline{\bullet} \text{ is the time average operator} \tag{2.40}
$$

Statistics used in equation (2.40) are progressively accumulated during the calculation and a sliding averaging procedure is used to remove information from the initial transient phase. For some flows where the calculation of statistics on the whole simulation time is a nonsense (helicopter rotor, re-entry capsule...) phase averages can be used instead. With respect to the baseline $k-\epsilon$ model we notice that:

- the production term in the k equation is premultiplied by the blending parameter α;
- the expression for the eddy viscosity is modified via the modeled kinetic energy ratio. This is equal to 1 when all the turbulent kinetic energy is modeled ($k_r = 0$) so that the RANS eddy viscosity is recovered in this limit, and equal to 0 if all of the kinetic energy is resolved ($k = 0$), allowing the model to degenerate into DNS in the vanishing mesh size limit.

In addition to the preceding modifications, the energy transfer parameter α can be introduced also in the momentum equation through the Reynolds-stress tensor, which is modified in the following way:

$$
\rho \tau_{t_{ij}} = 2\alpha\mu_t \overline{S}_{ij} - \frac{2}{3}\tau_{kk}\delta_{ij} \tag{2.41}
$$

In regions where α is equal to 1, the model works in RANS mode; in regions where α is positive and smaller than 1 the model works in LES mode; when $\alpha < 0$, the contribution to the Reynolds stresses becomes negative and acts as an anti-diffusion which amplifies existing resolved velocity fluctuations. The blending parameter α acts through two mechanisms: it pre-multiplies the Reynolds stress tensor, lowering the modeled Reynolds stresses in well-resolved regions; it pre-multiplies the production term in the turbulent kinetic energy equation, lowering the amount of modeled kinetic energy produced by the model and,

indirectly, the eddy viscosity. Note that α may become negative in highly resolved regions characterized by a too large amount of modeled kinetic energy. As a consequence, the diffusive terms in the momentum equation change their sign. This amplifies flow instabilities by converting turbulent diffusion in antidiffusion, and enables effective model transition from RANS to LES mode by enriching the frequency spectrum. This differs from the more commonly used approach, which corresponds to an injection of energy via some random forcing of the resolved flow[47]; rather, it works to enhance the existing instabilities and modes. Moreover, the energy transfer is local in spectral space. It tends to take energy from the model (which has most of its energy at scales just below the mesh resolution) and preferentially delivers it to the resolved flow at almost the same length scale (just above the mesh resolution). Since in the present work we focus on wall-bounded flows, we modify the PG model by introducing a shielding function that enforces a RANS mode in attached boundary-layers. Precisely, we use the same shielding function suggested for DDES (see eqs (2.33,2.34)) to detect attached boundary-layers and to force parameter α toward 1 when the f_d function (2.33) is lower than 0.8.

2.2 Choice of the characteristic length scale

The philosophy of hybrid RANS/LES strategies is to produce the best solution possible for a given mesh resolution, since it computes as much of the turbulence from first principles as the mesh will allow [41]. Many hybrid RANS/LES models have, in their LES part, a Smagorinsky-like lower limit for the subgrid viscosity. However, different hybrid RANS/LES models reached this lower limit in different ways: for example, in the DES [8] approach, Smagorinsky-like subgrid viscosity is directly imposed, whereas in the SAS approach [42], this is just reach as lower limit for the subgrid viscosity. Let us remind that the Smagorinsky subgrid viscosity is of the form:

$$\mu_{sgs} \propto S\Delta^2 \tag{2.42}$$

where Δ is a characteristic grid size: $\Delta = \sqrt[3]{\Delta_x\Delta_y\Delta_z}$. Here, Δ can be viewed as an isotropic length scale. In a pure LES, the subgrid viscosity cut the turbulent spectrum just before the Kolmogorov scale. In this region of turbulent spectrum, the dissipation phenomenon, which is an isotropic mechanism, is predominant.
In all hybrid RANS/LES models, the RANS model is modified according to the characteristic grid size, so to become a subgrid scale model and can be seen as a dynamic subgrid model. For DDES for example, it can be considered as a dynamic one-equation subgrid model in regions working in the LES mode.
In the original DES approach, the expression for Δ is given by the maximum of the grid lengths in each direction:

$$\Delta_{max} = \max(\Delta_x, \Delta_y, \Delta_z) \tag{2.43}$$

it is based on the hypothesis that in RANS boundary-layers, Δ_{max} is significantly greater than the local distance to the wall to recover a Spalart-Allmaras a RANS behaviour in boundary-layers. If the grid is finer in one direction, which is typically the case in a grid suited for a RANS (to model attached boundary layers), this extra-resolution has no influence on the model using Δ_{max}, it stays in the RANS mode[8]. This is not the case with the length scale Δ_{iso} (equation (2.44)) which is considered by several authors. This length scale is influenced by the third directions of the grid, it can be more suited than Δ_{max} (because $\Delta_{iso} \leq \Delta_{max}$) in the LES regions, but non physical in RANS regions.

$$\Delta_{iso} = \sqrt[3]{\Delta_x\Delta_y\Delta_z} \tag{2.44}$$

The most promising length scale (for the LES regions only), in our opinion, is the one proposed by Chauvet [53]. This is a flow dependent length scale based on the vorticity. The idea is to consider the average cross section of the cell normal to the vorticity vector. We propose a version of this length scale well-suited for unstructured solvers:

$$\Delta_\omega = \sqrt{\frac{\sum_i^{Nf} |\ \boldsymbol{\omega}.\mathbf{S_i}\ |}{2\ ||\ \boldsymbol{\omega}\ ||}}, \tag{2.45}$$

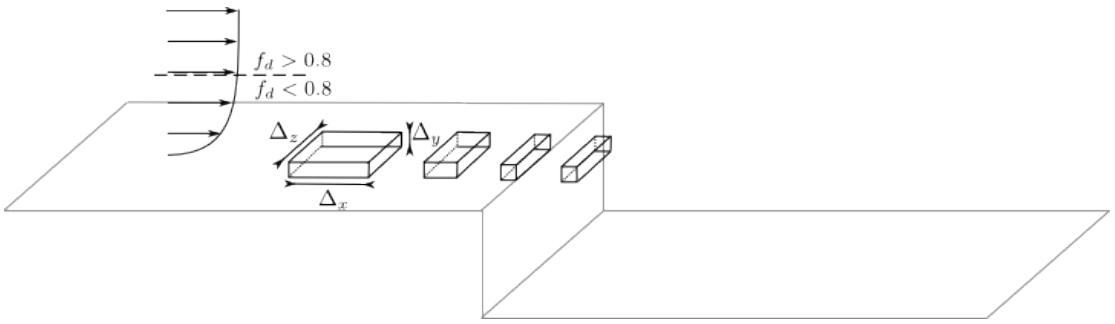

Figure 2.5: Characteristic grid size on a backward facing step like flow and shielding function

where $\boldsymbol{\omega}$ is the vorticity vector, $\mathbf{S_i}$ is the oriented surface i of a given cell and Nf the number of faces which compose a given cell. The Figure 2.5 gives a good idea of the length scale values on the mesh of a backward facing step. For example, just after the separation point, we have:

$$\boldsymbol{\omega} = (0, 0, w_z)^T, \tag{2.46}$$

and,

$$\mathbf{S_i} = (0, 0, \Delta_x \Delta_y)^T. \tag{2.47}$$

We have:

$$\Delta_\omega = \sqrt{\frac{1}{2}(\Delta_x \Delta_y + \Delta_x \Delta_y)} = \sqrt{\Delta_x \Delta_y}. \tag{2.48}$$

Just after the separation point, the Kelvin-Helmholtz structures are 2D and the spanwise resolution should have no influence. When the vortices become 3D, the Δ_ω scale is no longer $\Delta_x \Delta_y$, and turn into surfaces weighted by the vorticity vector.
The most promising length scales, in our opinion, are the flow dependent Δ_ω for LES regions and $\Delta_{\max}$ for RANS region. A relevant compromise would be an hybridization between these length scales.

Figure 2.5 allows to have a good idea of the value of Δ_{max}, Δ_{iso} , Δ_ω. For example, in the attached boundary-layer, and at the beginning of the shear layer, $\Delta_\omega = \sqrt{\Delta_x \Delta_y}$, which is very good in the shear layer because the vortical structures in the beginning are 2D cylinders, but very bad in the attached boundary-layer because $\Delta_\omega << d_w$. Upstream from the separation point, $\Delta_{max} = \Delta_x >> d_w$, which is well suited to RANS boundary-layer ($\widetilde{d} = d_w$ for DDES approach), and next to the separation point $\Delta_{max} = \Delta_z << d_w$ ($\widetilde{d} = C_{DES}\Delta_z$ for DDES approach) which can induced a wrong modeling of the boundary-layer.

2.3 Remarks about hybrid RANS/LES models

The philosophy of the three turbulence models we decribed above (SAS, DDES, Perot & Gadebush) differs. The SAS turbulence model can be seen as an improved URANS model because the LES subgrid viscosity is not imposed as in DDES. The SAS model, the LES subgrid viscosity is just a lower bound but there is no evidence that the model will reach it. Concerning the Perot & Gadebush model, the local α function is supposed to make the $k - \epsilon$ model turn into a subgrid model. Unlike SAS and DDES models which are widely used in industry and research, Perot & Gadebush model has been calibrated only for an isotropic decaying turbulence, and there is limited experience concerning this approach. In the Section 4, we assess and compare these models for some well-documented test cases.

2.4 On the importance of using consistent approximations of space derivatives

In the FLUSEPA solver (for more details about the solver, please refer to Section 3.1 on page 37), turbulence transport equations are solved in a coupled way along with the mean-field/filtered field equations. Thanks to the successive correction algorithm described in Section 3.2.1 page 48, when a third order discretization is constructed, second-order accurate first derivatives and first order accurate second derivatives on arbitrary grids are also automatically computed. For a second-order reconstruction, rigourously first-order approximation of the first derivatives of any quantity are also automatically obtained on any arbitrary grid. An accurate approximation of spatial derivatives on any arbitrary grid is of the utmost importance for turbulent flow simulations, because all component of turbulence models are based on it. For example, on a turbomachinery blade, where the grid is highly irregular and where the turbulence model plays a important role, it could be decisive to have a consistent gradient regardless of the grid. This is even more true for models which use information about second derivative (the SAS model for example): a poor approximation of the second derivative can have dramatic consequences on the model , for it is its key ingredient.

2.5 On the realizability condition

The realizability notion introduced by [56] and [57] is the condition for a physical quantity to be a correlation of a fluctuating quantity. For example, if a turbulent quantity is a sum of roots, e.g the dissipation rate $\epsilon = 2\nu\overline{s'_{ij}s'_{ij}}$, then this quantity must be positive. The realizability conditions applied to the Reynolds stress tensor ($R_{ij} = \overline{u'_i u'_j}$) are:

$$\forall \alpha \quad R_{\alpha\alpha} \geqslant 0 \tag{2.49}$$

$$\forall \alpha, \beta \quad \alpha \neq \beta \quad R^2_{\alpha\beta} \leqslant R_{\alpha\alpha} R_{\beta\beta} \tag{2.50}$$

$$\det[R] \geqslant 0. \tag{2.51}$$

This is a theoretical way to explain the realizability notion. We are entitled to wonder what is the realizability notion concretely. For this purpose, the study of Sinha *et al.* [58] is very interesting to illustrate the notion of realizability and go further to built a realistic model. In this reference, a direct numerical simulation and linear analysis of a isotropic turbulence interacting with a shock [59] [60] is carried out. It is know that compression, shock unsteadiness, pressure-velocity correlation, entropy fluctuations in the upstream flow play an important role in the interaction [59] [60] [61]. Figure 2.6 shows the evolution of turbulent kinetic energy when isotropic turbulence crosses a shock for a standard turbulence model, a model satisfying the realizability conditions and a modified turbulence model proposed by Sinha. Across a shock, there is a turbulence kinetic energy leap followed by a decrease of the latter. Figure 2.6 clearly shows that RANS turbulence models in their standard formulation fail to predict the behavior of turbulent kinetic energy. In particular, the amplification of k is too high. We see that the realizability conditions which help to improve the prediction fail also to predict the turbulence kinetic energy decrease after the shock, especially when the Mach number is high. Sinha *et al.* propose an improvement of the $k-\epsilon$ turbulence model to correctly predict the amplification of k. They modify the k equation to incorporate the shock-unsteadiness mechanism and model it using linear analysis. The resulting equation yields a significant improvement over the existing models. The model improvement proposed by Sinha *et al.*, shows a concrete example of the usefulness of realizability, and it opens the discussion concerning more realistic turbulence models for such compressible applications. Note that the Spalart-Almarras turbulence model does not exhibit the same issue as $k-\epsilon$ concerning the jump of eddy viscosity throught a shock (see Paragraph 2.5 on page 35) because the production term in the transport equation is based on the vorticity. Note also that the production limiter recommended by Menter for the $k-\omega$ SST model [62]:

$$P_k = \min(P_k, 20\beta^*\rho\omega k), \tag{2.52}$$

is a also a kind of realizability condition.
We can illustrate the realizability problem by a very practical example: in the case of the calculation of the

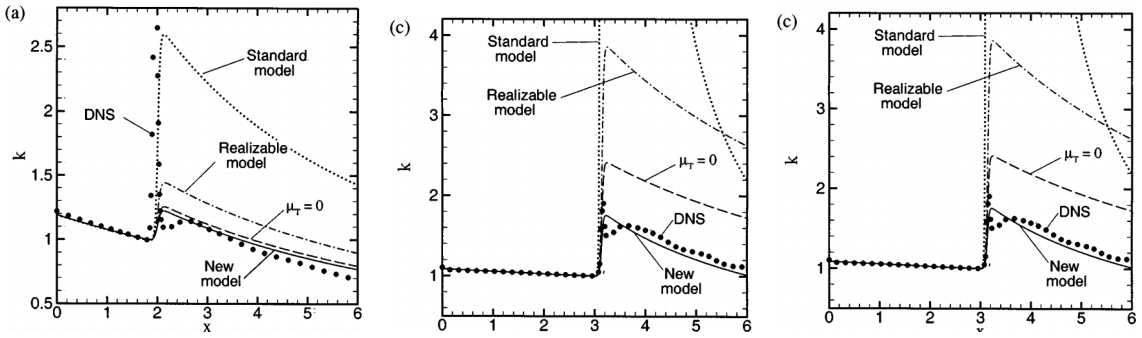

(a) Mach 1.29 (b) Mach 2.0 (c) Mach 3.0

Figure 2.6: Evolution of k in the interaction of homogeneous isotropic turbulence with a normal shock at different Mach number [58]

transonic launcher shrinkage described in section 5.1, figure 5.2, there is a shock boundary-layer interaction on the fairing due to flow acceleration. If the turbulence model is not realizable, the turbulent viscosity can be overestimated as we can see on figure 2.6, leading to the wrong boundary-layer thickness after the shock and at the separation point of the shrinkage. This overestimation of the boundary-layer thickness could modify the dynamics of the LES part of the simulation in the recirculation bubble.

2.6 Conclusions

In this Chapter we presented three promising turbulence models particularly suitable to trigger convective Kelvin-Helmholtz instabilities on arbitrary grids thanks to some recent improvements proposed in the literature. The importance of having (at least) consistent (regardless of the grid) derivatives to calculate the source terms of turbulence models was reminded. Finally, we illustrate the importance of the realizability condition for compressible applications.

Chapter 3

Numerical method and improvements

Contents

3.1 FLUSEPA solver

In this work, the solver in use is FLUSEPA[1], the unstructured finite-volume solver developed by Airbus Defense & Space to calculate compressible, multidimensional, unsteady, viscous and reactive flow with particles over bodies in relative motion. FLUSEPA was built to address industrial problematics on complex geometries, and highly compressible flows. The numerical strategy is based on Godunov methods [63], with orders of accuracy ranging from first order to locally fourth order[64]. The strength of the FLUSEPA algorithm is to keep the formal order of the scheme regardless of the grid in use. The numerical method ensuring this result is widely discussed in Section 3.2 on page 3.2. Several physical models are available : RANS turbulence models, Arrhenius-like models for chemistry, particle transport, multi-species fluids... In the following, we can show some applications of FLUSEPA. It allows to perform calculations on very complex geometries like the full scale launch pad to study blast waves (see figure 3.1). The solver can simulate stage separations of full scale launchers (see figures 3.3 and 3.2). Finally, advanced turbulence calculations are realized (see figure 3.4) thanks to the CFD strategy presented in this study, which allows to evaluate the levels and frequencies of pressure fluctuations.
The CHIMERA-like meshing strategy used in the solver FLUSEPA is based on a 3D intersection process [65] [66],[67],[68]. In the case of a space launcher, for example, the user meshes independently each part of the launcher, with their own boundary layers, and then, specifies the level of priority between the grids. In this study, most of grids are generated using this technique: this is the case, e.g., of the square cylinder 3.4.5 page 70, the axi-symmetric backward facing steps 4.2, page 82, and the space launchers 5, page 96.

[1] http://www.bulletins-electroniques.com/actualites/36354.htm

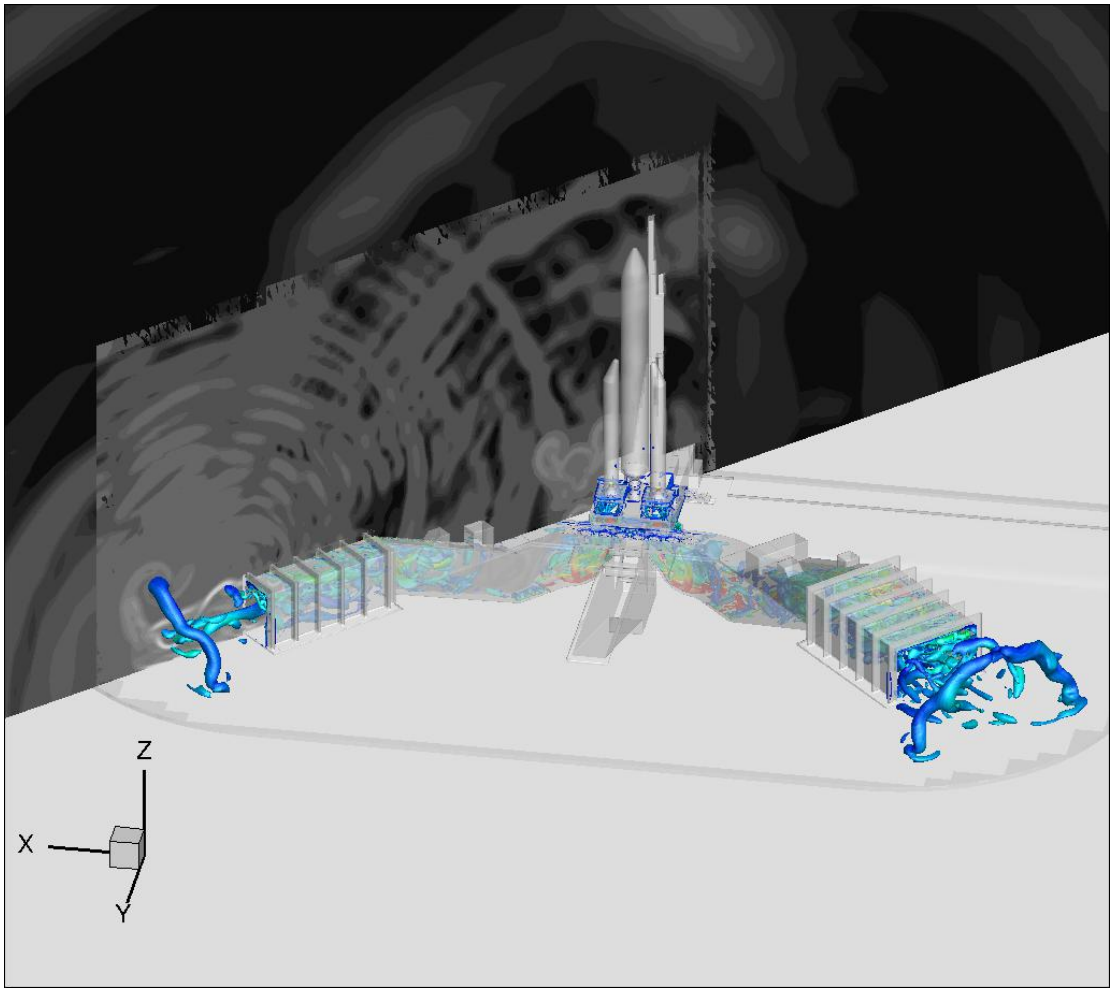

Figure 3.1: Ariane 5 blast wave simulation. Middle plane of the duct colored by schlieren and Q criterion colored by instantaneous velocity.

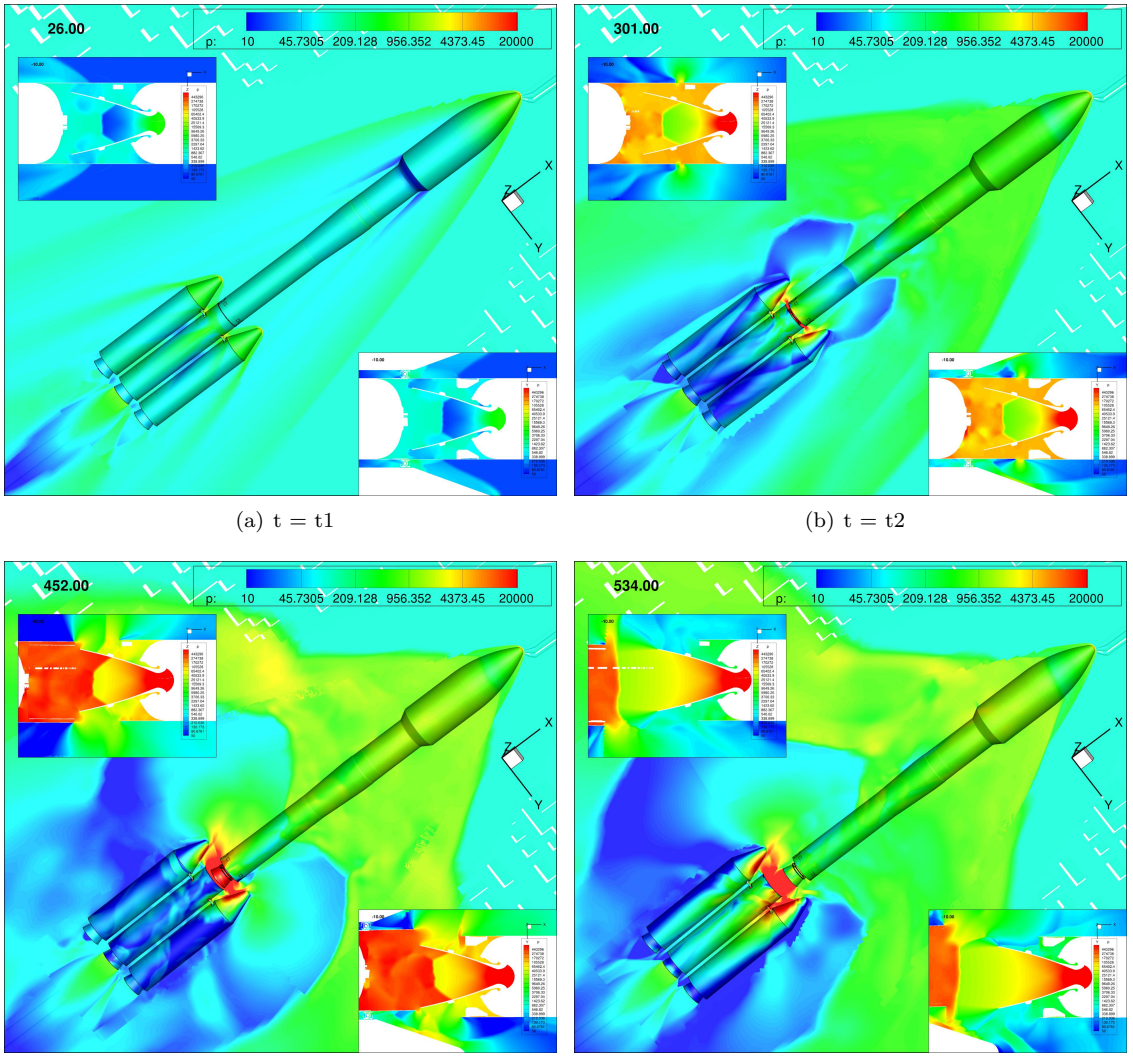

(a) t = t1

(b) t = t2

(c) t = t3

(d) t = t4

Figure 3.2: Stage separation of Ariane 6 space launcher, inter-stage nozzle, colored by pressure.

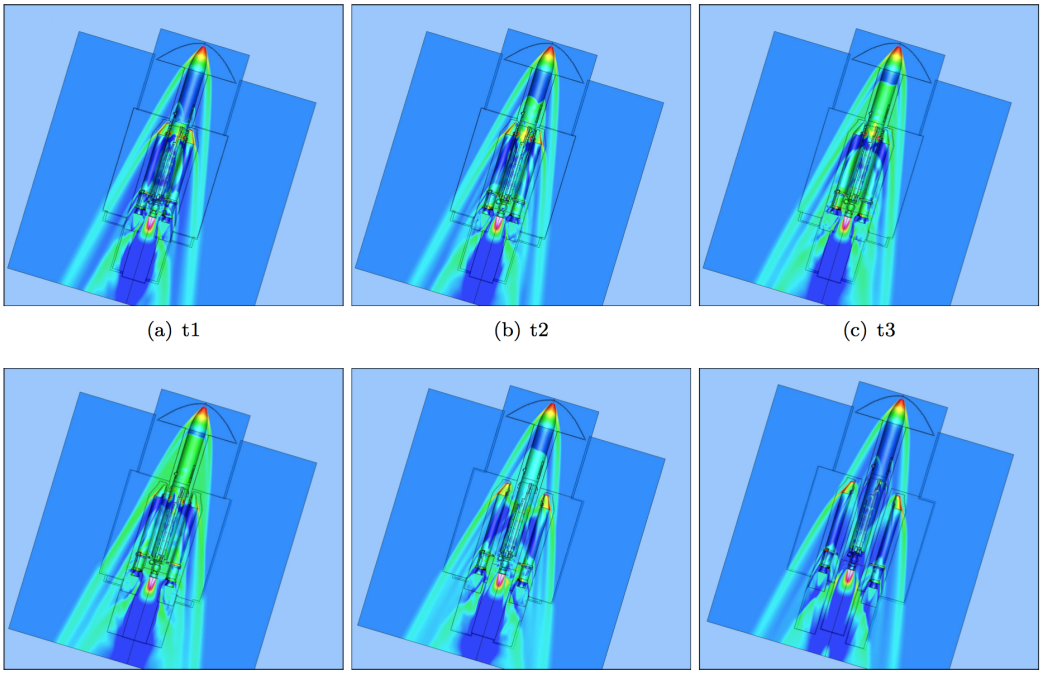

(a) t1 (b) t2 (c) t3

(d) t4 (e) t5 (f) t6

Figure 3.3: Ariane 5 stage separation

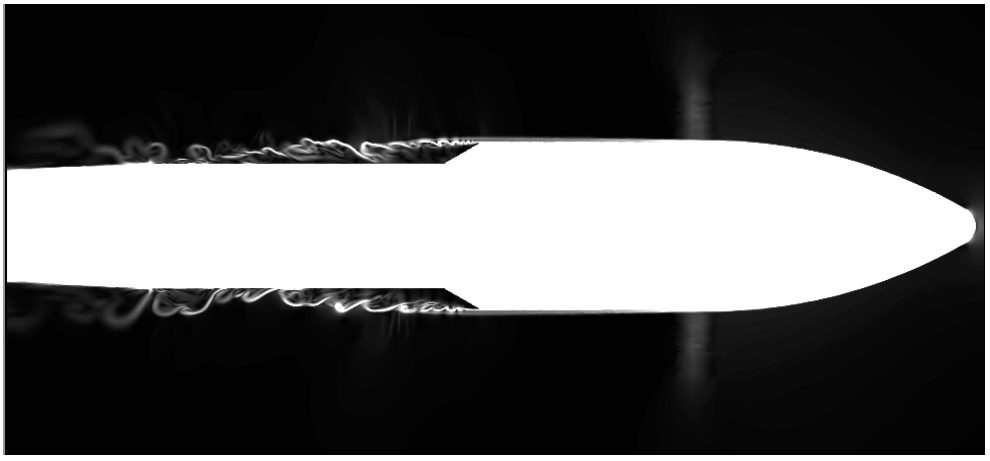

Figure 3.4: Instantaneous schlieren over a launcher shrinkage

3.2 Numerical strategy: high-order approximation on general grids

3.2.1 Numerical method

System (1.30) is approximated by means of a finite volume methodology on unstructured grids. The computational domain Ω_{CV} is partitioned in N cells Ω_J with boundary A_J, such that:

$$\Omega_{CV} = \bigcup_{J=1}^{N} \Omega_J \quad \text{and} \quad A_J = \bigcup_{K=1}^{P} A_{JK} \tag{3.1}$$

where index K denotes the K^{th} neighbour to cell Ω_J denoted Ω_K and A_{JK} the interface between two neighbours:

$$A_{JK} = \Omega_J \bigcap \Omega_K. \tag{3.2}$$

In each cell Ω_J, and for any field Ψ, we introduce the space average over one cell $\overline{\Psi}_J$ and the point-wise value at the cell center $\mathbf{x}_j$ of Ω_J, denoted Ψ_j (see figure 3.5). They are defined, respectively:

$$\overline{\Psi}_J = \frac{1}{\mid \Omega_J \mid} \iiint_{\Omega_J} \Psi \, d\Omega, \quad \text{and} \Psi_j = \Psi(\mathbf{x}_j), \quad \text{with} \quad \mathbf{x}_j = \frac{1}{\mid \Omega_J \mid} \iiint_{\Omega_J} \mathbf{x} \, d\Omega \tag{3.3}$$

In the above, $\mid \Omega_J \mid = \iiint_{\Omega_J} d\Omega$ denotes the volume of Ω_J. In the present approach, the problem unknowns are represented by the average volume of the conservative variables over each cell, i.e, the values:

$$\overline{\mathbf{w}}_J = \frac{1}{\mid \Omega_J \mid} \iiint_{\Omega_J} \mathbf{w} d\Omega, \tag{3.4}$$

Let us introduce $\mathcal{M}_J^{(m)}$, the m^{th} order volume moment of Ω_J, defined as:

$$\mathcal{M}_J^{(m)} = \frac{1}{\mid \Omega_J \mid} \iiint_{\Omega_J} (\mathbf{x} - \mathbf{x_j})^{\otimes m} d\Omega, \tag{3.5}$$

where, for any vector $\mathbf{v}$:

$$\mathbf{v}^{\otimes m} = \underbrace{\mathbf{v} \otimes \mathbf{v} \otimes ... \otimes \mathbf{v}}_{\text{m times}} \tag{3.6}$$

with $\otimes$ the dyad product between two vectors. Note that $\mathcal{M}^{(0)}$ is equal to the scalar unity and $\mathcal{M}^{(1)}$ is a null vector by definition of the cell center $\mathbf{x}_j$.

We also introduce $\mathcal{S}_{A_{JK}}^{(m)}$, the mth-order moment of A_{JK}, defined as:

$$\mathcal{S}_{A_{JK}}^{(m)} = \iint_{A_{JK}} (\mathbf{x} - \mathbf{x}_\Gamma)^{\otimes m} \cdot \mathbf{n} \, dS \tag{3.7}$$

Specifically, $\mathcal{S}_{A_{JK}}^{(0)}$ is the oriented surface of A_{JK}:

$$\mathcal{S}_{A_{JK}}^{(0)} = \iint_{A_{JK}} \mathbf{n} \, dS \tag{3.8}$$

With the preceding notations, the system of conservation laws referred to a computational cell writes:

$$\mid \Omega_J \mid \frac{d\overline{\mathbf{w}}_J}{dt} + \sum_{K=1}^{P} \iint_{A_{JK}} \mathbf{F} \cdot \mathbf{n} \, dS = 0 \tag{3.9}$$

where P is the number of faces of cell Ω_J.

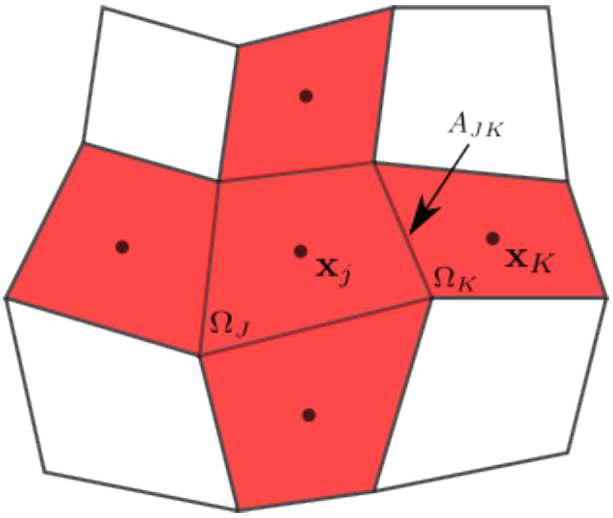

Figure 3.5: 2D sketch of a mesh, cell Ω_J

To complete the discretization, we need to find an approximation for the surface integral in 3.9 (flux term) as a function of the problem unknowns $\overline{\mathbf{w}}_J$. For this purpose we use a $k-exact$ reconstruction technique [69, 70], in conjunction with an efficient successive correction algorithm to achieve orders of accuracy greater than two.

For each grid cell Ω_J let us consider a neighborhood $s(J)$ made by the union of cell Ω_J and of its first direct neighbors (see Fig. 3.5), i.e. cells that share at least a face with Ω_J:

Definition 3.2.1 (k-exact function)**.** *A function ${}^k\Psi$ is said to be k-exact over $s(J)$ if its restriction to $s(J)$, ${}^k\Psi_{|_{s(J)}}$ is a polynomial of degree k. In other words, it exists a polynomial of degree k, ${}^k\mathcal{P}$ such that:*

$$ {}^k\Psi_{|_{s(J)}} =^k \mathcal{P}_{|_{s(J)}} $$

Now, let us call

$$ \overline{\Psi} = \left\{ \overline{\Psi}_J | J \in s(J) \right\} $$

the collection of the cell-averages of Ψ over the cells of $s(J)$, and denote $\mathcal{R}_{\overline{\Psi}}$

Definition 3.2.2 (k-exact reconstruction)**.** *A linear operator $\mathcal{R}_{\overline{\Psi}}$ is a k-exact reconstruction of a function Ψ over a grid neighborhood $s(J)$ if its restriction to $s(J)$ is a polynomial of degree k, i.e.:*

$$ (\mathcal{R}_{\overline{\Psi}}\,\Psi)_{|_{s(J)}} =^k \mathcal{P}_{|_{s(J)}} $$

Clearly, whenever Ψ is an m-exact function, $\Psi =^m \Psi$ with $m \leq k$, than:

$$ (\mathcal{R}_{\overline{\Psi}}\,\Psi)_{|_{s(J)}} \equiv^m \Psi_{|_{s(J)}}, $$

i.e. the reconstruction operator is exact. Otherwise, it represents a $k+1$ accurate approximation of Ψ on $s(J)$, according to a Taylor-series expansion.

Definition 3.2.3 (k-exact differentiation operator)**.** *A linear operator $\mathcal{D}^{(k)}_{\overline{\Psi}}$ is called a k-exact approximate differentiation operator over $s(J)$ if, for any m-exact function ${}^m\Psi$, with $m \leq k$, then:*

$$ (\mathcal{D}^{(k)}_{\overline{\Psi}}\,{}^m\Psi)_{|_j} = (\mathbf{D}^{(k)}\,{}^m\Psi)_{|_j} $$

where $\mathbf{D}^{(k)}(\bullet)\big|_j$ represents the kth spatial tensor derivative of Ψ at point $\mathbf{x}_j$.

In other terms, a k-exact differentiation operator provides an exact representation of the k^{th} derivative of ${}^m\Psi$. For a function Ψ that is not k-exact, it is easily shown through Taylor-series expansions that $\mathcal{D}^{(k)}_{\overline{\Psi}}\Psi = \mathbf{D}^{(k)}\Psi + O(h)$, i.e. the operator is at least first-order accurate.

In the following, we present a k-exact reconstruction of the solution within computational cells that can be used to find high-order approximations of Eq. (3.9). For robustness reasons, the reconstruction is applied to the primitive variables vector:

$$\mathbf{q} = (\mathbf{u}, P, T)^T, \quad \text{with} \quad \mathbf{q} = \mathbf{q}(\mathbf{w}) \tag{3.10}$$

Precisely, the primitive and conservative variables are related by:

$$\begin{cases} \mathbf{u} = (\rho\mathbf{u})/\rho \\ P = (\gamma-1)\left((\rho E) - \dfrac{1}{2}\dfrac{|\,\rho\mathbf{u}\,|^2}{\rho}\right) \\ T = \dfrac{P}{\rho R} \end{cases}$$

where the last two equation hold for perfect gas with constant R and constant specific heat ratio γ.
For further convenience, we introduce for each cell J the vector $\widetilde{q}_J = \widetilde{q}(\overline{\mathbf{w}}_J)$ defined as:

$$\widetilde{q}_J = (\widetilde{\mathbf{u}}_J, \widetilde{P}_J, \widetilde{T}_J)^T \tag{3.11}$$

with:

$$\begin{cases} \widetilde{\mathbf{u}}_J = (\overline{\rho\mathbf{u}})_J/\overline{\rho}_J \\ \widetilde{P}_J = (\gamma-1)\left((\overline{\rho E})_J - \dfrac{1}{2}\dfrac{|\,(\overline{\rho\mathbf{u}})_J\,|^2}{\overline{\rho}_J}\right) \\ \widetilde{T}_J = \dfrac{\widetilde{P}_J}{R\overline{\rho}_J} \end{cases} \tag{3.12}$$

Note that quantities $\widetilde{q}_J$ are second order accurate approximations of the pointwise values of the primitive variables at cell center $\mathbf{x}_j$. For instance, from the definition of volume average we get:

$$\widetilde{\mathbf{u}}_J = \frac{(\rho\mathbf{u})_j + \mathcal{O}(h^2)}{\rho_j + \mathcal{O}(h^2)} = \mathbf{u}_j + \mathcal{O}(h^2) \tag{3.13}$$

where h is a characteristic mesh size.
For the sake of clarity, in the following we first introduce the 2nd-order reconstruction procedure, then we generalize it to any order of accuracy by means of a successive correction procedure.

Second order k-exact reconstruction

A 2nd-order approximation of the flux integral in Eq. 3.9 is given by the classical second order formula:

$$\iint_{A_{JK}} \mathbf{F}\cdot\mathbf{n}\,dS = \mathbf{F}_\Gamma\cdot\mathcal{S}^{(0)}_{A_{JK}} + \mathbf{D}^{(\mathbf{1})}\mathbf{F}\Big|_\Gamma\cdot\mathcal{S}^{(1)}_{A_{JK}} + |A_{JK}|\mathcal{O}(h^2), \tag{3.14}$$

where $\mathbf{F}_\Gamma$ is the physical flux $\mathbf{F}$ at a point $\Gamma \in A_{JK}$, with $|A_{JK} = |\mathcal{S}^{(0)}_{A_{JK}}|$. For a flat cell interface, $\mathbf{n}$ is constant and Γ is the center of gravity of face A_{JK}, i.e.:

$$\mathbf{x_\Gamma} = \frac{1}{|\,A_{JK}\,|}\iint_{A_{JK}} \mathbf{x}\,dS$$

where $\mathcal{S}^{(1)}_{A_{JK}} = 0$. With this choice, equation (3.15) reduces to:

$$\iint_{A_{JK}} \mathbf{F}\cdot\mathbf{n}\,dS = \mathbf{F}_\Gamma\cdot\mathcal{S}^{(0)}_{A_{JK}} + |A_{JK}|\mathcal{O}(h^2) \tag{3.15}$$

For arbitrary skew grids, $\mathcal{S}^{(1)}_{A_{JK}} \neq 0$ in general. In this case, Γ is chosen in such a way to minimize the first-order error term in (3.14), see Appendix 8. To build the numerical flux $\mathbf{F}_\Gamma$, a second order approximation of $\mathbf{q}$ at point Γ is first constructed using information from cells at the left and at the right of face A_{JK} by using a linear reconstruction of the solution over Ω_J and Ω_K. Values of q reconstructed from the left and from the right are referred to as $\mathbf{q}_{\Gamma_L}$ and $\mathbf{q}_{\Gamma_R}$, respectively. An exact Riemann solver is then used to calculate the numerical flux $\mathbf{F}_\Gamma$.

A linear second-order accurate approximation of $\mathbf{q}$ over one cell is obtained by Taylor-expanding $\mathbf{q}$ around the cell center up to first-order terms:

$$\mathbf{q}(\mathbf{x}) = \mathbf{q}_j + \mathbf{D}^{(1)}\mathbf{q}\Big|_j \cdot (\mathbf{x} - \mathbf{x}_j) + \mathcal{O}(h^2) \tag{3.16}$$

where $\mathbf{D}^{(1)}\mathbf{q}\big|_j$ is the first order tensor derivative of $\mathbf{q}$ at point j, i.e, its gradient, and by replacing the pointwise values of $\mathbf{q}$ and $\mathbf{D}^{(1)}\mathbf{q}\big|_j$ by, respectively, a second-order and a first order approximation.

A straightforward second-order approximation for $\mathbf{q}_j$ is given by:

$$\mathbf{q}_j = \widetilde{\mathbf{q}}_J + \mathcal{O}(h^2) \tag{3.17}$$

To approximate $\mathbf{D}^{(1)}\mathbf{q}\big|_j$, we use a 1-exact differentiation operator according to Def. 3.2.2. This is written as a linear combination of cell averages:

$$(\mathcal{D}^{(1)}\overline{\mathbf{q}})\Big|_j = \sum_{K \in s(J)} \mathbf{W}_{JK}\overline{\mathbf{q}}_K \tag{3.18}$$

where $\mathbf{W}_{JK} = \mathcal{O}(\frac{1}{h})$ is the weight vector associated to the K^{th} cell of $s(J)$. Note that, if $\mathbf{q}$ is a 1-exact function, then for all $\Omega_J \in \Omega_{CV}$:

$$\mathbf{D^{(1)}}\mathbf{q} = \boldsymbol{\alpha} \tag{3.19}$$

with $\boldsymbol{\alpha}$ a constant vector, and

$$\mathbf{D^{(m)}}\mathbf{q} = 0 \quad \forall m \geq 2 \tag{3.20}$$

In this case, by integration of Eq. (3.16):

$$\overline{\mathbf{q}}_K = \mathbf{q}_k, \tag{3.21}$$

and

$$(\mathcal{D}^{(1)}\overline{\mathbf{q}})\Big|_j = \mathbf{D^{(1)}}\mathbf{q}\Big|_\mathbf{j} = \sum_{K \in s(J)} \mathbf{W}_{JK}\mathbf{q}_k \tag{3.22}$$

The last term can be expanded in Taylor series around $\mathbf{x}_j$, yielding:

$$(\mathcal{D}^{(1)}\overline{\mathbf{q}})\Big|_j = \sum_{K \in s(J)} \mathbf{W}_{JK}\left(\mathbf{q}_j + \mathbf{D}^{(1)}\mathbf{q}\Big|_j \cdot (\mathbf{x}_k - \mathbf{x}_j) + O(h^2)\right) \tag{3.23}$$

where second-order terms are null because of the 1-exactness of $\mathbf{q}$. Rearranging terms,

$$(\mathcal{D}^{(1)}\overline{\mathbf{q}})\Big|_j = \mathbf{q}_j \sum_{K \in s(J)} \mathbf{W}_{JK} + \sum_{K \in s(J)} (\mathbf{D}^{(1)}(\mathbf{q})\Big|_j \cdot (\mathbf{x}_k - \mathbf{x}_j))\mathbf{W}_{JK} \tag{3.24}$$

By equating Eq. (3.24) to Eq. (3.22) it is deduced that the 1-exactness conditions for the operator $\mathcal{D}^{(1)}$ are:

$$\sum_{K \in s(J)} \mathbf{W}_{JK} = 0, \quad \text{0-exactness condition} \tag{3.25}$$

$$\sum_{K \in s(J)} (\boldsymbol{\alpha} \cdot (\mathbf{x}_k - \mathbf{x}_j))\mathbf{W}_{JK} = \boldsymbol{\alpha}, \quad \forall \boldsymbol{\alpha} \tag{3.26}$$

In practice, the operator $\mathcal{D}^{(1)}$ is not applied to $\overline{\mathbf{q}}_J$ but instead to $\widetilde{\mathbf{q}}_J$. Actually, since $\widetilde{\mathbf{q}}_J = \overline{\mathbf{q}}_J + \mathcal{O}(h^2)$, then:

$$(\mathcal{D}^{(1)}\overline{\mathbf{q}})\Big|_j = (\mathcal{D}^{(1)}\widetilde{\mathbf{q}})\Big|_j) + \mathcal{O}(h) \tag{3.27}$$

So, to the first order of accuracy, using $\widetilde{\mathbf{q}}$ in place of $\overline{\mathbf{q}}$ does not impact on the leading error term, but $\widetilde{\mathbf{q}}$ is more readily computed from the problem unknowns $\overline{\mathbf{w}}$ by means of Eqs (3.12). In summary, the final expression for the gradient approximation operator $\mathbf{D}^{(1)}\mathbf{q}\big|_j$ is:

$$(\mathcal{D}^{(1)}\widetilde{\mathbf{q}})\Big|_j = \sum_{K\in s(J)} \mathbf{W}_{JK}\widetilde{\mathbf{q}}_k \tag{3.28}$$

With $\mathbf{q}_j$ and $\mathbf{D}^{(1)}\mathbf{q}\big|_j$, approximated to the second and first order by means of equations (3.21) and (3.28), respectively, the left and right values of $\mathbf{q}$ at point Γ are computed as:

$$\begin{cases} \mathbf{q}_{\Gamma_L} = \mathbf{q}_j + (\mathcal{D}^{(1)}\widetilde{\mathbf{q}})\big|_j \cdot (\mathbf{x}_\Gamma - \mathbf{x}_j) + \mathcal{O}(h^2) \\ \mathbf{q}_{\Gamma_R} = \mathbf{q}_k + (\mathcal{D}^{(1)}\widetilde{\mathbf{q}})\big|_k \cdot (\mathbf{x}_\Gamma - \mathbf{x}_k) + \mathcal{O}(h^2) \end{cases}$$

where j and k denote the centers of cells J and K, respectively. A Riemann solver is finally used to calculate the numerical flux $\mathbf{F}_\Gamma$ from $\mathbf{q}_{\Gamma_L}$ and $\mathbf{q}_{\Gamma_R}$. Here we describe a MUSCL [63] type reconstruction. Limiters can be applied to the reconstructed values to avoid the appearance of spurious oscillations close to flow discontinuities.

Gradient computation on general meshes: method of simple correction

Coefficient $\mathbf{W}_{JK}$ are determined by mean of a quasi-Green formulation supplemented by a correction step to recover consistency on general meshes [71]. The correction step is essential to preserve consistency on arbitrary unstructured grid. We have seen in the preceding Section that a 1-exact differentiation operator applied to the primitive variables, $\mathcal{D}^{(1)}\mathbf{q}\big|_j$ is of the form (3.28). We still have to determine the coefficients W_{JK}.

There are several approaches for gradient computation on unstructured grids like Green-Gauss or Weighted-Least-Squares. For instance, these approaches are used in [72, 73, 74]. Using the Gauss-Green theorem:

$$\iiint_{\Omega_J} \mathbf{D}^{(1)}\mathbf{q}\Big|_j d\Omega = \oiint_{\partial\Omega_J} \mathbf{q}\,\mathbf{n} dS = \sum_{K=1}^{P} \iint_{A_{JK}} \mathbf{q}\,\mathbf{n}\, dS, \tag{3.29}$$

And applying the mean value theorem to the left hand side:

$$|\ \Omega_J\ |\ \mathbf{D}^{(1)}\mathbf{q}\Big|_j = \sum_{K=1}^{P} \iint_{A_{JK}} \mathbf{q}\,\mathbf{n}\, dS \tag{3.30}$$

The integrals on the right hand side can be approximated using a one-point-per-face integration scheme:

$$\iint_{A_{JK}} \mathbf{q}\,\mathbf{n}\, dS \simeq (\beta_K \overline{\mathbf{q}}_K + (1-\beta_K)\overline{\mathbf{q}}_J)\cdot \mathbf{A}_{JK}, \tag{3.31}$$

where $\mathbf{A}_{JK}$ is surface oriented from J to K, and β_K is a weight associated to cell K. Coefficients β_K are weights based on the relative distance of cell centers $\mathbf{x}_k$ to face A_{JK} compared to $||\mathbf{x}_k - \mathbf{x}_j||$.
Using (3.31) to compute the gradient from (3.30) corresponds to use equation (3.28) with weight vectors given by:

$$\mathbf{W}_{JJ} = \frac{1}{|\ \Omega_J\ |}\sum_{K\in s(J)} (1-\beta_K)\mathbf{A}_{JK} \quad \mathbf{W}_{JK} = \frac{1}{|\ \Omega_J\ |}\beta_K \mathbf{A}_{JK} \tag{3.32}$$

Formulation 3.31 is not consistent for any general grid: it always satisfies the first one of conditions (the 0-exactness condition) (3.25), but not the second one (the 1-exactness conditon).

Since the approximation operator (3.28) is a linear application, it can be represented by a matrix $\mathbf{M}_1$ such that:

$$\sum_{K\in s(J)} (\boldsymbol{\alpha}\cdot(\mathbf{x}_k - \mathbf{x}_j)).\mathbf{W}_{JK} = \mathbf{M}_1\boldsymbol{\alpha}, \quad \forall \boldsymbol{\alpha} \tag{3.33}$$

For a 1-exact function ${}^1\Psi$:

$$\overline{{}^1\Psi}_K - \overline{{}^1\Psi}_J = \mathbf{D^{(1)}}{}^1\Psi\Big|_j \cdot (\mathbf{x}_k - \mathbf{x}_j), \tag{3.34}$$

multiplying by $\beta_K \mathbf{A}_{JK}$ and summing over K:

$$\sum_{K\in s(J)} \beta_K(\overline{{}^1\Psi}_K - \overline{{}^1\Psi}_J)\mathbf{A}_{JK} = \sum_{K\in s(J)} \beta_K \, \mathbf{D^{(1)}}\Psi^{(1)}\Big|_j \cdot (\mathbf{x}_k - \mathbf{x}_j))\mathbf{A}_{JK}, \tag{3.35}$$

Or, by reordering and using the fact that cell faces form a closed surface,

$$\sum_{K\in s(J)} \left(\beta_K \overline{{}^1\Psi}_K + (1-\beta_K)\overline{{}^1\Psi}_J\right) \mathbf{A}_{JK} = \sum_{K\in s(J)} \left(\beta_K(\overline{{}^1\Psi}_K - \overline{\Psi}_J^{(1)})\right) \mathbf{A}_{JK}. \tag{3.36}$$

Combining equations (3.30), (3.31), (3.33), and (3.36), we get finally:

$$\mathbf{D}^{(1)}\overline{{}^1\Psi}\Big|_j = \mathbf{M}_1^{-1} \sum_{K\in s(J)} \left(\beta_K \overline{{}^1\Psi}_K + (1-\beta_K)\overline{{}^1\Psi}_J\right) \mathbf{A}_{JK} \tag{3.37}$$

which differs by the standard quasi-Green gradient approximation by the correction matrix $\mathbf{M}_1^{-1}$. For a generic function Ψ, the gradient approximation $\mathcal{D}_{\mathbf{1}}^{(1)}$:

$$(\mathcal{D}_{\mathbf{1}}^{(1)}\overline{{}^1\Psi})\Big|_j = \mathbf{M}_1^{-1} \sum_{K\in s(J)} \left(\beta_K \overline{{}^1\Psi}_K + (1-\beta_K)\overline{{}^1\Psi}_J\right) \mathbf{A}_{JK} \tag{3.38}$$

is by construction 1-exact, according to Definition 3.2.3, and as such it is first-order accurate for any function Ψ and any general mesh.

The matrix $\mathbf{M}_1$ is call hereafter the "simple correction" matrix, and is given by:

$$\mathbf{M}_1 = \sum_{K=1}^{P} \beta_K(\mathbf{x}_k - \mathbf{x}_j) \otimes \mathbf{A}_{IJ} \tag{3.39}$$

Note that for regular Cartesian grid, $M_1 = \mathbb{I}$: thus, the role of M_1 is to correct the quasi-Green gradient approximation to enforce first order accuracy on any grid.

Higher order k-exact reconstruction

Higher order approximations of the fluxes and, consequently, higher-order schemes, can be obtained by using a polynomial reconstruction of higher degree for the primitive variables, along with high-order integration formulae for the flux terms in (3.9). Unlike previous work [75] that uses costly Gauss quadrature formulas, here we adopt one-point integration formulae based on high-accurate approximations of the flux and its derivatives at a point Γ of the cell interface.
In the following, we first introduce the one-point integration formula, then we illustrate the high-order reconstruction procedure over each cell. Finally, we derive approximations of the flux and its successive derivatives at point Γ from the surrounding cell center values.

One point integration formula for the fluxes The construction of higher order schemes starts with the development of a high-accurate approximation formula for the flux term:

$$\iint_{A_{JK}} \mathbf{F}\cdot\mathbf{n}\, dS, \tag{3.40}$$

to replace equation (3.15) that is only second-order accurate. This is achieved by expanding $\mathbf{F}$ in Taylor series around a suitable integration point Γ of A_{JK}. Plugging this expression into (3.40) gives:

$$\iint_{A_{JK}} \mathbf{F}\cdot\mathbf{n}\, dS = \sum_{m=0}^{n-1} \frac{1}{m!}\mathbf{D}^{(m)}\,\mathbf{F}|_\Gamma \cdot \mathcal{S}_{A_{JK}}^{(m)} + |A_{JK}|\mathcal{O}(h^n) \tag{3.41}$$

where $\mathbf{D}^{(l)}\ \mathbf{F}|_\Gamma$ is the lth tensor derivative of $\mathbf{F}$ at point Γ, and h a characteristic grid size. We recall that:

$$\mathbf{D}^{(0)}\mathbf{F}\Big|_\Gamma = \mathbf{F}|_\Gamma\,,\ \mathbf{D}^{(1)}\mathbf{F}\Big|_\Gamma = \mathbf{grad}(\mathbf{F})|_\Gamma \quad \text{and} \quad \mathcal{S}^{(0)}_{A_{JK}} = \iint_{A_{JK}} \mathbf{n}\,dS \tag{3.42}$$

Finally, 3.41 writes:

$$\iint_{A_{JK}} \mathbf{F}\cdot\mathbf{n}\,dS = \mathbf{F}|_\Gamma \cdot \mathcal{S}^{(0)}_{A_{JK}} + \sum_{m=1}^{n-1} \frac{1}{m!}\mathbf{D}^{(m)}\ \mathbf{F}|_\Gamma \cdot \mathcal{S}^{(m)}_{A_{JK}} + |A_{JK}|\mathcal{O}(h^n) \tag{3.43}$$

Note that, for a flat interface, $\mathcal{S}^{(1)}_{A_{JK}} = 0$ and we can rewrite the previous sum:

$$\iint_{A_{JK}} \mathbf{F}\cdot\mathbf{n}\,dS = \mathbf{F}|_\Gamma \cdot \mathcal{S}^{(0)}_{A_{JK}} + \sum_{m=2}^{n-1} \frac{1}{m!}\mathbf{D}^{(m)}\ \mathbf{F}|_\Gamma \cdot \mathcal{S}^{(m)}_{A_{JK}} + |A_{JK}|\mathcal{O}(h^n) \tag{3.44}$$

In the following, we assume for simplicity flat cell interfaces. If this hypothesis is not verified, then point Γ is selected as the point that minimizes the first-order error term (see Appendix 8).

To achieve a nth-order approximation of the surface integral, the flux and its derivatives at point Γ have to be reconstructed from cell-centered averages with suitable accuracy: precisely, $\mathbf{D}^{(m)}\mathbf{F}\big|_\Gamma$ has to be reconstructed at order $n-m$. For instance, to achieve 3rd order accuracy ($n=3$), $\mathbf{F}|_\Gamma$ has to be reconstructed at order 3, $\mathbf{D}^{(1)}\mathbf{F}\big|_\Gamma$ at order 2 and $\mathbf{D}^{(2)}\mathbf{F}\big|_\Gamma$ at order 1. For this purpose, we choose to rewrite the mth derivatives of the flux in terms of the mth derivatives of the primitive variables $\mathbf{D}^{(m)}\mathbf{q}$. In turn, these are evaluated by means of a high-order k-exact reconstruction, along with the successive correction algorithm of Section 3.2.1. This change of variable involves a negligible additional cost, since approximations of the derivatives $\mathbf{D}^{(m)}\mathbf{q}$ are already used in other steps of the method. For stability reasons, a donor cell technique [76] is used to chose information reconstructed from the left or from the right side of a given interface according to the local advection direction

High order k-exact reconstruction procedure To calculate approximations of the solution at cell faces, high-order polynomials are constructed over each cell by using again Taylor-series expansions. These are obtained by including higher-order terms in Eq. (3.16):

$$\mathbf{q}(\mathbf{x}) = \mathbf{q}_j + \mathbf{D}^{(1)}\Big|_j \cdot (\mathbf{x}-\mathbf{x}_j) + \sum_{m=2}^{n-1} \mathbf{D}^{(m)}\Big|_j \cdot (\mathbf{x}-\mathbf{x}_j)^{\otimes m} + O(h^n) \tag{3.45}$$

A nth-order reconstruction of the primitive variables is obtained by truncating (3.45) at order $n-1$ and by approximating $\mathbf{q}_j$ at order n, $\mathbf{D}^{(1)}\big|_j$ at order $n-1$ and $\mathbf{D}^{(m)}\big|_j$, $m=2,\dots,n-1$ at order $n-m$.

First, a high-accurate approximate deconvolution procedure is developed to construct pointwise values of the variables at cell centers from the problem unknowns. Similarly to the 2nd-order scheme of Section 3.2.1, the polynomial reconstruction is applied to the primitive variables.
By Taylor-series expanding the primitive variables $\mathbf{q}$ around the cell center $\mathbf{x}_j$, and by averaging over the cell, one gets:

$$\mathbf{q}_j = \overline{\mathbf{q}}_J - \frac{1}{|\Omega_J|}\sum_{m=1}^{n-1}\frac{1}{m!}\mathcal{M}^{(m)}_J : \mathbf{D}^{(m)}\mathbf{q}\Big|_j + \mathcal{O}(h^n) \tag{3.46}$$

where $\mathcal{M}^{(m)}_J$ is the m^{th} volume moment of Ω_J, given by Equation (3.5), $\mathbf{D}^{(m)}\mathbf{q}\big|_j$ is the m^{th}-order tensor derivative of $\mathbf{q}$ at point $\mathbf{x}_j$ and : denotes the inner product between two m^{th}-order tensors. Note that the contribution of first order derivatives (i.e. the term $m=1$ in the sum) vanishes because first-order moments with respect to the volume center of Ω_J are identically null.
An approximation of $\mathbf{q}_j$ at order $n>2$ requires to find an $(n-m)$th-order accurate approximation for the m^{th} derivative $\mathbf{D}^{(m)}\mathbf{q}\big|_j$ as well as an nth-order approximation for $\overline{\mathbf{q}}_J$.
Both $\overline{\mathbf{q}}_J$ and $\mathbf{D}^{(m)}\mathbf{q}\big|_j$ have to be computed from the problem unknowns $\overline{\mathbf{w}}_J$, for which purpose we use

the procedure described in the following.

As a first step, we start writing an approximation for $\overline{\mathbf{q}}_J$. Note that:

$$\overline{\mathbf{q}}_J = \widetilde{\mathbf{q}}_J + \mathcal{O}(h^2), \tag{3.47}$$

where $\widetilde{\mathbf{q}}_J$ is directly related to the problem unknowns $\overline{\mathbf{w}}_J$ through equations (3.12). To achieve a higher-order approximation for $\overline{\mathbf{q}}_J$, we need to correct the second order error term.
Precisely, we look for a relation of the form:

$$\overline{\mathbf{q}}_J = \widetilde{\mathbf{q}}_J + \Delta\mathbf{q} + \mathcal{O}(h^n), \tag{3.48}$$

The correction term $\Delta\mathbf{q}$ depends on the specific primitive variable under consideration ($\mathbf{u}$, P or T). For the sake of brevity, hereafter we describe just only the general principles of the procedure. First, $\widetilde{\mathbf{q}}_J = \widetilde{\mathbf{q}}(\overline{\mathbf{w}}_J)$ is Taylor-series expanded in order to express average value of conservative variables $\mathbf{w}_J$ in term of their pointwise values $\mathbf{w}_j$ and their successive derivatives at point $\mathbf{x}_j$, $\mathbf{D}^{(m)}\mathbf{w}\Big|_j$:

$$\widetilde{\mathbf{q}}_J = \widetilde{\mathbf{q}}(\overline{\mathbf{w}}_J) = \widetilde{\mathbf{q}}\left(\mathbf{w}_j + \frac{1}{|\Omega_J|}\sum_{m=2}^{n-1}\frac{1}{m!}\mathcal{M}_J^{(m)} : \mathbf{D}^{(m)}\mathbf{w}\Big|_j + \mathcal{O}(h^n)\right) \tag{3.49}$$

In its turn, $\widetilde{\mathbf{q}}$ (3.49) is Taylor-series expanded around $\mathbf{w}_j$, and its derivatives are re-written in terms of the conservatives variables, to get:

$$\widetilde{\mathbf{q}}_J = \mathbf{q}_j + \delta\mathbf{q}\left(\mathbf{D}^{(2)}\mathbf{w}\Big|_j, \mathbf{D}^{(3)}\mathbf{w}\Big|_j, ..., \mathbf{D}^{(n-1)}\mathbf{w}\Big|_j\right) \tag{3.50}$$

where δq represents again a correction term, which depends on $\mathbf{D}^{(m)}$, $\quad m = 2, \ldots, n-1$, allowing to evaluate $\mathbf{q}_j$ from $\widetilde{\mathbf{q}}_J$ to an order of accuracy greater than 2.

Substracting equation (3.50) from equation (3.46) and re-arranging terms, one finally obtains:

$$\Delta\mathbf{q} = \overline{\mathbf{q}}_J - \widetilde{\mathbf{q}}_J + \mathcal{O}(h^n) \tag{3.51}$$

The important thing to note here is that, unlike equation (3.50), $\Delta\mathbf{q}$ depends only on derivatives of $\mathbf{q}$ at point $\mathbf{x}_j$ up to order $n-2$, and not $n-1$ since the error terms depending on $(n-1)$th derivatives cancel (see Appendix 7.1 for more details). Moreover, getting an nth-order approximation for $\overline{\mathbf{q}}_J$ requires only an $(n-m-1)^{th}$ order approximation for $\mathbf{D}^{(m)}\mathbf{q}\Big|_j$.
The required approximations are constructued by mean of the successive corrections algorithm described in the following Section.

Method of successive corrections

The higher-order approximation of the derivatives and of $\overline{q}_J$ required for the k-exact reconstruction and flux integration are obtained by means of a recursive procedure, based on successive corrections of the truncation error terms.

At the beginning of the procedure, a first-order approximation of the first derivatives at point $\mathbf{x}_j$ is obtained by applying the 1-exact operator $\mathcal{D}_1^{(1)}$ of Section 3.2.1 to $\widetilde{\mathbf{q}}$, which is a second-order approximation for $\overline{\mathbf{q}}$.

The preceding first-order approximation allows to construct a third-orderd approximation for $\overline{\mathbf{q}}_J$ by using Equations (3.47)-(3.50).

Then, the first-order differentiation operaton can be re-applied to this higher-order approximation of $\overline{\mathbf{q}}$. The associated truncation error is of the form:

$$\mathcal{E}_1^{(1)} = (\mathcal{D}_1^{(1)}\widetilde{\mathbf{q}})\Big|_J - \mathbf{D}^{(1)}\mathbf{q}\Big|_j = \mathbf{D}^{(2)}\mathbf{q}\Big|_j \cdot \mathcal{H}_1 + O(h^2) \tag{3.52}$$

where $\mathcal{H}_1$ is a matrix that depends only on the geometrical properties of the mesh in use, the elements of which are $O(h)$.

An approximation of the 2nd derivatives at point $\mathbf{x}_j$, $\mathbf{D}^{(2)}\big|_j$, is obtained by applying $\mathcal{D}_1^{(1)}$ twice to $\overline{\mathbf{q}}_J$. This leads, on general meshes, to an inconsistent operator:

$$\left(\mathcal{D}_1^{(1)}\left(\mathcal{D}_1^{(1)}\overline{\mathbf{q}}\right)\right)\Big|_J = \mathbf{D}^{(2)}\Big|_j + O(1)$$

Similarly to the procedure used in Section 3.2.1 to construct $\mathcal{D}_1^{(1)}$, a 1-exact (hence, consistent) approximation for the second derivatives is obtained by setting:

$$\left(\mathcal{D}_1^{(1)}\left(\mathcal{D}_1^{(1)}\overline{\mathbf{q}}\right)\right)\Big|_J = M_2\left(\mathcal{D}_1^{(2)}\overline{\mathbf{q}}\right)\Big|_J \tag{3.53}$$

where M_2 is a linear application such that:

$$\left(\mathcal{D}_1^{(2)}\overline{\mathbf{q}}\right)\Big|_J = M_2^{-1}\left(\mathcal{D}_1^{(1)}\left(\mathcal{D}_1^{(1)}\overline{\mathbf{q}}\right)\right)\Big|_J = \mathbf{D}^{(2)}\mathbf{q}\Big|_j + O(h)$$

Details about the construction of M_2 are given in [75].

The first-order approximation of the second-order derivatives can be used to correct the truncation error of $\mathcal{D}_1^{(1)}$ in Eq. (3.52), leading to a second-order approximation for the first derivatives:

$$\left(\mathcal{D}_2^{(1)}\overline{\mathbf{q}}\right)\Big|_J = \mathbf{D}^{(1)}\mathbf{q}\Big|_j + O(h^2) \tag{3.54}$$

Finally, the 3rd-order approximation of $\overline{\mathbf{q}}_J$, the second-order approximation of $\mathbf{D}^{(1)}\mathbf{q}\big|_j$, and the first-order approximation of $\mathbf{D}^{(2)}\mathbf{q}\big|_j$ can be used to build a 3-exact reconstruction formula for q over one cell Ω_J, according to Eq. (3.45).

The preceding procedure can be repeated iteratively to further increase the order of accuracy. Precisely:

- The second-order approximation of $\mathbf{D}^{(1)}\big|_j$ and the first-order approximation of $\mathbf{D}^{(2)}\big|_j$ can be used to correct the preceding third-order approximation of $\overline{\mathbf{q}}_J$ (Eq. 3.47), thus obtaining a fourth-order approximation.
- The 2-exact operator for the first derivatives and the 1-exact operator for the second derivatives are applied to the fourth-order approximation.
- An approximation for the third-order derivatives is obtained by applying $\mathcal{D}_1^{(1)}$ to $\left(\mathcal{D}_1^{(2)}\overline{\mathbf{q}}\right)\Big|_J$.
- The resulting inconsistent third differentiation operator is corrected via a suitable linear application, M_3, leading to a 1-exact operator, denoted $\mathcal{D}_1^{(3)}$
- The first-order approximation of the third derivatives is used to correct the first-order truncation error term of $\mathcal{D}_1^{(2)}$, of the form:

$$\mathcal{E}_1^{(2)} = \left(\mathcal{D}_1^{(2)}\overline{\mathbf{q}}\right)\Big|_J - \mathbf{D}^{(2)}\mathbf{q}\Big|_j = \mathbf{D}^{(2)}\mathbf{q}\Big|_j \cdot \mathcal{H}_2 + O(h^2) \tag{3.55}$$

  where $\mathcal{H}_2$ is again a matrix that depends only on the geometrical properties of the mesh in use, the elements of which are $O(h)$. After correction, a 2-exact, second differentiation operator is obtained, denoted $\mathcal{D}_2^{(2)}$.
- Similarly, $\mathcal{D}_1^{(3)}$ and $\mathcal{D}_2^{(2)}$ are used to correct the second-order truncation error term of $\mathcal{D}_2^{(1)}$, leading to a 3-exact first differentiation operator, $\mathcal{D}_3^{(1)}$
- The higher-order approximations of $\overline{\mathbf{q}}_J$ and of the derivatives are used finally to build a 4-exact approximation of $\mathbf{q}$ over a cell.

In a more general way, an n-exact approximation of $\mathbf{q}$ can be obtained through the following:

Algorithm *[Successive correction algorithm]*

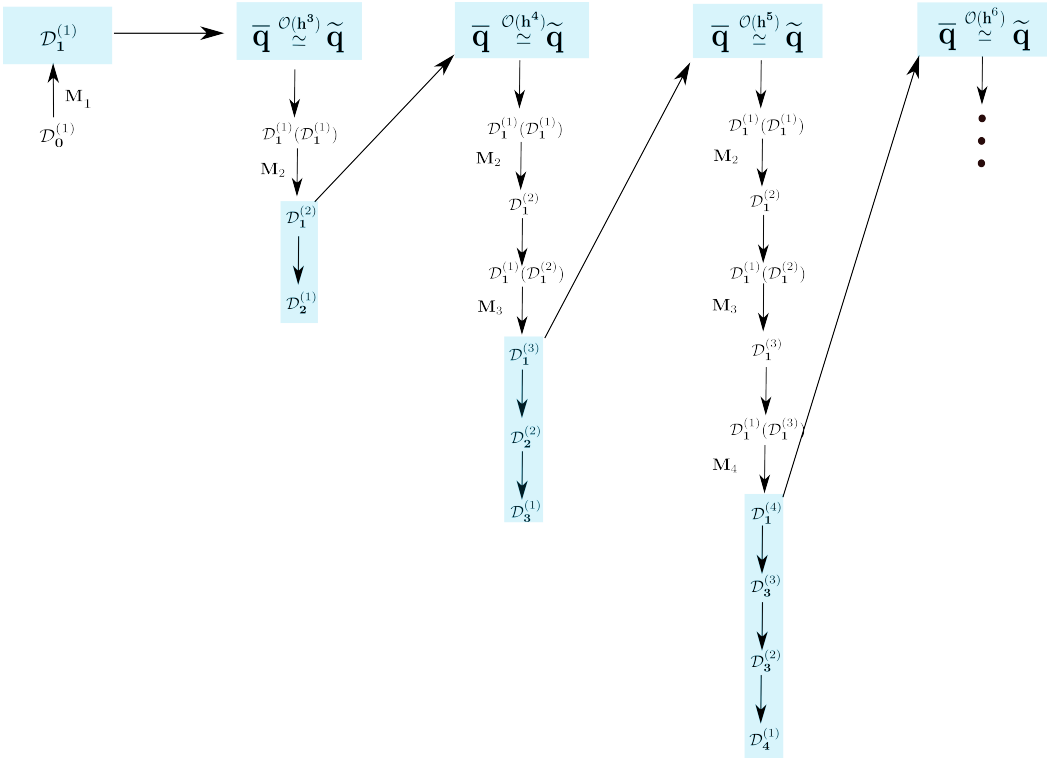

Figure 3.6: The three first steps of the successive corrections algorithm.

1. Initialization: compute $\widetilde{\mathbf{q}}_J = \widetilde{\mathbf{q}}(\overline{w}_J)$ from Eq. (3.12)
2. Set $\overline{\mathbf{q}}_J \leftarrow \widetilde{\mathbf{q}}_J$

($*$ with an error $O(h^2)$ $*$)

3. Set $\left(\mathcal{D}_1^{(1)}\overline{\mathbf{q}}\right)\Big|_J \leftarrow \left(\mathcal{D}_1^{(1)}\widetilde{\mathbf{q}}\right)\Big|_J$

($*$ with an error $O(h)$ $*$)

4. **for** $m \leftarrow 1$ **to** n
5. **do** Use $\left(\mathcal{D}_m^{(1)}\overline{\mathbf{q}}\right)\Big|_J$, $\left(\mathcal{D}_{m-1}^{(2)}\overline{\mathbf{q}}\right)\Big|_J, \ldots, \left(\mathcal{D}_1^{(m-1)}\overline{\mathbf{q}}_J\right)\Big|$ to compute
6. $\overline{\mathbf{q}}_J = \widetilde{\mathbf{q}}_J + \Delta\mathbf{q} + O(h^{m+2})$
7. **for** $k \leftarrow 1$ **to** m
8. Set $\left(\mathcal{D}_{m-k+1}^{(k)}\overline{\mathbf{q}}\right)\Big|_J \leftarrow \left(\mathcal{D}_{m-k+1}^{(k)}\overline{\mathbf{q}}\right)\Big|_J$

($*$ Differentiate the highest-order estimate available for $\overline{\mathbf{q}}$ $*$)
($*$ using the highest-order available differentiation operators $*$)

9. Compute
10. $\left(\mathcal{D}_1^{(1)}\left(\mathcal{D}_1^{(m)}\overline{\mathbf{q}}\right)\right)\Big|_J = \mathbf{D}^{(m+1)}\mathbf{q}\big|_j + O(1)$
11. Compute
12. $\left(\mathcal{D}_1^{(m+1)}\overline{\mathbf{q}}\right)\Big|_J = M_{m+1}^{-1}\left(\mathcal{D}_1^{(1)}\left(\mathcal{D}_1^{(m)}\overline{\mathbf{q}}\right)\right]\Big|_J = \mathbf{D}^{(m+1)}\mathbf{q}\big|_j + O(h)$ **for** $l \leftarrow m$ **to** 1
13. **do** Use $\left(\mathcal{D}_1^{(m+1)}\overline{\mathbf{q}}\right)\Big|_J$, $\left(\mathcal{D}_2^{(m)}\overline{\mathbf{q}}\right)\Big|_J, \ldots, \left(\mathcal{D}_{m-l+1}^{(l+1)}\overline{\mathbf{q}}\right)\Big|_J$ to
14. correct the truncation error of $\left(\mathcal{D}_{m-l+1}^{(l)}\overline{\mathbf{q}}\right)\Big|_J$ and
15. obtain $\left(\mathcal{D}_{m-l+2}^{(l)}\overline{\mathbf{q}}\right)\Big|_J = \mathbf{D}^{(l)}\mathbf{q}\big|_j + O(h^{m-l+1})$
16. **return** the $m+2$ reconstruction of $\mathbf{q}$ at a point $\mathbf{x}$, $\mathbf{q}(\mathbf{x}) = \mathbf{q}_j + \sum_{m=1}^{n-1}\left(\mathcal{D}_{n-m}^{(m)}\overline{\mathbf{q}}\right)\Big|_J \cdot (\mathbf{x}-\mathbf{x}_j)^{\otimes m}$

The figure 3.6 gives a illustration of the three first steps of the successive corrections algorithm.

Note that, from a numerical point of view, the numerical cross derivatives does not respect the Schwarz theorem, especially on irregular grids. To overcome this issue, we perform a average of numerical cross derivatives calculated in each direction.

Integration of the numerical flux In Section 3.2.1, we presented a nth-order one-point integration formula (3.44) for the flux through a cell interface. The formula involves an nth-order approximation of the flux density at the integration point Γ, $\mathbf{F}|_\Gamma$, as well as $n-m$th-order approximations of its mth derivatives.

To calculate $\mathbf{F}|_\Gamma$, k-exact reconstruction of the primitive variable vector $\mathbf{q}$ over cells at the left and at the right of the interface are used to approximate $\mathbf{q}$ at point Γ to the nth order of accuracy from the left and from the right, respectively:

$$\begin{cases} \mathbf{q}_{\Gamma_L} = \mathbf{q}_j + \sum_{m=1}^{n-1} \left(\mathcal{D}_{n-m}^{(m)} \overline{\mathbf{q}}\right)\Big|_J \cdot (\mathbf{x}_\Gamma - \mathbf{x}_j)^{\otimes m} + \mathcal{O}(h^n) \\ \mathbf{q}_{\Gamma_R} = \mathbf{q}_k + \sum_{m=1}^{n-1} \left(\mathcal{D}_{n-m}^{(m)} \overline{\mathbf{q}}\right)\Big|_K \cdot (\mathbf{x}_\Gamma - \mathbf{x}_k)^{\otimes m} + \mathcal{O}(h^n) \end{cases}$$

where the indices j and k denote the centers of cells J and K, respectively; $m-n$th-accurate differentiation operators $\mathcal{D}_{n-m}^{(m)}$ are constructed via the successive correction algorithm. Similarly to the second-order scheme described in 3.2.1, a donor-cell method [76] is used to chose the left or right value. Eventually, limiters are applied to the reconstructed values.

Once the left and right values are known, an exact Riemann solver is finally used to calculate the numerical flux $\mathbf{F}_\Gamma$ from $\mathbf{q}_{\Gamma_L}$ and $\mathbf{q}_{\Gamma_R}$.

The next step is to reconstruct the corrective terms at the right-hand side of equation (3.44). For this purpose, we need to reconstruct the successive derivatives of the flux at point Γ, by using information from the right and from the left of the interface. Precisely, polynomial reconstructions of the lth derivative at the $n-l$th-order of accuracy are written by using approximations of the derivatives at the left and right cell centers, previously computed by using the successive correction algorithm:

$$\begin{cases} \left(\mathcal{D}_{n-l}^{(l)} \overline{\mathbf{q}}\right)\Big|_{\Gamma_L} = \left(\mathcal{D}_{n-l}^{(l)} \overline{\mathbf{q}}\right)\Big|_J + \sum_{m=l+1}^{n-l-1} \left(\mathcal{D}_{n-l-m}^{(m)} \overline{\mathbf{q}}\right)\Big|_J \cdot (\mathbf{x}_\Gamma - \mathbf{x}_j)^{\otimes m} + \mathcal{O}(h^{n-l}) \\ \left(\mathcal{D}_{n-l}^{(l)} \overline{\mathbf{q}}\right)\Big|_{\Gamma_R} = \left(\mathcal{D}_{n-l}^{(l)} \overline{\mathbf{q}}\right)\Big|_K + \sum_{m=l+1}^{n-l-1} \left(\mathcal{D}_{n-l-m}^{(m)} \overline{\mathbf{q}}\right)\Big|_K \cdot (\mathbf{x}_\Gamma - \mathbf{x}_k)^{\otimes m} + \mathcal{O}(h^{n-l}) \end{cases} \tag{3.56}$$

for any $l = 1, \ldots, n-1$.

Example: 3-exact reconstruction

In this paragraph, we explicit all the formulas needed to build a 3-exact reconstruction.

1. Formula (3.38) allows to built the operator $\mathcal{D}_{\mathbf{1}}^{(2)}\Big|_j$. This operator is applied to $\widetilde{\mathbf{q}}$ values with are directly related to the problem unknown $\overline{\mathbf{w}}$;
2. Formulas (7.8), (7.17) and (7.21) available in the appedix 6.2, allows calculate a third order approximation for $\overline{\mathbf{q}}$;
3. Section 3.2.1 gives the procedure to obtain $\mathcal{D}_{\mathbf{2}}^{(1)}\Big|_j$ and $\mathcal{D}_{\mathbf{1}}^{(2)}\Big|_j$ from the third order $\overline{\mathbf{q}}$ values;
4. Thanks to $\mathcal{D}_{\mathbf{1}}^{(2)}\Big|_j$, the values $\mathbf{q}_j$ can be computed from $\overline{\mathbf{q}}$ values thanks to the formula (3.46):
$$\mathbf{q}_j = \overline{\mathbf{q}}_J - \mathcal{M}_J^{(2)} : \mathcal{D}_{\mathbf{1}}^{(2)}\Big|_j + \mathcal{O}(h^3) \tag{3.57}$$
5. The left and right values of $\mathbf{q}$ at point Γ are computed thanks to $\mathcal{D}_{\mathbf{2}}^{(1)}$ and $\mathcal{D}_{\mathbf{1}}^{(2)}$ as:
$$\begin{cases} \mathbf{q}_{\Gamma_L} = \mathbf{q}_j + \mathcal{D}_{\mathbf{2}}^{(\mathbf{1})}(\overline{\mathbf{q}})\Big|_{\mathbf{j}} (\mathbf{x}_\Gamma - \mathbf{x}_j) + \mathcal{D}_{\mathbf{1}}^{(\mathbf{2})}(\overline{\mathbf{q}})\Big|_{\mathbf{j}} (\mathbf{x}_\Gamma - \mathbf{x}_j)^{\otimes 2} + \mathcal{O}(h^3) \\ \mathbf{q}_{\Gamma_R} = \mathbf{q}_k + \mathcal{D}_{\mathbf{2}}^{(\mathbf{1})}(\overline{\mathbf{q}})\Big|_{\mathbf{k}} (\mathbf{x}_\Gamma - \mathbf{x}_k) + \mathcal{D}_{\mathbf{1}}^{(\mathbf{2})}(\overline{\mathbf{q}})\Big|_{\mathbf{k}} (\mathbf{x}_\Gamma - \mathbf{x}_k)^{\otimes 2} + \mathcal{O}(h^3) \end{cases}$$

the left and right values operators $\mathcal{D}_{\mathbf{2}}^{(1)}\Big|_j$ and $\mathcal{D}_{\mathbf{1}}^{(2)}\Big|_j$ at point Γ are computed as:

$$\begin{cases} \mathcal{D}_{\mathbf{2}}^{(\mathbf{1})}(\overline{\mathbf{q}})\Big|_{\Gamma_L} = \mathcal{D}_{\mathbf{2}}^{(\mathbf{1})}(\overline{\mathbf{q}})\Big|_j + \mathcal{D}_{\mathbf{1}}^{(\mathbf{2})}(\overline{\mathbf{q}})\Big|_{\mathbf{j}}(\mathbf{x}_\Gamma - \mathbf{x}_j) + \mathcal{O}(h^2) \\ \mathcal{D}_{\mathbf{1}}^{(\mathbf{2})}(\overline{\mathbf{q}})\Big|_{\Gamma_L} = \mathcal{D}_{\mathbf{1}}^{(\mathbf{2})}(\overline{\mathbf{q}})\Big|_j + \mathcal{O}(h) \\ \mathcal{D}_{\mathbf{2}}^{(\mathbf{1})}(\overline{\mathbf{q}})\Big|_{\Gamma_R} = \mathcal{D}_{\mathbf{2}}^{(\mathbf{1})}(\overline{\mathbf{q}})\Big|_k + \mathcal{D}_{\mathbf{1}}^{(\mathbf{2})}(\overline{\mathbf{q}})\Big|_{\mathbf{k}}(\mathbf{x}_\Gamma - \mathbf{x}_k) + \mathcal{O}(h^2) \\ \mathcal{D}_{\mathbf{1}}^{(\mathbf{2})}(\overline{\mathbf{q}})\Big|_{\Gamma_R} = \mathcal{D}_{\mathbf{1}}^{(\mathbf{2})}(\overline{\mathbf{q}})\Big|_k + \mathcal{O}(h) \end{cases}$$

6. Numerical fluxes can be integrate using the formula (3.44) and the procedure described in 3.2.1. Note that for flat faces, the first derivatives are not needed since $\mathcal{S}_{\mathbf{AJK}}^{(\mathbf{1})} = 0$:

$$\iint_{A_{JK}} \mathbf{F}.\mathbf{n}dS = \mathbf{F}|_\Gamma \mathcal{S}_{\mathbf{AJK}}^{(\mathbf{0})} + \mathcal{S}_{A_{JK}}^{(2)} : \mathbf{D}^{(2)}\ \mathbf{F}|_\Gamma + \mathcal{O}(h^3) \tag{3.58}$$

Here we described a robust finite volume 3-exact reconstruction on any grid. Note that the scheme keep its robustness and accuracy on very general grid. This kind of strategy is very well adapted for industrial application.

3.2.2 Numerical properties

The numerical properties of the preceding family of numerical schemes are investigated for a simple 1D problem, namely, the linear advection equation:

$$\frac{\partial \alpha}{\partial t} + a\,\mathbf{D}^{(1)}\alpha = 0 \tag{3.59}$$

with $\mathbf{D}^{(1)}\alpha = \dfrac{\partial \alpha}{\partial x}$ for a 1D scalar problem, and $a \in \Re$. Equation 3.59 is discretized on a regular grid with space step h, so that cell centres are located at abcissas $x_j = ih$ and cell faces at $x_{j\pm\frac{1}{2}} = (j \pm \frac{1}{2})h$. By integration over one cell, (3.59) becomes:

$$h\frac{\partial \overline{\alpha}_J}{\partial t} + a(\alpha_{j+\frac{1}{2}} - \alpha_{j-\frac{1}{2}}) = 0 \tag{3.60}$$

where $\overline{\alpha}_J$ is the average value of α over the control volume $\Omega_J = [x_{j-\frac{1}{2}}, x_{j+\frac{1}{2}}]$:

$$\overline{\alpha}_J = \frac{1}{h}\int_{x_{j-\frac{1}{2}}}^{x_{j+\frac{1}{2}}} \alpha dx$$

To complete the numerical discretization, an approximation of $\alpha_{j\pm\frac{1}{2}}$ is constructed from cell averages over the neighbouring cells, by means of the upwind method describel in the preceding Section. For simplicity, assume $a > 0$: in this case, $\alpha_{j-\frac{1}{2}}$ and $\alpha_{j+\frac{1}{2}}$ are reconstructed at order n by using information from cell $j-1$ and j, respectively. We denote these upwind approximations as $\alpha_{L|_{j\pm\frac{1}{2}}}$, so that 3.60 rewrites:

$$\frac{\partial \overline{\alpha}_J}{\partial t} + \frac{a}{h}\mathcal{L}_k(\overline{\alpha})_{|J} = 0 \tag{3.61}$$

with $\mathcal{L}_k(\overline{\alpha})_{|J} = \left(\alpha_{L|_{j+\frac{1}{2}}} - \alpha_{L|_{j-\frac{1}{2}}}\right)$ and k the order of the k-exact reconstruction in use. In the following analysis, we consider approximations up to the fifth-order of accuracy. For the present 1D linear problem, the k-exact reconstruction algorithm finally leads to the following approximations of the flux difference,

for orders ranging from 2 to 5, respectively:

$$\mathcal{L}_2(\overline{\alpha})_{|J} = \frac{1}{4}\left(\overline{\alpha}_{j+1} + 3\overline{\alpha}_j - 5\overline{\alpha}_{j-1} + \overline{\alpha}_{j-2}\right) \tag{3.62}$$

$$\mathcal{L}_3(\overline{\alpha})_{|J} = \frac{1}{32}\left(\overline{\alpha}_{j+2} + 7\overline{\alpha}_{j+1} + 22\overline{\alpha}_j - 38\overline{\alpha}_{j-1} + 9\overline{\alpha}_{j-2} - 1\overline{\alpha}_{j-3}\right) \tag{3.63}$$

$$\mathcal{L}_4(\overline{\alpha})_{|J} = \frac{1}{384}\left(-4\overline{\alpha}_{j+3} + 15\overline{\alpha}_{j+2} + 96\overline{\alpha}_{j+1} + 255\overline{\alpha}_j - 468\overline{\alpha}_{j-1}\right. \tag{3.64}$$

$$\left. +117\overline{\alpha}_{j-2} - 8\overline{\alpha}_{j-3} - 3\overline{\alpha}_{j-4}\right) \tag{3.65}$$

$$\mathcal{L}_5(\overline{\alpha})_{|J} = \frac{1}{6144}\left(-17\overline{\alpha}_{j+4} - 47\overline{\alpha}_{j+3} + 324\overline{\alpha}_{j+2} + 1468\overline{\alpha}_{j+1} + 3930\overline{\alpha}_j\right. \tag{3.66}$$

$$\left. -7386\overline{\alpha}_{j-1} + 1988\overline{\alpha}_{j-2} - 196\overline{\alpha}_{j-3} - 81\overline{\alpha}_{j-4} + 17\overline{\alpha}_{j-5}\right) \tag{3.67}$$

3.2.3 Truncation error analysis

To investigate the numerical properties of the preceding approximation, we rewrite it in terms of cell center pointwise values α_i. For this purpose, cell avergaged values in (3.61) (with $\mathcal{L}_k$ given by one of the operators (3.62)-(3.67)) are replaced by the following development

$$\alpha_j = \overline{\alpha}_J - \frac{h^2}{24}\,\mathbf{D}^{(2)}\alpha\Big|_j - \frac{h^4}{1920}\,\mathbf{D}^{(4)}\alpha\Big|_j + \mathcal{O}(h^6), \tag{3.68}$$

After some algebra, the truncation errors $\mathcal{E}$ associated to the upwind k-exact schemes up to the 5th order of accuracy are written as:

$$\mathcal{E}_{\mathcal{L}_2} = -\frac{ah^2}{24}\,\mathbf{D}^{(3)}\alpha\Big|_i + \frac{ah^3}{8}\,\mathbf{D}^{(4)}\alpha\Big|_i + \mathcal{O}(h^4) \tag{3.69}$$

$$\mathcal{E}_{\mathcal{L}_3} = \frac{ah^3}{16}\,\mathbf{D}^{(4)}\alpha\Big|_i - \frac{199ah^4}{5760}\,\mathbf{D}^{(5)}\alpha\Big|_i + \mathcal{O}(h^5) \tag{3.70}$$

$$\mathcal{E}_{\mathcal{L}_4} = -\frac{19ah^4}{5760}\,\mathbf{D}^{(5)}\alpha\Big|_i - \frac{3ah^5}{64}\,\mathbf{D}^{(6)}\alpha\Big|_i + \mathcal{O}(h^6) \tag{3.71}$$

$$\mathcal{E}_{\mathcal{L}_5} = -\frac{19ah^5}{768}\,\mathbf{D}^{(6)}\alpha\Big|_i + \frac{17ah^6}{1008}\,\mathbf{D}^{(7)}\alpha\Big|_i + \mathcal{O}(h^7) \tag{3.72}$$

Inspection of the truncation errors (3.69) shows that odd-order schemes are dominant dissipative whereas even order scheme are dominant dispersive. Increasing the spatial order of accuracy from 2 to 3 leads to a reduction of the dispersive error (from $\frac{ah^2}{24}\,\mathbf{D}^{(3)}\Big|_i$ to $\frac{199ah^4}{5760}\,\mathbf{D}^{(5)}\Big|_i$), whereas the dissipation error remains of the same order, even if the error constant is twice smaller. A similar effect is obtained by increasing the order of accuracy from four to five, but the improvement in the dissipation error constant is slightly smaller (reduction by a factor 1.895). On the contrary, going from third to fourth order accuracy improves essentially the dissipation error (from $\frac{ah^3}{16}\,\mathbf{D}^{(4)}\alpha\Big|_i$ to $\frac{3ah^5}{64}\,\mathbf{D}^{(6)}\alpha\Big|_i$), whereas the dispersion error remains of the same order, although with a ten times smaller error constant.

3.2.4 Spectral properties

Truncation error analysis provides information on the behavior of the numerical schemes in the limit of vanishing mesh size. For finite grids, however, an analysis of the spectral properties of the spatial operator is useful to get insight on the numerical representation of a given solution wavelength.

Consider again the linear advection equation (3.59). The Fourier transform of (3.59) writes:

$$\widehat{\partial_t \alpha} = -i\dot{a}\xi\frac{\widehat{\alpha}}{\Delta t} \tag{3.73}$$

with ξ the reduced wave number and $\dot{a} = \frac{ah}{\Delta t}$ the CFL number. The right-hand side of the preceding equation is the exact transport operator in the spectral space. On the other hand, taking the Fourier

Order of accuracy	2	3	4	5
Relative operation count	1	3	9	27
Points per wave length for dissipation	18	15	10	9.8
Points per wave length for dispersion	17	14	14	12

Table 3.1: Resolvability of k-exact schemes of different orders

transform of the discretized advection equation rewritten in terms of the pointwise values α gives:

$$\widehat{\partial_t \alpha} = -\dot{a}\widehat{\mathcal{L}}\frac{\widehat{\alpha}}{\Delta t} \tag{3.74}$$

where $\mathcal{L} \in \mathbb{C}$ is the Fourier symbol of the spatial discretization.

By analogy with equation (3.73), we define a modified wavenumber $\xi^* = -i\widehat{\mathcal{S}}$, so that (3.74) rewrites:

$$\widehat{\partial_t \alpha} = -i\dot{a}\xi^*\frac{\widehat{\alpha}}{\Delta t}$$

For an infinitely accurate scheme, $\xi^* = \xi$ (ξ being a pure real number). In practice, $\xi^* \neq \xi$ because of approximation errors. Specifically, the imaginary part of ξ^* is generally different from zero and it introduce a damping of the solution mode $\widehat{\alpha}$, whereas its real part govern the dispersion errors. To measure how accurately a numerical scheme represents a given wavenumber, we introduce the normalized dispersion error:

$$\mathcal{P}_\xi = \frac{|\mathcal{R}e(\xi^*) - \xi|}{\pi},$$

and the dissipation function:

$$\mathcal{A}_\xi = 1 - \exp(\mathcal{I}m(\xi^*)).$$

If $\xi^* = \xi$, then $\mathcal{P}_\xi = \mathcal{A}_\xi = 0$. Figure 3.7 shows the dispersion ($\mathcal{P}$) and dissipation ($\mathcal{A}$) errors as functions of the modified wave number $\xi = k\Delta x$ for k-exact schemes ranging from order 2 to order 5. All of these schemes exhibit a significant dissipation error. For a more quantitative analysis, Table 3.2.4 provides the number of points per wave length necessary to achieve a dissipation error of 10^{-3}, as well as the computational cost in terms of relative operation count relative to the second order scheme.

The Table 3.2.4 shows that increasing the order of accuracy does not improve the dissipation error significantly, compared to the additional computational cost. Specifically, reducing the required number of points per wavelength by a factor of approximately two requires using the 5th-order accurate scheme instead of the second-order one, but this leads to an increase by factor 27 of the computational cost in terms of operation count, which is not acceptable. Table 3.2.4 provides also the number of points per wave length required to achieve a dispersion error of 10^{-3}. Using a third accurate scheme leads to a significant reduction of the dispersion error and to a moderate reduction of the dissipation error, while the overcost of a factor 3 compared to the second-order scheme remains acceptable. This is why in the following of this paper we restrict our attention to schemes with orders of accuracy up to 3. In order to further reduce the dissipation error, instead of increasing the order of accuracy, we suggest to reduce the dissipative error by locally recentering the approximations in flow regions dominated by small vortical structures, which are susceptible to be overdamped. The recentering strategy is discussed the following Section.

3.3 Local Centering of Numerical fluxes in Vortex-Dominated Regions

An important source of errors in RANS/LES simulations is represented by the numerical dissipation introduced by the approximation scheme in use for the inviscid fluxes (see e.g. [77, 36, 78]), which has to be as small as possible in order to preserve vortical structures. In the preceding Section, we introduced several upwind k-exact schemes. It was shown that the 3rd-order scheme, which represents a reasonable tradoff between accuracy and computational cost, requires about 18 points per wavelength to achieve a sufficiently small damping error. This leads to unacceptably dense computational grids for practical

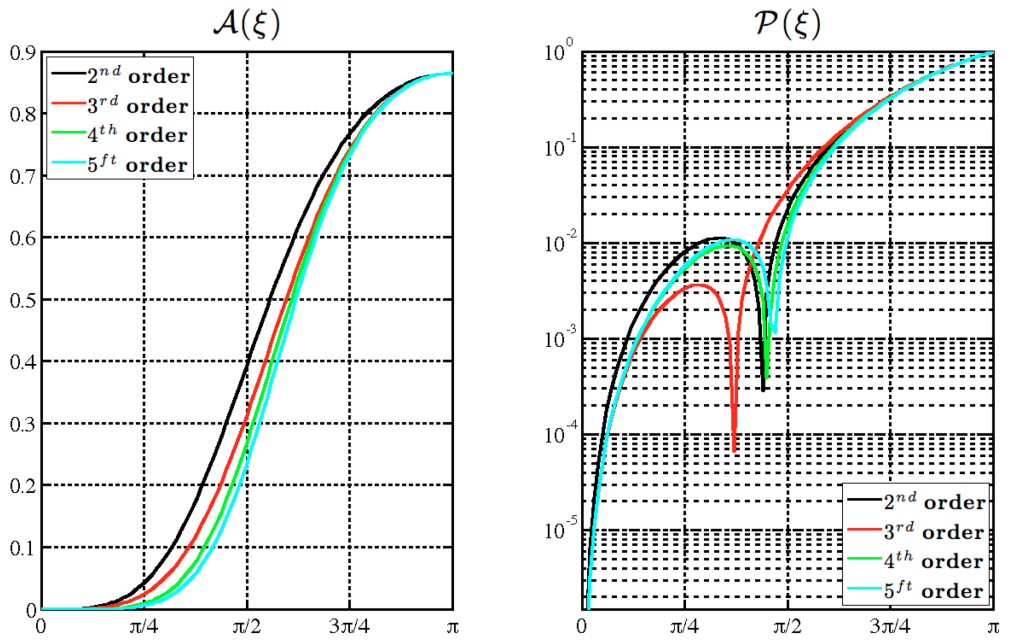

(a) Dissipation ($\mathcal{A}$) and dispersion ($\mathcal{P}$) errors on the upwind schemes.

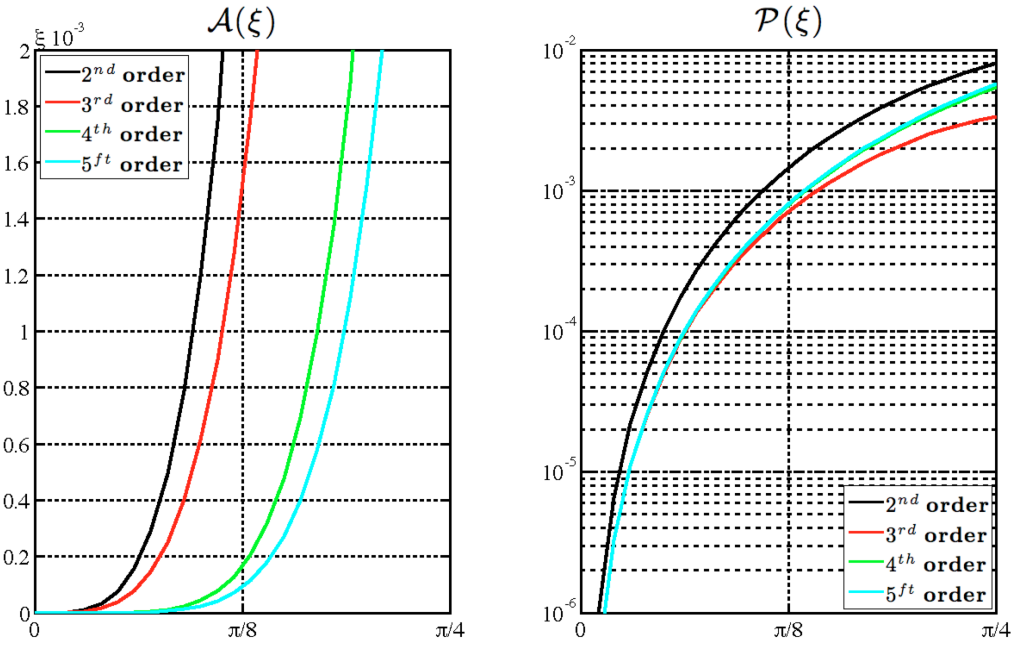

(b) Close up of the preceding figures.

Figure 3.7: Dissipation ($\mathcal{A}$) and dispersion ($\mathcal{P}$) errors on the upwind schemes.

applications. To reduce the numerical dissipation introduced by the upwind scheme in vortex-dominated regions, we adopt a local centering strategy, described hereafter. We aim at building a hybrid scheme, centered in vortical regions and upwind elsewhere. The resulting hybrid scheme is referred-to hereafter as VC-scheme, standing for vortex-centered scheme. Similar approaches were developed in [77], where a hybrid scheme is constructed by blending of a fourth-order centered scheme in LES regions and and of a third-order or fifth-order upwind scheme in RANS regions, and [36], where a local upwind correction is added to a purely centred, nominally second-order scheme wherever spurious grid-to-grid oscillations, or "wiggles", are detected by means of a suitable sensor. Differently from Refs [77, 36], the present strategy automatically leads to a stable discretization, without need for empirical blending functions or oscillation sensors.

We start with rewriting the upwind spatial operator $\mathcal{L}$ in Eq. (3.61) as the sum of a purely centered operator $\mathcal{L}_C$, and a numerical dissipation term $\mathcal{L}_D$:

$$\mathcal{L} = \mathcal{L}_C + \mathcal{L}_D \tag{3.75}$$

where:

$$\mathcal{L}_C = \frac{1}{2}\left(\mathcal{L}_R + \mathcal{L}_L\right),$$

with $\mathcal{L}_L$ and $\mathcal{L}_R$ the upwind and the downwind operators, respectively, and

$$\mathcal{L}_D = -\frac{1}{2} sgn(a)\left(\mathcal{L}_R - \mathcal{L}_L\right).$$

Introducing a blending function $\psi \in [0,1]$ that multiplies the dissipation term, gives the following hybrid scheme:

$$\mathcal{L}_{VC} = \mathcal{L}_C + \psi\mathcal{L}_D \tag{3.76}$$

where the suffix VC stands for "vortex centered" or, equivalently:

$$\mathcal{L}_{VC} = \frac{1 - sgn(a)\psi}{2}\mathcal{L}_R + \frac{1 + sgn(a)\psi}{2}\mathcal{L}_L, \quad \text{with} \quad \psi \in [0,1] \tag{3.77}$$

Clearly, for $\psi = 0$ the preceding scheme is fully centered and for $\psi = 1$ the upwind scheme is recovered.
For advection-diffusion problems of the form:

$$\frac{\partial \alpha}{\partial t} + a\frac{\partial \alpha}{\partial x} = (\nu + \nu_t)\frac{\partial^2 \alpha}{\partial x^2}, \tag{3.78}$$

it is well-known that a purely centered second-order accurate approximation of the convective terms leads to stable solutions under the standard stability conditions:

$$Re_g \leq 2; \quad CFL \leq 1$$

where $Re_g = \dfrac{|a|h}{\nu + \nu_t}$ is called the grid Reynolds number, based on the characteristic cell size h, and the sum of the molecular ν and eddy viscosity ν_t, and CFL is the well-known Courant-Friedrichs-Lewy number. A similar analysis can be applied, e.g., to a hybrid scheme of the form (3.76) with $\mathcal{L}_C$ the purely centered second-order operator:

$$\mathcal{L}_C = a\frac{\alpha_{j+1} - \alpha_{j-1}}{2\,h}$$

and $\mathcal{L}_D$ the numerical dissipation of the first-order upwind scheme:

$$\mathcal{L}_D = -\frac{|a|}{2h}(\alpha_{j+1} - 2\alpha_j + \alpha_{j-1})$$

With this choice, Eq. (3.76) reduces to the second-order centered scheme when $\psi = 0$ and to the first-order upwind scheme for $\psi = 1$. Using a forward Euler scheme for the time discretization, the corresponding difference equation writes:

$$\frac{\alpha_j^{n+1} - \alpha_j^n}{\Delta t} + a\left(\frac{\alpha_{j+1}^n - \alpha_{j-1}^n}{2\,h}\right) - \psi\frac{|a|}{2h}\left(\alpha_{j+1}^n - 2\alpha_j^n + \alpha_{j-1}^n\right) = (\nu + \nu_t)\frac{\alpha_{j+1}^n - 2\alpha_j^n + \alpha_{j-1}^n}{h^2} \tag{3.79}$$

or also:

$$\alpha_j^{n+1} = A\alpha_{j+1}^n + B\alpha_j^n + C\alpha_{j-1}^n \tag{3.80}$$

where:

$$A = -\frac{|a|(1-\psi)\Delta t}{2\,h} + \frac{(\nu+\nu_t)\Delta t}{h^2} \tag{3.81}$$

$$B = 1 - \frac{|a|\psi\Delta t}{h} - \frac{2(\nu+\nu_t)\Delta t}{h^2} \tag{3.82}$$

$$C = \frac{|a|(1+\psi)\Delta t}{2\,h} + \frac{(\nu+\nu_t)\Delta t}{h^2} \tag{3.83}$$

According to Godunov's theorem, the preceding difference equation preserves monotonicity, and so does not generate spurious oscillations, if and only if all of the coefficients are positive.

Clearly, from the third one of Eqs (3.81) it appears that $C \geq 0$ for any positive h, Δt and ψ.

The condition $A \geq 0$ is satisfied if:

$$\psi \geq 1 - 2\frac{(\nu+\nu_t)}{|a|h} = 1 - \frac{2}{Re_g}. \tag{3.84}$$

which leads to:

$$\psi \geq \max\left(0, 1 - \frac{2}{Re_g}\right), \text{ since } \psi \in [0,1] \tag{3.85}$$

For $\psi = 0$, the preceding expression reduces to the standard constraint on the grid Reynolds number for the purely centered scheme, whereas for a purely upwind scheme, $\psi = 1$ and the condition is satisfied for any Re_g.

Finally, $B \geq$ if:

$$\Delta t \leqslant \left(\frac{\psi}{\Delta_{\tau_1}} + \frac{1}{\Delta_{\tau_2}}\right)^{-1} \tag{3.86}$$

with $\Delta_{\tau_1} = h/\mid a \mid$ and $\Delta_{\tau_2} = h^2/2(\nu+\nu_t)$ are respectively the inviscid and viscous characteristic times. When $\psi \geq \max\left(0, 1 - \frac{2}{Re_g}\right)$(when the scheme is re-centered) we get:

$$\Delta t \leqslant \min(\Delta_{\tau_1}, \Delta_{\tau_2}), \text{since } \psi \in [0;1] \tag{3.87}$$

if $\psi = 1$ (when the scheme is fully upwind) we have:

$$\Delta t \leqslant \left(\frac{1}{\Delta_{\tau_1}} + \frac{1}{\Delta_{\tau_2}}\right)^{-1} \leqslant \min(\Delta_{\tau_1}, \Delta_{\tau_2}) \tag{3.88}$$

The equation (3.88) demonstrates that the re-centering strategy allows the CFL stability condition to be less restrictive.

In the following, we focus on the hybrid scheme obtained by applying the centering procedure to the 3rd-order k-exact upwind scheme. Such a scheme is somewhere in between the baseline scheme and a 4th-order, zero-dissipative scheme. Its truncation error is given by:

$$\mathcal{E}^3_{\mathcal{L}^c_{FV}} = \psi\frac{h^3}{16}\left.\frac{\partial^4\alpha}{\partial x^4}\right|_i - \frac{199h^4}{5760}\left.\frac{\partial^5\alpha}{\partial x^5}\right|_i + \mathcal{O}(h^4)$$

This is similar to Eq. (3.70) with the dissipative error term multiplied by ψ. When $\psi = 0$ the dissipation term vanishes and the leading error term is 4th-order and purely dispersive.

The recentering procedure improves resolvability with respect to the baseline scheme: table 3.2 gives the number of points per wavelength required by the hybrid scheme to achieve a dissipation error lower than 10^{-3} as a function of the blending function. The number of required points per wavelenght decreases when ψ is reduced from 1 to 0, the damping error being strictly zero when $\psi = 0$. For instance, the 80 % recentered scheme requires a similar number of points per wavelength as the 4th-order scheme. When

Re_g	∞	10	5	3.33	2.5	2.12	2.04	≤ 2
ψ	1	0.8	0.6	0.4	0.2	0.06	0.02	0
% recentering	0	20	40	60	80	94	98	100
Points per wavelength	15	14.1	12.3	11.7	10.4	8.8	6.73	no damping

Table 3.2: Number of points per wavelengths as a function of the recentering function.

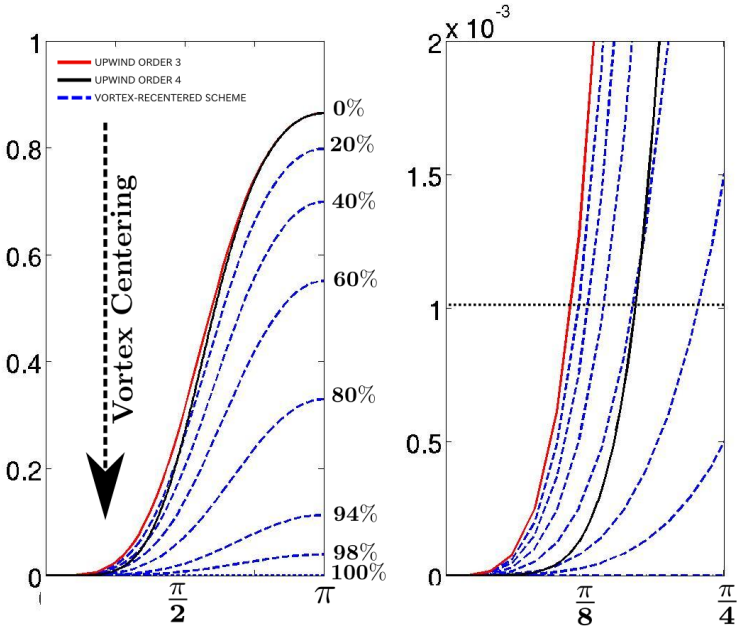

Figure 3.8: Dissipation error of the hybrid scheme for different choices of ψ

$\psi = 0$, the scheme is zero-dissipative and the necessary energy drain is ensured by only laminar and eddy viscosities. On the other hand, the introduction of the recentering function has an almost negligible impact on the computational cost of the simulation.

To investigate the stability of the k-exact hybrid scheme for advection-diffusion problems of the form (3.78), we further assume that viscous terms are approximated by a standard second-order scheme. For all of the computations presented in the following, time integration is performed via the second-order accurate Heun scheme, which writes for the present linear model problem:

$$\alpha^{n+1} = \alpha^n \left(1 + \mathcal{C}\Delta t + \frac{\Delta t^2}{2}\mathcal{C}^2\alpha\right),$$

The stability region of the Heun scheme is given by the set of complex numbers $\widehat{\mathcal{C}}\Delta t$ such that:

$$\left|1 + \widehat{\mathcal{C}}\Delta t + \frac{(\widehat{\mathcal{C}}\Delta t)^2}{2}\right| \leq 1$$

where $\widehat{\mathcal{C}}$ represents the Fourier symbol of the spatial discretization. The boundary of this region is represented by the red curve in figure 3.9. For the hybrid spatial discretization scheme under investigation, the Fourier symbol $\widehat{\mathcal{C}}$ depends on the reduced wave number under consideration and on ψ, the CFL number and Re_g. The fully discrete scheme is stable when the locus of $\widehat{\mathcal{C}}$ as a function of the reduced wave number must lie within the stabiility region of the time discretization scheme. Figure 3.9 shows the locus of the spatial approximation for different choices of ψ and two different choices of the grid Reynolds number, namely, $Re_g = 2$, which corresponds to the upper acceptable value for the purely centred second order

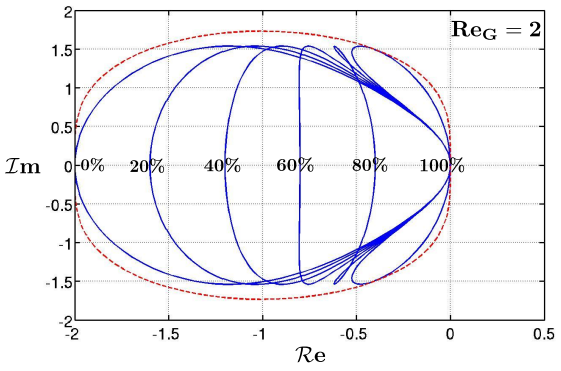

(a) Stable

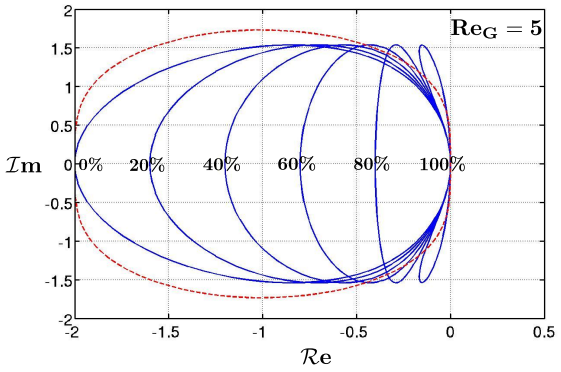

(b) Instable

Figure 3.9: Stability of the third order recentered numerical scheme coupled with a second order Heun temporal scheme

scheme, and $Re_g = 5$. The CFL number is taken equal to 1. For lower values of CFL, the locus of the spatial operator is smaller and the resulting fully discreti scheme is certainly stable. When the scheme is fully upwind, i.e. for $\psi = 1$ (0% recentering) the scheme is stable for any Re_g. When the scheme is 100% centered ($\psi = 0$), then the spatial locus is tangent to the boundary of the stability domain when $Re_g = 2$, which corresponds to the limit value according to Eq. (3.84), and partly outside of it for $Re_g > 2$. Also note that it is possible to obtain a stable scheme for $Re_g > 2$ by using just a partial recentering. For instance, for $Re_g = 5$, stability is achieved if the scheme is recentered by about 40% or less, i.e. for $\psi \gtrapprox 0.6$, which is in agreement with the simple relation (3.84).

In practice, ψ is not constant throughout the computational domain, but is allowed to vary between 0 and 1 according to the local flow features: in regions dominated by fine vortical structures ψ has to be as close to zero as possible, whereas in regions charaterized by strong compressibility effects, like shock waves, ψ must tend to 1 to ensure robustness. In this work, the blending function is related to the vortex sensor introduced by Ducros et al. [79], defined as:

$$\Phi = \frac{(div(\mathbf{u}))^2}{(div(\mathbf{u}))^2 + \mid rot(\mathbf{u}) \mid^2}, \tag{3.89}$$

This sensor tends to 0 in nearly incompressible and/or highly rotational regions, whereas it tends to 1 in highly compressible and/or irrotational regions. Moreover, according to the preceding stability analysis, in regions where $\psi = 0$, 100% centering is allowed only if $Re_g \leq 2$, otherwise the local recentering rate has to satisfy the constraint (3.84). This is achieved by defining the local blending function as follows:

$$\psi = \max\left(\Phi, 1 - \frac{2}{Re_g}\right) \tag{3.90}$$

With the preceding formulation, only partial recentering is allowed in vortex-dominated regions with insufficient grid resolution, which ensures the minimal amount of numerical dissipation to damp grid-to-grid oscillations.

The following equation gives the expression of the grid Reynolds number computed in practice for in a general mesh:

$$\mathcal{R}e_g = \frac{2\Omega \parallel \mathbf{u} \parallel^2}{\sum_{\mathrm{i}} \mid \mathbf{u_i}.\mathbf{n}S_i \mid (\nu + \nu_t)}, \tag{3.91}$$

where Ω is the volume of a given cell, S_i is the surfaces that compose the volume Ω, $\mathbf{n}$ is the outer-oriented unit normal and $\mathbf{u_i}$ is the velocity vector extrapolated to the faces i.
Note that, in the latest version of the VC scheme, the grid Reynolds number is no longer defined globally in cells (3.91) but for each faces of a given cell. In other words, in a given cell, all faces can be recentred differently, depending on the physics. For example, in the beginning of a shear-layer, when the Kelvin-Helmholtz instabilities are essentially 2D, the scheme is fully recentred in the spanwise and the transversal directions because the velocities in these directions are very small. The scheme can be totally recentred in the longitudinal direction, according to the grid Reynolds number.

3.4 Numerical results

In this Section, the second and 3rd-order k-exact upwind schemes and the hybrid VC scheme are first applied to some well documented test cases. The objective is twofold: i) to demonstrate the capability of k-exact schemes to ensure high-order accuracy on general grids; ii) to prove the effectiveness of the VC strategy to preserve vortical structures while preventing spurious oscillations. Then, the proposed VC 3-exact scheme is applied to the hybrid RANS/LES simulation of a transonic flow over a square cylinder.

3.4.1 Preliminary validations: Ringleb flow

To verify the accuracy of the preceding numerical schemes, we consider an inviscid transonic test case, the so-called Ringleb flow[80], for which an exact solution for the steady aerodynamic field is available. Details about this configuration can be found in [80]. The analytic solution is defined implicitly along streamlines, and leads to the inversion of a system. For details, please refer to the appendix 10 page IX. The analytical solution is integrated over each cell by means of 6th-order Gauss quadrature formulae, to obtain initial values for the cell-averaged conservative variables. These are given as an input to the finite-volume solver. Using a 6th-order quadrature formula avoids polluting the initial solution with integration errors that would be comparable to the order of accucy of the scheme in use. The exact solution is also used to enforce the boundary conditions. Initially, calculations are run using the second and third-order accurate upwind schemes on a set of smooth computational grids composed by 192, 768, 3072,12288 and 49152 quadrangular cells, respectively. Afterwards, the capability of the scheme to preserve accuracy on highly deformed grids is demonstrated by using a set of grids obtained by randomly shaking the nodes of the preceding ones. Computations are carried out using a CFL of 0.9 and are stopped when the non-dimensional residual reach 10^{-7}.
For each grid, the L_2 norm of the error with respect to the exact solution for the cell-averaged primitive variables resulting from the k-exact reconstruction is plotted versus a typical mesh size $h = 1/\sqrt{DOF}$, with DOF the number of degrees of freedom, here equal to the number of cells. The results are represented in Figure 3.11 for the pressure. Similar results are obtained for the other primitive variables. The computed convergence orders are in fair agreement with the nominal ones, both for the second-order and the third-order upwind scheme. Using highly irregular, shaken grids does not affect the convergence orders.

3.4.2 Vortex advection

In the following we consider the advection of a Lamb vortex [81] by an inviscid uniform flow with Mach number equal to $\sqrt{2}$. In a cylindrical reference frame attached to the vortex center, the azimuthal velocity,

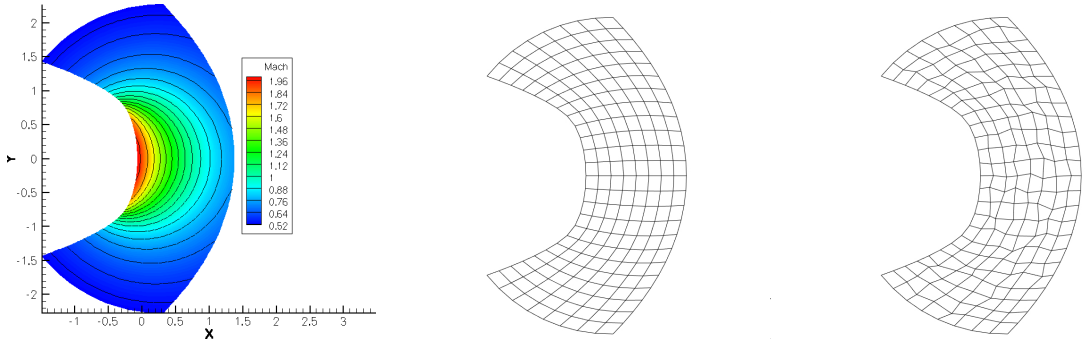

(a) Mach repartition (b) Cartesian grid (c) Shaken grid

Figure 3.10: Exact solution, Mach number contours. View of a smooth and a shaken grid of 828 cells

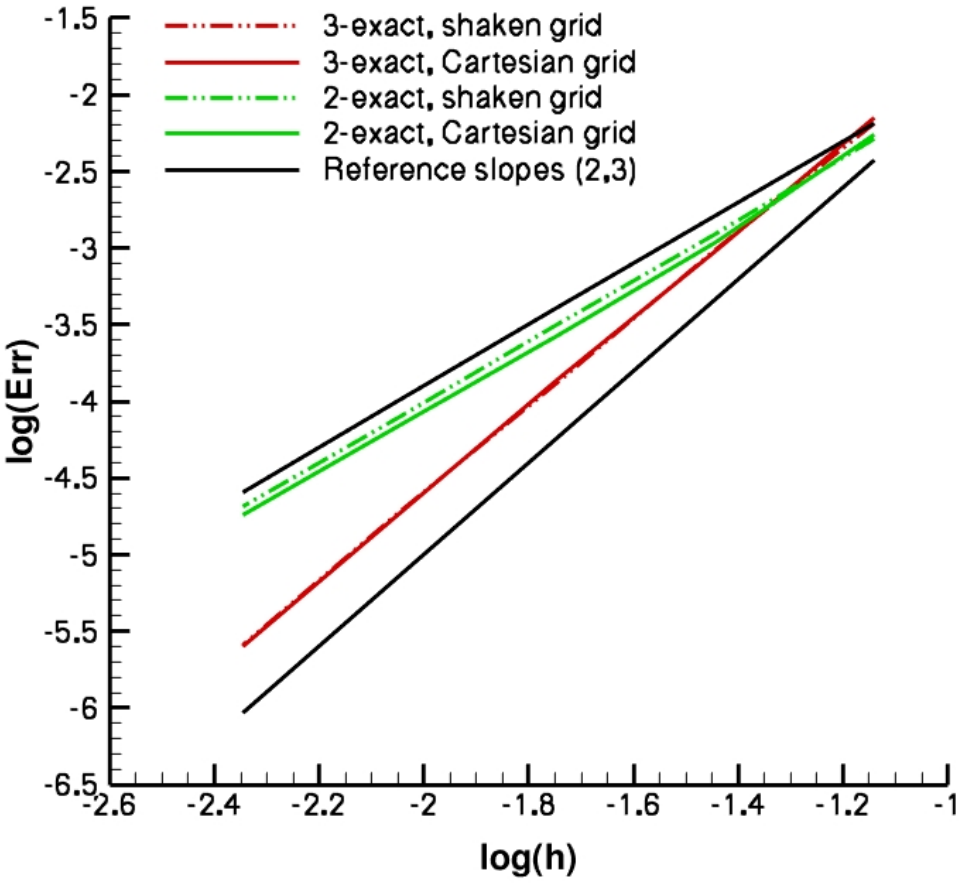

Figure 3.11: Ringleb flow. Grid convergence of the pressure field. $h = 1/\sqrt{nDOFs}$, where nDOFs is the number of degrees of freedom.

temperature and pressure field are prescribed through the following relations:

$$V_\theta(r) = \frac{\Gamma}{2\Pi r}\left[1 - \exp\left(\eta^2\right)\right] \tag{3.92}$$

$$T(r) = \frac{\Gamma}{\Pi a_0^2}\left[-\exp\left(\eta^2\right)\right] \tag{3.93}$$

$$P(r) = \frac{\Gamma^2}{8\Pi^2 a_0^2}\left[\frac{1}{\eta}\left(1 - \exp\left(\eta^2\right)\right)^2 + g(\eta) + g(2\eta)\right] \tag{3.94}$$

where $\eta = r/a_0$, $g(\eta) = 2\int_\eta^\infty \exp(-\xi)d\xi$. The solution is computed on a set of 7 square grids with a number of equally spaced quadrangular cells ranging from 40000 to 640000. A very small time step is used in order to rule out numerical errors related to the time integration method. Periodic boundary conditions are imposed at grid borders. The vortex is advected along the mesh diagonal over a length of three diagonals. To demonstrate the ability of the present method to preserve high accuracy on any grid, simulations are also run on a set of irregular quadrangular grids, obtained by randomly shaking the nodes of the preceding Cartesian grids. Figure 3.16 shows a close-up of a Cartesian and a shaken grid. Similarly to the preceding test case, we investigate the grid convergence of the numerical solution and, specifically, of the conservative variables. Figure 3.12 shows the L_2 norm of the error with respect to the exact solution for the pressure field, versus the characteristic mesh size h. Similar results are obtained for the other variables. The computed convergence orders obtained for the 2nd-order and the 3rd-order k-exact schemes are in fair agreement with the nominal ones, both on Cartesian and shaken grids. This is not achieved when using, for instance, a standard upwind finite volume scheme using a 1D 3rd-order reconstruction of the variables along mesh lines, without corrections for mesh deformations. For this scheme, the convergence order is equal to 1 on the highly deformed shaken grids.

For a more detailed analysis of the k-exact approach, the convergence order of the 1st and 2nd derivatives of the computed field is also investigated. For this purpose, different numerical approximations of the derivatives are compared to the analytical derivatives available for the exact solution.

Figure 3.13 shows the convergence of the L_2 error of the pressure gradient versus the mesh size for a standard approximation based on the standard Gauss-Green relation (3.30), (3.31) –used in most finite volume solvers–, for the consistent 1-exact first differentiation operator (3.38), obtained by correcting (3.30),(3.31) by the linear operator M_1, and for the 2-exact first differentiation operator resulting from the successive correction procedure of Section 3.2.1. The 1-exact and 2-exact operators provide, respectively, a 1st-order and a 2nd-order approximation of the gradient on any grid, whereas the Gauss-Green operator becomes inconsistent on irregular grids. In particular, the introduction of the correction operator M_1 is what makes the difference between the 1-exact and the standard operator. This correction is then an essential ingredient to ensure a consistent approximation for the gradients, independently of the grid in use. Similar results are obtained for the gradients of other variables, like the velocities or the temperature.

Similarly, figure 3.14 shows the convergence of the L_2 error for second derivatives of the pressure field. In this case, a baseline appproximation obtained by applying twice the 1-exact first differentiation operator is compared to a 1-exact 2nd-differentiation operator obtained by correcting the preceding one by means of the linear application M_2, see Eq. 3.53. Only the 1-exact operator ensures 1st-order convergence of the second-derivatives on any grid, whereas the straightforward procedure leads to an inconsistent solution.

Finally, it is interesting to quantify the influence of the Δq correction on the grid convergence of the method. On shaken grid, we clearly show on figure 3.15 that the third order is not recovered without Δq correction. Actually, we see that the numerical scheme losses its order when the mesh is refined. With Δq, the scheme keeps its order without condition.

Note that flow solvers often require approximations of the first and second derivatives, for instance to compute source terms in transport-equation turbulence models. Using standard Gauss-Green approximations of the gradients is inconsistent, namely, on highly deformed grids often used to simulate industrial configurations, leading to significant numerical errors.

3.4.3 Viscous advection and shock-vortex interaction

In addition to k-exact reconstructions, another important ingredient of the present numerical stratrategy is the vortex-centering procedure illustrated in Section 3.3. This problem, initially proposed by Shu1997[82] is

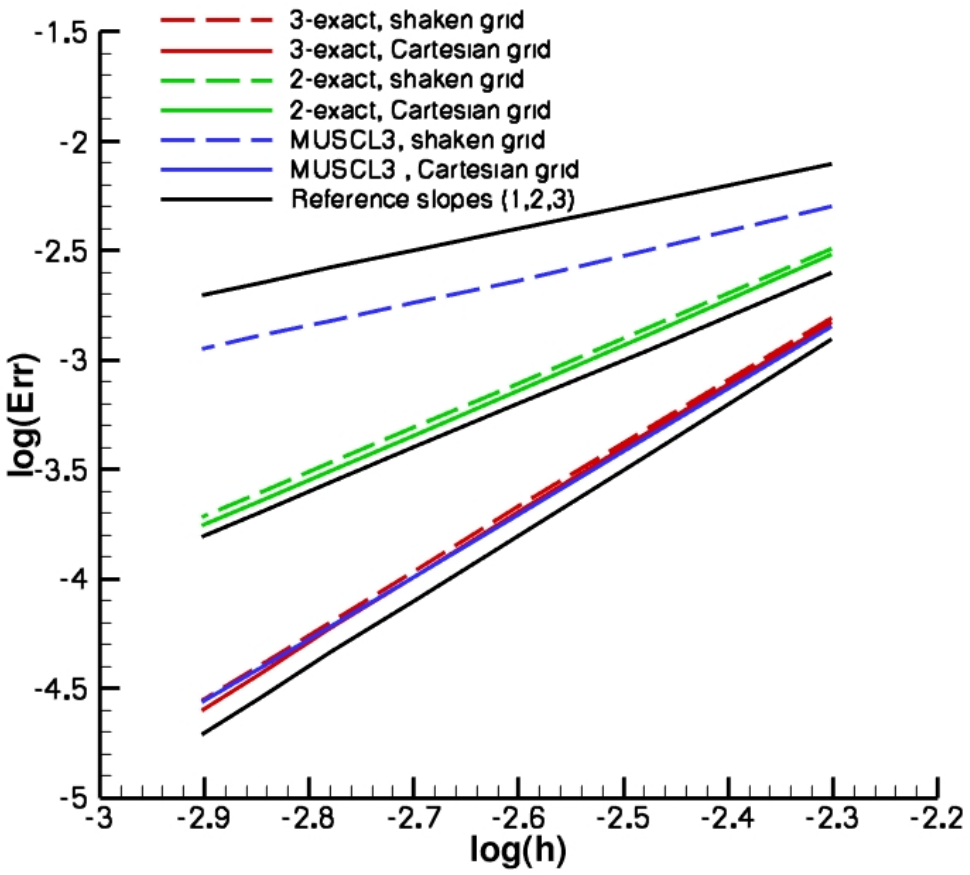

Figure 3.12: Vortex advection. Grid convergence of the L_2 norm of the error for the pressure field.

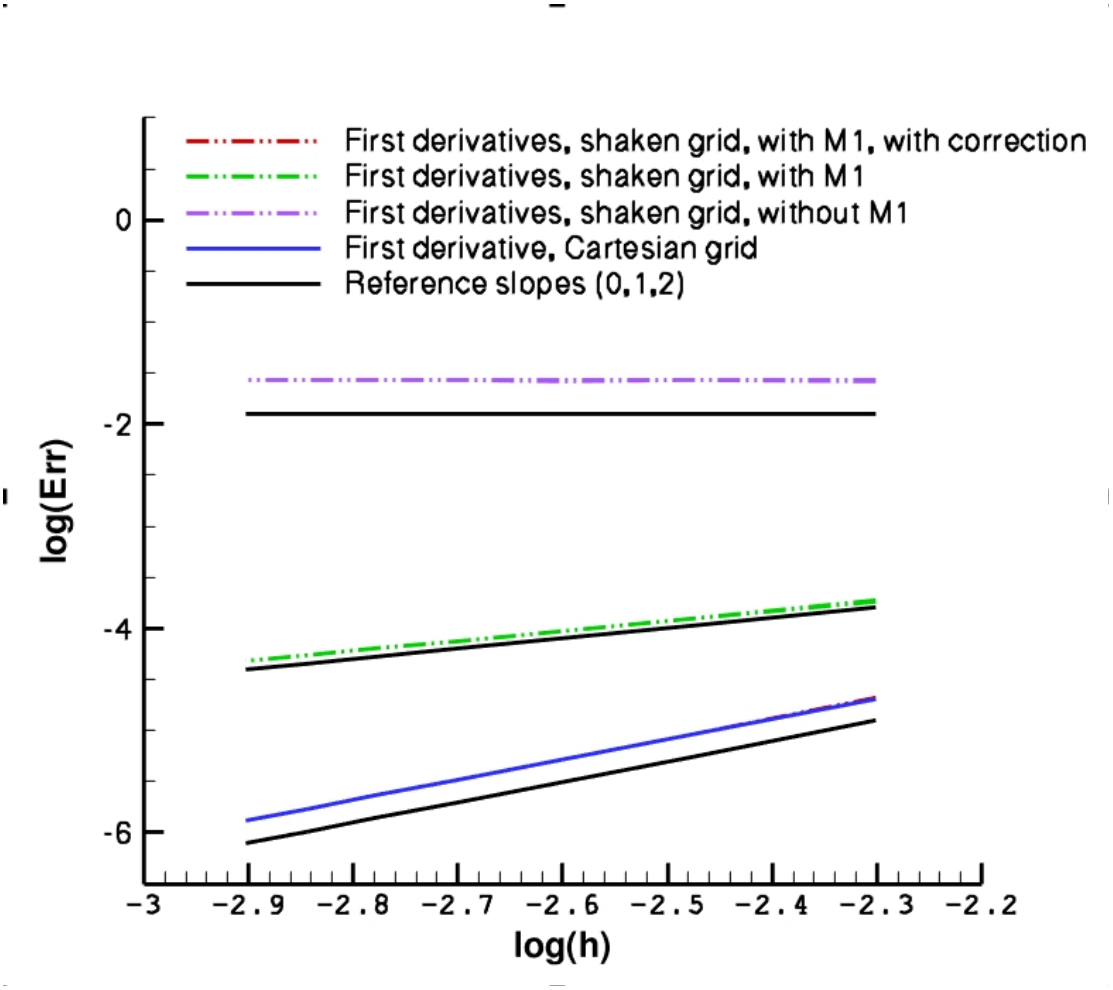

Figure 3.13: Grid convergence of the pressure gradient.

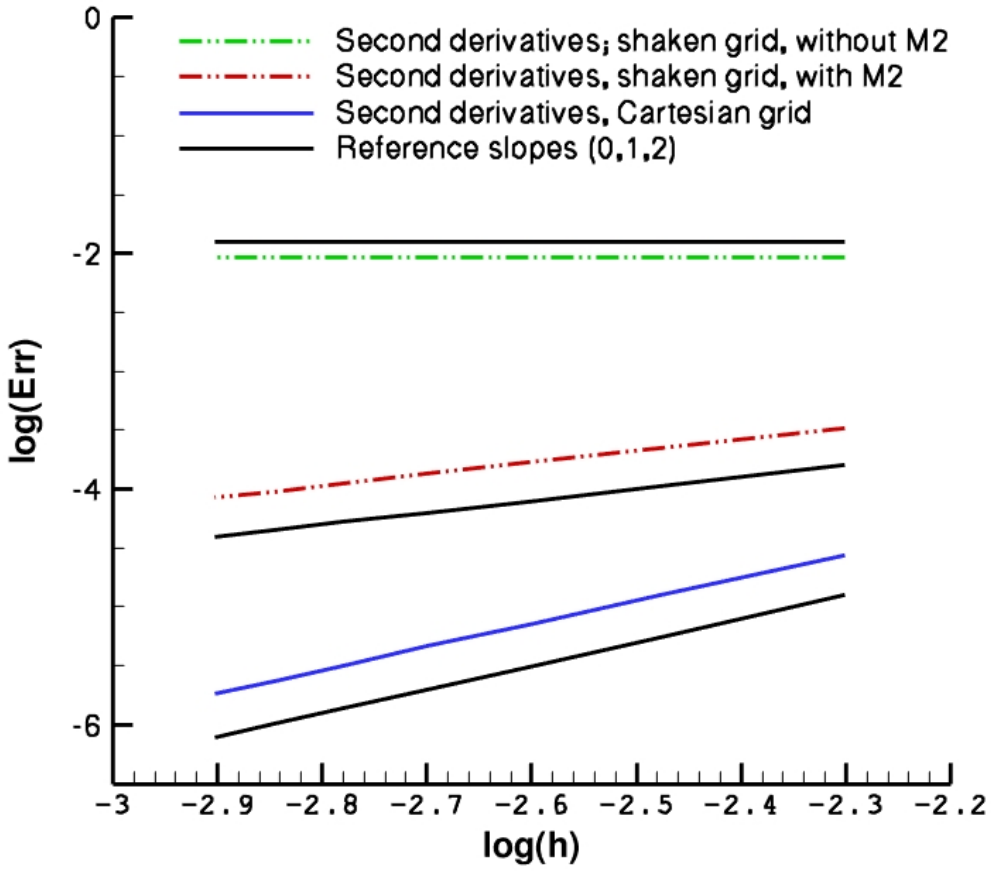

Figure 3.14: Vortex advection.Grid convergence of the second spatial derivatives.

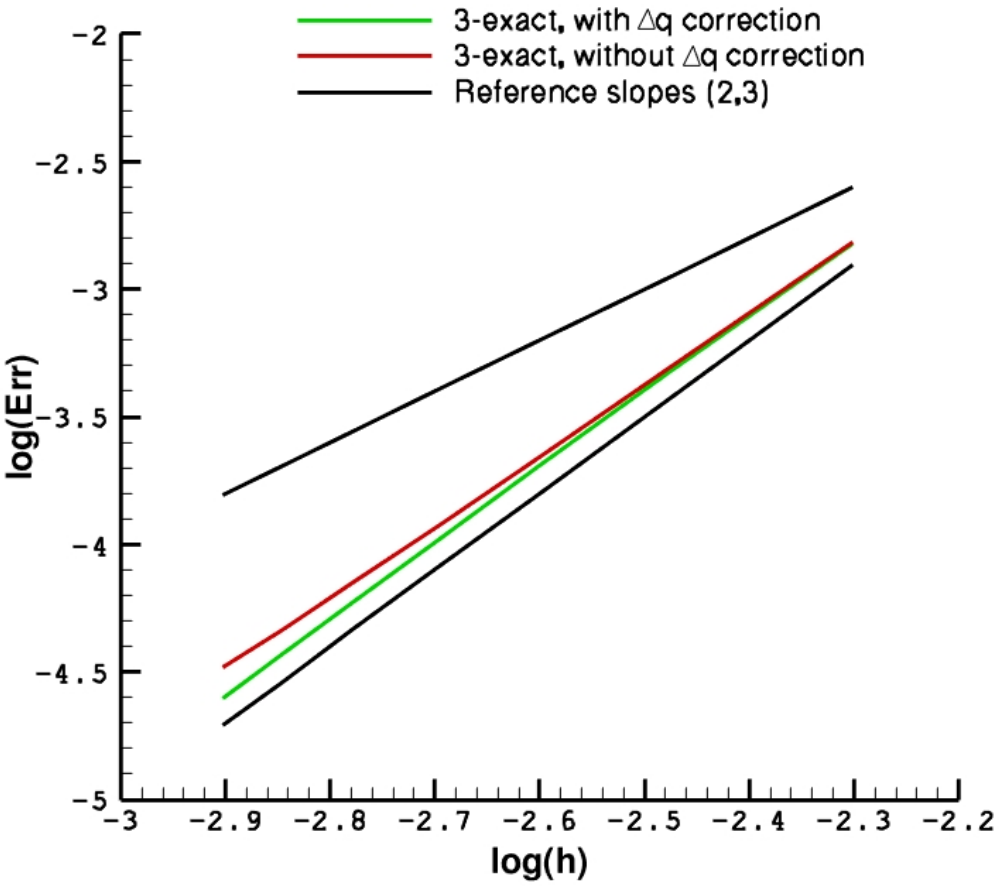

Figure 3.15: Vortex advection.Influence of the $\mathbf{\Delta q}$ correction, $h = 1/\sqrt{nDOFs}$, where nDOFs is the number of degrees of freedom.

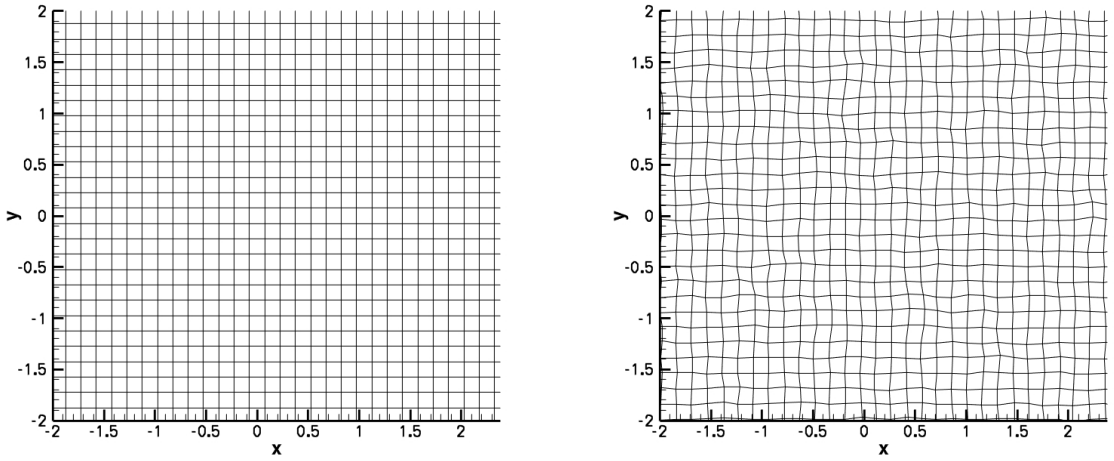

(a) Cartesian grid

(b) Shaked grid

Figure 3.16: Zoom on meshes

usually computed under an inviscid flow hypothesis. Here, we consider a viscous flow in order to investigate the effect of the VC procedure. To validate the VC procedure illustrated in Section 3.3, we consider just only the the vortex advection but we include viscous effects, so that it makes sense to define a grid reynolds number. The vortex is initially located at point $X = Y = 0$ in the computational domain, and it is advected by an uniform flow with Mach number equal to 0.3. Simulations are carried out on three grids of increasing density, composed by 35x250, 50x375 and 120 x 860 cells, respectively. Time integration is stopped after an elasped time corresponding to 50 core length. The time step in use corresponds to a CFL of about 0.95. A reference' solution is obtained by running the code on a very fine mesh (100 points by vortex). Numerical results displayed in Figure 3.17 are in agreement with the truncation error study (equation 3.72): the 2nd-order k-exact scheme is mainly dispersive and it introduces a phase lead of the numerical solution with respect to the physical one, in addition to significant numerical dissipation. The third-order scheme is less dispersive (its dispersion error is fourth-order and is based on fifth derivatives), and predicts a final vortex location that is close to the exact one. Nevertheless it is still too much dissipative. The local centering procedure has no impact on dispersion errors, but it reduces numerical dissipation significantly, both for the second-order and the third-order scheme.

In the following, only the third order upwind and the third order VC scheme are retained for further investigation.

Then, the fully upwind and the vortex-centered 3-exact schemes are applied to the computation of the vortex interaction with a steady shock with an upsteam Mach number 1.1. The computational domain is the same we used in the previous test cast, we just add a steady shock in the middle of the computational domain. Computations are carried out on a grid composed by 50×375 quadrangular cells, such that the vortex core is discretized by 10 points. Figure 3.18 presents the vorticity contours and the pressure isolines computed by using the fully upwind 3-exact scheme and the VC scheme, at the middle of the computational domain, when the vortex crosses the shock. Both schemes capture the shock in a sharp and non-oscillatory way. The weak unsteady shocks generated by the interactions are also reasonably well captured by both schemes. The VC scheme better preserves vorticity than the upwind scheme, leading to a stronger interaction. This is better seen on Figure 3.19, which shows the vorticity distribution along the line $y = 0$ for the two schemes under investigation. The numerical solutions are compared to a reference generated by using a grid 10 times finer in both directions. Finally, Figure 3.20 shows the contours of the Ducros criterion. It can be seen that both vertical and shock regions are identified clearly, so that the scheme remains upwind across shoks and in irrotational regions and is centered elsewhere.

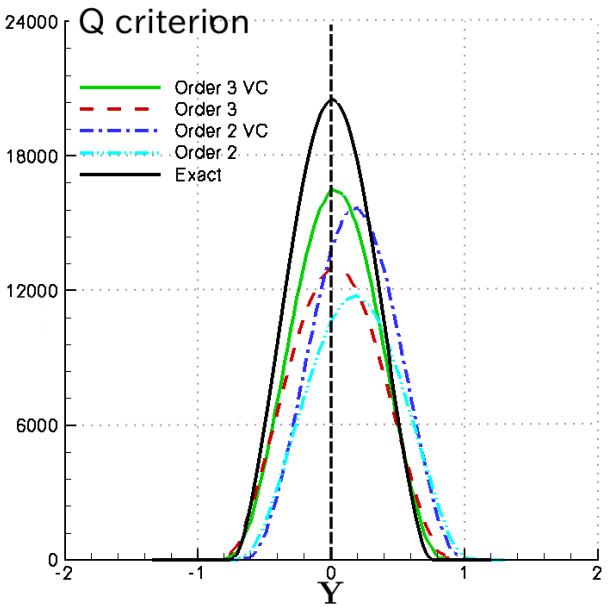

Figure 3.17: Distribution of the Q-criterion across the vortex for fully upwind and vortex-centered schemes

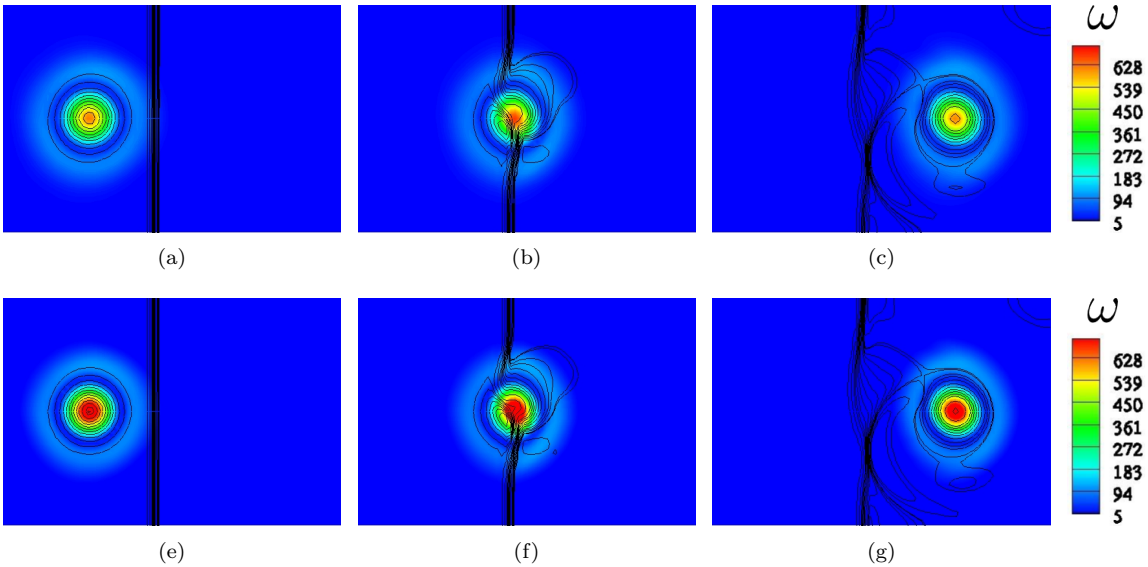

Figure 3.18: Vorticity contours and pressure isolines at times $t = 0.048$ (top), $t + 0.053$ (middle), and $t = 0.06$ (bottom=. Left column: fully upwind 3rd order scheme; right column: VC scheme.

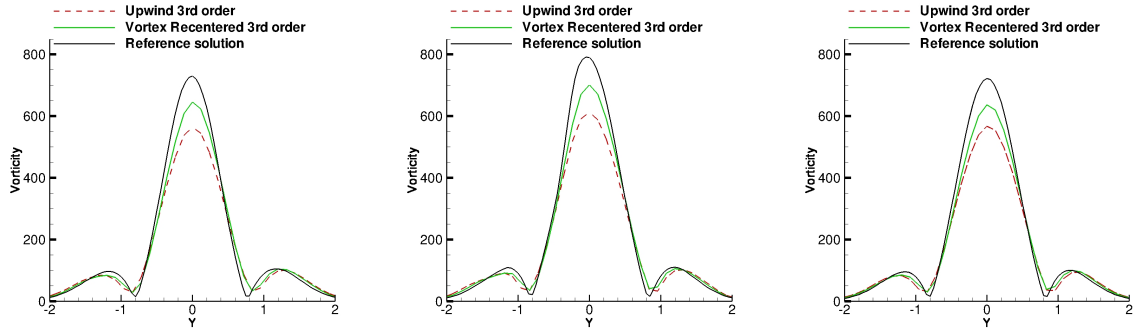

(a) t=0.048 (b) t=0.053 (c) t=0.060

Figure 3.19: Vorticity distribution along the centerline $y = 0$.

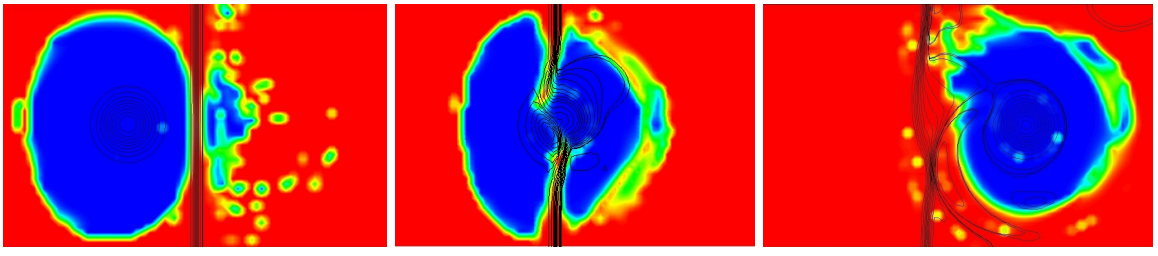

(a) (b) (c)

Figure 3.20: Contours of the Ducros sensor across the shock in the 50×375 grid

3.4.4 Viscous Taylor-Green vortex

The viscous Taylor-Green Vortex (TGV) is an unsteady viscous flow problem dominated by energy transfer from large to small flow scales. This problem has been proven to be an excellent testing bench to study the resolvability properties of high-order schemes in view of subsequent application to fine-scale turbulence simulations [83, 84, 85, 78].
A three-dimensional vortex is set as an initial condition for 3D-computation. Because of vortex-stretching and vortex tilting mechanisms, the vortex breaks up, giving origin to smaller and smaller structures. At finite Reynolds number, the kinetic energy is transfered from larger to smaller scales and dissipated by the smallest one; the test case gives thereby a simple model of the energy cascade. The Taylor-Green vortex is an example of nonlinear fluid flow with kinetic energy transfer from large to small scales and is a good milestone to assess the applicability of numerical schemes to Large Eddy Simulation (LES).

Computations are run in a period cubic domain corresponding to $(0, 2\pi)^3$. The Reynolds number is set to 1600 and the average initial Mach number is taken small enough to reproduce an incompressible flow behavior. We run computations using the 3-exact upwind and the VC scheme using grids of different resolutions and precisely: $128^3, 192^3, 256^3, 330^3$ cells, and compare the results to a DNS obtained on a 512^3 with a pseudo-spectral, provided as a reference for the First International Workshop on High-Order CFD Methods held at the 50th AIAA Aerospace Meeting (https://www.grc.nasa.gov/hiocfd/)

Precisely, we consider the time evolution of the kinetic energy dissipation rate, i.e. the time derivative of the kinetic energy integrated over the computational domain, and of the global enstrophy, i.e. the integral of the local enstrophy per unit volume over the computational domain. The required derivatives and integrals are calculated by using approximation formulae of higher order than the numerical schemes under investigation, to avoid polluting the numerical solutions with post-processing errors (see appendix 11 page XI for more details about post-processing errors)

Figure 3.21 shows the effect of mesh resolution on the grid convergence of the time evolution of the enstrophy. The solution converges progressively toward the reference DNS both for the upwind and the VC scheme, even if the grid resolution used in the present study in still too coarse for DNS. The VC scheme preserves small structures created after the initial vortex-stretching phase better than the fully upwind scheme, leading to a higher enstrophy peak. Precisely, the solution of the VC scheme on the 256^3 grid is almost superposed to the solution of the upwind scheme on a 320^3 grid, which implies a gain of more than a factor of 2 in terms of computational cost (the time step allowed on the coarse grid being 1.25 times greater than the one used on the finer one. The total enstrophy is an integral quantity, which provides information about the overall behavior of the numerical solution. For a more detailed investigation of the local behavior, a spectral analysis is carried out to check if the energy cascade is correctly reproduced. Figure 3.22 shows the energy spectra at non-dimensional times $t = 6$,9 and 12 for both numerical schemes under investigation, using several grids. These were computed by taking the discrete spatial Fourier transform of the whole computational domain at a given time. First of all, we remark that the vortex centered scheme remains stable and correctly dissipates the small structures (i.e, high wave numbers): precisely, the the energy cascade does not overshoot the -5 slope in the high wave number range. Moreover for all of the spectra in figure 3.22 thel -5/3 slope is recovered in the inertial range. Figure 3.22 (c) corresponds to a time after the enstrophy peak. At this time, a -5 slope is found in the dissipative range of the energy spectrum, especially when using the VC scheme on the 320^3 grid. This -5 slope is observed by Lance and Bataille in the dissipation range for turbulent single phase flow [86]. This observation is consistent with the philosophy of vortex-centering scheme. At $t = 12s$, the energy cascade create has created energy in the whole range of wave numbers: reducing or suppressing the numerical dissipation allows to reproduce the physical energy depletion in the dissipation range since only the molecular dissipation plays a role in this range.

3.4.5 Transonic square cylinder

As a final application, we consider the transonic turbulent flow around a square cylinder at a Mach number of 0.9 and a Reynolds number of 4×10^5 based on the cylinder side and free-stream conditions. The flow conditions are set as to mimic the experiment by Nakagawa [87]. The problem is quite challenging for numerical solvers, due to the presence of boundary layers, vortex shedding into the wake, interactions between Kelvin-helmohltz instabilities in the shear layers and the von Karman vortex street, and shock waves. Turbulence effects are taken into account by using the Perot & Gadebusch [41] hybrid RANS/LES model, which is based on the a $k - \epsilon$ realizable two equation closure model. The simulations are carried

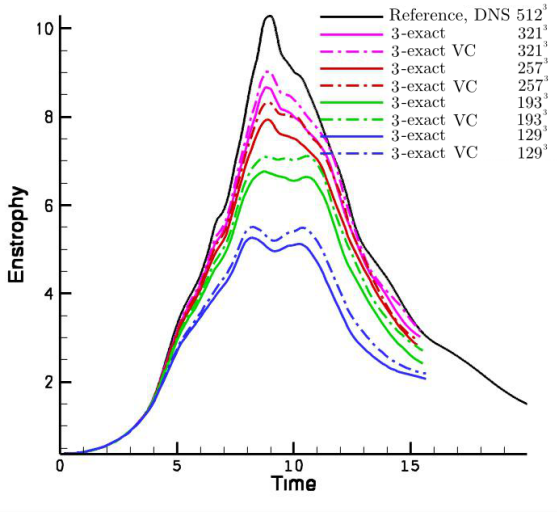

Figure 3.21: Time evolution of the total enstrophy

out on a computational grid containing approximately 2 millions hexahedrical cells with a y^+ of about 10 on the upper and lower surfaces of the cylinder. Figure 3.23 shows the overlapped grids used to discretize the computational domain . Standard wall functions are used to model the flow behavior in the viscous sublayer. The RANS/LES simulation is initialized by using a preliminary RANS $k-\epsilon$ simulation. The aim of this test case is testing the robustness of the flux-centering procedure and the effectiveness of the proposed vortex sensor.

Figure 3.24 provides snapshots of two iso-surfaces of the Q-criterion colored by the kinetic energy, along with isolines of the Mach number on the midspan plane. Strong lambda-like shock waves, approximately normal to the wake, are formed at dowstream end of the vortex formation region. The wake is characterized by a von Karman street composed by vortices coming from the shear layers on both lower and upper surfaces of the square cylinder. In Figure 3.24 *(b)*, the iso-surface is chosen in order to highlight structures coming from the shear layer that merge into the far wave.

Figure 3.25 shows the iso-surface $\Phi = 1$ of Ducros sensor, which governs the blending function ψ. The vortical wake is completely included in this envelop, i.e. turbulent structures are captured with a minimal amount of numerical dissipation. The Ducros sensor locates vortices correctly in the wake of the cylinder and allows to recenter the numerical scheme.

For a more quantitative validation of the proposed strategy, we investigate the dominating frequencies of the flow using sensors located at positions $(4, 0, 0)$ and $(10, 6.5, 0)$ where the components refert to the streamwise, transverse and spanwise coordinate, respectively, the origin is located at the middle of the backward face of the cylinder and the distances are referred to the side of the square (see also figure 3.24 *(b)*). The selected positions correspond to a point along the axis in the near wake of the cylinder and to a point close to the upper shock. The veloxity spectra, shown in figure 3.24, exhibit peaks at Strouhal numbers of about 0.12 for the first sensor and to about 0.13 for the second one. This indicates a strong coupling of the shock and with the von Karman street, which is in a good agreement with the study of Nakagawa [87]. The spectrum captured by sensor 1 displays also a secondary peak for a Strouhal number of about 1. This could be due to the vorteces coming from the shear layers of the square cylinder even if the grid used for this case is not fine enough to resolve correctly the Kelvin-helmoholz instabilities in the shear layer observed for example in the experimental study of Williamson[88].

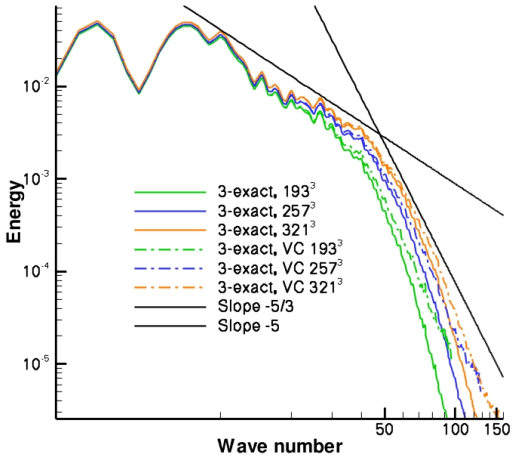

(a) t=6s

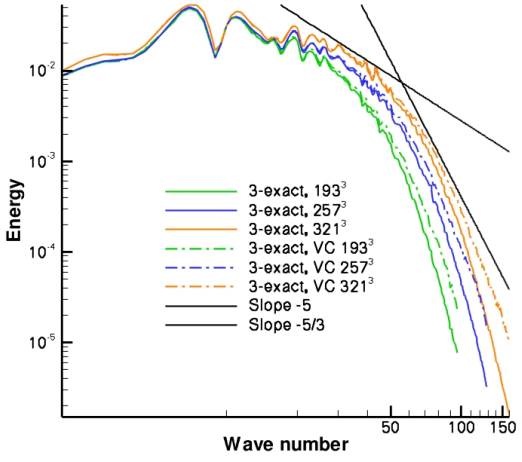

(b) t=9s

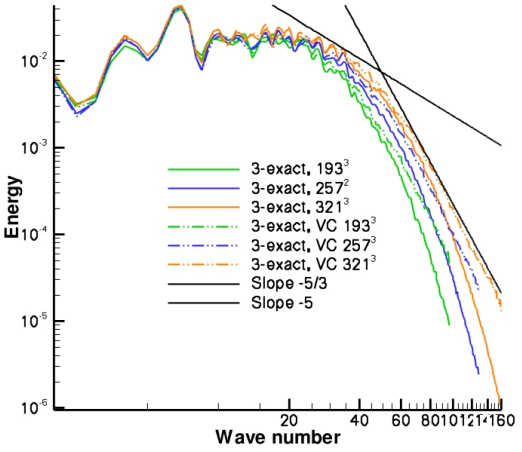

(c) t=12s

Figure 3.22: Energy spectra for the TGV problem at different non-dimentional times.

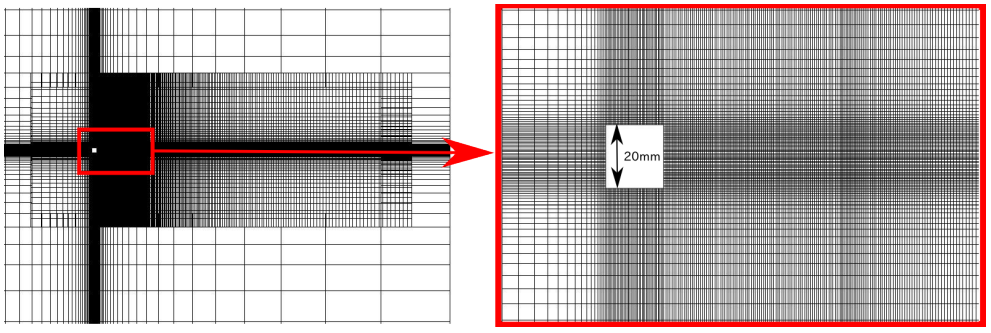

Figure 3.23: Overlapped grid for the square cylinder test case.

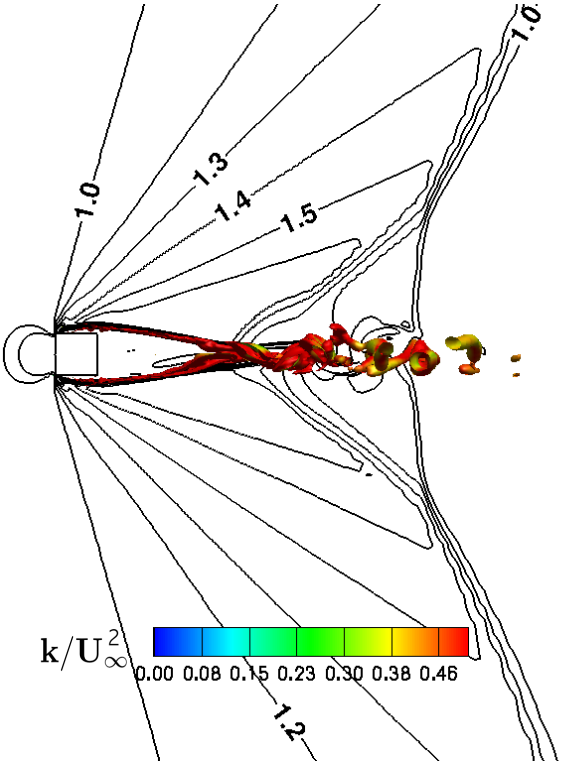

(a) Q=10^6

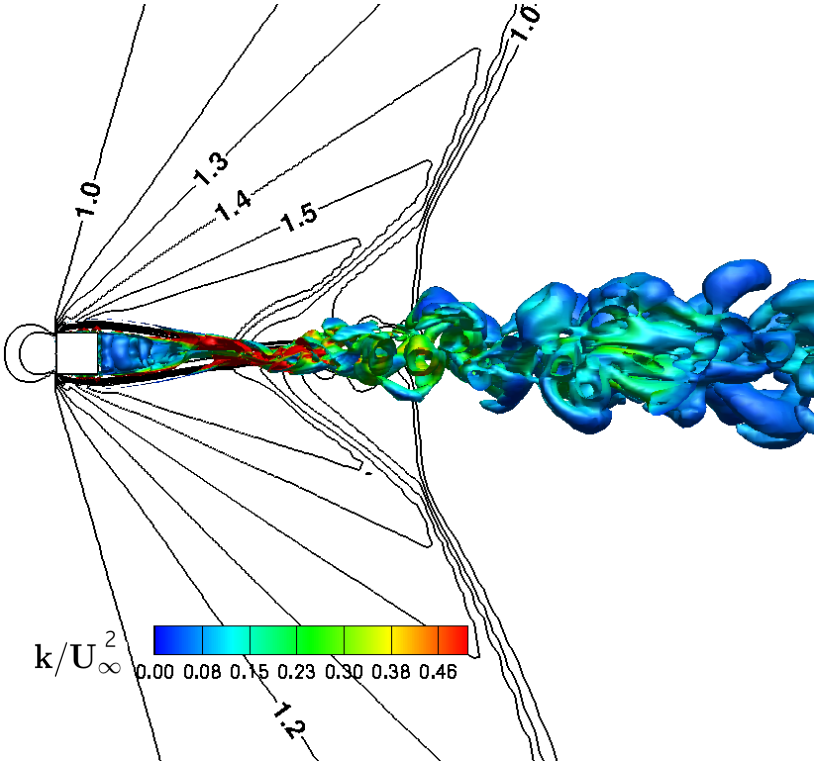

(b) Q=10^8

Figure 3.24: Q iso-surface colored by vorticity and iso-Mach lines.

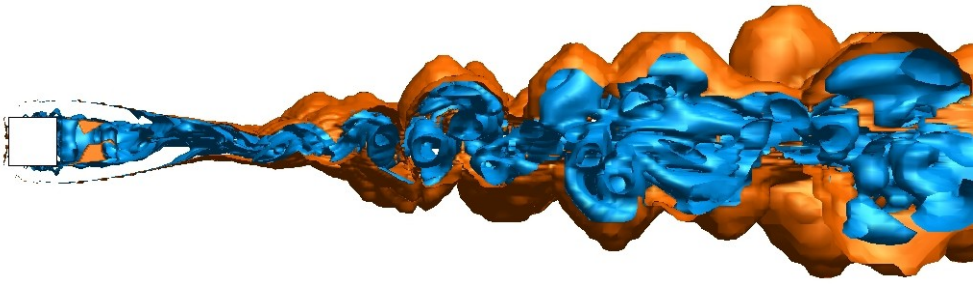

Figure 3.25: Inside the orange envelope, the Ducros sensor is equal to zero and the VC function ψ allows to reduce the numerical dissipation.

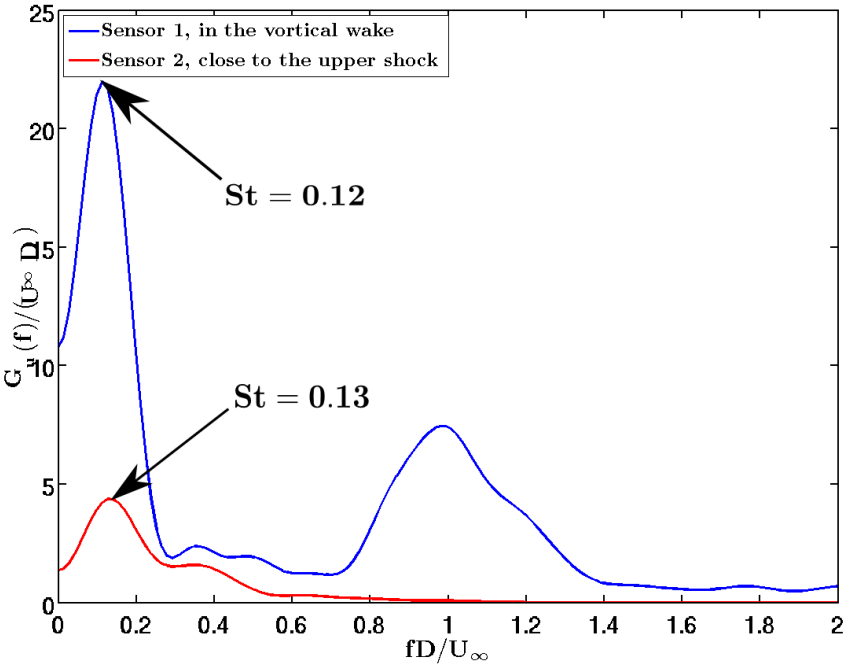

Figure 3.26: Power Spectral Density of longitudinal velocity fluctuations.

3.5 Conclusions

In this Chapter, we presented and validated a robust and accurate finite volume numerical scheme which keeps its formal accuracy regardless of the grid in use. In order to decrease significantly numerical dissipation in vortex dominated regions without increasing the complexity and the computational cost of the discretization significantly, a numerical treatment called VC (Vortex Centering) was introduced. When applied to a third-order upwind scheme, the VC correction leads to a fourth-order accurate, non dissipative scheme in vortex-dominated regions, while keeping a 3rd-order upwind scheme in shock-dominated regions. In this manner, only the eddy viscosity introduced by the turbulence model acts in vortical regions.

Chapter 4

Validation of the strategy

Contents

Simulations in this chapter are carried out using the k-exact VC scheme presented in Section 3.3 page 54. This scheme introduces a minimum of numerical viscosity in the vortex dominated regions of the flow. We use the Perot & Gadebusch model presented in Section 2.1.3 page 30, with its improvement concerning the calculation of α parameter, the SAS model with the Benyoucef correction and the Δ_ω length scale presented in section 2.1.1 page 24 and the DDES model presented in section 2.1.2 page 28, with the Δ_ω length scale. We use also wall laws for attached boundary-layers modeled with the RANS approach. This allow to use large values of y^+ ($10 < y^+ < 50$ in the following applications). According to Goncalves and Houdeville [89], the use of a wall laws does not change the behavior of the turbulence models and does not deteriorate them. On the contrary, it allows us to correct some of their weaknesses coming from the wall damping functions. Using large values of y^+ save considerably the computation cost with an explicit time discretization.

4.1 2D Backward facing step with PG, SAS and DDES

The first test case is a geometrically 2D backward facing step with an upper wall. This case was experimentally studied by Moreau *et al.* [7]. The geometrical features and measures of the computational domain used in this study are given in figure 4.1. The length before the step is chosen so as to obtain a boundary-layer thickness of $0.37h$ just before the separation point. The Reynolds number based on inlet conditions and step height is equal to 40000. Hereafter, we show results obtained with the PG, SAS and DDES models. Numerical simulations using ZDES [1] modeling on a fine mesh of 3.9 million points provided by Deck [10] are taken as a reference for assessing the present results. For all the calculations, the useful unsteady calculation is performed over a total duration of $T * U_\infty/h = 300$. Details of the numerical parameters used in the present and reference simulations are presented in Tab. 4.1. Grids 1, 2 and 3 differ only by refinement in the spanwise direction, where the number of grid point is doubled. The y^+ and x^+(at the beginning of the step) for grids 1, 2 and 3 is equal to 15.

[1] Zonal Detached Eddy Simulation [10]

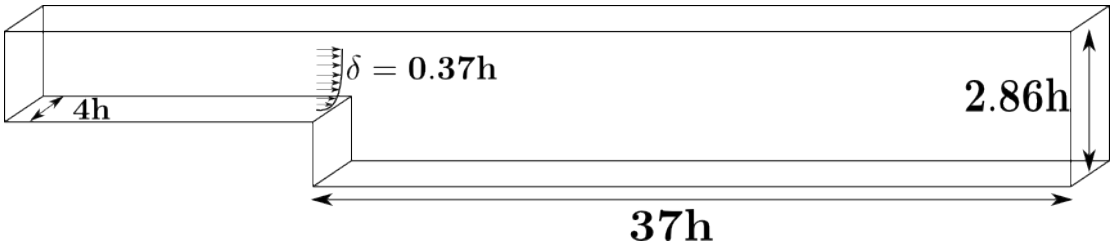

Figure 4.1: Sketch of the computational domain.

	Present calculations	ZDES ONERA,[10],
Number of cells and near-wall resolution	grid 1 : 7×10^5, $z^+ = 300$, $x^+ = y^+ = 15$ grid 2 : 1.4×10^6, $z^+ = 150$, $x^+ = y^+ = 15$ grid 3 : 2.8×10^6, $z^+ = 75$, $x^+ = y^+ = 15$	4.10^6, $y^+ = 1$
Model	PG, SAS, DDES	ZDES

Table 4.1: Numerical parameters used in the present and reference calculations.

4.1.1 Effect of grid refinement

First of all, we investigate the effect of grid resolution for a given HRL model. Precisely, we carry out simulations with the PG model on the three grids of Tab.4.1. Figure 4.2 (a,b,c) shows snapshots of isosurfaces of the λ_2 criterion colored by mean velocity on the three grids. Refinement in the spanwise direction leads to the appearence of finer and finer structures, indicating some form of grid convergence of the model as precedingly observed by Perot and Gadebusch for isotropic decaying turbulence [41]. We can also observe the formation of hairpin vortices in the recirculation bubble after a vortex pairing mechanism and longitudinal vortices are generated downstream of the reattachment point.

4.1.2 Unsteady properties

RMS of longitudinal velocity fluctuations are shown in figure 4.5 (b). They are in good agreement with the reference ZDES calculation and reasonably close to the experiments, even on the coarser grid. Thanks to the non-dissipative numerical scheme, there is no delay in the appearance of Kelvin Helmholtz instabilities in the shear-layer: physical perturbations are not damped, and backscatter of energy is fostered. Since grid 2 provides satisfactory results when using the PG model, in the following, we carry out computations

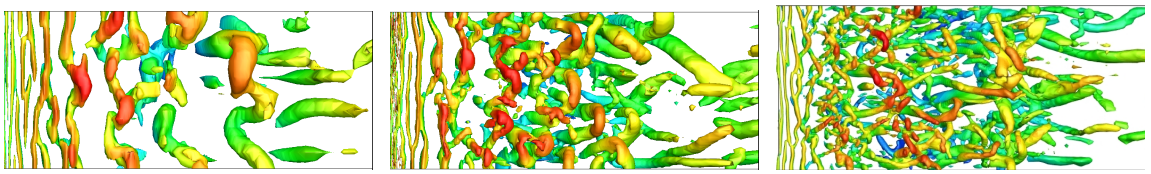

(a) PG-VC grid 1 (b) PG-VC grid 2 (c) PG-VC grid 3

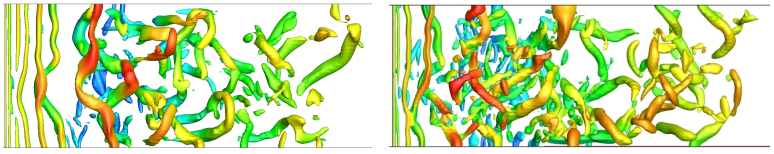

(d) SAS-VC grid 2 (e) DDES-VC grid 2

Figure 4.2: Iso surface of $\lambda_2 = -7000$ colored by mean velocity.

	PG-VC grids 1,2,3	SAS-VC grid 2	DDES-VC grid 2	Driver *et al* [12] (experiment)	Le *et al* [91] (DNS)	Hall **et al** [3] (experiment)
X_r/h	6.2	6.0	6.1	6.1	6.28	6.8

Table 4.2: Reattachment point

with the SAS and DDES models using this grid only.

Calculations with the SAS-SST turbulence model are performed using the grid 2 described in Tab. 4.1 and the VC numerical scheme. Figure 4.2 (d) shows the isosurfaces of the λ_2 criterion colored by mean velocity. Thanks to the limiter applied to the von Karman length scale (see Equation 2.29) and to the use of a low-dissipative numerical scheme there is no delay in the appearance of Kelvin Helmholtz instabilities in the shear-layer. A qualitative comparison between figure 4.2 (b) and 4.2 (d) shows that, on the same grid, the PG model allows to capture finer turbulent structures. The reason for this is that the level of eddy viscosity with the SAS turbulence model is greater than the one with PG model. Despite the differences observed between SAS and PG model on the vortical structures, figure 4.6 (a) shows that SAS model gives a good prediction of the mean flow. The reattachment point, located at $X_r/H = 6.0$, is reasonably close to the preceding PG results and to the experiments (see tab 4.2). The shorter reattachment length predicted by SAS is due to the larger amount of eddy viscosity introduced by this model compared to PG. Figure 4.6 (b) shows that the RMS of longitudinal velocity fluctuations are also in good accordance with the experiments and to results of the PG model on grid 2. Present results show that, thanks to the use of a numerical scheme well suited for HRL computations, using artificial forcing like ZFLES[2][47] is not necessary. Finally, calculations with the DDES turbulence model are also performed using grid 2 described of Tab. 4.1 and the VC numerical scheme. Figure 4.2(e) shows the isosurfaces of the λ_2 criterion colored by mean velocity. Thanks to the new length scale proposed by Chauvet [53] and to the use of a low-dissipative numerical scheme there is no delay in the appearance of Kelvin Helmholtz instabilities in the shear-layer. Despite the differences observed between DDES and PG model on the vortical structures (which are slightly finer for the latter model), figure 4.6 (a) shows that DDES model gives also a good prediction of the mean velocity profiles. The reattachment point, located at $X_r/H = 6.1$, is slightly shifted upstream but it remains close to preceding results and experiments (see tab 4.2). Figure 4.6 (b) shows that the RMS of longitudinal velocity fluctuations are also in reasonably good agreement with the experiments and with the results of the PG model on grid 2. The preceding results show that the choice of the specific HRL model has a limited impact on the accuracy of the simulations. In [90] it is shown that, on the contrary, using a low dissipative numerical scheme is of the utmost importance for achieving the correct behavior. Nevertheless, in present calculations we find that the PG model, thanks to its local backscattering mechanism, is slightly more accurate that SAS and DDES on a given grid. This is why we conserve this model for the following analyses.

4.1.3 Mean flow analysis

Figure 4.5 (a) shows the average streamwise velocity field and streamlines on grid 2, as well as the streamwise locations used to extract statistics of the velocity field. The shape of the secondary recirculation bubble in the corner is in good agreement with the PIV streamlines of the experiment of Hall *et al.* [3]. Mean profiles of the longitudinal velocity taken at different streamwise locations in the recirculation bubble are shown in Fig. 4.5 (a). Present results are in good agreement with the experiments and with the reference ZDES solution by Deck [10], obtained on a grid of 4.10^6 cells, despite the use of substantially coarser grids. Of course, simulation result for grid 3 better predict the mean flow in the recirculation bubble, especially for the first three profiles of figure 4.5. The location of the reattachment point for grids 1, 2 and 3 is listed in tab 4.2. They are close to the experimental values of Hall *et al.* [3], of Driver *et al.* [12], and to the direct simulation of Le *et al.* [91] .

[2]Zonal Forced LES

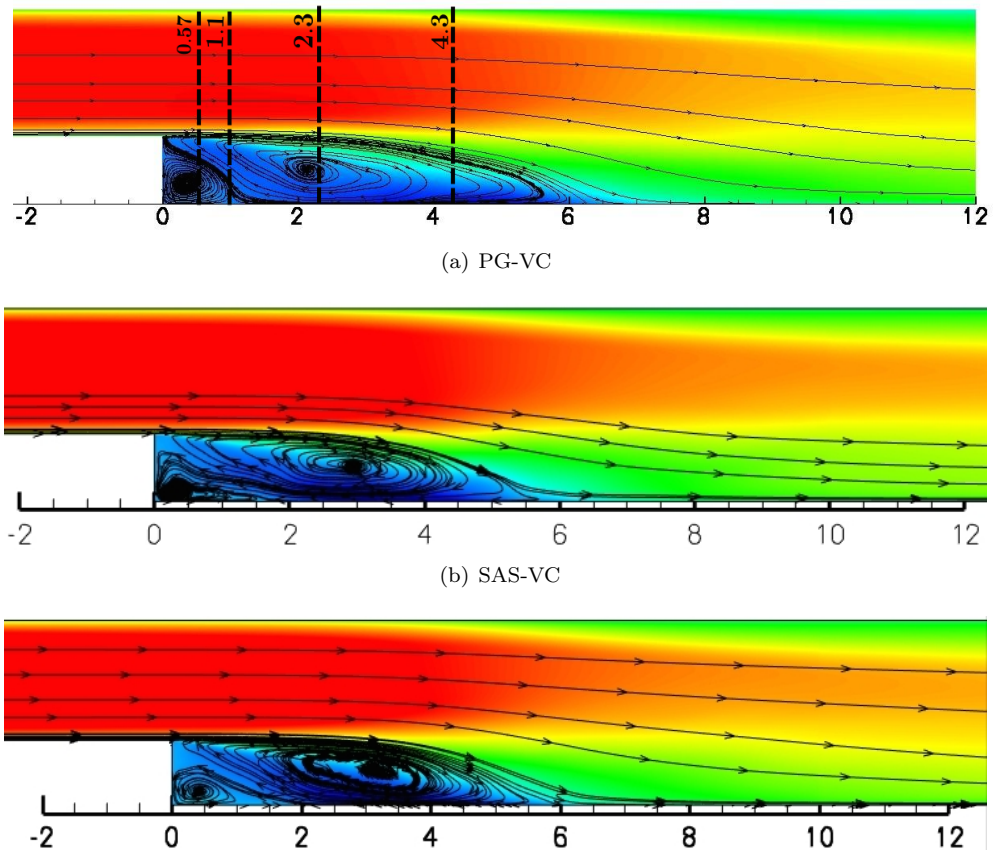

(a) PG-VC

(b) SAS-VC

(c) DDES-VC

Figure 4.3: Contour of mean longitudinal velocity

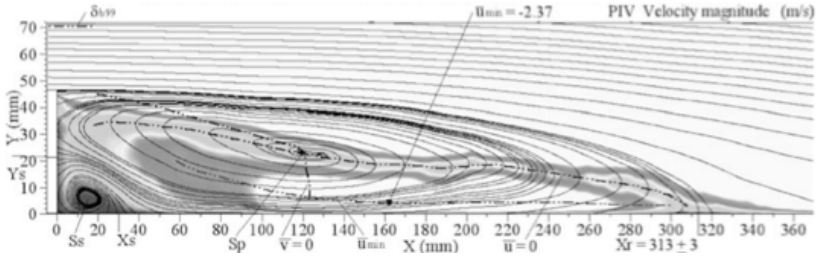

Figure 4.4: PIV of Hall[3]

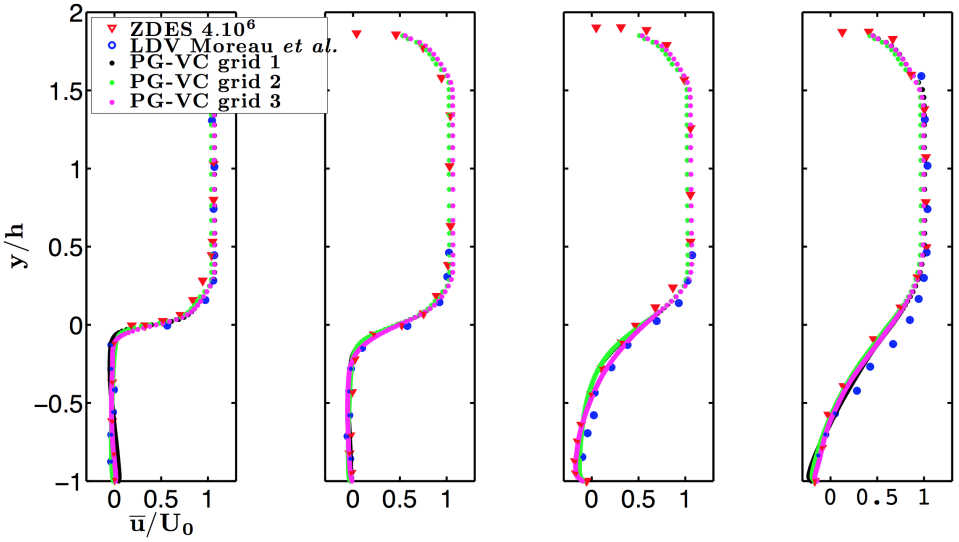

(a) Mean longitudinal velocity

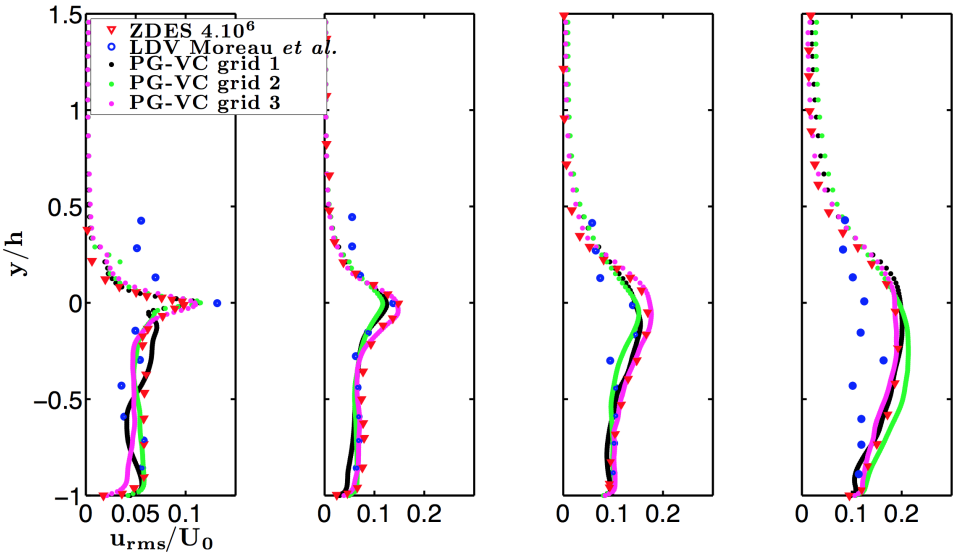

(b) Rms longitudinal velocity

Figure 4.5: Mean and rms longitudinal velocity at different locations in the recirculation bubble. PG-VC strategy, different grid resolutions.

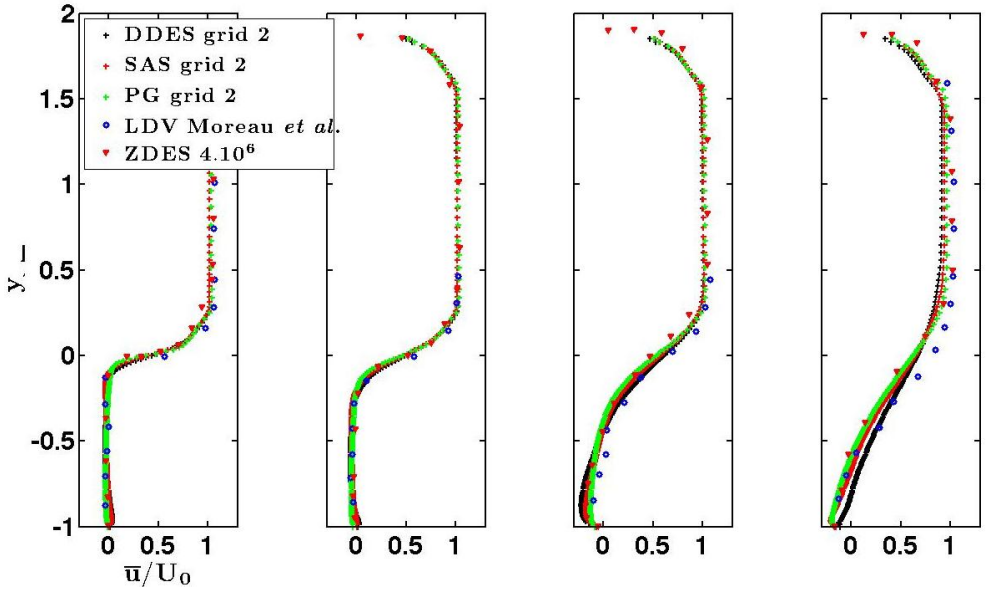

(a) Mean longitudinal velocity

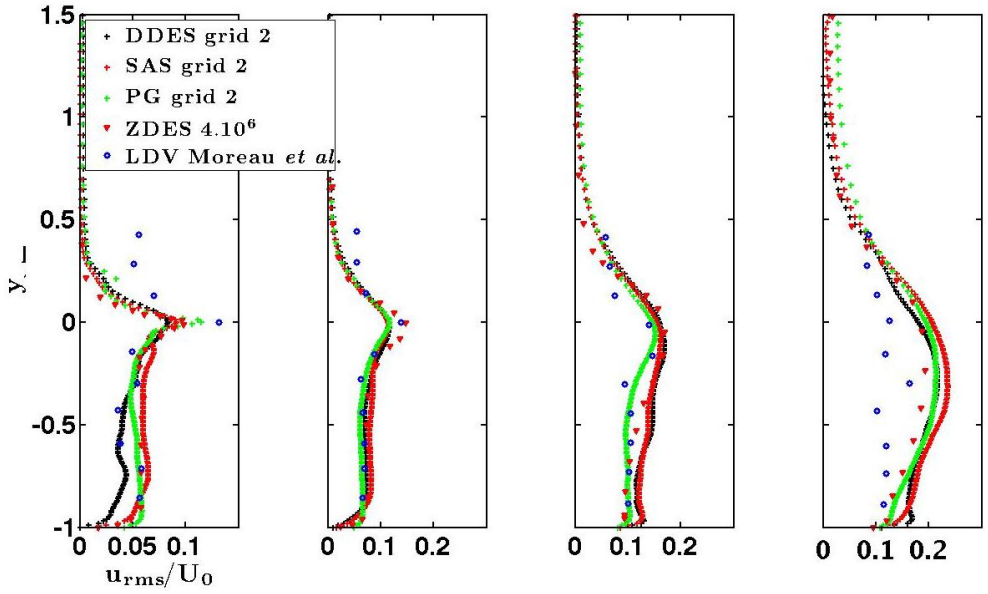

(b) Rms longitudinal velocity

Figure 4.6: Mean and rms longitudinal velocity at different locations in the recirculation bubble for PG-VC, DDES-VC and SAS-VC strategies on grid 2.

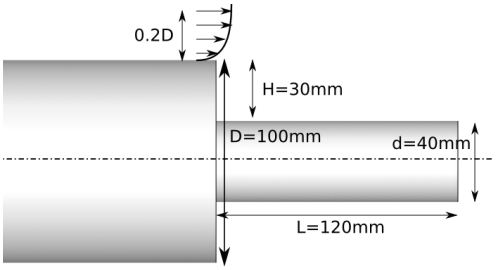

Figure 4.7: Schematic of the axisymmetric backward facing step.

	ZDES [10]	Present calculations	Experiments
Re	1.2×10^6	1.2×10^6	1.2×10^6
Number of cells	grid 1 : $5 \times 10^6, N_z = 97$, [22] grid 2 : $8 \times 10^6, N_z = 147$, [22] grid 3 : $12 \times 10^6, N_z = 240$, [20], [17]	5.7×10^6 $N_z = 120$ $x^+ = y^+ = 50$	Deprés *et al.* [15] Meliga *et al.* [16]

Table 4.3: Detail on calculations and experiments. N_z is the azimuthal resolution.

4.2 Axisymetric backward facing step with PG, SAS and DDES

The second test case is an axisymmetric backward facing step experimentally studied by Deprés *et al.* [15] and Meliga *et al.* [16]. The geometrical features and measures are provided on figure 4.7. The upstream length before the step is chosen so as to obtain a boundary-layer thickness of 0.2D just before the separation point. Present calculations was carried out by using the PG, DDES and SAS-SST turbulence models coupled with the VC scheme on a grid of 5.7×10^6 cells with average y^+ of the first cell close to the wall of about 50. The x^+ at the beginning of the step is equal to 50. This is rather coarse, but allows keeping computational costs to within an industrially acceptable level. Results are compared to the available experimental data and to ZDES calculations [22] [20] with differents grids listed in Tab. 4.3. For all of the calculations presented in this section, the step time is $10^{-7}s$ and the useful unsteady calculation is performed over a total duration of $T * U_\infty / H = 300$.

4.2.1 Unsteady properties

Figures 4.8 (a), (b), (c) represent a snapshot of the instantaneous flow field, showing the coherent structures in the recirculation area downstream of the backward facing step. We can see a three-dimensionalization process very similar so that of the 2D backward facing step flow. Hairpin vortices appear after the separation point and longitudinal vortices are generated downstream of the reattachment point. Figures 4.8 (c) show a delay on the triggering of convective instabilities for SAS-SST model. Figure 4.9 (a), (b), (c) shows respectively a snapshot of eddy viscosity for PG, DDES and SAS models. On these figures, we can see the large amount of RANS eddy viscosity coming from the upstream boundary-layer and the grid sensitization of the models into the recirculation area. In this case, the DDES model provides the lowest turbulent viscosity of all the models. This is there more turbulent structures can be observed on figure 4.8 (b) than on figures 4.8 (a) and (c). This can be seen also from figure 4.10 (a), (b), (c) which represents the resolved kinetic energy. DDES modeling provides more resolved kinetic energy than other models, especially in the recirculation area. Delay on convective instabilities triggering is bring out by the lack of resolved kinetic energy at the detachment point on figure 4.10 (c). Figures 4.11 (a) and (b) show the time-averaged distribution of modelled to total kinetic energy ratio. This figures show that the PG model resolves kinetic energy essentially in the shear layer and models the rest, whereas the SAS-SST models the shear layers and resolves the recirculation area.. Due to the nature of DDES, which is based on S-A turbulence model, it is not possible to display such a quantity since there is only one transport equation for ν_t. The figure shows that in the attached boundary-layers, the turbulent kinetic energy is fully modeled, i.e. they are treated in a RANS mode. We can see the effect of the delay on convective

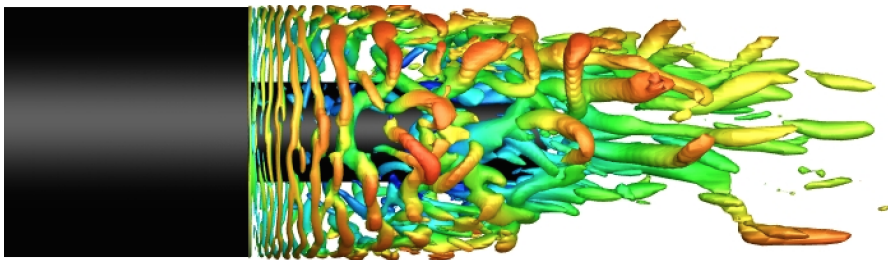

(a) Perot & Gadebush

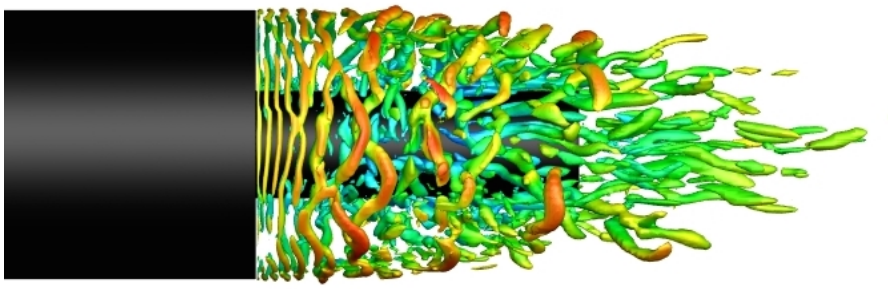

(b) DDES

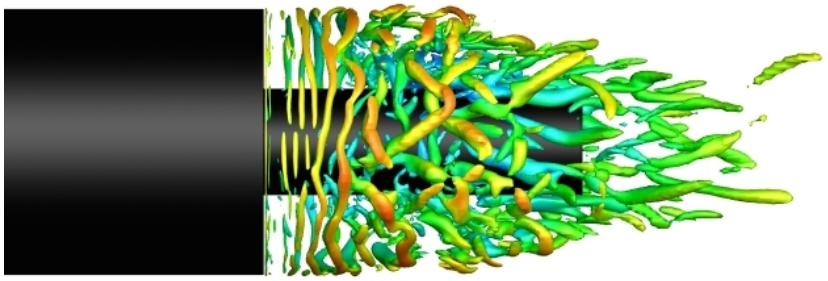

(c) SAS-SST

Figure 4.8: Coherent structures = isosurface of $\lambda_2 D/u_\infty$=10 colored by instantaneous longitudinal velocity.

instabilities on the two first rms profiles of figure 4.14 (b): the peak of velocity fluctuations is much less pronounced for the SAS model. Finally, numerical schlieren calculated in the recirculation area figure 4.12 allows to bring out both delay in the appearance on convective instabilities and for SAS model (figure 4.12 (c)) and the richness of the DDES in terms of vortical structures. Figure 4.14 (b) shows that longitudinal velocity fluctuations level and shape is very similar to the 2D case showed of Figure 4.6 (b). It is interesting to notice that it is only the turbulent viscosity that plays a role in the dissipation of turbulent structures because we use the VC scheme in vortical dominated regions of the flow, the numerical dissipation is very low.

Figure 4.13 shows the RMS of pressure fluctuations. The maximum of pressure fluctuation is located at the reattachment point. We see thanks to the figure 4.13 the delay of the Perot & Gadebush turbulence model to reattach (see tab 4.4). The DDES calculation is very close to the ZDES calculation on grid 2 and very close to the SAS calculation regarding the figure 4.13. The shape of the Cp_{rms} evolution is closer to the reference values with the DDES and SAS model than with the PG turbulence model. We can see that, PG turbulence model provides a Cp_{rms} closer to the experiment but with a maximum location too much downstream compared to the experiments and reference. The fact that the PG level of Cp_{rms} is lower than the other model is because there is a lake of energy in the high frequencies because of the too high turbulent viscosity. This is better shown by the spectral analysis in Section 4.2.3.

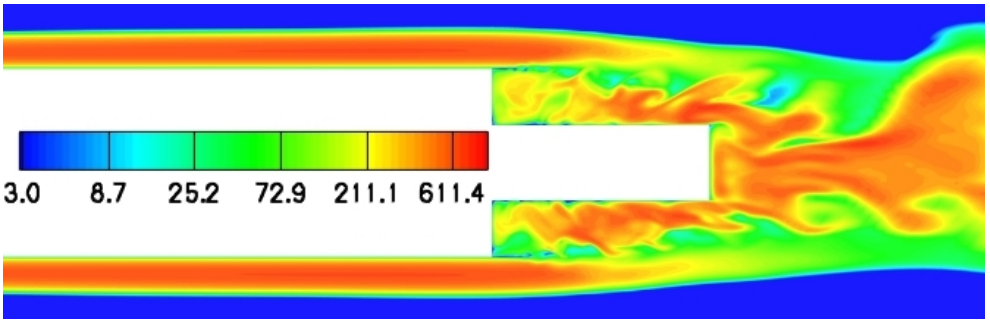

(a) Perot & Gadebush

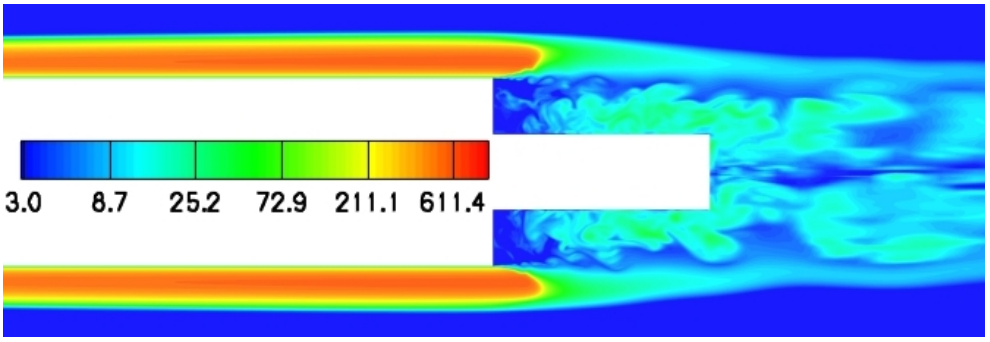

(b) DDES

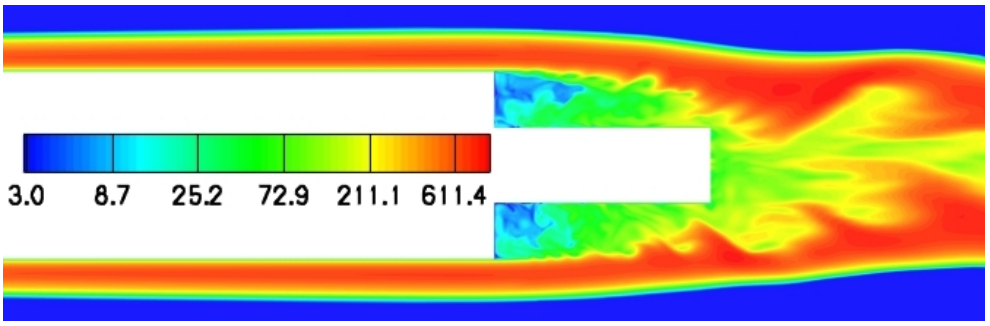

(c) SAS

Figure 4.9: Snapshot of the eddy viscosity ratio ν_t/ν (exponential range)

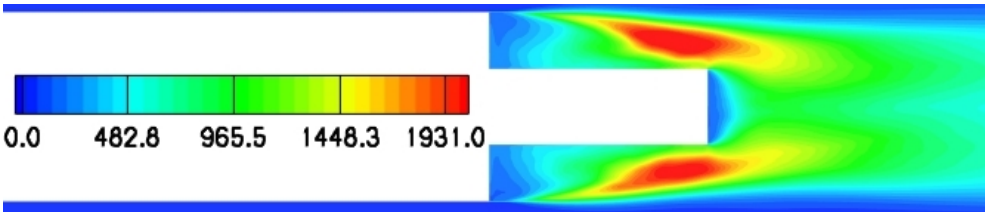

(a) Perot & Gadebush

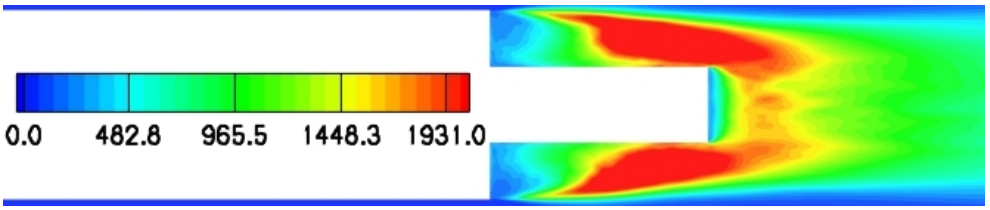

(b) DDES

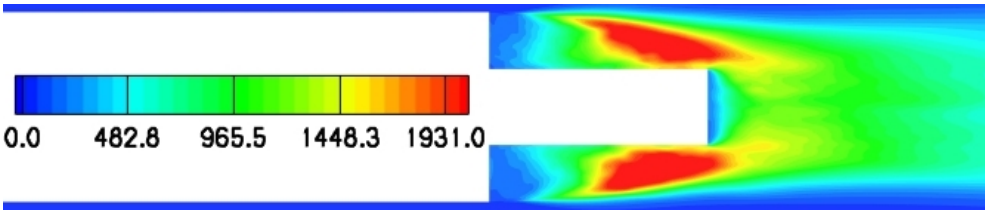

(c) SAS

Figure 4.10: Snapshot of the resolved kinetic energy

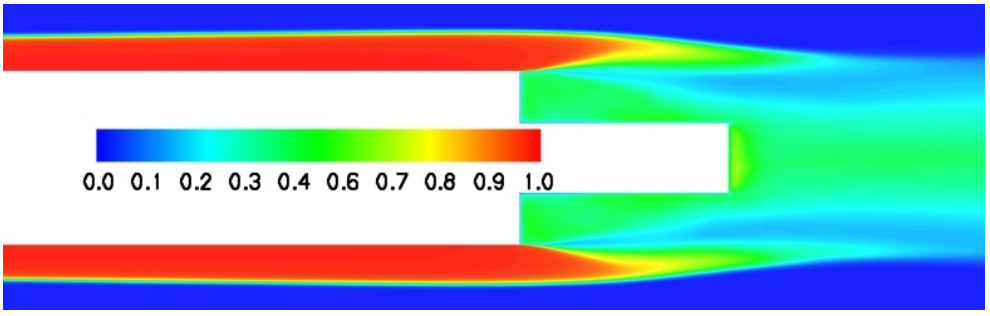

(a) Perot & Gadebush

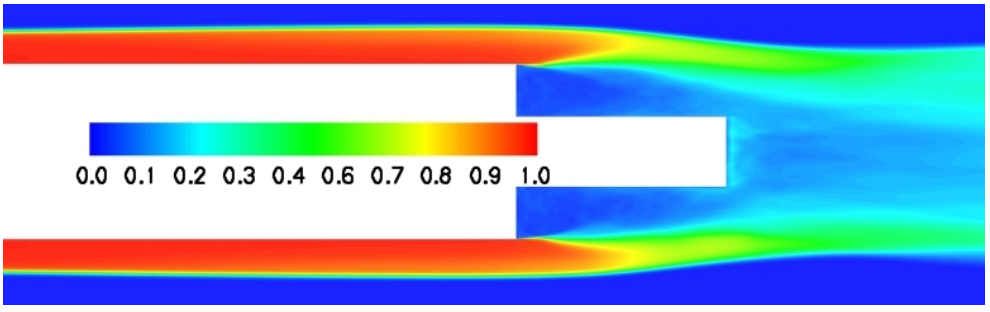

(b) SAS

Figure 4.11: Mean modeled to total kinetic energy ratio

(a) Perot & Gadebush

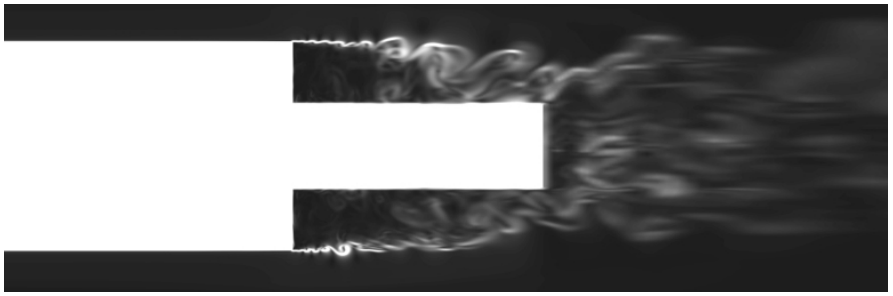

(b) DDES

(c) SAS-SST

Figure 4.12: Numerical schlieren in the mixing layer.

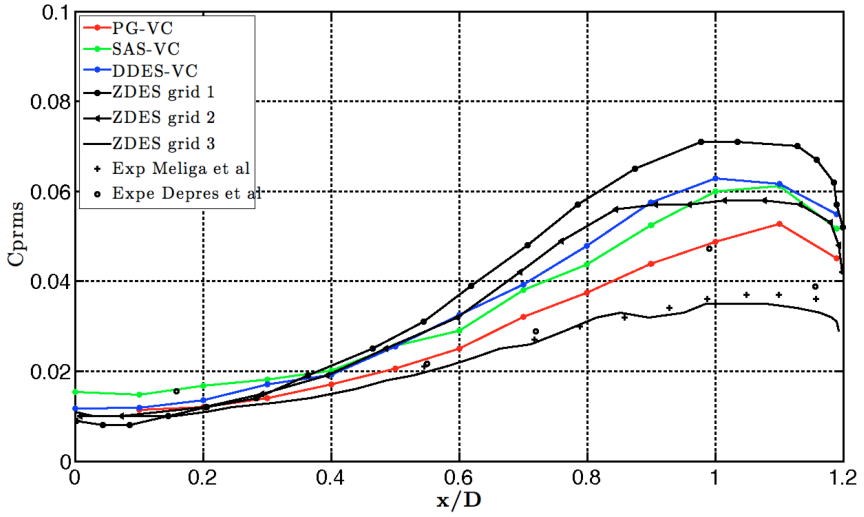

(a) Cp_{rms}

Figure 4.13: Pressure fluctuation coefficient on the wall in the recirculation area.

	PG-VC	SAS-VC	DDES-VC	ZDES	Lê [92] (experiment)	Deprés et al (experiment)
X_r/D	1.16	1.12	1.1	1.1	1.11	1.3

Table 4.4: Reattachment point

4.2.2 Mean flow analysis

Figure 4.14 (a) shows mean velocity profiles taken at the same location of the 2D case (x/H=0.57, 1.1, 2.3, 4.3). The shape of the velocity profiles is very similar to the profiles showed at figure 4.6 (a) for the 2D case. The computed mean flow is characterized by a main recirculation bubble with a secondary corner vortex and with solid reattachment point as it can be seen in figure 4.15 (a), (b), (c) . The reattachment point of the present calculations, reference calculation and experiment are presented on tab 4.4. These values are close to the reattachment point predicted by the ZDES calculation and by the measurements of Lê [92] and Deprés *et al.* The model closer than the experiment reattachment point is the DDES.

Figure 4.17 shows that the present calculation provides an accurate prediction of pressure coefficient level but the point of minimum C_p is located downstream with respect to the ZDES calculations. Figure 4.16 (a), (b), (c) show the contour of C_p values. These pictures show up the downstream shift of the reattachment point and of the minimum of pressure coefficient with the PG model.

4.2.3 Spectral properties

To go further in the comparative study of the turbulence models, it is interesting to look at the wall pressure spectrum. This study is analog to the spectrum analysis done in section 3.4.4 page 70 except here, we look for the model behavior and not the numerical scheme behavior because we know that there is a very low numerical dissipation in the recirculation area (negligible with respect to the turbulent viscosity). Figure 5.4 (a) shows the spectrum of wall pressure fluctuations at $x/D = 0.7$ for PG-VC, SAS-VC and DDES-VC strategies. We see that all turbulence models recovers the dominating frequencies of the physical phenomena described by Weiss [17] (see figure 1.4) and by the study of Deck and Torigny[22]: $Str_D = 0.2$, due to the buffeting phenomena, and at several frequencies corresponding to $0.3 < Str_D < 1$, corresponding to the shear-layer reattachment to the wall (the flapping motion). Concerning the frequency $Str_D = 0.08$, we can wonder why this frequency is so energetic. First, we can remark that if we calculate the Strouhal number using the diameter of the wind tunnel, we find that the frequency of $Str_D = 0.08$

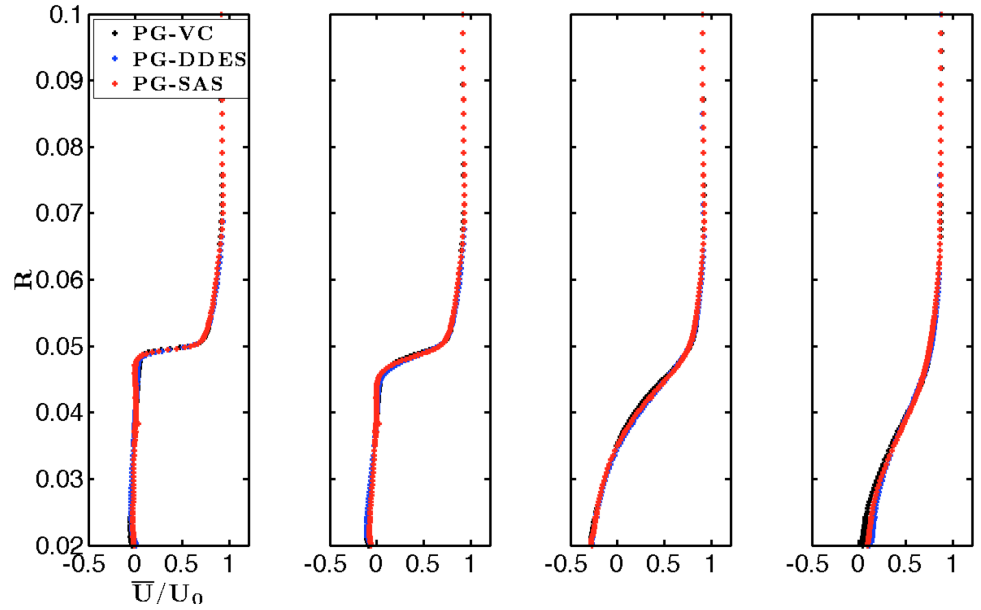

(a) Mean longitudinal velocity

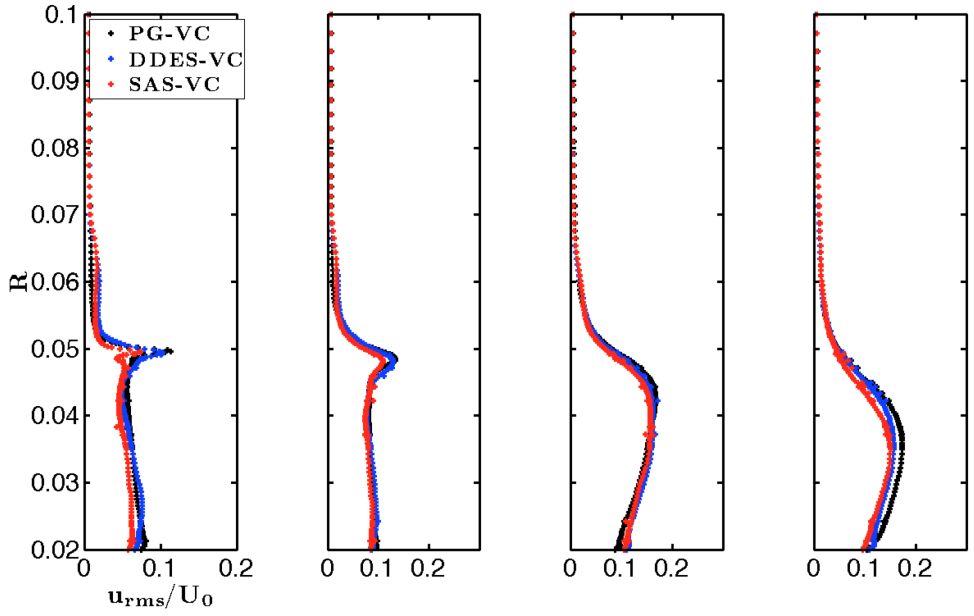

(b) Rms longitudinal velocity

Figure 4.14: Mean and rms longitudinal velocity at different locations in the recirculation bubble for PG-VC, DDES-VC and SAS-VC strategies.

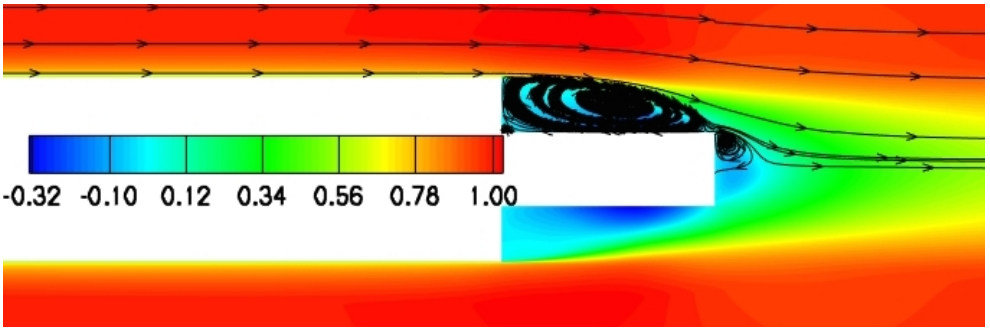

(a) Perot & Gadebush

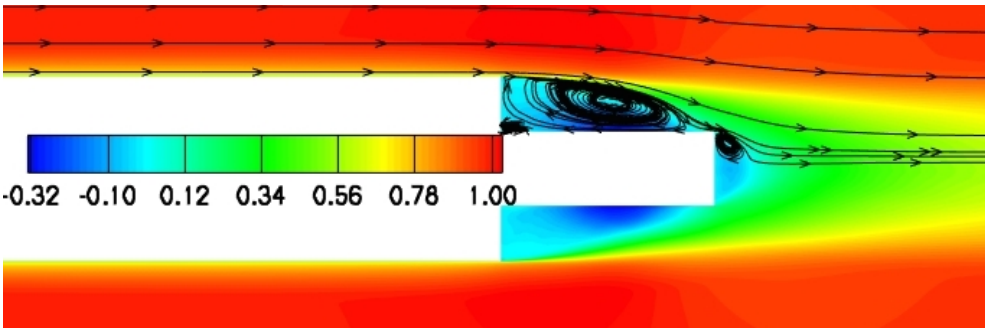

(b) DDES

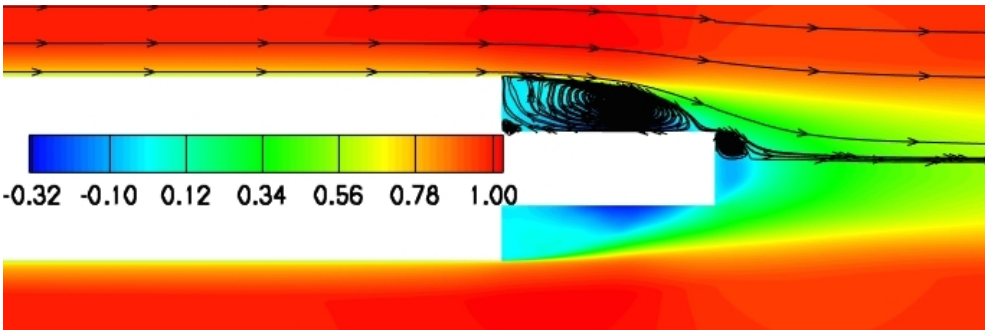

(c) SAS

Figure 4.15: Mean flow $\overline{u}/U_\infty$

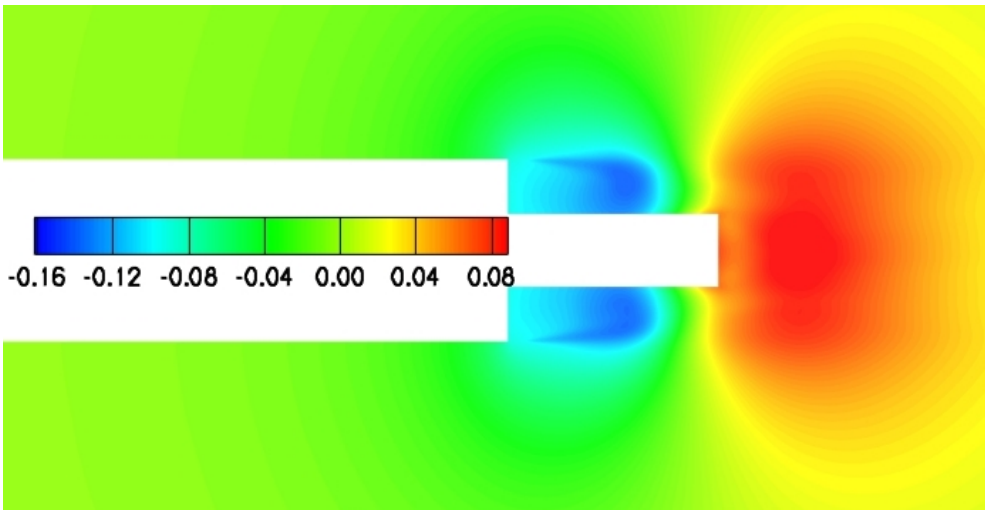

(a) Perot & Gadebush

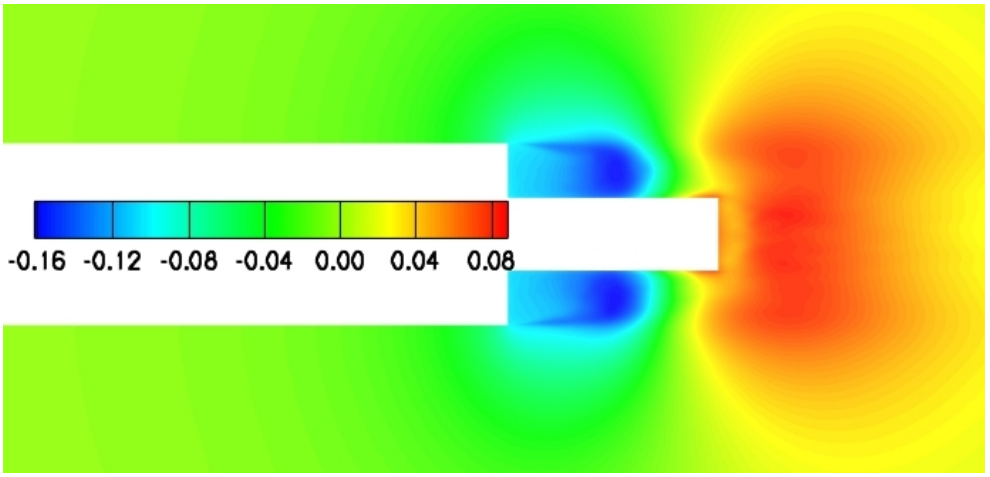

(b) DDES

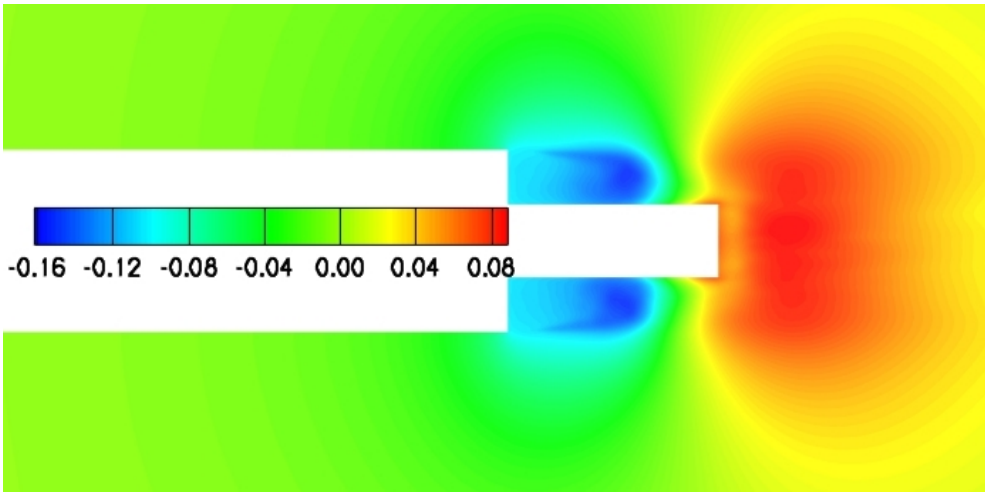

(c) SAS

Figure 4.16: Mean pressure coefficient $(\overline{P} - P_{ref})/P_{dyn}$

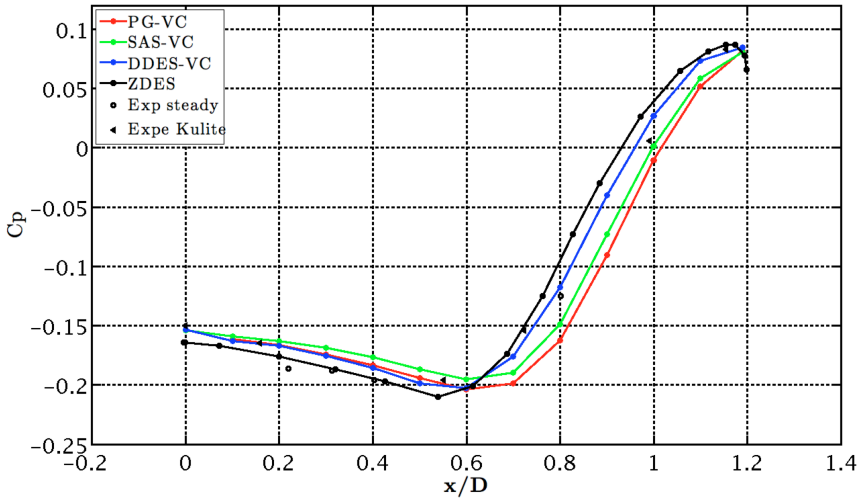

(a) Cp

Figure 4.17: Pressure coefficient on the wall in the recirculation area.

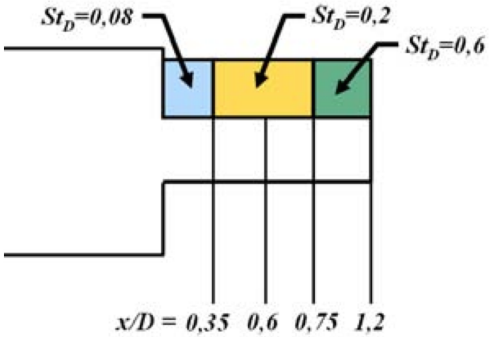

Figure 4.18: Spatial organization of dominating frequencies on antisymmetric backward facing step [20]

becomes $Str_{Lwindtunnel} = 0.96$(see figure 4.20). This is a good clue that allows us to say that this low frequency is maybe driven by the confinement $L_{windtunnel}$. We perform a calculation with PG-VC strategy in a numerical wind tunnel without confinement (where the symmetry boundaries are located very far from the body), figure 4.21 shows that the confinement amplifies the low frequency but don't make it disappear. We can conclude that the confinement and the very low frequency phenomena in the recirculation area may be coupled. In the previous section, we find that the level of Cp_{rms} with the PG-VC strategy is lower than with the other models. It can be explained by the figure 5.4 (b) which shows the energy decay of turbulence at $x/D = 0.7$ on the wall. We can see clearly the effect of the too high dissipation of the PG model: the energy is dissipated by the turbulent viscosity very early compared to DDES and SAS. We can see also that the energy with the DDES is slightly higher than with SAS. These results confirm the qualitative analysis of the previous paragraph, i.e. the fact that PG introduces more turbulent viscosity and thus captures less vortical structures and less energy.

4.3 Influence of the numerical strategy

In this section we further investigate the influence of the numerical scheme. First, the figure 4.22 shows the location of the activation of the vortex centering function ψ (see equation (3.90) page 59). We see that the numerical scheme is fully recentered in most part of the recirculation area and especially at the

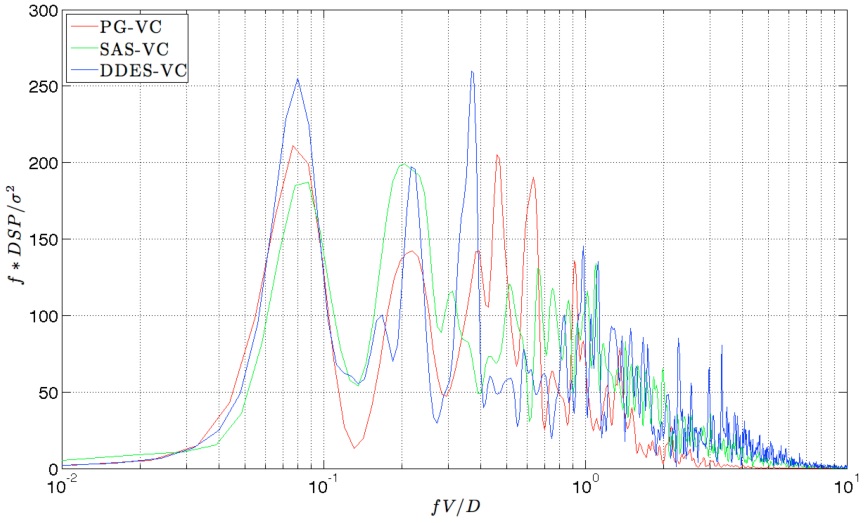

(a) semi-log

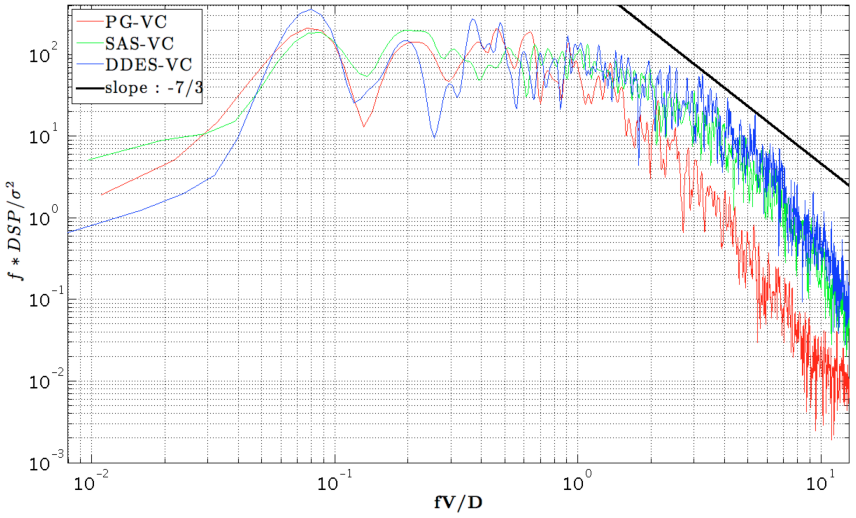

(b) log-log

Figure 4.19: PSD of pressure on three sensors along the emergency, X/D = 0.7.

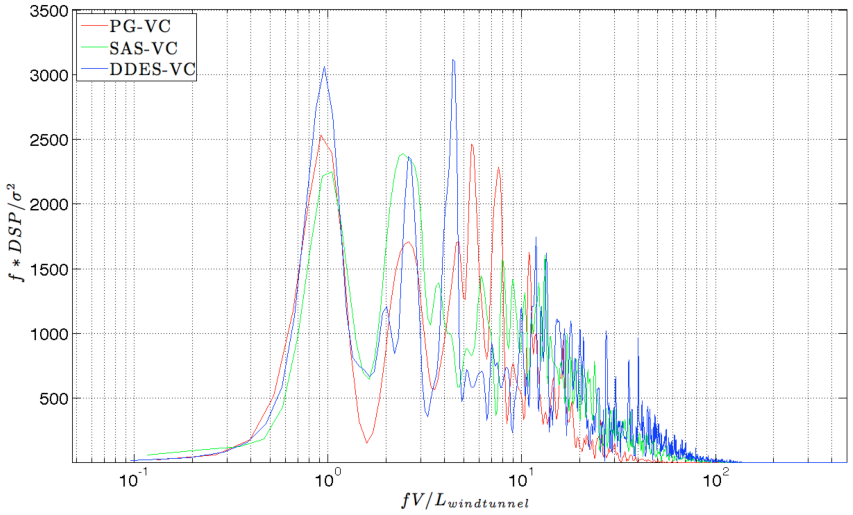

Figure 4.20: PSD of pressure on three sensors along the emergency, X/D = 0.7, normalization with the diameter of numerical wind tunnel

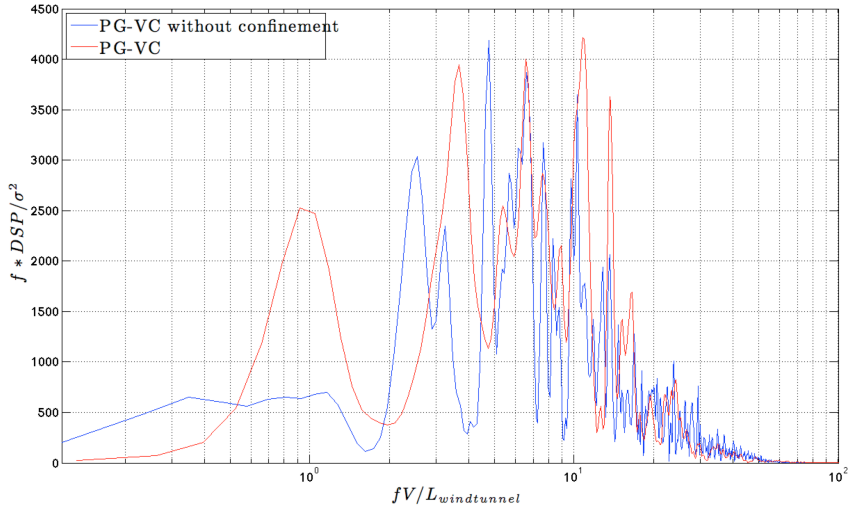

Figure 4.21: Effect of wind tunnel confinement, X/D = 1.0

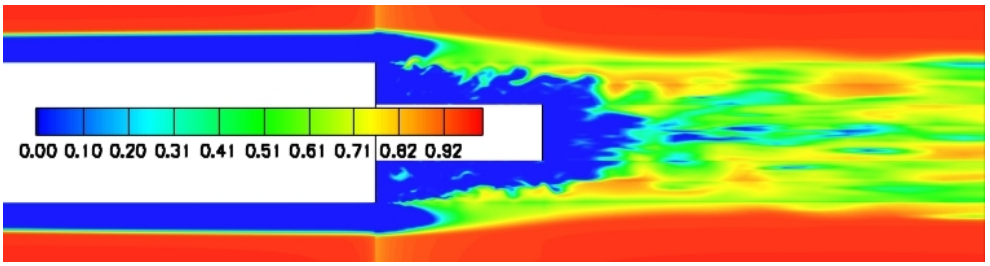

Figure 4.22: Vortex centering function ψ

beginning of the shear-layer, which helps the triggering of Kelvin-Helmholtz instabilities. In the rest of the shear-layer, the numerical scheme is partially re-centered, about 60%, which leads to a strong reduction of the dissipation (see Tab. 3.2 on 58 and Figure3.8 on page 58). Note that, the scheme is fully recentred in the azimuthal direction thanks to the recentering-by-faces technique. To be convinced by the influence of the numerical scheme, we perform a DDES calculation without the VC strategy. Figures (a,b) and (c,d) shows pressure lines and contours in the shear-layer of the axisymmetric backward facing step with and without the VC scheme respectively. We clearly see that VC scheme decreases the numerical dissipation in the recirculation area, and to allows triggering Kelvin-Helmholtz instabilities. The VC scheme allows to resolve shear-layers with a very low grid resolution. In figure 4.23, we see that the VC scheme needs less than 6 points per vortex to resolve the shear-layer. The third oder scheme without the VC improvement needs about 15 points by wavelenght to resolve vortices (see Tab. 4.1 on page 77).

4.4 Conclusions

In this Chapter, we assessed the SAS, PG and DDES approaches carrying out numerical simulations of 2D and axisymmetric backward facing steps with the VC scheme. Specifically, axisymmetric case allowed to discriminate between the models. We saw that the level of turbulent viscosity is not the same for all the models in the LES region of the flow. The DDES provided the smallest level of turbulent viscosity, which allowed to resolve smaller turbulent structures. However, the DDES does not return to the RANS mode, far from the wall, when the grid becomes very coarse after the step emergency. SAS and PG approaches, although less efficient in the LES region, seems to recover a RANS mode when a coarse grid is encountered (see 4.9 (a), (b), (c)). Finally, the VC scheme was found to be an essential ingredient not to dissipate turbulent structures generated by convective instabilities (see Figure 4.22 on page 94).

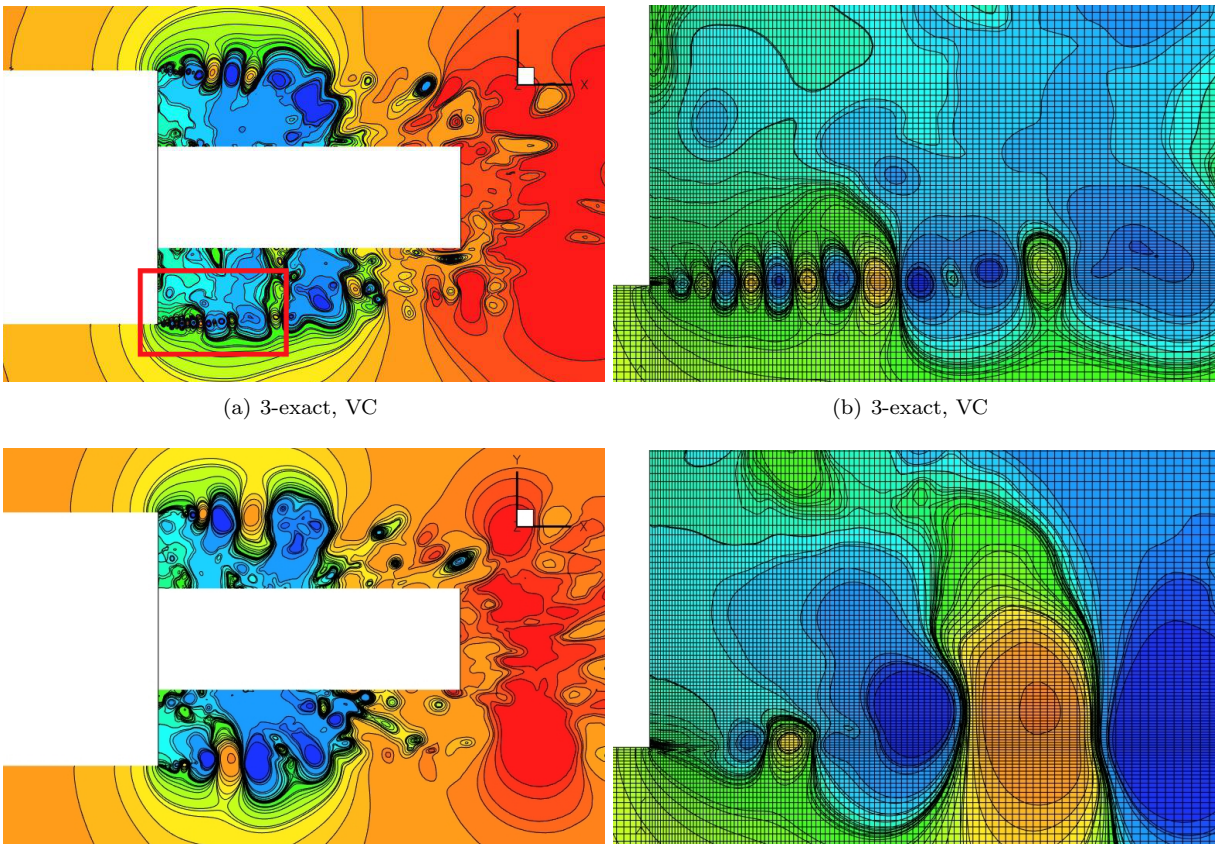

(a) 3-exact, VC

(b) 3-exact, VC

(c) 3-exact

(d) 3-exact

Figure 4.23: Visualization of the scheme resolvability in the shear-layers of axisymmetric backward facing step. Pressure lines and contours. The upwind 3-exact scheme needs more point to resolve vortices than the 3-exact VC scheme.

Chapter 5

Industrial applications

Contents

In this Section, we investigate the feasibility of the proposed HRL approach for complex industrial configurations by applying the PG model, along with the high-order vortex-centered scheme, to simulate the flow around a realistic geometry. The calculations are carried out with the PG-VC strategy.

5.1 Launcher shrinkage

The following application is 1/60 scale model of a real space launcher skrinkage. Figure 5.1 shows the overlapped grids used to discretize the computational domain. The grid is composed of several intersected grids. The resulting overall hybrid grid is composed by Cartesian patches and irregular regions composed by tetrahedral and hexahedral cells. An effort was made to generate a grid as regular as possible in the wake region. Tab. 5.2 gives some details about the calculation, especially the grid resolution next to the boundary layer separation (x^+ and y^+) and the azimutal resolution $\Delta\phi$. In the following, D and d are respectively the large and the small diameters of the launcher. The unsteady calculation is carried out over a total duration of $T * U_\infty/(D-d) = 200$ after the numerical transient. Numerical results are compared with an experiments, conducted on a very similar configuration, called "exp. K" [93].The objective is to investigate the feasibility of the PG-VC approach for an industrial configuration.
The mean flow, is presented in figure 5.2 (c). The flow separates at the shirinkage, than reattaches downstream. The reattachment point is in good agreement with the experiments (see Tab. 5.1). Figure 5.2 (a) shows the instantaneous Q criterion around the shrinkage of the launcher colored by Mach number. This figure demonstrates the interest of the strategy. The numerical scheme has to be robust and accurate at the same time. In the recirculation area for example, the heads of Kelvin-Helmholtz vortices are supersonic and can generate local compressibility effects as it can be seen on the Figure 5.2 (b), which provides a numerical Schlieren of the flow.. There is also an interaction between the shock and the boundary layer on the fairing of the launcher. For a quantitative assessment of the results, figures 5.3 (a) and (b) show respectively the evolution of mean pressure and fluctuating pressure coefficients along the shrinkage of the launcher as a function of the longitudinal axis normalized with respect to the recirculation length. We can see that both Cp and Cp_{rms} are very close to the experiment. Figure 5.4 shows the comparison between experimental data and numerical results of the pre-multiplied by the frequency pressure spectral density of pressure on the wall next to the reattachment point in the recirculation area. The simulation allows to resolve flapping and buffeting phenomena, in other words, the vortical structures responsible for aerodynamic loads. Finally, figure 5.2 (d) shows that the kinetic energy in attached boundary-layers is fully modeled while shear-layers and recirculation area are partially resolved. In these regions, the modeled kinetic energy is replaced by the resolved one.

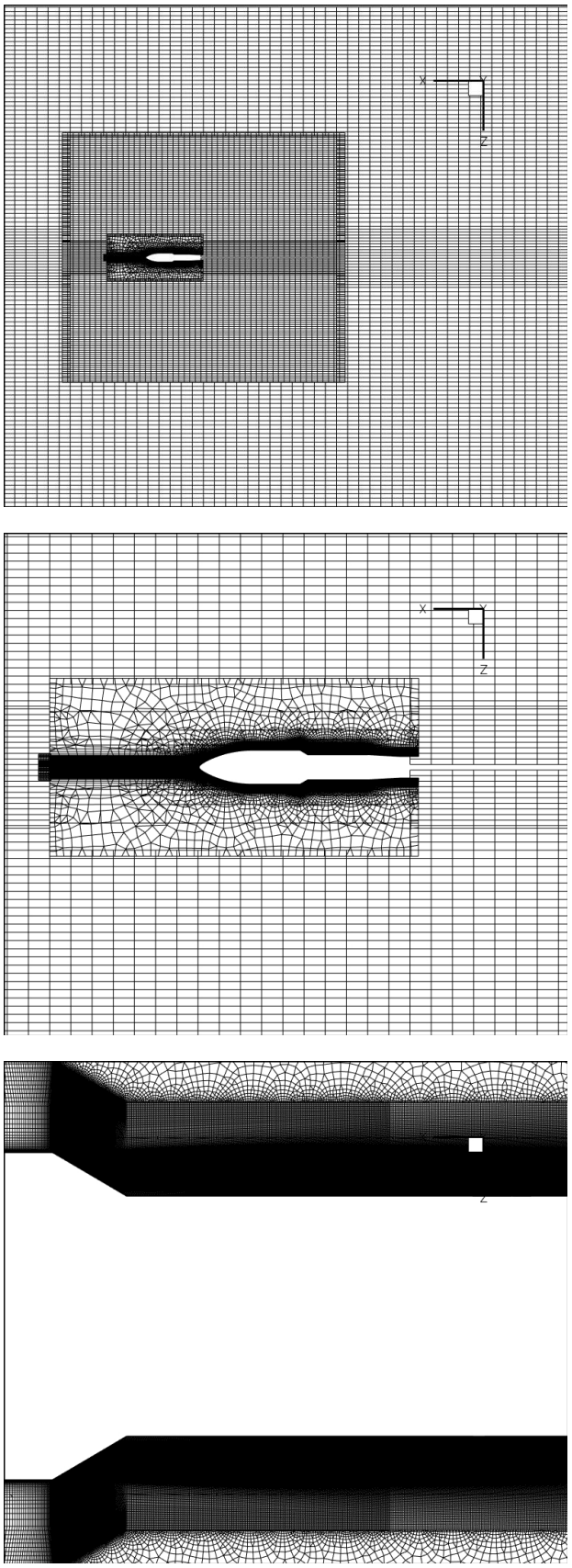

Figure 5.1: Overlapped grid on the shrinkage

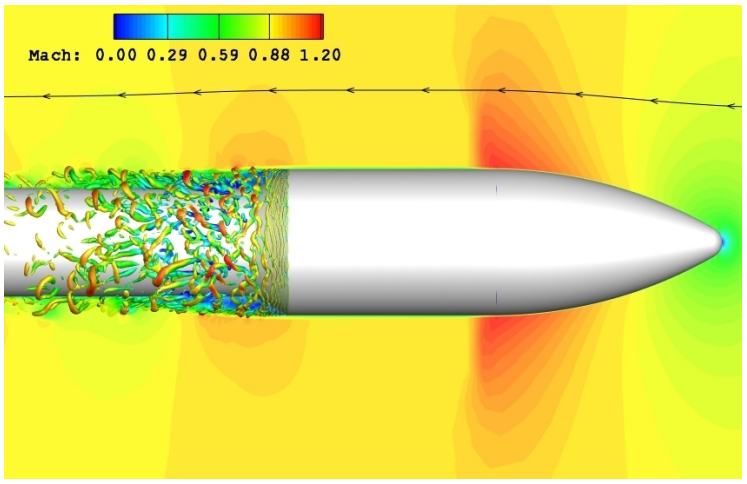

(a) Iso Q criterion colored by Mach number

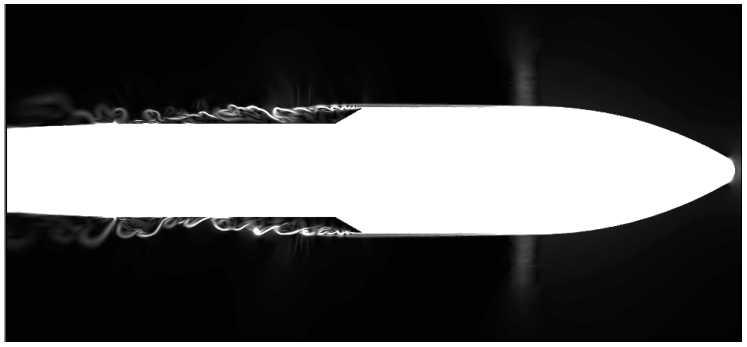

(b) Instantaneous shlieren

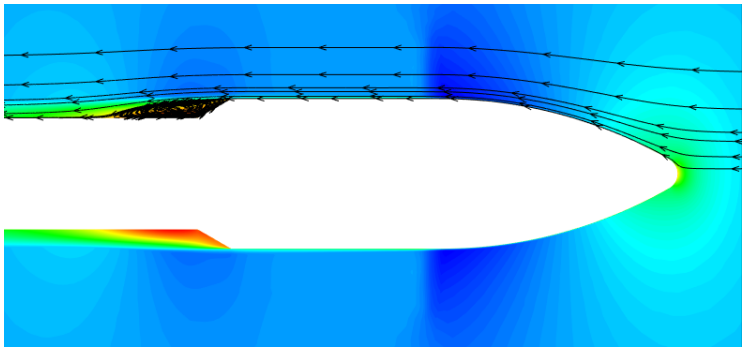

(c) Mean longitudinal velocity

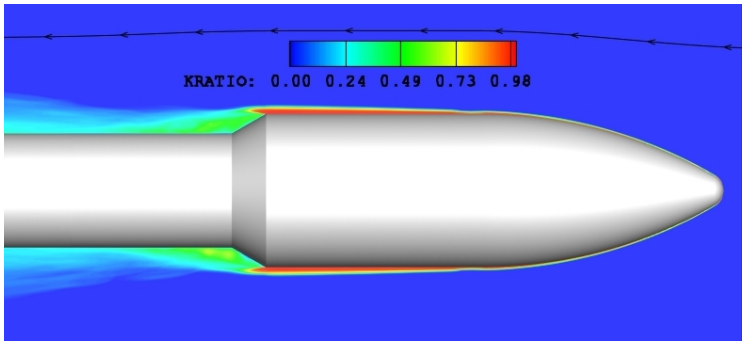

(d) Mean modeled to total kinetic energy ratio

Figure 5.2: Instantaneous and mean flow over the shrinkage.

	Present calculation	Exp. K
x_r/h	6.1	5.8

Table 5.1: reattachment length (x_r) to shrinkage ($h = (D-d)/2$) high ratio

Re_D	Cells	y^+	x^+	$\Delta\phi$
9.10^5	15M	30	50	2 deg

Table 5.2: Calculation settings

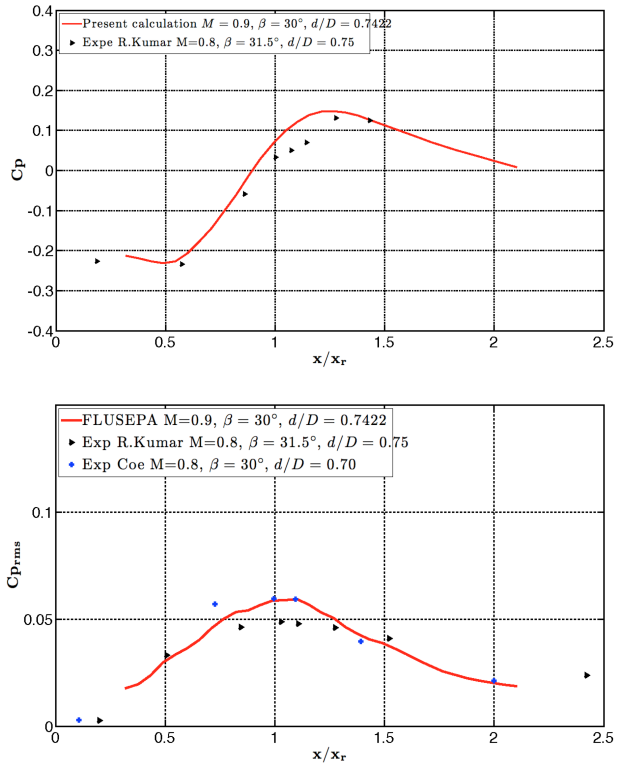

Figure 5.3: Longitudinal distribution of the average and fluctuating pressure coefficient.

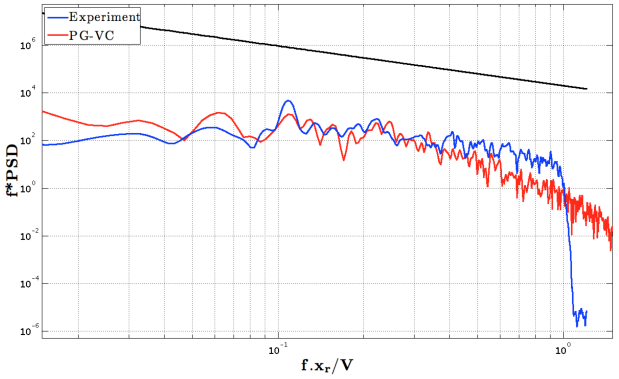

Figure 5.4: Power spectral density of a wall-pressure-sensor in the recirculation bubble as a function of Strouhal number based on recirculation length

AoA	Δt	Re	M_∞	P_0
0	$0.1\mu s$	2.10^6	0.8	66500

Table 5.3: Calculation settings

5.2 Ariane 5 launcher

The following application is 1/60 scale model of the Ariane 5 launcher. The computational mesh is presented in figure 5.5. The total number of grid elements is equal to 20 millions and the y^+ at the beginning of the separated region is 20. The azimuthal resolution equal to 2 deg.. The numerical parameters used for the calculation are given in the Tab. 5.3. The useful unsteady calculation is performed over a total duration of $T * U_\infty/H = 40$ after the numerical transient. Since this is not long enough to converge properly the statistics, so that heareafter we provide a preliminary analysis but the calculation is still running. Figure 5.7 shows that the Kelvin-Helmholtz instabilities are clearly installed and are triggered without delay. Figure 5.6 gives an overview of the instantaneous field at the base of the launcher. Figure 5.8 shows the comparison between the experiment and the calculation for pressure and fluctuating pressure coefficients in the recirculation area of the launcher. We see that there is a good agreement between the calculation and the experiment for both Cp and Cp_{rms}. Note that these results have to be considered with some caution because the calculation needs to be more statistically converged.

5.3 Conclusions

In this Chapter we demonstrated the feasibility of the PG model with the VC scheme for realistic launcher configurations. The calculations provided accurate results compare to the experiments (namely for C_p, Cp_{rms} and dominating frequencies) although the calculation on Ariane 5 launcher needs to be continued to converge the statistics properly. The same calculation with the DDES approach will be carried out in the near future, to compare the approaches.

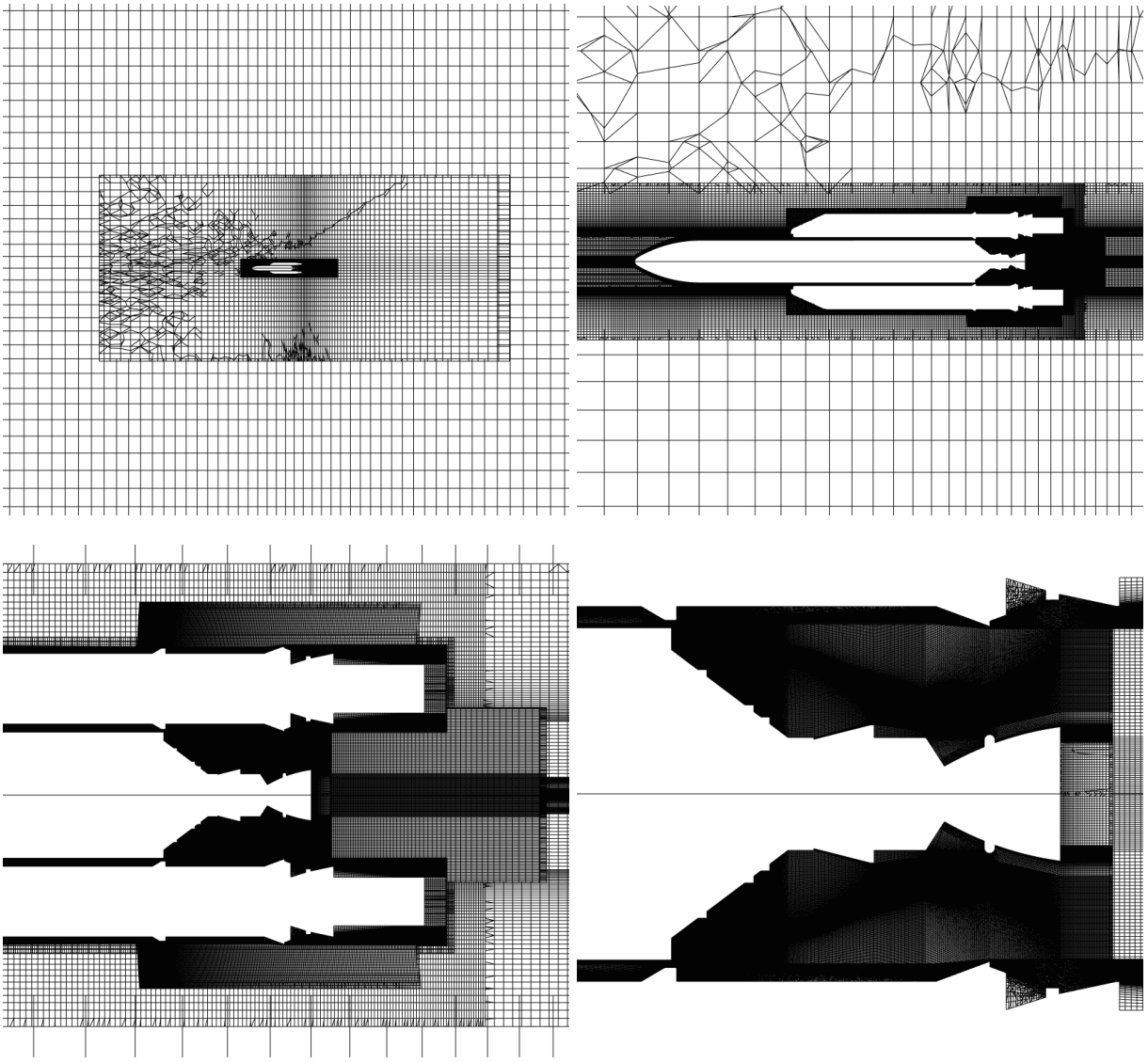

Figure 5.5: Overlapped grid on the Ariane 5 spatial launcher

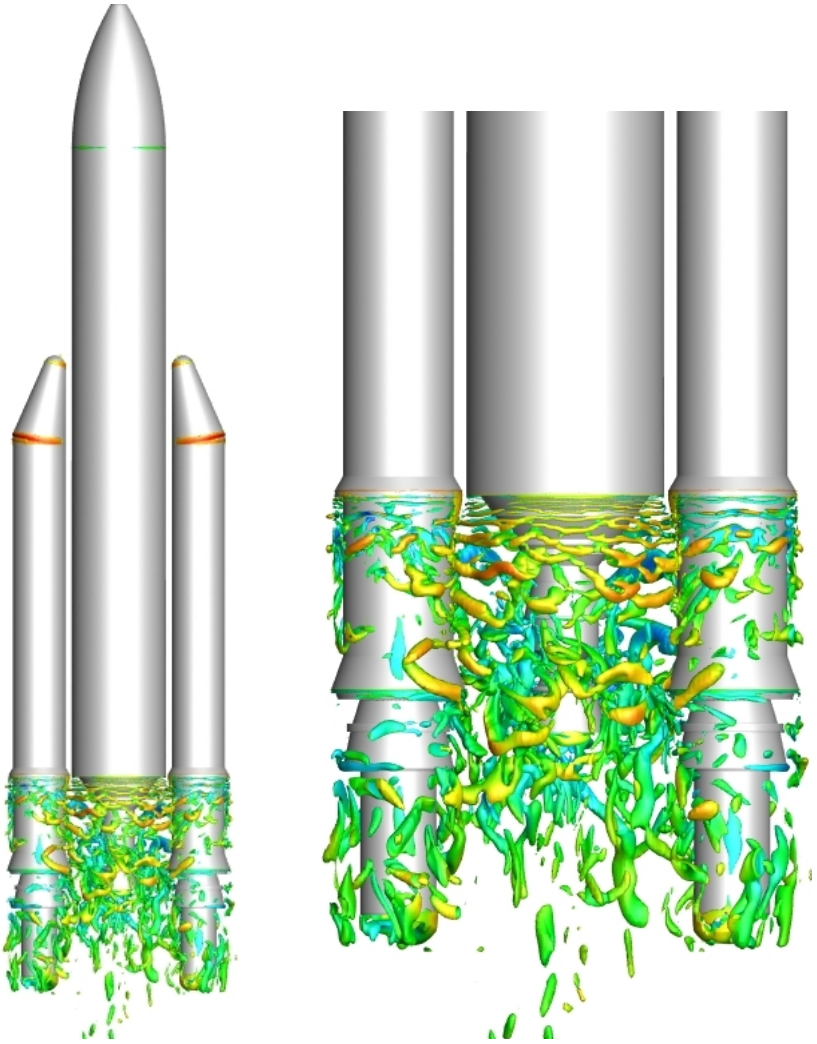

Figure 5.6: Instantaneous flow around Ariane 5 launcher. Q criterion colored by instantaneous velocity.

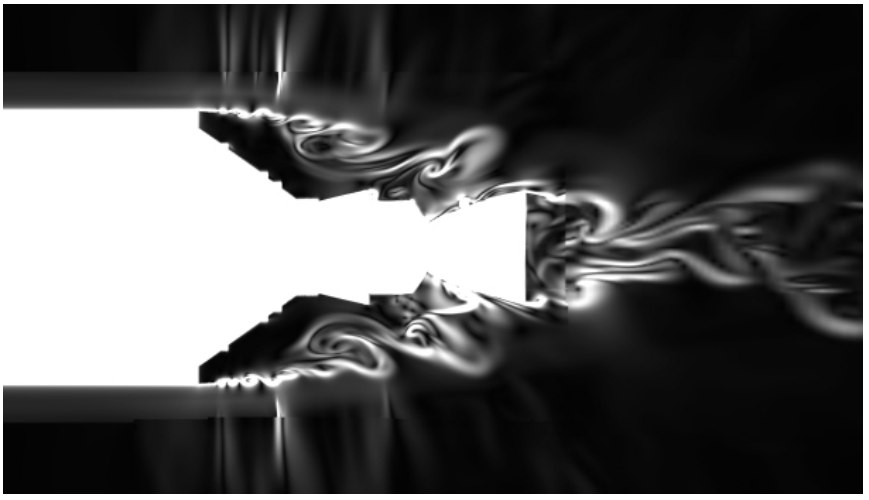

Figure 5.7: Instantaneous Schlieren around Ariane 5 launcher in the plane without boosters.

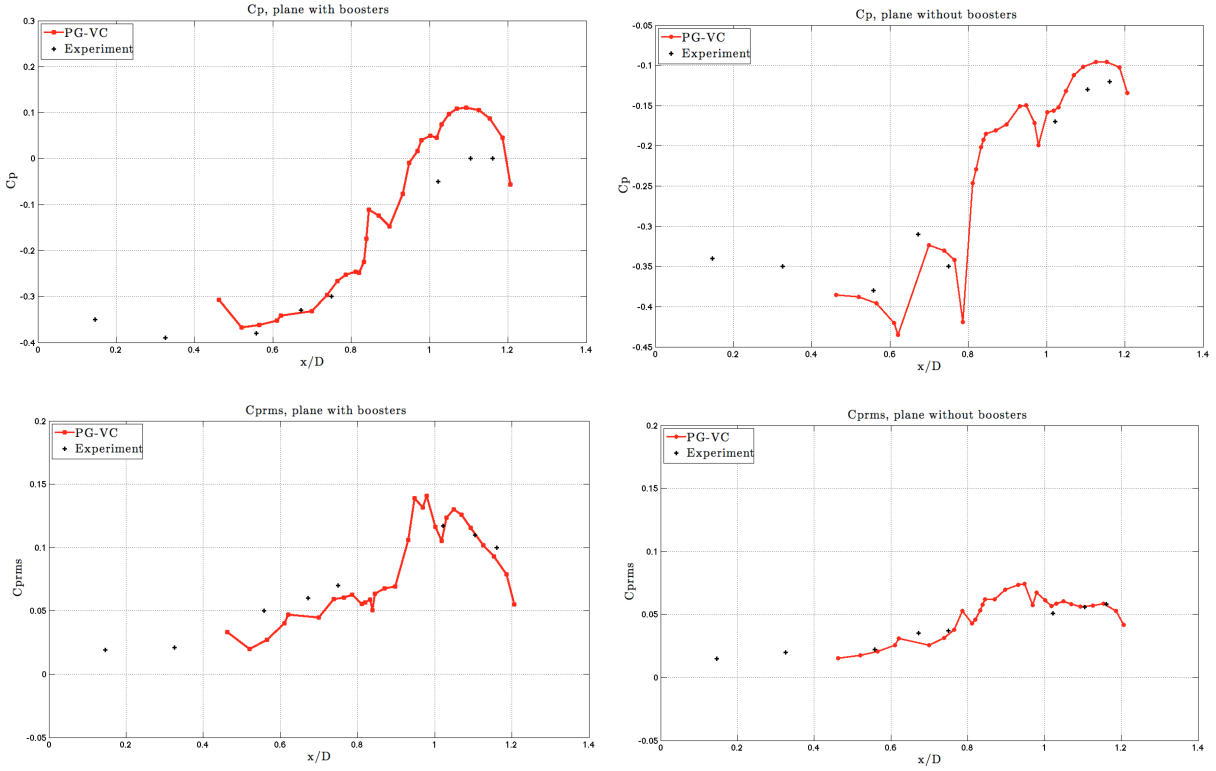

Figure 5.8: C_p and Cp_{rms} in the recirculation area.

Chapter 6

Conclusions and perspectives

Contents

6.1 Conclusions

6.1.1 Accurate low-dissipative numerical scheme

In Section 3.2 on page 41 we presented and validated a robust and accurate numerical scheme well suited for highly compressible flows allowing to resolve turbulent structures with a moderate number of grid points per wavelength. The numerical scheme keeps its formal order of accuracy regardless of the grid thanks to a k-exact reconstruction of the solution and its derivatives in each computational cell. A vortex centering strategy is used to locally reduce numerical dissipation in vortical flow regions while conserving an upwind discretization scheme in highly compressible regions.

Resolvability of the spatial discretization

A spectral analysis of the upwind k-exact schemes written for a 1D advection problem, was carried out to identify the numerical filter (dissipation and phase error) introduced by the spatial discretization as a function of the nominal order of the schemes (see 3.2.2 on page 52). The numerical results were illustrated with several numerical tests (see 3.4 on page 60) but also for more complex configurations, such as the axisymetric backward facing step. For the last applications, results of the numerical study about the scheme resolvability were recovered in terms of number of grid points required to discretize vortices generated by Kelvin-Helmholtz instabilities (see Figures 4.22 (c) and (d) in Section 4.23 on page 95).

The VC (Vortex Centered) scheme

The previous resolvability analysis drove us to conclude that, with grid resolutions typically used in industrial applications, the numerical dissipation introduced by the spatial schemes is not compatible with hybrid RANS/LES simulations.
In an attempt to reach the best possible compromise between resolvability and computational cost, we restricted our attention to the 3-exact scheme, which provides sufficiently low dispersion errors with a moderate increase in computational complexity with respect to the baseline second-order scheme, and reduced numerical dissipation in vortex-dominated regions by local re-centering of the method: the Vortex

Centered scheme. Re-centering of the numerical fluxes leads to a fourth-order accurate, non dissipative scheme in vortex-dominated regions, while keeping a 3rd-order upwind scheme in shock-dominated regions (see Section 3.3 on page 54).
The stability criterion of the VC scheme was found performing an analytical analysis on classical upwind and centered second order schemes which allowed to define a suitable recentering function (see Eq. (3.90)). The behaviour of this function has been studied in the Fourier space for the 3-exact VC scheme applied to a 1D advection-diffusion equation. This function is based on the grid Reynolds number, calculated taking into account both laminar and turbulent viscosities, which allows to realize the coupling between the numerical scheme and the turbulence model. In other words, the numerical scheme is stabilized thanks to the subgrid viscosity provided by the turbulence model in use. The number of points per wavelength prediced by the spectral analysis for a 1D advection-diffusion equation was found to be equal to the number of points necessary to discretize vortices generated in a shear layer (see Figures 4.23 (a) and (b) on page 95).
In summary, the proposed strategy represents a good compromise between accuracy and computational cost which allows to perform unsteady compressible turbulence numerical simulations.

6.1.2 Turbulence modeling

In this research, we assessed three hybrid RANS/LES models with different theorical ground the same grids and the VC scheme. We chose to carry out calculations using improved version of these models to be suitable for the departure of Kelvin-Helmholtz instabilities and boundary-layer protection. With the first test case (i.e the 2D backward facing step on Section4.1 on page 76), we cannot conclude about which model is better. The second test case, (i.e the axisymmetric backward facing step on Section4.2 on page 82), clearly discriminate the models. We list hereafter the strength and the weakness of each model.

PG model

The strength of the PG model is that it uses a local function to adapt the resolution of the model. We saw that the PG model in its original version has no difficulty in triggering Kelvin-Helmholtz instabilities in shear layers. However, there are several weakness concerning this approach due to the fact that it has been calibrated only for an isotropic decaying turbulence, and there is limited experience concerning this approach. Firstly, the calculation of the resolved kinetic energy depends on statistics, which have a little physical meaning for some flows (helicopter rotor, re-entry capsule...). Secondly, the attached boundary layer can be not easy to protect, even with the blending function f_d (see Eq. (2.33) for more details). Indeed, the recirculation bubbles can be confused with boundary-layers by the function f_d. If a computational domain is initialized with a RANS solution, the α parameter of the PG model misses a part of the recirculation bubble which remains in RANS mode.

SAS strategy

The SAS is a model that can be easily implemented in existing solvers, by adding the source therm Q_{SAS} to the transport equation of ω in the classical $k-\omega$ SST RANS model (see Eq. 2.14). However, to calculate the source term Q_{SAS}, we need the second derivative of the velocity. On arbitrary meshes, the second derivative has to be at least first order accurate (consistency condition). Thanks to the successive corrections algorithm we presented in Section 3.2.1 on page 48, the consistency of the second derivative is ensured regardless of the grid. Another remark is that the SAS strategy is fully automatic and ensures a good protection of the attached boundary-layers, however, without the Benyoucef correction, the model is unable to trigger Kelvin-Helmholtz instabilities. Even with this correction, we saw a delay in the triggering of such convective instabilities for the axisymmetric backward facing step (see Section 4.2 on page 82). Concerning the philosophy of the model itself, the subgrid viscosity is not imposed as a LES one, it is just a lower bound for the $L_{\nu K}$ length scale. The model can be seen as a improved URANS model instead of a hybrid RANS/LES model because we found that, in the LES part of the flow, the lower bound for the subgrid viscosity is not reached (see Figure 4.9 (c)). The lower bound that we consider for ν_t is reached by the DDES approach (see Figure 4.9 (d)).

DDES approach

Similarly to the SAS strategy, the DDES is quite simple to implement in a solver. The user has to replace the $\tilde{d}$ in the transport equation of the Spalart-Almaras model, with a new length scale, for instance the one defined in eq. (2.35). The model is fully automatic and allows to preserve the RANS mode in attached boundary-layers. We do not observe trigger delay for the Kelvin-Helmholtz instabilities using the DDES approach improved by the hybrid length scale Δ_ω (see Eq. 2.35). However, we can underline that, the DDES approach does not recover a RANS mode far from the wall, even if the grid resolution cannot support a LES solution. For example, regarding the eddy viscosity contours on Figure 4.9, we see that downstream the axisymmetric step, SAS and PG approach recover a RANS mode and the eddy viscosity increases where the grid is not fine enough to support an LES solution. The eddy viscosity provided by DDES remains in the LES mode, the turbulence is quickly diffused by the lack of grid point. Note that this issue has no influence in the applications we have done in this research.

This approach, coupled with the VC scheme seems to be the winning couple for our industrial applications since this strategy is accurate and needs no user intervention. We retain for the time being this solution, nevertheless, future research will concern the interaction between supersonic jet and turbulence with re-burning phenomena, where several length scales of several chemical spaces coexist. For an aerothermals applications, a one equation subgrid model might not be accurate enough. This is why we plan to assess a future version of DDES based on the RANS $k-\sqrt{k}L$ model (remember that $\sqrt{k}L \propto \nu_t$) which allows to add a transport equation for the modeled kinetic energy.

6.1.3 Industrial applications

We performed two calculations on real space launcher geometries (wind tunnel models) using the PG model and the VC scheme. The launcher shrinkage numerical simulation provided a good prediction of mean and fluctuating pressure coefficient compared to the experiments. The buffeting frequency is also properly recovered and in good agreement with the experiment. Concerning the Ariane 5 simulation, preliminary results showed a good agreement with experiment regarding mean and fluctuating pressure coefficient but the calculation needs to be continued in order to properly converge the statistics.
The same calculations using the DDES are running in order to compare the two approaches.

6.2 Perspectives

The present research allows us to perform unsteady turbulence calculations on wind tunnel models. Remember that the FLUSEPA solver is able to perform full scale URANS simulations (see Section 3.1 on page 37). The next step is logically to perform hybrid RANS/LES on full scale geometries of launchers. The major issue is that, to get the same level of turbulence as we resolve on wind tunnel model, the number of grid cells needed beyond current computering capabilities since the increasing of the Reynolds number, even with the multi-overlapping method we use. We have to find a solution to overcome this issue.

The first solution is to use automatic mesh adaptation (a PhD is currently is underway). This strategy allows to have good grid resolution only in regions dominated by vortical structures and to have the best grid as possible on the shock waves. Unsteady mesh adaptation is consistent with hybrid RANS/LES simulations, especially when the both techniques use the same kind of sensors to increase their resolution. The sensors in RANS/LES and mesh adaptation are often very close, for example, the error estimator α of the Perot & Gadebush turbulence model is originally an error estimator for mesh adaptation[41]. It belongs to the family of sensors based on the comparison between resolved and modeled kinetic energy, (i.e the work of Probst and Reuss [94]).
Other mesh adaptation techniques are based on the numerical error estimation. For instance, Mesri *et al.* propose a grid adaptation based on the calculation the Hessian and the gradient of the pressure to estimate the numerical errors concerning a finite element solver. This philosophy is very close to the SAS model of Menter, where the adaptation (on the model point of view) sensor is based on the Hessian and the gradient of velocity.

Finally, we remember that the VC scheme is stabilized thanks to the grid Reynolds number (see Eq. 3.90), which allows to realize the coupling between the numerics and the models. Indeed, this strategy provides the link between numerics, models and unsteady meshes, automatically. However, automatic mesh adaptation may move away the hypothesis we have done concerning the extra terms ($\mathcal{A} = \mathcal{B} = 0$, see Section 1.2 on page 14 for more details).

The second solution is to increase the performances and the scalability of FLUSEPA, another PhD is underway concerning the HPC issues. Performance analysis were carried out in order to highlight the bottlenecks of the algorithms, notably on an Ariane 5 lift-off and on Ariane 5 EAP separation simulations. Expressing more precisely the parallelism by a fine grain task graph approach and exploiting it by a runtime system is currently under evaluation.

List of Figures

Bibliography

[1] P. brenner and M. Pollet. Highly unsteady flows about bodies in relative motion. In *3AF, Toulouse*, 2005.

[2] NASA. Shadowgraph images of re-entry vehicles. 1960. GPN-2000-001938.

[3] S.D. Hall, M.Behinia, C.A.J. Fetcher, and G.L. Morrison. Investigation of the secondary corner vortex in a benchmark turbulent backward-facing step using cross-correlation particle imaging velocimetry. *Experiments in FLuids*, 35:139–151, 2003.

[4] J. Kostas, J. Soria, and M.S. Chong. Particle image velocimetry measurement of a backward-facing step flow. *Experiments in Fuids*, 33:838–853, 2002.

[5] I. Lee and J. Sung. Characteristics of wall pressure fluctuations in separated and reattaching flows over a backward facing step: Part 1. *Experiments in Fluids*, 30:262–272, 2001.

[6] P. G. Spazzini, G. Luso, M. OnoM. Onorato. Zurlo, and G.M. Di Cicca. Unsteady behavior of back-facing step. *Experiments in Fluids*, 2001.

[7] P. Moreau, J. Labbé, F.Dupoirieux, and R.Borghi. Experimental and numerical study of a turbulent recirculation zone with combustion. *Turbulent Shear Flows*, 5:337–346, 1987.

[8] P.R Spalart, W.-H Jou, M. Strelets, and S.R. Allmaras. Comments on the feasibility of les for wings and on the hybrid rans/les approach. In *Advances in DNS/LES, Proceedings of the First AFOSR International Conference on DNS/LES*, 1997.

[9] B. Sainte-Rose, N. Bertier, and S. Deck. Dupoirieux. A DES method applied to a backward facing step reactive flow. *Combustion for aerospace propulsion*, 337:340–351, 2009.

[10] S. Deck. Recent improvement in the Zonal Detached Eddy Simulation (ZDES) formulation. *Theorical and Computational FLuid Dynamics*, 26:523–550, 2011.

[11] H. Le, L.vitz Moin P. Moin, and John Kim. Direct numerical simulation of turbulent flow over a backward-facing step. *Journal of Fluid Mechanics*, 1997.

[12] D.M. Driver, H. Lee Seegmiller, and J.G. Marvin. Time-dependant behavior of a reattaching shear layer. *AIAA Journal*, 25:345356, 1985.

[13] T.R.Troutt, B. Scheelke, and T.R. Norman. Organizes structures in a reattaching separated flow filed. *Journal of Fluid Mechanics*, 143:413–427, 1984.

[14] K. Sasaki and M. Kiya. Three-dimensional vortex structure in a leading-edge separation bubble at moderate reynolds numbers. *Journal of Fluid Engineering*, 113:405–410, 1991.

[15] D. Deprés, P. Reijasse, and P. Dussauge. Analysis of unsteadiness in after-body transonic flows. *AIAA Journal*, 2004.

[16] P.Meliga and P.Reijasse. Unsteady transonic flow behind an axisymmetric afterbody with two boosters. *Proceedings of the 25th AIAA Applied Aerodynamics Conference,*, Paper No.2007-4564, Miami, 2007.

[17] Pierre-Elie Weiss. *Simulation numérique et analyse physique d'un écoulement d'arrière-corps axisymétrique et application au contrôle des charges latérales.* PhD thesis, Université Pierre et Marie Curie, 2010.

[18] S.C. Morris and J.F Foss. Turbulent boundary layer to single-stream shear layer: the transition region. *Journal of Fluid Mechanics*, 187-221(495), 2003.

[19] D.E. Abbott and S. J. Kline. Experimental investigation of subsonic turbulent flow over single and double backward facing steps. *Journal of Basic engineering*, 317325, 1962.

[20] P.E. Weiss, S. Deck, J.C. Robinet, and P. Sagaut. On the dynamics of axisymmetric turbulent separating/reattaching flows. *Physics of Fluids*, 21, 2009.

[21] M. Marie, S. Deck, and P.E.Weiss. From pressure fluctuations to dynamics loads on axisymetric strep flow with minimal number of kilites. *Computers and Fluid*, 1222, 2009.

[22] S.Deck and P.Torigny. Unsteadiness of an axisymmetric separating-reattaching flow. *Physics of Fluids*, 19:065103, 2007.

[23] H. Tennekes and J. Lumley. *A first course in turbulence.* The MIT press, 1972.

[24] Jean Lemay. *Turbulence, cours GMC-7020.* Université Laval, Quebec.

[25] Joseph Smagorinsky. General circulation experiments with the primitive equations. *Monthly Weather Review*, 91 (3):99–163, 1963.

[26] D. Drikakis. Advances in turbulent flow computations using high-resolution methods. *Progress in Aerospace Sciences*, 39:412–424, 2003.

[27] Eric Garnier, Michelle Mossi, Pierre Sagaut, Pierre Comte, and Michel Deville. On the use of shock-capturing schemes for large-eddy-simulation. *Journal of computational Physics*, 153:273–311, 1999.

[28] George D. Birkhoff. Proof of the ergodic theorem. *Department of Mathematics, Harvard University, NAS*, 1931.

[29] David C.Wilcox. *Turbulence Modelling For CFD.* DCW industries, 2006.

[30] J. V. Boussinesq. *Essai sur la théorie des eaux courantes.* Académie des Sciences de Paris, XXVIII, 1877., 1877.

[31] M. Germano. From LES to RANS : Towards a bridging model. *Direct and Large-Eddy Simulation III*, ERCOFTAC Series Volume 7:225–236, 1999.

[32] Randolph P. Lillard, Michael E. Olsen, Gregory A. Blaisdell, and Anastasios S. Lyrintzis. The lagRST model: a turbulence model for non-equilibrium flows. *AIAA Journal*, 2011.

[33] F. Hamba. Analysis of filtered Navier-Stokes equation for hybrid RANS/LES. *Physics of Fluids*, 17:(1–12), 2011.

[34] M. Germano. Properties of the hybrids RANS/LES filter. *Theorical and computational fluid dynamics*, 17:(225–231), 2004.

[35] M. Sanchez-Rocha and S. Menon. The compressible hybrid RANS/LES forulation using an additive operator. *Physics of Fluids*, 228:(2037–2062), 2008.

[36] Ivan Mary and Pierre Sagaut. Flow around a high-lift airfoil using les. *AIAA Journal*, 40(6):1139–1145, 2002.

[37] Emmanuel Labourasse and Pierre Sagaut. Reconstruction of turbulent fluctuations using a hybrid rans/les approach. *Journal of computational Physics*, 182(1):301–336, 2002.

[38] P. R. Spalart. Detached eddy simulation. *Annual Review of Fluid Mechanics*, 41:181–202, 2009.

[39] S. Deck and R. Laraufie. Numerical investigation of the flow dynamics past a three-element aerofoil. *Journal of Fluid Mechanics*, 732:401–444, 2013.

[40] Sharath S.Girimaji. Partially-averaged navier-stokes model for turbulence:a reynolds-averaged navier-stokes to direct numerical simulation bridging method. *Journal of Applied Mechanics*, 73:413–421, 2006.

[41] J.Blair Perot and Jason Gadebush. A self-adapting turbulence model for flow simulation at any mesh resolution. *Physics of Fluids*, 19:1–11, 2007.

[42] F.R Menter and Y. Egorov. The scale-adaptative simulation method for unsteady turbulent flow predictions. part 1 : Theory and model description. *Flow Turbulence Combust*, 25:85:113–138, 2010.

[43] Bruno Chaouat and Roland Schiestel. From single-scale turbulence models to multiple-scale and subgrid scale models buy fourier transform. *Theorical and Computational FLuid Dynamics*, pages 1–29, 2006.

[44] F.R Menter, Y. Egorov, and D.Rusch. Steady and unsteady flow modelling using the k-$\sqrt{k}$l model. *Turbulence, Heat and Mass Transfer 5*, 20:1–6, 2006.

[45] P.R Spalart, S. Deck, S. Shur, M. Squires, M. Strelets, and A. Travin. A new version of detached-eddy simulation, resistant to ambiguous grid densities. *Theorical and Computational FLuid Dynamics*, 20:181–195, 2006.

[46] F.R Menter and Y. Egorov. Scale-adaptive simulation and zonal forcing. In *ANSYS*, 2012.

[47] F. Menter et al. Scale-adaptive simulation with artificial forcing. *Progress in Hybrid RANS/LES Modelling*, pages 235–246, 2010.

[48] J.C. Rotta. über eine methode zur berechnung turbulenter scherströmungen. *aerodynamische Versuchsanstalt Gttingen*, Rep. 69 A14, 1968.

[49] Farid Benyoucef. *Amélioration de la prévision des écoulement turbulents par une approche URANS avancée*. PhD thesis, Université de Toulouse, 2013.

[50] P.R Spalart and S.R. Allmaras. A one-equation turbulence model for aerodynamic flows. *Recherche Aerospatiale*, 1:5–21, 1994.

[51] S. Catris and B. Aupoix. Density corrections for turbulence models. *Aerospace Science Technologies*, 4:1–11, 2000.

[52] Sharath S. Girimaji and Khaled S.Abdol-Hamid. Partially-averaged navier-stokes model for turbulence: Implementation and validation. *AIAA*, 14:1–14, 2005.

[53] N. Chauvet, S. Deck, and L. Jacquin. Zonal-detached-eddy simulation of a controlled propulsive jet. *AIAA Journal*, 45(10):2458–2473, 2007.

[54] W. Jones and B. Launder. The prediction of the laminarization with a two- equation model of turbulence. *International Journal of Heat and Mass Transfer*, 15:301–304, 1972.

[55] B. Launder and D. Spalding. Application of the energy-dissipation model of turbulence to the calculation of flow near a spinning disc. *Letters in Heat and Mass Transfer*, 1:131–138, 1974.

[56] U. Schumann. Realisability of Reynolds stress turbulence models. *Physics of Fluids*, 20:721–725, 1972.

[57] R. du Vachat. Realisability inequalities in turbulent flows. *Physics of Fluids*, 20:551–556, 1977.

[58] K. Sinha, K. Mahesh, G. Graham, and V. Candler. Modeling shock unsteadiness in shock turbulent interaction. *Physics of Fluids*, 15(8), 2003.

[59] K. Malesh, S.K. Lele, and P. Moin. The influence of entropy fluctuations on the interaction of turbulence with a shock wave. *Journal of Fluid Mechanics*, 334(353), 1997.

[60] S. Lee, S.K. Lele, and P. Moin. Interaction of isotropic turbulence with shock waves; effect of shock strength. *Journal of Fluid Mechanics*, 340(225), 1997.

[61] K. Malk Malesh, S. Lee, S.K. Lele, and P. Moin. The interaction of an isotropic filed of acoustic waves with a shock wave. *Journal of Fluid Mechanics*, 300(383), 1995.

[62] F.R. Menter. Zonal two equation $k-\omega$ turbulence models for aerodynamic flows. *AIAA*, 93-2906, 1993.

[63] B. van Leer. Towards the ultimate conservative difference scheme. v. a second-order sequel to godunov's method. *Journal of Computational Physics*, 32:101–136, 1979.

[64] Pierre Brenner. Race to accuracy: Finite volume formulation still in the game. Technical report, Airbus Defense & Space, internal report, 2008.

[65] G. Monge. *Géométrie Descriptive*. PARIS, BAUDOUIN, Imprimeur du Corps législatif et de linstitut national, AN VII (1799)., 1799.

[66] Pierre Brenner. Three dimensional aerodynamics with moving bodies applied to solid propellant. *27th Joint Propulsion Conference, Sacramento, USA*, 1991.

[67] Pierre Brenner. Simulation du mouvement relatif de corps soumis a un écoulement instationnaire par une méthode de chavauchement de maillage. In *AGARD conference proceedings 578 : Progress and challenges in CFD methods and Algotithms, Seville, Spain*, 1995.

[68] Pierre Brenner. A conservative overlapped grid method to simulate tocket stage separation. In *3rd symposium on overset composite grid and solution technology, Los Alamos*, 1996.

[69] T.J. Barth. Recent developments in high order k-exact reconstruction on unstructured meshes. In *Reno, AIAA-93-0668*, 1993.

[70] F. Haider, P. Brenner, B. Courbet, and J. P. Croisille. Efficient implementation of high order reconstruction in finite volume methods. *Finite Volumes for Complex Application VI-Problem & Perspectives, Springer Proceedings in Mathematics*, 4:553–560, 2011.

[71] Pierre Brenner. Unsteady flows about bodies in relative motion. *1st AFOSR Conference on Dynamic Motion CFD Proceedings, Rutgers University, New Jersey, USA,*, 1996.

[72] H.Q. Yang, Z.J. Chen, Andrzej Przekwas, and Jonathan Dudley. A high-order cfd method using successive differentiation. *Journal of Computational Physics*, 281:690707, 2015.

[73] D. Caraeni and D.C. Hill. Efficient 3rd-order finite-volume discretization using iterative quadratic data reconstruction on unstructured grids. Technical report, AIAA Paper 2009-1332, 2009.

[74] E. Shima, K.Kitamura, and T. Haga. Greengauss/weighted-least-squares hybrid gradient reconstruction for arbitrary polyhedra unstructured grids. Technical report, AIAA JOURNAL, 2013.

[75] F. Haider. *Discrétisation en maillage non structuré général et application LES*. PhD thesis, UPMC, 2009.

[76] Richard A. Gentry, Robert E. Martin, and Bart J. Daly. An Eulerian differencing method for unsteady compressible flow problems. *Journal of computational Physics*, 1:87–118, 1966.

[77] A. Travin, M. Shur, M. Strelets, and P.R. Spalart. Physical and numerical upgrades in the detached-eddy simulation of complex turbulent flows. In R. Friedrich and W. Rodi, editors, *Advances in* LES *of Complex Flows*, volume 65 of *Fluid Mechanics and Its Applications*, pages 239–254. Springer Netherlands, 2002.

[78] G. Aubard, P. Stefanin Volpiani, X. Gloerfelt, and J.-C. Robinet. Comparison of subgrid-scale viscosity models and selective filtering strategy for large-eddy simulations. *FTC*, 91(3):497–518, 2013.

[79] F.Ducros, V.Ferrand, F.Nicoud, C.Weber, and D.Darracq. Large eddy simulation of the shock/turbulence interaction. *Journal of Computational Physics*, 152:517–549, 1999.

[80] F. Ringleb. Exakte losungen der differentialgleichungen einer adiabatischen gasstromung. *Journal of Applied Mathematics and Mechanics*, 20:185–198, 1940.

[81] H. Lamb. *Hydrodynamics*. Dover, 1932.

[82] CW. Shu. Essentially non-oscillatiory and weighted eseentially non-oscillatory schemes for hyperbolic consevation laws. *ICASE Report*, 97:65, 1997.

[83] D. Fauconnier, C. Bogey, and E. Dick. On the performance of relaxation filtering for large-eddy simulation. *Journal of Turbulence*, 14(1):22–49, 2013.

[84] M. E. Brachet, D. Meiron, S. Orszag, B. Nickel, R. Morf, and U. Frisch. The Taylor-Green vortex and fully developed turbulence. *Journal of Statistical Physics*, 34(5-6):1049–1063, 1984.

[85] Stefan Hickel, Nikolaus A. Adams, and J. Andrzej Domaradzki. An adaptative local deconvolution method for implicit les. *Journal of Computational Physics*, 213:413–436, 2006.

[86] M. Lance and J. Bataille. Turbulence in the liquid phase of a bubble air-water flow. *Advances in Two-Phase Flow and Heat Transfer, NATO ASI Series*, 63:403–427, 1983.

[87] T. Nakagawa. Vortex shedding behind a square cylinder in transonic flows. *Journal of Fluid Mechanics*, 178:303–323, 1987.

[88] A Prasard and Charles H. K. Williamson. The instability of the shear layer separating from a bluff body. *Journal of fluid mechanics*, 333:375–402, 1996.

[89] E. Goncalves and R. Houdeville. Reassessment of the wall functions approcah for RANS computation. *Aerospace science and Technologie*, 5:114, 2000.

[90] G. Pont, P. Cinnella, J-C. Robinet, and Pierre Brenner. Development of numerical schemes for hybrid rans/les modelling in an industrial cfd solver. In *AIAA Conference*, 2013.

[91] Hung Le, Pravitz Moin, and John Kim. Direct simulation of turbulent flow over a backward facing step. *Journal of Fluid Mechanics*, 2374:330–2349, 1997.

[92] T.H H L. *Etude expérimentale du couplage entre l' écoulement transonique d'arrière-corps et les charges latérales dans les tuyères propulsives*. PhD thesis, Universit de Poitier, 2005.

[93] R. Kumar and P.R Viswanath. Mean and fluctuating pressure in boat-tail separated flows at transonic speeds. *Journal of Spacecraft and Rockets*, 39:430–438, 2002.

[94] Axel Probst, Tobias Knopp, Sylvia Reuss, and Matthias Orlt. Assessment of local les-resolution sensors for hybrid rans/les simulations. In *5th Symposium on Hybrid RANS-LES Methods*, 2014.

[95] Second international workshop on high-order cfd methods. *http://www.dlr.de/as/desktopdefault.aspx/tabid-8170/13999_read-35550/*.

Chapter 7

Relation between $\overline{\mathbf{q}}$ and $\widetilde{\mathbf{q}}$

In this appendix we derive expressions relating average values of the primitive variables over one cell, $\overline{\mathbf{q}}_J$, to the average of conservative variables, via vector $\widetilde{\mathbf{q}}_J$, *i.e* equation (3.48). These expressions have to be derived independently for each component of $\overline{\mathbf{q}}_J$.

A Relation for the average velocity $\overline{\mathbf{u}}_J$

For the velocity, equation (3.46) writes :

$$\overline{\mathbf{u}}_J = \mathbf{u}_j + \sum_{m=2}^{n-1} \frac{1}{m!} \mathcal{M}_J^{(m)} : \mathbf{D}^{(m)}\mathbf{u}\Big|_j + \mathcal{O}(h^n) \tag{7.1}$$

On the other hand, average values of the conservative variables can be combined to compute :

$$\widetilde{\mathbf{u}}_J = \frac{\overline{\rho\mathbf{u}}_J}{\overline{\rho}_J} \tag{7.2}$$

Average values of ρ and $\overline{\rho\mathbf{u}}$ can also be expanded by using a relation similar to (3.46). Pluggin into (7.2) leads to :

$$\widetilde{\mathbf{u}}_J = \mathbf{u}_j - \frac{\mathbf{u}_j}{\overline{\rho}_J} \sum_{m=2}^{n-1} \frac{1}{m!} \mathcal{M}_J^{(m)} : \mathbf{D}^{(m)}\rho\Big|_j + \frac{1}{\overline{\rho}_J} \sum_{m=2}^{n-1} \frac{1}{m!} \mathcal{M}_J^{(m)} : \mathbf{D}^{(m)}\rho\mathbf{u}\Big|_j + \mathcal{O}(h^n) \tag{7.3}$$

Subtracting (7.3) from (7.1) and after some algebra, we get :

$$\overline{\mathbf{u}}_J - \widetilde{\mathbf{u}}_J = \Delta\mathbf{u}^{m-2} - \frac{1}{\overline{\rho}_J} \mathcal{M}_J^{(m-1)} : \left(\sum_{l=1}^{n-2} \binom{n-1}{l} \mathbf{D}^{(m-1-l)}\rho\Big|_j \otimes \mathbf{D}^{(l)}\mathbf{u}\Big|_j \right) + \mathcal{O}(h^n) \tag{7.4}$$

with :

$$\Delta\mathbf{u}^{m-2} = -\frac{1}{\overline{\rho}_J} \left\{ \sum_{m=2}^{n-2} \frac{1}{m!} \mathcal{M}_J^{(m)} : \left(\sum_{l=0}^{m} \binom{m}{l} \mathbf{D}^{(m-l)}\rho\Big|_j \otimes \mathbf{D}^{(l)}\mathbf{u}\Big|_j - \overline{\mathbf{u}}_j \, \mathbf{D}^{(m)}\rho\Big|_j - \overline{\rho}_J \, \mathbf{D}^{(m)}\mathbf{u}\Big|_j \right) \right\} \tag{7.5}$$

Note that density gradients $\mathbf{D}^{(m)}\rho\big|_j$ do not need to be reconstructed, since they can be recast in terms of pressure and temperature by using the equation of state :

$$\rho = \frac{P}{RT}$$

and

$$\mathbf{D}^{(m)}\rho\Big|_j = \frac{1}{R}\sum_{l=0}^{m}\binom{m}{l}\mathbf{D}^{(m-l)}P\Big|_j \otimes \mathbf{D}^{(m)}T^{-1}\Big|_j \tag{7.6}$$

$$= \frac{1}{R}\sum_{l=0}^{m}\binom{m}{l}\mathbf{D}^{(m-l)}P\Big|_j \otimes \left[(-1)^l l! T_j^{-(l+1)}\,\mathbf{D}^{(m)}T\Big|_j\right] \tag{7.7}$$

For a 3-exact reconstruction, $\Delta\mathbf{u}^{m-2}=0$ and (7.4) becomes :

$$\overline{\mathbf{u}}_J - \widetilde{\mathbf{u}}_J = -\frac{1}{\overline{\rho}_J}\mathcal{M}_J^{(2)} : \left(\mathbf{D}^{(1)}\rho\Big|_j \otimes \mathbf{D}^{(1)}\mathbf{u}\Big|_j\right) + \mathcal{O}(h^3) \tag{7.8}$$

wich requires a 1^{st}-order approximation of the gradients in $\mathbf{x}_j$to achieve third oder of accuracy.

B Relation for the average pressure $\overline{P}_J$

We use again a relation of the form of (3.46) to develop $\overline{P}_J$.
Moreover :

$$\widetilde{P}_J = (\gamma-1)\left((\overline{\rho E})_J - \frac{1}{2}\frac{|\,(\overline{\rho\mathbf{u}})_J\,|^2}{\overline{\rho}_J}\right) \tag{7.9}$$

Once again, the average conservative variables in equation (7.9) are expanded by means of (3.46), leading to :

$$\widetilde{\mathbf{P}}_J = \mathbf{P}_j - (\gamma-1)\frac{\rho_j}{\overline{\rho}_J}\frac{|\,\mathbf{u}_j\,|^2}{2}\sum_{m=2}^{n-1}\frac{1}{m!}\mathcal{M}_J^{(m)} : \mathbf{D}^{(m)}\rho\Big|_j + (\gamma-1)\left[\sum_{m=2}^{n-1}\frac{1}{m!}\mathcal{M}_J^{(m)} : \left(\mathbf{D}^{(m)}\rho E\Big|_j - \frac{1}{2\overline{\rho}_J}\,\mathbf{D}^{(m)}\mid\rho\mathbf{u}_j\mid^2\Big|_j\right)\right] + \mathcal{O}(h^n) \tag{7.10}$$

With a similar procedure, to that used for $\mathbf{u}$, we finally get :

$$\overline{\mathbf{P}}_J - \widetilde{\mathbf{P}}_J = \Delta\mathbf{P}^{n-2} - \frac{(\gamma-1)}{\overline{\rho}_J}\frac{\mathcal{M}_J^{(m-1)}}{(n-1)!} : \left[\sum_{l=1}^{n-2}\binom{n-1}{l}\mathbf{D}^{(m-1-l)}\rho\Big|_j \otimes \mathbf{D}^{(m)}\mid\rho\mathbf{u}_j\mid^2\Big|_j\right] + \mathcal{O}(h^n) \tag{7.11}$$

with :

$$\Delta\mathbf{P}^{n-2} = -\sum_{m=2}^{n-2}\frac{1}{m!}\mathcal{M}_J^{(m)} : \left\{\frac{(\gamma-1)}{\overline{\rho}_J}\left[\overline{\rho}_J\,\mathbf{D}^{(m)}(\rho E)\Big|_j + \rho_j\frac{|\,\mathbf{u}_j\,|^2}{2}\,\mathbf{D}^{(m)}\rho\Big|_j - \frac{1}{2}\,\mathbf{D}^{(m)}\mid\rho\mathbf{u}_j\mid^2\Big|_j\right] - \mathbf{D}^{(m)}P\Big|_j\right\} \tag{7.12}$$

Product derivatives like $\mathbf{D}^{(m)}(\rho E)$ or $\mathbf{D}^{(m)}\mid\rho\mathbf{u}_j\mid^2$ can be developed in terms of primitive :

$$\mathbf{D}^{(m)}\mid\rho\mathbf{u}_j\mid^2\Big|_j = \sum_{l=0}^{m}\binom{m}{l}\mathbf{D}^{(l)}\rho\Big|_j \otimes \mathbf{D}^{(l)}\mid\mathbf{u}_j\mid^2\Big|_j \tag{7.13}$$

$$\mathbf{D}^{(m)}(\rho E)\Big|_j = \sum_{l=0}^{m}\binom{m}{l}\mathbf{D}^{(m-l)}\rho\Big|_j \otimes \mathbf{D}^{(l)}E\Big|_j \tag{7.14}$$

$$= \sum_{l=0}^{m}\binom{m}{l}\mathbf{D}^{(m-l)}\rho\Big|_j \otimes \left[C_v\,\mathbf{D}^{(l)}T\Big|_j + \frac{1}{2}\,\mathbf{D}^{(m)}\mid\mathbf{u}_j\mid^2\Big|_j\right] \tag{7.15}$$

and,

$$\mathbf{D}^{(m)}\mid\mathbf{u}_j\mid^2\Big|_j \sum_{l=0}^{m}\binom{m}{l}\mathbf{D}^{(m-l)}\mathbf{u}_j\Big|_j \otimes \mathbf{D}^{(l)}\mathbf{u}_j\Big|_j \tag{7.16}$$

For a 3−exact reconstruction :

$$\overline{\mathbf{P}}_J - \widetilde{\mathbf{P}}_J = -\frac{(\gamma-1)}{\overline{\rho}_J}\mathcal{M}_J^{(2)} : \left\{ \mathbf{D}^{(1)}\rho\Big|_j \otimes \left[\mathbf{D}^{(1)}\rho\Big|_j \otimes \mid \mathbf{u}_j \mid^2 + 2\rho_j \, \mathbf{D}^{(1)} \mid \mathbf{u}_j \mid \Big|_j \right] \right\} + \mathcal{O}(h^3) \tag{7.17}$$

C Relation for the average pressure $\overline{T}_J$

We proceed again as in the two preceding cases. This time, we develop the average conservative variables in :

$$\widetilde{T} = \frac{\widetilde{P}}{R\overline{\rho}} \tag{7.18}$$

After some developments, is it possible to prove that :

$$\overline{\mathbf{T}}_J - \widetilde{\mathbf{T}}_J = \Delta\mathbf{T}^{n-2} - \frac{1}{\overline{\rho}_J}\frac{1}{(n-1)!}\mathcal{M}_J^{(n-1)} : \left\{ \sum_{l=1}^{n-2} \binom{n-1}{l} \mathbf{D}^{(m-1-l)}T\Big|_j \otimes \left[\mathbf{D}^{(l)}\rho\Big|_j - \frac{1}{2c_V\overline{\rho}_J} \mathbf{D}^{(l)}\rho \mid \mathbf{u} \mid^2 \Big|_j \right] \right\} + \mathcal{O}(h^n) \tag{7.19}$$

$$\Delta\mathbf{T}^{n-2} = -\sum_{m=2}^{n-2} \frac{1}{m!}\mathcal{M}_J^{(m)} : \left\{ \frac{-T_j}{\overline{\rho}_J} \mathbf{D}^{(m)}\rho) \Big|_j + (\gamma-1)\frac{\rho_j}{\overline{\rho}_J}\frac{\mid \mathbf{u} \mid_j^2}{\overline{\rho}_J} \mathbf{D}^{(m)}\rho\Big|_j + \frac{(\gamma-1)}{\overline{\rho}_J R} \mathbf{D}^{(m)}P\Big|_j - \mathbf{D}^{(m)}T\Big|_j \right\} \tag{7.20}$$

Again, $\Delta\mathbf{T}^{n-2}$ is null for $n = 3$.

For the 3^{rd}-order reconstruction :

$$\overline{\mathbf{T}}_J - \widetilde{\mathbf{T}}_J = -\frac{1}{\overline{\rho}_J}\mathcal{M}_J^{(2)} : \left\{ \mathbf{D}^{(1)}\rho\Big|_j \otimes \left[\mathbf{D}^{(1)}T\Big|_j - \frac{1}{2c_V\overline{\rho}_J} \mathbf{D}^{(1)}\rho \mid \mathbf{u} \mid^2 \Big|_j \right] \right\} + \mathcal{O}(h^n) \tag{7.21}$$

D Numerical approximation of $\overline{\mathbf{q}}_J - \widetilde{\mathbf{q}}_J$

After development of all product derivatives, expressions in equation (7.4), (7.11) and (7.19), only on the volume moments of order $n-1$ and derivatives of the primitive variables of order $n-2$. Thus, n^{th}-order accuracy is achieved by replacing exact derivatives of order $m \leq n-2$ with a numerical approximation of order $n-m-1$.

Chapter 8

Choice of the integration point Γ

If the face are not flat, the integration point is chosen in order to minimize the first order truncation error for the numerical integration. We can explicit the formula (3.44) at the second order of accuracy at the point Γ :

$$\iint_{A_{JK}} \mathbf{F}.\mathbf{n}dS = \mathbf{F}|_{\Gamma}.\mathcal{S}^{(\mathbf{0})}_{\mathbf{AJK}} + \underbrace{\mathbf{D}^{(\mathbf{1})}\mathbf{F}\Big|_{\Gamma} : \mathcal{S}^{(\mathbf{1})}_{\mathbf{AJK}}}_{\mathcal{E}_{\Gamma}} + \mid \mathcal{S}^{(\mathbf{0})}_{\mathbf{AJK}} \mid \mathcal{O}(h^2), \tag{8.1}$$

the same integration can be done on another point b knowing :

$$\mathbf{F}|_{\Gamma} = \mathbf{F}|_{b} + (\mathbf{x}_{\Gamma} - \mathbf{x}_{b}).\ \mathbf{D}^{(\mathbf{1})}(\mathbf{F})\Big|_{b}, \tag{8.2}$$

We can replace $\mathbf{F}|_{\Gamma}$ in equation (8.1) :

$$\iint_{A_{JK}} \mathbf{F}.\mathbf{n}dS = \mathbf{F}|_{b}.\mathcal{S}^{(\mathbf{0})}_{\mathbf{AJK}} + \underbrace{\mathbf{D}^{(\mathbf{1})}\mathbf{F}\Big|_{\Gamma} : \mathcal{S}^{(\mathbf{1})}_{\mathbf{AJK}} + \left((\mathbf{x}_{\Gamma} - \mathbf{x}_{b}).\ \mathbf{D}^{(\mathbf{1})}(\mathbf{F})\Big|_{b}\right).\mathcal{S}^{(\mathbf{0})}_{\mathbf{AJK}}}_{\mathcal{E}_{\mathbf{b}}} + \mid \mathcal{S}^{(\mathbf{0})}_{\mathbf{AJK}} \mid \mathcal{O}(h^2) \tag{8.3}$$

The integration error $\mathcal{E}_b$ can be expressed as a function of the integration error $\mathcal{E}_b$:

$$\mid \mathcal{E}_{\mathbf{b}} \mid^2 = \mid \mathcal{E}_{\mathbf{\Gamma}} \mid^2 + \left((\mathbf{x}_{\Gamma} - \mathbf{x}_{b}).\ \mathbf{D}^{(\mathbf{1})}(\mathbf{F})\Big|_{b}\right)^2 (\mathcal{S}^{(0)}_{A_{JK}})^2 + 2\ \mathbf{D}^{(\mathbf{1})}\mathbf{F}\Big|_{\Gamma} : \mathcal{S}^{(\mathbf{1})}_{\mathbf{AJK}}.\left((\mathbf{x}_{\Gamma} - \mathbf{x}_{b}).\ \mathbf{D}^{(\mathbf{1})}(\mathbf{F})\Big|_{b}\right).\mathcal{S}^{(0)}_{A_{JK}} \tag{8.4}$$

If we chose Γ so as to have $\mathcal{S}^{(\mathbf{1})}_{\mathbf{AJK}} \perp \mathcal{S}^{(\mathbf{0})}_{\mathbf{AJK}}$ we have :

$$\mid \mathcal{E}_{\mathbf{b}} \mid^2 = \mid \mathcal{E}_{\mathbf{\Gamma}} \mid^2 + \left((\mathbf{x}_{\Gamma} - \mathbf{x}_{b}).\ \mathbf{D}^{(\mathbf{1})}(\mathbf{F})\Big|_{b}\right)^2 (\mathcal{S}^{(0)}_{A_{JK}})^2 \tag{8.5}$$

and more simply,

$$\mathcal{E}_{\mathbf{b}} \geq \mathcal{E}_{\mathbf{\Gamma}} \quad \forall \quad b \quad \textbf{and} \quad \mathbf{D}^{(\mathbf{1})}(\mathbf{F}) \tag{8.6}$$

Lets define the point Γ :

$$\mathcal{S}^{(\mathbf{1})}_{\mathbf{AJK}}.\mathcal{S}^{(\mathbf{0})}_{\mathbf{AJK}} = 0 \tag{8.7}$$

$$\Rightarrow \left(\iint_{A_{JK}} (\mathbf{x} - \mathbf{x}_{\mathbf{\Gamma}}) \otimes \mathbf{n}dS\right).\mathcal{S}^{(\mathbf{0})}_{\mathbf{AJK}} = 0 \tag{8.8}$$

$$\Rightarrow \mathbf{O\Gamma}(\mathcal{S}^{(\mathbf{0})}_{\mathbf{AJK}})^2 = \iint_{A_{JK}} \mathbf{OM}.(\mathbf{n}dS.\mathcal{S}^{(\mathbf{0})}_{\mathbf{AJK}}) \tag{8.9}$$

To conclude, the point Γ is chosen in order to verify : $\mathbf{O\Gamma}(\mathcal{S}^{(\mathbf{0})}_{\mathbf{AJK}})^2 = \iint_{A_{JK}} \mathbf{OM}.(\mathbf{n}dS.\mathcal{S}^{(\mathbf{0})}_{\mathbf{AJK}})$ and this choice minimize the integration error of convective fluxes.

Chapter 9

Error estimation of the third order numerical scheme

Lets introduce the third order spatial operator:

$$\mathcal{H}_{III} = \frac{-\overline{\alpha}_{i+3} + 3\overline{\alpha}_{i+2} + 24\overline{\alpha}_{i+1} + 66\overline{\alpha}_i - 117\overline{\alpha}_{i-1} + 27\overline{\alpha}_{i-2} - 2\overline{\alpha}_{i-3}}{96} \tag{9.1}$$

The truncation error is calculating at the point i, link the average values to the point i is needed to estimate the truncation analysis of the scheme :

$$\alpha_{i+3} = \alpha_i + 3h \left.\frac{\partial \alpha}{\partial x}\right|_i + \frac{9h^2}{2} \left.\frac{\partial^2 \alpha}{\partial x^2}\right|_i + \frac{9h^3}{2} \left.\frac{\partial^3 \alpha}{\partial x^3}\right|_i + \frac{27h^4}{8} \left.\frac{\partial^4 \alpha}{\partial x^4}\right|_i + \mathcal{O}(h^5) \tag{9.2}$$

$$\alpha_{i+2} = \alpha_i + 2h \left.\frac{\partial \alpha}{\partial x}\right|_i + 2h^2 \left.\frac{\partial^2 \alpha}{\partial x^2}\right|_i + \frac{4h^3}{3} \left.\frac{\partial^3 \alpha}{\partial x^3}\right|_i + \frac{2h^4}{3} \left.\frac{\partial^4 \alpha}{\partial x^4}\right|_i + \mathcal{O}(h^5) \tag{9.3}$$

$$\alpha_{i+1} = \alpha_i + h \left.\frac{\partial \alpha}{\partial x}\right|_i + \frac{h^2}{2} \left.\frac{\partial^2 \alpha}{\partial x^2}\right|_i + \frac{h^3}{6} \left.\frac{\partial^3 \alpha}{\partial x^3}\right|_i + \frac{h^4}{24} \left.\frac{\partial^4 \alpha}{\partial x^4}\right|_i + \mathcal{O}(h^5) \tag{9.4}$$

$$\alpha_{i-1} = \alpha_i - h \left.\frac{\partial \alpha}{\partial x}\right|_i + \frac{h^2}{2} \left.\frac{\partial^2 \alpha}{\partial x^2}\right|_i - \frac{h^3}{6} \left.\frac{\partial^3 \alpha}{\partial x^3}\right|_i + \frac{h^4}{24} \left.\frac{\partial^4 \alpha}{\partial x^4}\right|_i + \mathcal{O}(h^5) \tag{9.5}$$

$$\alpha_{i-2} = \alpha_i - 2h \left.\frac{\partial \alpha}{\partial x}\right|_i + 2h^2 \left.\frac{\partial^2 \alpha}{\partial x^2}\right|_i - \frac{4h^3}{3} \left.\frac{\partial^3 \alpha}{\partial x^3}\right|_i + \frac{2h^4}{3} \left.\frac{\partial^4 \alpha}{\partial x^4}\right|_i + \mathcal{O}(h^5) \tag{9.6}$$

$$\alpha_{i-3} = \alpha_i - 3h \left.\frac{\partial \alpha}{\partial x}\right|_i + \frac{9h^2}{2} \left.\frac{\partial^2 \alpha}{\partial x^2}\right|_i - \frac{9h^3}{2} \left.\frac{\partial^3 \alpha}{\partial x^3}\right|_i + \frac{27h^4}{8} \left.\frac{\partial^4 \alpha}{\partial x^4}\right|_i + \mathcal{O}(h^5) \tag{9.7}$$

We know how to link the average values to the values at the center of gravity of a given cell:

$$
\begin{aligned}
\overline{\alpha}_i &= \alpha_i + \frac{h^2}{24}\left.\frac{\partial^2\alpha}{\partial x^2}\right|_i + \frac{h^4}{1920}\left.\frac{\partial^4\alpha}{\partial x^2}\right|_i + \mathcal{O}(h^6) \\
\overline{\alpha}_{i+3} &= \alpha_{i-3} + \frac{h^2}{24}\left.\frac{\partial^2\alpha}{\partial x^2}\right|_{i+3} + \frac{h^4}{1920}\left.\frac{\partial^4\alpha}{\partial x^4}\right|_{i+3} + \mathcal{O}(h^6) \\
\overline{\alpha}_{i+2} &= \alpha_{i+2} + \frac{h^2}{24}\left.\frac{\partial^2\alpha}{\partial x^2}\right|_{i+2} + \frac{h^4}{1920}\left.\frac{\partial^4\alpha}{\partial x^4}\right|_{i+2} + \mathcal{O}(h^6) \\
\overline{\alpha}_{i+1} &= \alpha_{i+1} + \frac{h^2}{24}\left.\frac{\partial^2\alpha}{\partial x^2}\right|_{i+1} + \frac{h^4}{1920}\left.\frac{\partial^4\alpha}{\partial x^4}\right|_{i+1} + \mathcal{O}(h^6) \\
\overline{\alpha}_{i-1} &= \alpha_{i-1} + \frac{h^2}{24}\left.\frac{\partial^2\alpha}{\partial x^2}\right|_{i-1} + \frac{h^4}{1920}\left.\frac{\partial^4\alpha}{\partial x^4}\right|_{i-1} + \mathcal{O}(h^6) \\
\overline{\alpha}_{i-2} &= \alpha_{i-2} + \frac{h^2}{24}\left.\frac{\partial^2\alpha}{\partial x^2}\right|_{i-2} + \frac{h^4}{1920}\left.\frac{\partial^4\alpha}{\partial x^4}\right|_{i-2} + \mathcal{O}(h^6) \\
\overline{\alpha}_{i-3} &= \alpha_{i-3} + \frac{h^2}{24}\left.\frac{\partial^2\alpha}{\partial x^2}\right|_{i-3} + \frac{h^4}{1920}\left.\frac{\partial^4\alpha}{\partial x^4}\right|_{i-3} + \mathcal{O}(h^6)
\end{aligned}
$$

Lets express the second derivatives at the point i:

$$
\begin{aligned}
\left.\frac{\partial^2\alpha}{\partial x^2}\right|_{i+3} &= \left.\frac{\partial^2\alpha}{\partial x^2}\right|_i + 3h\left.\frac{\partial^3\alpha}{\partial x^3}\right|_i + \frac{9h^2}{2}\left.\frac{\partial^4\alpha}{\partial x^4}\right|_i + \mathcal{O}(h^3) \\
\left.\frac{\partial^2\alpha}{\partial x^2}\right|_{i+2} &= \left.\frac{\partial^2\alpha}{\partial x^2}\right|_i + 2h\left.\frac{\partial^3\alpha}{\partial x^3}\right|_i + 2h^2\left.\frac{\partial^4\alpha}{\partial x^4}\right|_i + \mathcal{O}(h^3) \\
\left.\frac{\partial^2\alpha}{\partial x^2}\right|_{i+1} &= \left.\frac{\partial^2\alpha}{\partial x^2}\right|_i + h\left.\frac{\partial^3\alpha}{\partial x^3}\right|_i + \frac{h^2}{2}\left.\frac{\partial^4\alpha}{\partial x^4}\right|_i + \mathcal{O}(h^3) \\
\left.\frac{\partial^2\alpha}{\partial x^2}\right|_{i-1} &= \left.\frac{\partial^2\alpha}{\partial x^2}\right|_i - h\left.\frac{\partial^3\alpha}{\partial x^3}\right|_i + \frac{h^2}{2}\left.\frac{\partial^4\alpha}{\partial x^4}\right|_i + \mathcal{O}(h^3) \\
\left.\frac{\partial^2\alpha}{\partial x^2}\right|_{i-2} &= \left.\frac{\partial^2\alpha}{\partial x^2}\right|_i - 2h\left.\frac{\partial^3\alpha}{\partial x^3}\right|_i + 2h^2\left.\frac{\partial^4\alpha}{\partial x^4}\right|_i + \mathcal{O}(h^3) \\
\left.\frac{\partial^2\alpha}{\partial x^2}\right|_{i-3} &= \left.\frac{\partial^2\alpha}{\partial x^2}\right|_i - 3h\left.\frac{\partial^3\alpha}{\partial x^3}\right|_i + \frac{9h^2}{2}\left.\frac{\partial^4\alpha}{\partial x^4}\right|_i + \mathcal{O}(h^3)
\end{aligned}
$$

And for the fourth derivatives:

$$
\begin{aligned}
\left.\frac{\partial^4\alpha}{\partial x^4}\right|_{i+3} &= \left.\frac{\partial^4\alpha}{\partial x^4}\right|_i + \mathcal{O}(h) \\
\left.\frac{\partial^4\alpha}{\partial x^4}\right|_{i+2} &= \left.\frac{\partial^4\alpha}{\partial x^4}\right|_i + \mathcal{O}(h) \\
\left.\frac{\partial^4\alpha}{\partial x^4}\right|_{i+1} &= \left.\frac{\partial^4\alpha}{\partial x^4}\right|_i + \mathcal{O}(h) \\
\left.\frac{\partial^4\alpha}{\partial x^4}\right|_{i-1} &= \left.\frac{\partial^4\alpha}{\partial x^4}\right|_i + \mathcal{O}(h) \\
\left.\frac{\partial^4\alpha}{\partial x^4}\right|_{i-2} &= \left.\frac{\partial^4\alpha}{\partial x^4}\right|_i + \mathcal{O}(h) \\
\left.\frac{\partial^4\alpha}{\partial x^4}\right|_{i-3} &= \left.\frac{\partial^4\alpha}{\partial x^4}\right|_i + \mathcal{O}(h)
\end{aligned}
$$

so :

$$\overline{\alpha}_{i+3} = \alpha_{i+3} + \frac{h^2}{24}\left[\left.\frac{\partial^2\alpha}{\partial x^2}\right|_i + 3h\left.\frac{\partial^3\alpha}{\partial x^3}\right|_i + \frac{9h^2}{2}\left.\frac{\partial^4\alpha}{\partial x^4}\right|_i + \mathcal{O}(h^3)\right] + \frac{h^4}{1920}\left[\left.\frac{\partial^4\alpha}{\partial x^4}\right|_i + \mathcal{O}(h)\right]$$
$$\overline{\alpha}_{i+2} = \alpha_{i+2} + \frac{h^2}{24}\left[\left.\frac{\partial^2\alpha}{\partial x^2}\right|_i + 2h\left.\frac{\partial^3\alpha}{\partial x^3}\right|_i + 2h^2\left.\frac{\partial^4\alpha}{\partial x^4}\right|_i + \mathcal{O}(h^3)\right] + \frac{h^4}{1920}\left[\left.\frac{\partial^4\alpha}{\partial x^4}\right|_i + \mathcal{O}(h)\right]$$
$$\overline{\alpha}_{i+1} = \alpha_{i+1} + \frac{h^2}{24}\left[\left.\frac{\partial^2\alpha}{\partial x^2}\right|_i + h\left.\frac{\partial^3\alpha}{\partial x^3}\right|_i + \frac{h^2}{2}\left.\frac{\partial^4\alpha}{\partial x^4}\right|_i + \mathcal{O}(h^3)\right] + \frac{h^4}{1920}\left[\left.\frac{\partial^4\alpha}{\partial x^4}\right|_i + \mathcal{O}(h)\right]$$
$$\overline{\alpha}_{i-1} = \alpha_{i-1} + \frac{h^2}{24}\left[\left.\frac{\partial^2\alpha}{\partial x^2}\right|_i - h\left.\frac{\partial^3\alpha}{\partial x^3}\right|_i + \frac{h^2}{2}\left.\frac{\partial^4\alpha}{\partial x^4}\right|_i + \mathcal{O}(h^3)\right] + \frac{h^4}{1920}\left[\left.\frac{\partial^4\alpha}{\partial x^4}\right|_i + \mathcal{O}(h)\right]$$
$$\overline{\alpha}_{i-2} = \alpha_{i-2} + \frac{h^2}{24}\left[\left.\frac{\partial^2\alpha}{\partial x^2}\right|_i - 2h\left.\frac{\partial^3\alpha}{\partial x^3}\right|_i + 2h^2\left.\frac{\partial^4\alpha}{\partial x^4}\right|_i + \mathcal{O}(h^3)\right] + \frac{h^4}{1920}\left[\left.\frac{\partial^4\alpha}{\partial x^4}\right|_i + \mathcal{O}(h)\right]$$
$$\overline{\alpha}_{i-3} = \alpha_{i-3} + \frac{h^2}{24}\left[\left.\frac{\partial^2\alpha}{\partial x^2}\right|_i - 3h\left.\frac{\partial^3\alpha}{\partial x^3}\right|_i + \frac{9h^2}{2}\left.\frac{\partial^4\alpha}{\partial x^4}\right|_i + \mathcal{O}(h^3)\right] + \frac{h^4}{1920}\left[\left.\frac{\partial^4\alpha}{\partial x^4}\right|_i + \mathcal{O}(h)\right]$$

Simplifying the equation below we get :

$$\overline{\alpha}_{i+3} = \alpha_{i-3} + \frac{h^2}{24}\left.\frac{\partial^2\alpha}{\partial x^2}\right|_i + \frac{h^3}{8}\left.\frac{\partial^3\alpha}{\partial x^3}\right|_i + \frac{361h^4}{1920}\left.\frac{\partial^4\alpha}{\partial x^4}\right|_i + \mathcal{O}(h^5)$$
$$\overline{\alpha}_{i+2} = \alpha_{i+2} + \frac{h^2}{24}\left.\frac{\partial^2\alpha}{\partial x^2}\right|_i + \frac{h^3}{12}\left.\frac{\partial^3\alpha}{\partial x^3}\right|_i + \frac{161h^4}{1920}\left.\frac{\partial^4\alpha}{\partial x^4}\right|_i + \mathcal{O}(h^5)$$
$$\overline{\alpha}_{i+1} = \alpha_{i+1} + \frac{h^2}{24}\left.\frac{\partial^2\alpha}{\partial x^2}\right|_i + \frac{h^3}{24}\left.\frac{\partial^3\alpha}{\partial x^3}\right|_i + \frac{41h^4}{1920}\left.\frac{\partial^4\alpha}{\partial x^4}\right|_i + \mathcal{O}(h^5)$$
$$\overline{\alpha}_{i-1} = \alpha_{i-1} + \frac{h^2}{24}\left.\frac{\partial^2\alpha}{\partial x^2}\right|_i - \frac{h^3}{24}\left.\frac{\partial^3\alpha}{\partial x^3}\right|_i + \frac{41h^4}{1920}\left.\frac{\partial^4\alpha}{\partial x^4}\right|_i + \mathcal{O}(h^5)$$
$$\overline{\alpha}_{i-2} = \alpha_{i-2} + \frac{h^2}{24}\left.\frac{\partial^2\alpha}{\partial x^2}\right|_i - \frac{h^3}{12}\left.\frac{\partial^3\alpha}{\partial x^3}\right|_i + \frac{161h^4}{1920}\left.\frac{\partial^4\alpha}{\partial x^4}\right|_i + \mathcal{O}(h^5)$$
$$\overline{\alpha}_{i-3} = \alpha_{i-3} + \frac{h^2}{24}\left.\frac{\partial^2\alpha}{\partial x^2}\right|_i - \frac{h^3}{8}\left.\frac{\partial^3\alpha}{\partial x^3}\right|_i + \frac{361h^4}{1920}\left.\frac{\partial^4\alpha}{\partial x^4}\right|_i + \mathcal{O}(h^5)$$

We linked the average values to the values at the point i using the derivative at the point i. We can use these results in the first Taylor expansion :

$$\overline{\alpha}_{i+3} = \alpha_i + 3h\left.\frac{\partial\alpha}{\partial x}\right|_i + \frac{9h^2}{2}\left.\frac{\partial^2\alpha}{\partial x^2}\right|_i + \frac{9h^3}{2}\left.\frac{\partial^3\alpha}{\partial x^3}\right|_i + \frac{27h^4}{8}\left.\frac{\partial^4\alpha}{\partial x^4}\right|_i + \frac{h^2}{24}\left.\frac{\partial^2\alpha}{\partial x^2}\right|_i + \frac{h^3}{8}\left.\frac{\partial^3\alpha}{\partial x^3}\right|_i + \frac{361h^4}{1920}\left.\frac{\partial^4\alpha}{\partial x^4}\right|_i + \mathcal{O}(h^5)$$
$$\overline{\alpha}_{i+2} = \alpha_i + 2h\left.\frac{\partial\alpha}{\partial x}\right|_i + 2h^2\left.\frac{\partial^2\alpha}{\partial x^2}\right|_i + \frac{4h^3}{3}\left.\frac{\partial^3\alpha}{\partial x^3}\right|_i + \frac{2h^4}{3}\left.\frac{\partial^4\alpha}{\partial x^4}\right|_i + \frac{h^2}{24}\left.\frac{\partial^2\alpha}{\partial x^2}\right|_i + \frac{h^3}{12}\left.\frac{\partial^3\alpha}{\partial x^3}\right|_i + \frac{161h^4}{1920}\left.\frac{\partial^4\alpha}{\partial x^4}\right|_i + \mathcal{O}(h^5)$$
$$\overline{\alpha}_{i+1} = \alpha_i + h\left.\frac{\partial\alpha}{\partial x}\right|_i + \frac{h^2}{2}\left.\frac{\partial^2\alpha}{\partial x^2}\right|_i + \frac{h^3}{6}\left.\frac{\partial^3\alpha}{\partial x^3}\right|_i + \frac{h^4}{24}\left.\frac{\partial^4\alpha}{\partial x^4}\right|_i + \frac{h^2}{24}\left.\frac{\partial^2\alpha}{\partial x^2}\right|_i + \frac{h^3}{24}\left.\frac{\partial^3\alpha}{\partial x^3}\right|_i + \frac{41h^4}{1920}\left.\frac{\partial^4\alpha}{\partial x^4}\right|_i + \mathcal{O}(h^5)$$
$$\overline{\alpha}_{i-1} = \alpha_i - h\left.\frac{\partial\alpha}{\partial x}\right|_i + \frac{h^2}{2}\left.\frac{\partial^2\alpha}{\partial x^2}\right|_i - \frac{h^3}{6}\left.\frac{\partial^3\alpha}{\partial x^3}\right|_i + \frac{h^4}{24}\left.\frac{\partial^4\alpha}{\partial x^4}\right|_i + \frac{h^2}{24}\left.\frac{\partial^2\alpha}{\partial x^2}\right|_i - \frac{h^3}{24}\left.\frac{\partial^3\alpha}{\partial x^3}\right|_i + \frac{361h^4}{1920}\left.\frac{\partial^4\alpha}{\partial x^4}\right|_i + \mathcal{O}(h^5)$$
$$\overline{\alpha}_{i-2} = \alpha_i - 2h\left.\frac{\partial\alpha}{\partial x}\right|_i + 2h^2\left.\frac{\partial^2\alpha}{\partial x^2}\right|_i - \frac{4h^3}{3}\left.\frac{\partial^3\alpha}{\partial x^3}\right|_i + \frac{2h^4}{3}\left.\frac{\partial^4\alpha}{\partial x^4}\right|_i + \frac{h^2}{24}\left.\frac{\partial^2\alpha}{\partial x^2}\right|_i - \frac{h^3}{12}\left.\frac{\partial^3\alpha}{\partial x^3}\right|_i + \frac{161h^4}{1920}\left.\frac{\partial^4\alpha}{\partial x^4}\right|_i + \mathcal{O}(h^5)$$
$$\overline{\alpha}_{i-3} = \alpha_i - 3h\left.\frac{\partial\alpha}{\partial x}\right|_i + \frac{9h^2}{2}\left.\frac{\partial^2\alpha}{\partial x^2}\right|_i - \frac{9h^3}{2}\left.\frac{\partial^3\alpha}{\partial x^3}\right|_i + \frac{27h^4}{8}\left.\frac{\partial^4\alpha}{\partial x^4}\right|_i + \frac{h^2}{24}\left.\frac{\partial^2\alpha}{\partial x^2}\right|_i - \frac{h^3}{8}\left.\frac{\partial^3\alpha}{\partial x^3}\right|_i + \frac{41h^4}{1920}\left.\frac{\partial^4\alpha}{\partial x^4}\right|_i + \mathcal{O}(h^5)$$

Finally, we get :

$$
\begin{aligned}
\overline{\alpha}_i &= \alpha_i + \frac{h^2}{24}\left.\frac{\partial^2\alpha}{\partial x^2}\right|_i + \frac{h^4}{1920}\left.\frac{\partial^4\alpha}{\partial x^4}\right|_i \mathcal{O}(h^6)\\
\overline{\alpha}_{i+3} &= \alpha_i + 3h\left.\frac{\partial\alpha}{\partial x}\right|_i + \frac{109h^2}{24}\left.\frac{\partial^2\alpha}{\partial x^2}\right|_i + \frac{37h^3}{8}\left.\frac{\partial^3\alpha}{\partial x^3}\right|_i + \frac{6841h^4}{1920}\left.\frac{\partial^4\alpha}{\partial x^4}\right|_i + \mathcal{O}(h^5)\\
\overline{\alpha}_{i+2} &= \alpha_i + 2h\left.\frac{\partial\alpha}{\partial x}\right|_i + \frac{49h^2}{24}\left.\frac{\partial^2\alpha}{\partial x^2}\right|_i + \frac{17h^3}{12}\left.\frac{\partial^3\alpha}{\partial x^3}\right|_i + \frac{1441h^4}{1920}\left.\frac{\partial^4\alpha}{\partial x^4}\right|_i \mathcal{O}(h^5)\\
\overline{\alpha}_{i+1} &= \alpha_i + h\left.\frac{\partial\alpha}{\partial x}\right|_i + \frac{13h^2}{24}\left.\frac{\partial^2\alpha}{\partial x^2}\right|_i + \frac{5h^3}{24}\left.\frac{\partial^3\alpha}{\partial x^3}\right|_i + \frac{121h^4}{1920}\left.\frac{\partial^4\alpha}{\partial x^4}\right|_i + \mathcal{O}(h^5)\\
\overline{\alpha}_{i-1} &= \alpha_i - h\left.\frac{\partial\alpha}{\partial x}\right|_i + \frac{13h^2}{24}\left.\frac{\partial^2\alpha}{\partial x^2}\right|_i - \frac{5h^3}{24}\left.\frac{\partial^3\alpha}{\partial x^3}\right|_i + \frac{121h^4}{1920}\left.\frac{\partial^4\alpha}{\partial x^4}\right|_i + \mathcal{O}(h^5)\\
\overline{\alpha}_{i-2} &= \alpha_i - 2h\left.\frac{\partial\alpha}{\partial x}\right|_i + \frac{49h^2}{24}\left.\frac{\partial^2\alpha}{\partial x^2}\right|_i - \frac{17h^3}{12}\left.\frac{\partial^3\alpha}{\partial x^3}\right|_i + \frac{1441h^4}{1920}\left.\frac{\partial^4\alpha}{\partial x^4}\right|_i + \mathcal{O}(h^5)\\
\overline{\alpha}_{i-3} &= \alpha_i - 3h\left.\frac{\partial\alpha}{\partial x}\right|_i + \frac{109h^2}{24}\left.\frac{\partial^2\alpha}{\partial x^2}\right|_i - \frac{37h^3}{8}\left.\frac{\partial^3\alpha}{\partial x^3}\right|_i + \frac{6841h^4}{1920}\left.\frac{\partial^4\alpha}{\partial x^4}\right|_i + \mathcal{O}(h^5)
\end{aligned}
$$

If we replace the quantities calculated below in the spatial operato(9.1), we have :

$$
\begin{aligned}
\mathcal{L}_{VF}(\overline{\alpha})|_i &= \left.\frac{-\overline{\alpha}_{i+3} + 3\overline{\alpha}_{i+2} + 24\overline{\alpha}_{i+1} + 66\overline{\alpha}_i - 117\overline{\alpha}_{i-1} + 27\overline{\alpha}_{i-2} - 2\overline{\alpha}_{i-3}}{96}\right|_i\\
&= \frac{h}{96}\left[-3\left.\frac{\partial\alpha}{\partial x}\right|_i + 6\left.\frac{\partial\alpha}{\partial x}\right|_i + 24\left.\frac{\partial\alpha}{\partial x}\right|_i + 177\left.\frac{\partial\alpha}{\partial x}\right|_i - 54\left.\frac{\partial\alpha}{\partial x}\right|_i + 6\left.\frac{\partial\alpha}{\partial x}\right|_i\right]\\
&+ \frac{h^2}{96}\left[-\frac{109}{24}\left.\frac{\partial^2\alpha}{\partial x^2}\right|_i + \frac{147}{24}\left.\frac{\partial^2\alpha}{\partial x^2}\right|_i + \frac{312}{24}\left.\frac{\partial^2\alpha}{\partial x^2}\right|_i + \frac{66}{24}\left.\frac{\partial^2\alpha}{\partial x^2}\right|_i - \frac{1521}{24}\left.\frac{\partial^2\alpha}{\partial x^2}\right|_i + \frac{1323}{24}\left.\frac{\partial^2\alpha}{\partial x^2}\right|_i - \frac{218}{24}\left.\frac{\partial^2\alpha}{\partial x^2}\right|_i\right]\\
&+ \frac{h^3}{96}\left[-\frac{37}{8}\left.\frac{\partial^3\alpha}{\partial x^3}\right|_i + \frac{17}{4}\left.\frac{\partial^3\alpha}{\partial x^3}\right|_i + 5\left.\frac{\partial^2\alpha}{\partial x^2}\right|_i + \frac{195}{8}\left.\frac{\partial^3\alpha}{\partial x^3}\right|_i - \frac{153}{4}\left.\frac{\partial^3\alpha}{\partial x^3}\right|_i + \frac{37}{4}\left.\frac{\partial^3\alpha}{\partial x^3}\right|_i\right]\\
&+ \frac{h^4}{96}\left[-\frac{6841}{1920}\left.\frac{\partial^4\alpha}{\partial x^4}\right|_i + \frac{1441}{640}\left.\frac{\partial^4\alpha}{\partial x^4}\right|_i + \frac{121}{80}\left.\frac{\partial^2\alpha}{\partial x^2}\right|_i + \frac{11}{320}\left.\frac{\partial^4\alpha}{\partial x^4}\right|_i - \frac{4719}{640}\left.\frac{\partial^4\alpha}{\partial x^4}\right|_i + \frac{12969}{640}\left.\frac{\partial^4\alpha}{\partial x^4}\right|_i - \frac{6841}{960}\left.\frac{\partial^4\alpha}{\partial x^4}\right|_i\right]
\end{aligned}
$$

$$
\mathcal{L}_{VF}(\overline{\alpha})|_i = \left.\frac{\overline{\alpha}_{i+2} + 11\overline{\alpha}_{i+1} + 34\overline{\alpha}_i - 58\overline{\alpha}_{i-1} + 13\overline{\alpha}_{i-2} - \overline{\alpha}_{i-3})}{48}\right|_i = h\left.\frac{\partial\alpha}{\partial x}\right|_i + \frac{h^4}{16}\left.\frac{\partial^4\alpha}{\partial x^4}\right|_i + \mathcal{O}(h^5) \quad (9.8)
$$

We demonstrate the accuracy of the third oder spatial operator through a truncation error analysis.

Chapter 10

Initialization of the Ringleb flow problem

The equation of the Ringleb problem are :

$$a = \sqrt{\left(1 - \frac{\gamma - 1}{2} q^2\right)}; \quad \rho = a^{\frac{2\gamma}{\gamma - 1}}; \quad p = \frac{1}{\rho} a^{\frac{2\gamma}{\gamma - 1}}; \quad J = \frac{1}{a} + \frac{1}{3a^3} + \frac{1}{5a^5} - \frac{1}{2} ln\left(\frac{1-a}{1+a}\right) \tag{10.1}$$

$$x(q,k) = \frac{1}{2\rho}\left(\frac{2}{k^2} - \frac{1}{q^2}\right) - \frac{J}{2} \quad \text{and} \quad y(q,k) = \pm \frac{1}{k\rho q}\sqrt{1 - \left(\frac{q}{k}\right)^2}, \tag{10.2}$$

where a is the speed of sound, q is the velocity magnitude, k is a streamline parameter, p is the pressure, x and y are the coordinates of the streamlines and γ is the heat capacity ration (equal to 1.4 for the air). To initialize the calculation, we need to inverse the system (10.2) but it won't be used on this form. We can remark that the system (10.2) represent a circle of center $\left(-\frac{J}{2}, 0\right)$. We can start from the equation (10.2) to isolate the q variable :

$$\left(x + \frac{J}{2}\right)^2 + y^2 = \frac{1}{4\rho^2}\left(\frac{2q^2 - k^2}{k^2 q^2}\right)^2 + \frac{1}{\rho^2 k^2 q^2}\left(\frac{k^2 - q^2}{k^2}\right)$$

$$\Longrightarrow \left(x + \frac{J}{2}\right)^2 + y^2 = \left(\frac{q^4 - q^2k^2 - \frac{1}{4}k^4 + q^2k^2 - q^4}{\rho^2 k^4 q^4}\right) \tag{10.3}$$

$$\Longrightarrow \left(x + \frac{J}{2}\right)^2 + y^2 = \frac{1}{4\rho^2 q^4} \tag{10.4}$$

$$\Longrightarrow q = \left[4\rho^2\left(\left(x + \frac{J}{2}\right)^2 + y^2\right)\right]^{-1/4}, \tag{10.5}$$

$$\tag{10.6}$$

Now, we can find the relationship for the k variable :

$$\left(x + \frac{J}{2}\right) 2\rho = \frac{2}{k^2} - \left[4\rho^2\left(\left(x + \frac{J}{2}\right)^2 + y^2\right)\right]^{1/2}$$

$$\Longrightarrow k = \left[\rho\left(x + \frac{J}{2}\right) + \rho\left[\left(x + \frac{J}{2}\right)^2 + y^2\right]^{1/2}\right]^{-1/2} \tag{10.7}$$

It is simpler to inverse the system (10.6) than the system (10.2) because we resolve variables one by one. In practice, we use a Newton algorithm to calculate the variable q, and then we calculate the variable k with the formula 10.7. We know the exact solution of the Ringleb flow on each grid point, but it is not sufficient. It is very important to be aware that the study concern a finite volume solver (FLUSEPA). In a finite volume solver, the unknowns are the averaged conservative variables, that why, the Ringleb flow problem inputs have to be the averaged conservative variables. We can only calculate an approximation of the conservative inputs knowing the exact point values, its not a problem, the only thing we have to be careful is to calculate an higher order approximation than the numerical scheme itself. To do so, we use a six order Gauss integration to calculate conservative variables from the point values. In 2D, the quads are split into two triangles and Gauss integration is performed on each triangle, in 3D, tetrahedrons are split into 8 tetrahedrons, and Gauss integration is performed on each tetrahedron. This lead to know a six order accurate initial solution for the conservative variables which represent the inputs of the Ringleb flow for a finite volume solver which allows checking the numerical orders of convergence provided by the numerical schemes under investigation.

Chapter 11

Post-treatments for the Taylor-Green vortex problem

Lets define the so called "enstrophy" quantity :

$$\omega = \overline{w_i' w_i'} \tag{11.1}$$

where w_i is the fluctuating vorticity. The dissipation rate of the turbulent kinetic energy reads :

$$\epsilon = -\frac{dk}{dt} \tag{11.2}$$

Quantities Ω and ϵ are linked [24] :

$$\epsilon \simeq \nu \overline{w_i' w_i'} \tag{11.3}$$

Note that the equality is exact for homogeneous and isotropic turbulence. So we have :

$$-\frac{dk}{dt} = \nu \overline{w_i' w_i'} \tag{11.4}$$

To compare the calculations with DNS, it is usual to calculate the following quantities which are the time derivative of the total kinetic energy :

$$K = \frac{1}{(2\pi)^3} \iiint_{[0;2\pi]^3} \frac{1}{2}\rho \mid\mid \mathbf{u} \mid\mid^2 dxdydz \tag{11.5}$$

and the total enstrophy :

$$\Omega = \frac{1}{(2\pi)^3} \iiint_{[0;2\pi]^3} \frac{1}{2}\rho \mid\mid \boldsymbol{\omega} \mid\mid^2 dxdydz. \tag{11.6}$$

As we demonstrate below, $-\frac{dK}{dt} = \nu\Omega$, and it implies that physically, it is strictly equivalent to compare the results with Ω or with $-\frac{dK}{dt}$. For example, in the reference DNS [95], is the enstrophy curve is multiplied by the reference viscosity ($\nu = 0.00125$), it becomes exactly superimposed on the curve which illustrate the quantity $-\frac{dK}{dt}$. There is no physical reason to have different numerical results concerning Ω and $\frac{dK}{dt}$. We can conclude that calculating Ω or $\frac{dK}{dt}$ from the numerical simulation is post-processing dependent. For example, lets try to quantify the numerical error done when calculating Ω. Numerically, the enstrophy calculated at the center of gravity i of each cells I is summed over the whole computational domain :

$$(2\pi)^3\Omega = \sum_{[0;2\pi]^3} \left[\iiint_{[0;2\pi]^3} \left(\Omega_i + \mathcal{O}(h^2)\right) dV \right] \tag{11.7}$$

$$= (2\pi)^3 \sum_{[0;2\pi]^3} \Omega_i + (2\pi)^3 \mathcal{O}(h^2) \tag{11.8}$$

here, we remark that the numerical integration is polluted by an order 2 error. Actually, this is not the most important error, lets calculate the enstrophy in the cell I using a n^{th} order space differentiation operator to calculate gradients :

$$\mathcal{D}^{(1)}_{\mathbf{N}}(u) \simeq \mathbf{D}^{(1)}u + \frac{h^n}{C}\mathbf{D}^{(n)}u \tag{11.9}$$

If we use the previous operator to calculate the enstrophy, we get :

$$\Omega_i \sim \left(\mathbf{D}^{(1)}(u)\right)^2 + 2\mathbf{D}^{(1)}(u)\frac{h^n}{C}\mathbf{D}^{(n)}u + \left(\frac{h^n}{C}\mathbf{D}^{(n)}u\right)^2 \tag{11.10}$$

And finally, the equation (11.8) becomes :

$$\Omega \sim \underbrace{\sum_{[0;2\pi]^3}\left(\mathbf{D}^{(1)}(u)\Big|_i\right)^2}_{\text{Total enstrophy}} + \underbrace{\sum_{[0;2\pi]^3} 2\,\mathbf{D}^{(1)}(u)\Big|_i \frac{h^n}{C}\mathbf{D}^{(n)}u + \sum_{[0;2\pi]^3}\left(\frac{h^n}{C}\,\mathbf{D}^{(n)}u\Big|_i\right)^2}_{\text{Error term due to space derivative approximation}} + \underbrace{\mathcal{O}(h^2)}_{\text{Integration error}} \tag{11.11}$$

We demonstrate that the calculation of enstrophy is polluted by two kind of errors, an error due to the gradient operator and an error due to the numerical integration. Practically, we remark that the most important error is due to the choice of differentiation operator. To calculate the enstrophy, we choose an seven order accurate gradient operator since it is the minimum order not to be polluted by the truncation error.

Modèles de turbulence auto-adaptatifs pour la simulation des écoulements compressibles instationnaires

RESUME : Cette thèse est principalement dédiée à la simulation des écoulements massivement décollés dans le domaine spatial. Nous avons restreint notre étude aux écoulements d'arrière-corps, pour lesquels ces décollements sont imposés par des changements brutaux de la géométrie. Dans le domaine spatial, le caractère fortement compressible des écoulements rencontrés impose l'utilisation de schémas numériques robustes. D'un autre coté, la simulation fine de la turbulence impose des schémas d'ordre élevé et peu dissipatifs. Ces deux spécifications, apparemment contradictoires, doivent pourtant coexister au sein d'une même simulation. Les modèles de turbulence ainsi que les schémas de discrétisation sont indissociables et leur couplage doit impérativement être considéré. Les schémas numériques doivent garder leur précision formelle sur des géométries complexes et des maillages très irréguliers imposés par le contexte industriel. Cette étude analyse le schéma de discrétisation utilisé dans le code de calcul FLUSEPA développé par Airbus Defence & Space. Ce schéma est robuste et précis pour des écoulements avec chocs et il présente une faible sensibilité au maillage (l'ordre 3 étant conservé même sur des maillages fortement perturbés). Malheureusement, le schéma possède une trop faible résolvabilité liée à un niveau de dissipation trop élevé pour envisager des simulations hybrides RANS/LES. Pour pallier cet inconvénient, nous nous sommes penchés vers une solution basée sur un recentrage conditionnel et local : dans les zones dominées par des structures tourbillonnaires, une fonction analytique assure un recentrage local lorsque la stabilité numérique le permet. Cette condition de stabilité assure le couplage entre le schéma et le modèle. De cette manière, les viscosités laminaire et tourbillonnaire sont les seules à jouer un rôle dans les régions dominées par la vorticité et servent aussi à stabiliser le schéma numérique. Cette étude présente de plus une comparaison qualitative et quantitative de plusieurs modèles hybrides RANS/LES, à iso maillage et schéma numérique. Pour cela, un certain nombre d'améliorations (notamment de leur capacité à résoudre les instabilités de Kelvin-Helmohlotz sans retard), proposées dans la littérature ou bien introduites dans cette thèse, sont prises en compte. Les applications numériques étudiées concernent des géométries allant de la marche descendante au lanceur spatial complet à échelle réduite.

Mots clés : Volumes finis d'ordre élevé, VC scheme, maillages non-structurés et irréguliers, FLUSEPA, modèles hybride RANS/LES, turbulence, multi-chevauchement de maillages par intersection conservatives, lanceurs spatiaux, applications industrielles.

Self adaptive turbulence models for unsteady compressible flows

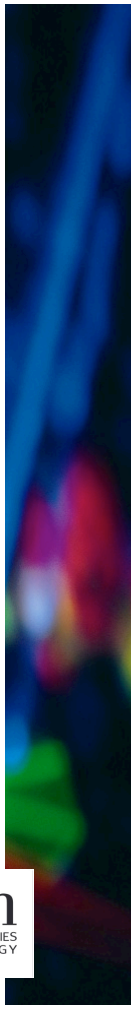

ABSTRACT: This thesis is mainly dedicated to the simulation of massively separated flows in the aerospace domain. We restricted our study to afterbody flows, where the separation is imposed by abrupt geometry changes. In the aerospace domain, highly compressible flows require the use of robust numerical schemes. On the other hand, the simulation of turbulence imposes high-order low dissipative numerical schemes. These two specifications, apparently contradictory, must coexist within the same simulation. The coupling between turbulence models and discretization schemes is of the utmost importance and must be considered. Numerical schemes should keep their formal accuracy on complex geometries and on very irregular meshes imposed by the industrial context. In this research, we analyze the discretization scheme implemented in the FLUSEPA solver, developed by Airbus Defence & Space. Such a scheme is robust and accurate for flows with shocks and exhibits a low sensitivity to the grid (the third order of accuracy being ensured, even on highly irregular grids). Unfortunately, the scheme possesses a too low resolvability related to a too high numerical dissipation for RANS/LES simulations. To circumvent this problem, we considered a conditional and local re-centering strategy: in regions dominated by vortical structures, an analytic function provides local re-centering when a numerical stability condition is satisfied. This stability condition ensures the coupling between the numerical scheme and the model. In this way, only the turbulent and the laminar viscosities play a role in regions dominated by vorticity, and also allow to stabilize the numerical scheme. This study provides also a qualitative and quantitative assessment of several hybrid RANS/LES models, using the same grids and discretization scheme. For this purpose some recent improvements (improving their ability to trigger the Kelvin-Helmohlotz instabilities without delay), proposed in the litterature or suggested in this work, are taken into account. Numerical applications include geometrical configurations ranging from a backward facing step to realistic launcher configurations.

Keywords : High order finite volumes, VC scheme, irregular grids, unstructured grids, FLUSEPA, hybrid RANS/LES models, turbulence, conservative grid intersections, space launchers, industrial applications.

ARTS ET MÉTIERS ParisTech

ParisTech
INSTITUT DES SCIENCES ET TECHNOLOGIES
PARIS INSTITUTE OF TECHNOLOGY